Universidade de São Paulo
Instituto de Física

Supercondutividade não centrossimétrica e efeito de pico em materiais à base de rênio

Fábio Santos Alves Abud

Orientador: Prof. Dr. Renato de Figueiredo Jardim

Tese de doutorado apresentada ao Instituto de Física da Universidade de São Paulo, como requisito parcial para a obtenção do título de Doutor em Ciências.

Banca Examinadora:
Prof. Dr. Renato de Figueiredo Jardim - Orientador (IFUSP)
Prof. Dr. Daniel Reinaldo Cornejo (IFUSP)
Profa. Dra. Maria José Ramos Sandim (EEL USP)
Prof. Dr. Enzo Granato (INPE)
Prof. Dr. Mário Sérgio da Luz (UFMT)

São Paulo
2021

FICHA CATALOGRÁFICA
Preparada pelo Serviço de Biblioteca e Informação
do Instituto de Física da Universidade de São Paulo

Abud, Fábio Santos Alves

Supercondutividade não centrossimétrica e efeito de pico em materiais à base de rênio São Paulo, 2021.

Tese (Doutorado) – Universidade de São Paulo. Instituto de Física. Depto. de Física dos Materiais e Mecânica

Orientador: Prof. Dr. Renato de Figueiredo Jardim

Área de Concentração: Física

Unitermos: 1. Supercondutividade; 2. Propriedades dos sólidos; 3. Calor específico; 4. Física Experimental; 5. Materiais.

USP/IF/SBI-070/2021

Universidade de São Paulo
Instituto de Física

Noncentrosymmetric superconductivity and peak effect in rhenium based materials

Fábio Santos Alves Abud

Supervisor: Prof. Dr. Renato de Figueiredo Jardim

Thesis submitted to the Instituto de Física, Universidade de São Paulo in partial fulfillment of the requirements for the degree of Doctor of Science.

Examining Committee:
Prof. Dr. Renato de Figueiredo Jardim - Supervisor (IFUSP)
Prof. Dr. Daniel Reinaldo Cornejo (IFUSP)
Profa. Dra. Maria José Ramos Sandim (EEL USP)
Prof. Dr. Enzo Granato (INPE)
Prof. Dr. Mário Sérgio da Luz (UFMT)

São Paulo
2021

Acknowledgments

I would like to acknowledge my advisor, professor Renato F. Jardim, for giving me the opportunity to take on this PhD. His enthusiasm, continuous support, guidance and experience certainly encouraged me to pursuit the some times daunting task of conducting scientific research. I'm also grateful for the advices he gave me on various aspects of the academic life throughout the past years.

I also would like to acknowledge all of the DFMT staff, specially the technical staff whose help was central not only to conduct some routinely low temperatures experiments but also to create or adapt experimental setups in the development of this project.

I'm also indebted to the crystallography group of the FAP-IFUSP, specially to Társis Germano and Antônio Carlos Franco, who were always available and welcoming in the countless times that I had to run x-ray diffraction experiments.

Many thanks are also due to ours collaborators at DEMAR/EEL-Lorena, specially to professor Antonio Jefferson Machado and his student Lucas Corrêa, whose help in conducting the heat treatments at high temperatures was essential to the progress of this study.

I would also like to thank professor Milton Torikachvili from San Diego State University for the A.C. susceptibility and thermal conductivity measurements in several Re_3M samples.

A special thanks to professor James M. Valles Jr. for the generous hospitality at Brown University, where part of this work was conducted. I really appreciate his time and will to help during my pleasant stay in Providence, where I could learn a great deal of experimental physics while working on measurements of differential conductance in thin films.

I would like to acknowledge Dr. Carlos César B. Buffon for granting me access to LNNano/CNPEM amidst pandemic times, and to Leirson Palermo and Davi Miranda for the help in operating the LNNano's PPMS Dynacool.

Although this study was conducted in the last 4-5 years, it is the outcome of many more years in which I was fortunate enough to focus entirely on my education. I wish to thank all the friends and family whom, in a way or another, have made this possible. A very special thanks to Amanda, who has been supporting me and all my decisions since the beginning of this journey. My gratitude to her is ineffable.

This study was financed in part by the Coordenação de Aperfeiçoamento de Pessoal de Nível Superior - Brasil (CAPES) - Finance Code 001 and under Grant No. 88881.190253/2018-01, and from Brazil's agencies Fundação de Amparo à Pesquisa do Estado de São Paulo (FAPESP) under Grants No.2013/07296-2 and 2019/26141-6, and CNPq (Grants No. 444712/2014-3 and 301463/2019-0).

Abstract

The present manuscript provides a detailed and systematic experimental study of the superconducting properties of noncentrosymmetric (NCS) Re_3M (M = W, Ta, and Nb) materials with high rhenium atomic concentration. Owing to the lack of a center of inversion within the α-Mn NCS crystal structure, which develops in the Re-M binary systems, novel properties of the superconducting ground state may arise if the otherwise prohibited spin singlet-triplet admixture is realized. In addition to likely posses strong anti-symmetric spin-orbit coupling, the Re_3M compounds are weakly correlated materials. Some aspects of this study include the stabilization of the α-Mn phase via the partial atomic substitution of W by Nb or Ta and/or the annealing procedures at T = 1700 °C in Re_3M materials. Physical characterization through temperature and magnetic field dependent resistivity ρ(T,H), specific heat C_p(T,H), thermal conductivity κ(T,H), and magnetization M(T,H) of both single and multi phase Re_3M specimens, and the indirect study of flux pinning dynamics emerging close to the upper critical field (H_{c2}) were conducted. Polycrystalline samples of $Re_3M_xW_{1-x}$ solid solutions, M = Ta and Nb, and $0.0 \leq x \leq 0.5$, and $Re_{1-y}W_y$ compounds, $0.1 \leq y \leq 0.5$, were synthesized in an arc melting furnace and subsequently annealed at high temperatures under vacuum or inert atmosphere. From X-ray diffraction results, it is found that the α-Mn structure is stabilized in the Re_3Ta and Re_3Nb as cast materials, while the Re_3W material needs the heat treatment at T = 1700 °C to acquire a single α-Mn phase structure. In as cast samples, the partial atomic substitution in the $Re_3M_xW_{1-x}$ solid solutions is effective to stabilize the NCS structure when the tungsten content is below 75 at.% ($x > 0.25$). Two superconducting phases are believed to emerge in the centrosymmetric, as cast Re_3W material due to the two clear peaks in its specific heat results. In contrast, the annealed $Re_{1-y}W_y$ NCS materials, $0.25 \leq y \leq 0.28$, exhibit a single, well-defined peak marking the superconducting transition in specific heat results. However, the HxT phase diagram of the annealed Re_3W sample contains a bifurcation in the lowest temperature limit: two superconducting boundary lines mark a region with magnetic field quasi-independent electrical resistance curves. The Re_3Ta HxT phase diagram also displays an unconventional feature, even though all other physical properties probed here suggest a conventional, isotropic s-wave pairing. In the annealed solid solutions $Re_3M_{0.5}W_{0.5}$, the $\rho(T, H)$ features related to the peak effect (PE), where a maximum in the superconducting critical current J_c occurs in the vicinity of H_{c2}(T) boundary line, are more pronounced. Moreover, in the PE region, re-entrant and irreversible behaviors arise in the magneto-transport curves. Conversely, the PE is almost imperceptible in the results of the magnetic properties of Re_3M materials. To summarize, our main findings are that the low temperature thermodynamic data strongly suggest conventional, nodeless superconductivity in Re_3M NCS materials and the magneto-transport data near the phase boundary H_{c2}(T) exhibit features associated with the PE in all single α-Mn phase materials, being more pronounced in the annealed solid solution specimens.

Keywords: noncentrosymmetric superconductivity; peak effect; flux-line lattice; rhenium

Resumo

Esta tese compõe um estudo experimental detalhado e sistemático das propriedades supercondutoras de materiais não centrossimétricos (NCS) do tipo Re_3M (M = W, Ta, e Nb) e com alta concentração atômica de rênio. Devido à falta de um centro de simetria de inversão na estrutura cristalina NCS α-Mn, que comumente se desenvolve nos sistemas binários Re-M, novos tipos de propriedades supercondutoras podem surgir caso a mistura, de outro modo proibida, de estados spin-singleto/tripleto esteja presente. Além de possivelmente apresentar acoplamento spin-órbita anti-simétrico intenso, os compostos Re_3M são materiais de fraca correlação eletrônica. Alguns aspectos deste estudo incluem a estabilização da fase α-Mn através da substituição atômica parcial de W por Nb ou Ta e/ou por tratamentos térmicos, em T = 1700 °C, nos materiais Re_3M. Várias caracterizações de propriedades físicas foram conduzidas, tais como a dependência com temperatura e campo magnético externo da resistividade ρ(T,H), calor específico C_p(T,H), condutividade térmica κ(T,H), e magnetização M(T,H), além do estudo indireto do aspecto dinâmico do aprisionamento de fluxo magnético que surge próximo ao campo crítico superior (H_{c2}). Amostras policristalinas das soluções sólidas $Re_3M_xW_{1-x}$, com M = Ta e Nb e $0.0 \leq x \leq 0.5$, e $Re_{1-y}W_y$, $0.1 \leq y \leq 0.5$, foram produzidas através de um forno a arco e recozidas em altas temperaturas sob atmosferas inertes ou vácuo. Os resultados de difração de raios-X mostraram que a estrutura α-Mn é diretamente estabilizada nos materiais Re_3Ta e Re_3Nb como fundidos, e que o material Re_3W necessita do tratamento térmico em T = 1700 °C para adquirir fase única do tipo α-Mn. Nas amostras como fundidas, a substituição atômica parcial nas soluções sólidas $Re_3M_xW_{1-x}$ promove a estabilização da estrutura NCS somente quando o teor de tungstênio está abaixo de 75% ($x > 0.25$). Acredita-se que duas fases supercondutoras emerjam no material centrossimétrico Re_3W como fundido, dada a observação de dois picos nos resultados de calor específico. Em contraste, após o recozimento, todos materiais NCS do tipo $Re_{1-y}W_y$, $0.25 \leq y \leq 0.28$, mostram um único pico muito bem definido nos dados de calor específico. No entanto, o diagrama de fases HxT da amostra Re_3W contém uma bifurcação no limite de baixas temperaturas: duas linhas de fronteira delimitam a região onde as curvas de resistividade são quase independentes do campo magnético externo. O material Re_3Ta também exibe características anômalas em seu diagrama de fases HxT, apesar de todas outras propriedades físicas sugerirem supercondutividade convencional. Nas soluções sólidas $Re_3M_{0.5}W_{0.5}$ recozidas, as características em $\rho(T, H)$ associadas ao efeito de pico (EP), onde um máximo na corrente crítica supercondutora J_c ocorre nas proximidades da linha de fronteira H_{c2}(T), são mais pronunciadas. Além disso, na região do EP, comportamentos irreversíveis e re-entrantes surgem nas curvas de magneto-transporte. Por outro lado, o EP é praticamente nulo nas propriedades magnéticas dos materiais Re_3M. Em suma, nossas principais descobertas são que os dados termodinâmicos em baixas temperaturas sugerem fortemente que a supercondutividade é convencional nos materiais NCS Re_3M e que os dados de transporte eletrônico magnético, perto da fronteira de fases, mostram características marcantes do efeito de pico em todos materiais de fase única e com estrutura do tipo α-Mn, sendo mais pronunciadas nos espécimes de soluções sólidas.

palavras-chave: supercondutividade não-centrossimétrica; efeito de pico; rede de vortex; rênio

List of Figures

List of Tables

List of Abbreviations

CS centrosymmetric

NCS noncentrosymmetric

SC superconducting

BCS Bardeen-Cooper-Schrieffer. Used to indicate the microscopic theory of superconductivity.

GL Ginzburg-Landau. Refers to the phenomenological theory of superconductivity.

CN coordination number

AC as-cast

A.C. alternate current

D.C. direct current

List of Acronyms

ASOC Anti-symmetric spin-orbit coupling.

FLL Flux-line lattice.

PE Peak effect.

XRD X-ray diffraction.

RRR Residual resistance ratio.

List of Symbols

α**-Mn** Prototype NCS crystalline structure from the low temperature phase of elemental Mn.

T_C Superconducting critical temperature

k_B Boltzmann constant

H External (or applied) magnetic field

P External pressure

μ chemical potential

J Electrical current density

$\mathbf{H}_c$ Thermodynamic critical field

$\mathbf{H}_{c1}$ Lower critical field of type-II superconductors.

$\mathbf{H}_{c2}$ Upper critical field of type-II superconductors.

χ**-phase** Thermodynamic phase with NCS structure. α-Mn is a particular type of this phase.

Ψ Order parameter.

λ_L London penetration depth.

ξ_{GL} GL correlation length.

μ_0 Magnetic permeability of vacuum.

M effective mass of the "superconducting electrons". In the free electron approximation, it is twice the electronic mass m_e.

$\hbar$ Planck constant.

ξ_0 BCS coherence length.

ℓ Eletronic mean free path.

$\mathbf{J}_0$ Depairing critical current density.

$c^{\dagger}_{\vec{k},s}$ creation operator of single electronic state with momentum $\vec{k}$ and spin s.

Δ Superconducting gap parameter.

Δ_0 Zero temperature superconducting gap parameter.

N_0 Density of states at the Fermi level.

$V_{\vec{k},\vec{k'}}$ Effective potential between electrons of a Cooper pair.

$\vec{\gamma}_{\vec{k}}$ Momentum dependent anti-symmetric spin-orbit coupling parameter.

H_P**(0)** Zero temperature Pauli limiting field.

μ_B Bohr Magneton.

α Parameter used to modify the bare BCS results in order to include strong coupling corrections. It is the ratio Δ_0/k_BT_C.

ϕ_0 Quantum fluxoid.

α_M Maki parameter, calculated as $\sqrt{2}H_{c2}(0)/H_P(0)$.

λ_{SO} Spin-orbit scattering parameter.

$\mathbf{J}_c$ Critical current density.

$\mathbf{c}_{66}$ Shear modulus of the FLL.

$\mathbf{c}_{44}$ Tilt modulus of the FLL.

γ_n Sommerfeld constant of metals.

θ_D Debye temperature calculated from specific heat data.

t Reduced temperature (T/T_C).

G_i Ginzburg number.

Contents

Chapter 1

Introduction

The currently active experimental study of superconductors without an inversion center composes an important aspect to understand the general superconducting phenomena within research programs worldwide. Superconductivity still presents a wide variety of open scientific questions, even though its discovery has been made more than a hundred years ago by Kammerlingh Onnes. The first half of this period had been spent in reaching the consensus on its microscopic description, consisting of the quantum nature of paired electrons that become the charge carriers in the dissipationless electrical currents. Superconductivity, as well as superfluidity, is one of the few exceptions where the quantum correlations manifest itself in a macroscopically manner. In the superconducting case, an attractive electronic interaction between the electrons overcomes the Coulomb's repulsion in order to establish the effective superconducting pairing. In general, this fermionic interaction occurs via bosons exchange, and the electron-phonon coupling is the simplest scheme when the conventional cases are considered. The disturbance of the normal modes of the lattice vibrations (phonons) by the electrons gives rise to the electron-phonon coupling, gluing together the electrons in the paired configuration.

Solid state matter can be arranged in two distinct types of inner atomic structures: (i) with an (almost) ordered arrangement of the atomic positions, known as (quasi) crystalline materials; (ii) the atomic positions are randomly distributed inside the material, resulting in amorphous materials. Within the crystalline materials description, symmetry operations are often used to build ordered structures by repeating the unit cell - the minimal subset of ordered atoms that contains all the crystal symmetries. That is to say that it is possible to generate the unit cell,

and hence the whole structure, by applying symmetry operations - such as mirroring, rotations and translations - on even smaller parts of the unit cell: the atomic basis. One special kind of these spatial symmetries is called "Inversion symmetry", and its application in an atom whose position is described by the vector $\vec{r}$ leads to another atom in the -$\vec{r}$ position; i.e. it performs a mirroring symmetry in all three axis in relation to the origin of the coordinates. The material is called centrosymmetric (CS) if there is a point about which — the origin in the last sentence — it is possible to apply the inversion symmetry on all the atoms of the subset to build the entire structure. Conversely, if such point does not exist, the crystalline structure is known as noncentrosymmetric (NCS).

The present work is a study on materials that present both of the physical properties described above: the crystalline materials without a center of inversion that superconduct at low temperatures. Rhenium-based materials crystallizing in the α-Mn crystal structure were chosen to conduct the experimental study presented in this manuscript. In the following of this chapter, a survey of the phenomenology of both superconductivity and noncentrosymmetric materials is presented, as well as some physical properties of the materials presenting both ingredients. As the main focus of this work is the NCS rhenium-based superconductors, the last section of this chapter contains all the relevant information on what has been published in those systems so far. A more rigorous explanation of the interplay of these features is left to the chapter 2, that roughly describes the main theoretical framework upon which the experimental data analyses are conducted. In chapter 3, a brief overview of the experimental methods used to produce and characterize the polycrystalline samples of NCS rhenium-based superconductors is presented. Selected results of our experimental work in more than 30 Re_3M samples are described and discussed in chapter 4, which is split in two main sections: one dealing with the basic superconducting (SC) phenomena and the other mainly related to the magnetic field dependence of the SC properties in the $Re_3(Ta,Nb)_xW_{1-x}$ systems.

1.1 Superconductivity

This section introduces the basic phenomenology, physical properties, and key features of superconductors that led both to Ginzburg-Landau model and the development of the microscopic

description given by the Bardeen-Cooper-Schrieffer (BCS) theory. One of the key ideas developed in building the BCS theory has been the bound electron states carrying electrical current in superconductors, the so-called Cooper pairs. Moreover, this survey also works as the starting point for the more in-depth discussion of the phenomena in chapter 2, presenting the theoretical point of view.

As the name suggests, the best known property of a superconductor is its ability to carry a steady current without any voltage drop across the material below a certain superconducting critical temperature T_C. But dissipationless electrical current is not the only remarkable inherent property of superconductors: magnetic flux is expelled from a superconductor, a phenomenon discovered by Walter Meissner and known as the Meissner effect. In addition, the presence of an energy gap in the density of states makes the superconductor a poor heat conductor, in marked contrast with ordinary metals. Therefore, the study of superconducting materials spans a wide field of research, including its electrical responses to various external stimuli as well as the analyses of its magnetic and thermal properties under various, usually extreme, conditions.

The Meissner effect predicts the superconductor's response to an external magnetic field, and to briefly describe it, the transition of a metallic material to its superconducting counterpart under an external magnetic field is first considered. As the normal metallic phase is weakly diamagnetic or paramagnetic, the external magnetic field will penetrate the sample's volume. Following a simplistic heuristic argument, the material's resistance abruptly drops to zero during the superconducting transition and the supercurrents on its surface induce a spontaneous magnetization in the opposite direction of the external magnetic field. Therefore, a nearly null net magnetic field is present within the material below the superconducting transition temperature (T_C), meaning that the initial magnetic field inside the normal state must be expelled from material's interior below T_C. Considering only the perfect conductivity of the material, the Maxwell electrodynamics imposes that the magnetic field must be constant (or $dB/dt = 0$) inside the material [1], so it could have any arbitrary value. In superconductors, however, the Meissner effect requires that this constant magnetic field is essentially zero; in this way, superconductors are more than simple perfect conductors. That is to say a perfect conductor is a magnetic flux conserving medium while a superconductor is a magnetic flux expelling medium

[2].

Superconductors also exhibit a gapped density of states of normal electrons — closely related to the quasi-particles excitations from the superconducting ground state, i.e., a forbidden energy interval where there are no single-particle electron state occupied. This feature was suggested by the early measurements of the superconducting thermal properties and electromagnetic absorption. After concluding that superconductors were bad thermal conductors, it was suggested that the fundamental superconducting charges did not carry entropy at all. Such a hypothesis was further corroborated by specific heat data, in which an exponential decrease with temperature was observed in superconductors, implying a minimum excitation energy per particle close to $k_B T_C$, where k_B is the Boltzmann constant. However, this exponential dependence is only associated to an isotropic gap, in momentum space, and the anisotropic gap case was not anticipated by the original BCS theory. Moreover, measurements of electromagnetic absorption in thin lead films could also be interpreted by considering an energy gap of ~ 4 times $k_B T_C$ [3], meaning that the excitations always were produced in pairs. The BCS theory shed light on the nature of the superconducting gap [4], describing it as the minimum energy required to break a Cooper pair and creating the quasi-particle excitations in superconductors. In fact, the complexity of the energy gap is enhanced when the retarded nature of the electronic interaction is considered. Nonetheless, such a description falls outside the scope of the present work and the retarded effects will not be discussed in detail here.

In the above description, the superconductivity's emergence has been the main focus, but another relevant discussion is to understand how can the superconducting state be destroyed by external excitations. Superconducting phenomena can be suppressed by tuning thermodynamic variables, such as magnetic field H, pressure P or chemical potential μ, or even by dynamical variables as the electrical current density J. For the moment, only the response of the superconducting state under an external magnetic field H is considered, since it directly leads to the classification of type I and type II superconductors. Actually, the Meissner effect occurs only at rather low magnetic fields; beyond a critical field the superconductor abruptly returns to the normal phase. Type I superconductors exhibit this abrupt breakdown transition, leading to a drastic change in the magnetic properties at the thermodynamic critical field H_c: going from a

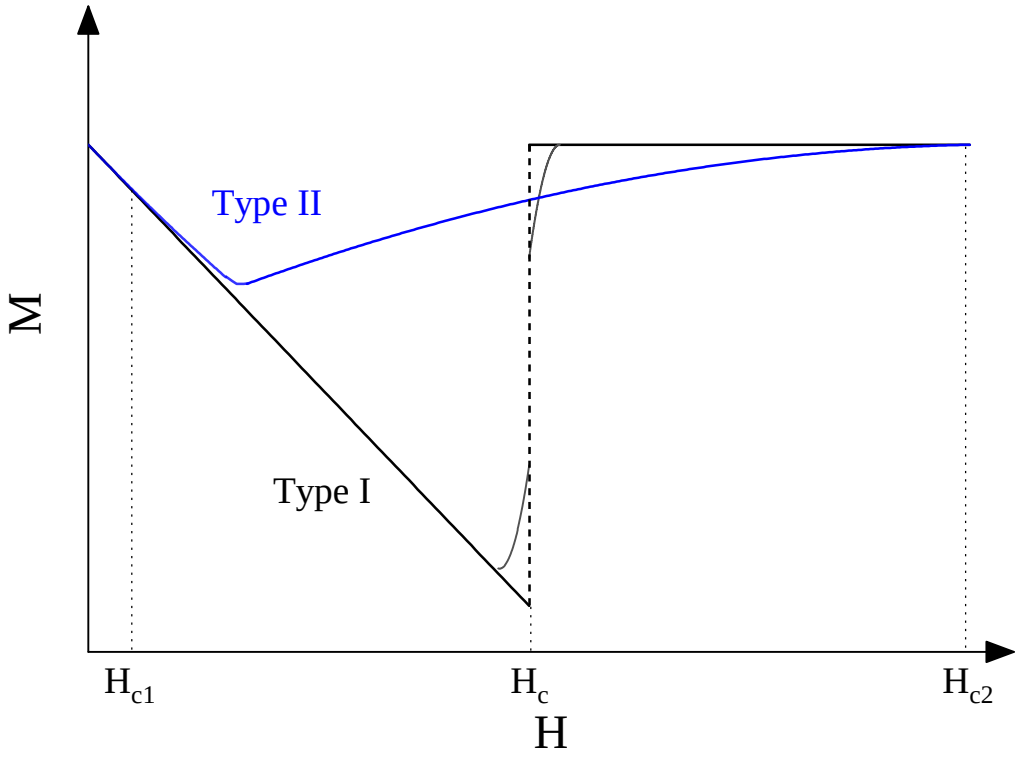

Figure 1.1: Magnetic response of the two types (I and II) of superconductors. The paler lines represent real curves, reflecting thermal broadening and/or material's homogeneity.

completely shielded state to normal paramagnetic (or weakly diamagnetic) state. This feature is exemplified by the dashed black line in Figure 1.1, which exhibits the magnetization M versus the external applied field H on a generic superconductor. In contrast, type II superconductors undergo the transition continuously, with the magnetic field penetrating slowly the sample's interior until the normal state is reached. In this case, the transition can be thought as a two step process: the Meissner effect is effective up to a lower critical field H_{c1}, beyond which the magnetic flux enter sample and increases in density as the magnetic field strength is further increased, eventually leading to the normal state at the upper critical field H_{c2}.

Seven years before the detailed microscopic description in the BCS theory, a phenomenological theory to treat superconductors was proposed by Ginzburg and Landau, known now as Ginzburg-Landau (GL) theory. It was built upon the previous work of Landau on phase transitions, which introduced the order parameter concept to deal with the different ordered thermodynamic states (phases). The GL theory captures the main results presented above, and in spite of being developed to treat cases near the superconducting transition, it also gives reliable estimates well below T_C.

The superconducting order parameter is a quantity closely linked to the degree of ordering in superconductors, and it is described by two real numbers, or by a complex number. The type of ordering taking place in a superconducting transition is related to the loss of spin-isotropy of the nearly-free electrons, since they must obey certain constrains for the interaction with other electrons be effective. After the BCS microscopic theory, its is known that this complex order parameter can be treated as the macroscopic wave-function of the superconducting condensate. Then, the physical meaning of the order parameter is both related to the charged superfluid density and its intrinsic phase coherence over macroscopic distances.

1.2 Noncentrosymmetric Materials

In crystallographic terms, the meaning of symmetry is closely associated to the operation that leaves the whole crystal's structure unchanged, i.e., with the final atomic configuration in coincidence with the initial spatial distribution. For instance, a cubic point lattice must have at least four 3-fold rotation axes as the symmetry elements [5], meaning that π/3 (π/n for n-fold symmetry) rotations on any of those axes do not alter the initial cubic configuration. Out of the four basic symmetry operations (rotation, translation, mirror, and inversion), the inversion symmetry plays a key role in this work and can be fully understood in the simple case of a cubic Bravais lattice, as it is illustrated in Figure 1.2. In this example, the center of the cube is the origin (O) of the coordinates axes and the positions of the points (corners) are defined by the set of vectors $\vec{R} = \{\vec{r}_i\}$, where i is the point (vertices) number. The definition of the inversion symmetry is the operation (represented by the operator $\mathscr{I}$) that leads $\vec{r}$ to - $\vec{r}$, i.e. $\mathscr{I}(\vec{r}) = -\vec{r}$; such an operation can be thought as composed of a rotation of π followed by reflection in a plane normal to the rotation axis (improper π-rotation). Therefore, the net result of applying $\mathscr{I}$ in each element of $\vec{R}$ is $\vec{R}$ itself. In this simple example, the inversion symmetry is accomplished by the fact that every point has another diagonally opposed to it, and the operation of $\mathscr{I}$ in each element of $\vec{R}$ leads to another element already in $\vec{R}$. In this way, the origin (O) is known as the center of inversion.

A useful concept to think on atomic ordering is the point lattice, an arrangement of mathematical points with various symmetries. Any three dimensional point ordering can be formed on

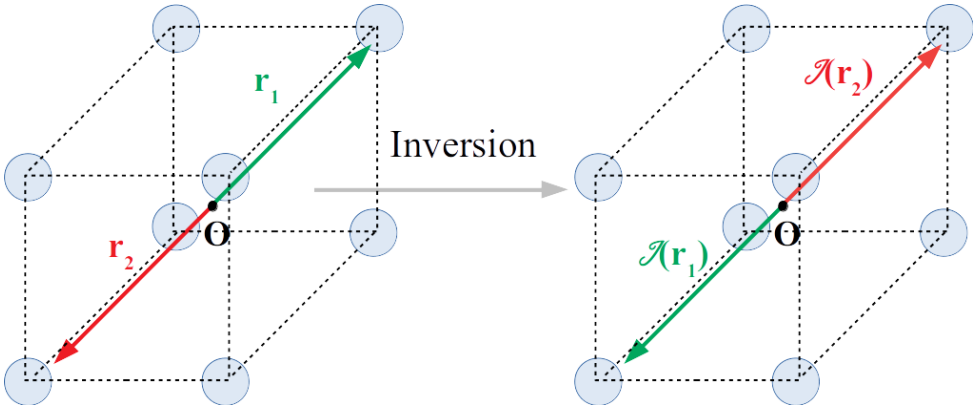

Figure 1.2: Example of the inversion symmetry in a simple cubic lattice.

the basis of 14 primitive point lattices, called the Bravais lattices. The actual description of the atomic arrangement in a crystal is made by positioning building blocks in relation to the lattice points, in order to create a periodic array of building blocks in three dimensions. These building blocks can be either single atoms or group of atoms having their internal set of rules, known as the atomic basis. Therefore, the complete structure of a given crystal is fully described by setting both its Bravais lattice and atomic basis. In addition to the lattice symmetry (defined by the specific Bravais lattice), it is also mandatory to establish the crystallographic point group * of each lattice point (related to the specific atomic basis) to define the full symmetry of a crystal. These two informations are contained in the space group definition, such that any crystal structure is reproduced if its space group and atomic basis are set.

As mentioned above, non-centrosymmetric NCS materials do not have an inversion center. Thus, this type of material can be described by NCS space groups, since the absence of an inversion center is contained in the crystallographic point group — more than half of the allowed crystallographic point groups (21 out of 32) do not posses any center of inversion. In this way, if the space group is known, an inspection of the point group is required to assert whether the material is NCS or not.

*The group of operations that leaves the unit cell unchanged. There are 32 crystallographic point groups in 3 dimensions.

1.3 Noncentrosymmetric superconductors

In superconductors that break inversion symmetry, Cooper pairs lacking a definite spatial symmetry would potentially emerge, being neither symmetric nor anti-symmetric under electron exchange [6]. This is translated into superconducting states exhibiting spin singlet/triplet admixtures. Although some peculiar superconducting properties have been related to the lack of a center of inversion, little compelling experimental evidence have emerged to support the correlation between NCS crystal structures and unconventional superconductivity. A dominant, or even sizable, triplet component has been established only in few cases. The few selected examples of NCS materials discussed below confirm the challenge in fully characterize the NCS superconducting properties, such as the pairing symmetry; the published results do not converge to a single, clear picture even in the weakly correlated class of NCS superconductors.

$CePt_3Si$ is a heavy-fermion magnetic material with a crystal structure that lacks mirror symmetry and superconducts below ~ 0.75 K, being the first known NCS superconductor (or, at least, the first being described as such) [7–9]. Nonetheless, as the superconductivity coexists with magnetic ordering, the complex structure of the superconductivity in this system is further enhanced by additional degrees of freedom. As discussed in the following chapters, the spin-orbit coupling is a key ingredient of NCS superconductivity, and to distinguish this effect from strongly correlated phenomena is a very challenging task. Therefore, materials with weak electronic correlation and NCS crystal structures seems to provide a somewhat easier picture to focus on the NCS inherent features. Other examples of NCS superconducting materials are presented in the remaining part of this section, but these examples are intended to highlight the NCS features and include only weak correlated materials.

The interplay between spin-orbit coupling and crystal structure has been highlighted in the $Li_2(Pd_{1-x}Pt_x)_3B$ system. The conventional spin-singlet Li_2Pd_3B superconductor is fundamentally modified by replacing Pd for Pt atoms, ultimately leading to a sizable spin-triplet component in the Li_2Pt_3B compound [10, 11]. In this context, the spin-orbit coupling strength (stronger in Pt than in its Pd counterpart) could be the source of such difference, as both superconducting materials lack a center of inversion.

Another material that has recently attracted attention is BiPd. In this case, the superconduct-

ing symmetry remains elusive: while single crystal specimens have exhibited highly anisotropic superconducting properties, suggesting two superconducting gaps [12, 13], other studies have pointed out the conventional features of the superconductivity in BiPd samples [14, 15].

The recent discovery of a NCS material with cubic structure in the Mg-Ir-B ternary system has also presented some rather puzzling results. As in the previous case, some of those results are interpreted within the two gap superconductivity scenario[16, 17], while others seems to support the conventional, single gap hypothesis [16, 18]. It is worth to mention that the spin-orbit coupling strength in this material is believed to be only a few times greater than its superconducting energy ($k_B T_c$) [16].

One more example with Pb as the heavy element is the $PbTaSe_2$ compound, whose hexagonal crystal structure is composed of intercalated Pb atoms between dichalcogenides $TaSe_2$ layers. Its superconducting properties seem to converge to a nodeless s-wave gap symmetry scenario [19–22], although some multiband superconductivity effects have also been observed in studies under pressure [23, 24].

Another NCS material believed to present unconventional superconducting features is the yttrium sesquicarbide Y_2C_3. These features include critical fields exceeding the paramagnetic limiting field, multigap superconductivity, and node lines in the superconducting gap [25–27]. Evidence for the conventional spin-singlet pairing, however, has also been presented [26, 28]. Besides, there has been a suggestion that inhomogeneities in Y_2C_3 may play an important role in defining its superconducting properties [29].

In all examples mentioned above, the NCS superconductivity is usually described in terms of pairing spin-1/2 fermions. Nonetheless, the half-Heusler material YPtBi might host a more intricate type of pairing and is also a candidate for topological superconductivity. As it is composed of only heavy elements, the spin-orbit coupling in YPtBi seems to be strong enough to create fermionic states with J = 3/2 [30, 31]. By considering the Cooper pairing taking place in these electronic states, other configurations of spin states would be possible, such as quintet (J = 2) and septet (J = 3) states [31, 32]. In this context, a superconducting gap with line nodes could be described by a spin singlet-septet admixture, agreeing with the published experimental results [32]. It is believed that the presence of even spin states would create internal magnetic

fields in superconductors, but time reversal symmetry breaking has not yet been observed in this material despite the efforts [33].

1.3.1 Rhenium-based noncentrosymmetric superconductors

As the main topic of this work is related to the rhenium-based NCS superconductors, a somewhat more detailed description than previous examples is presented below. All of the published data of these materials point to weakly correlated materials, as indicated by the low values of the Sommerfeld constant obtained in specific heat measurements. The starting point of this description is the occurrence of the NCS phase in the binary systems Re-M, where M stands for transition metals of the periods 4-6. Then, the published data in these systems are reviewed and followed by possible scenarios arising in the solid solutions.

As discussed below, the only stable NCS crystal structure achieved by combining rhenium with another transition metal is the cubic α-Mn type of structure. Therefore, before discussing the stability of the NCS phases in the system, a short digression on the α-Mn structure is presented. Actually, the thermodynamic phase named as χ-phase in the Re-M equilibrium phase diagrams is identified as having the same structure of the α-Mn phase, which is one of the three prototypes of the χ-phase, with $Re_{24}Ti_5$ and Mg_{17} Al_{12} being the others two. There are at least 26 binary A–B systems presenting the χ-phase, mainly composed of elements from group 3 to 6 located at the high coordination sites (A) combined with Tc, Re, or Os as B, being also present in some systems combining Mg, Al, and rare earths [34]. Among those systems, Re is the element forming the largest number of binary systems with the χ-phase (as well as the σ phase). In ternary extensions of the Re-based systems, the binary χ-phases may connect between the two binary systems in which it exists [35].

It is possible to draw some differences among the three prototypes by first describing the χ-phase crystal structure. The χ-phase has a body centered cubic ($b.c.c.$) type of structure, and each unit cell contains a set of well packed 58 atoms, sharing four different inequivalent sites. Figure 1.3 exhibits a sketch of the structure, with the four distinct sites being depicted by spheres of different sizes and colors. Each site have the following point symmetry: 2 atoms with $\bar{4}3m$ symmetry (2a); 8 atoms with $3m$ symmetry (8c); and two groups of 24 atoms with

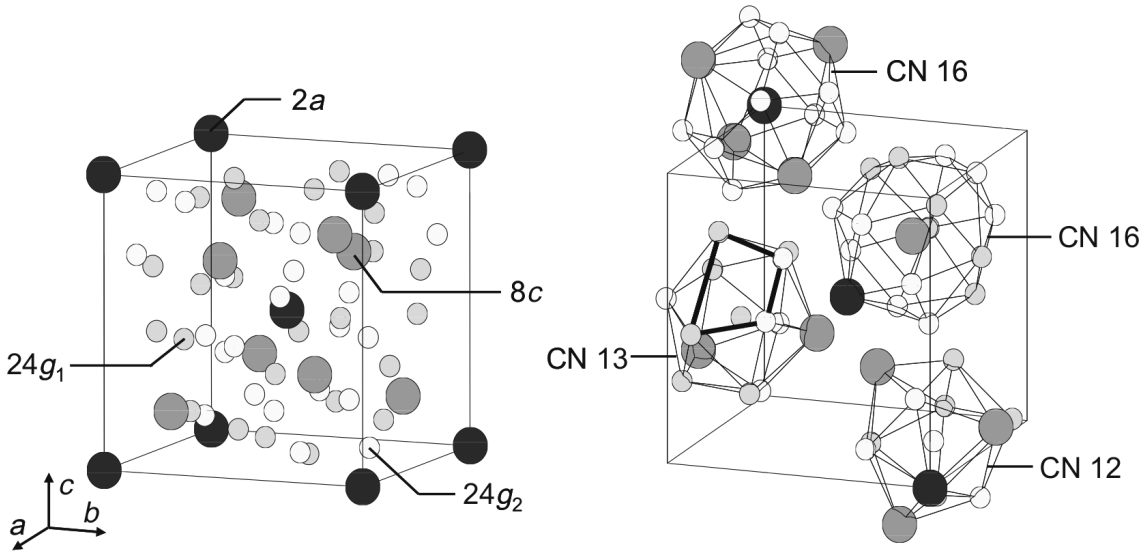

Figure 1.3: Structure of the α-Mn phase, adapted from Ref.34. The left side of the figure displays the distinct atomic positions. The polyhedra defining each coordination number are illustrated on the right side of the figure.

m symmetry ($24g_1$ and $24g_2$) [36]. It is readily seen that the inversion symmetry is preserved in the 2a sites, since they define the $b.c.c.$ structure, as exhibited by some $Re_{1-x}Nb_x$ materials [37]. Then, the NCS features of this structure come from the remaining 8c and 24g sites that compose the vast majority (56 out of 58) of sites not having any center of inversion.

The only difference among the prototypes is at the occupancy on each of the four sites, as displayed in Table 1.1. The structure α-Mn is originally used to describe the low temperature structure of the Mn element, meaning that no distinction is made on sites occupancies and any of the 58 atoms could be in any of the four positions. Therefore, the α-Mn structure seems to be the general description of the χ-phase. In binary M-Re (A-B) systems, however, the sites with the higher coordination number (CN) (16 at positions 2a and 8c) are believed to be occupied by the non-rhenium (A) elements in all three structures [38]. Then, rhenium (or B) atoms would be located at both 24g Wyckoff positions in the $Re_{24}Ti_5$ variant while the 24g site with higher coordination ($24g_1$ - CN = 13) is replaced by an A atom in the $Mg_{17}Al_{12}$ structure. In other words, rhenium atoms tend to be located at the lower symmetry (NCS) sites of the χ-phase structure in Re-M compounds. The compounds with Re:M ratio close to 3:1 studied in this work have rhenium concentration between the $Re_{24}Ti_5$ ($\sim$ 82 %at. Re) and Mg_{17} Al_{12} ($\sim$ 57 %at. Re) variants, so it is reasonable to expected that the $24g_1$ site will be occupied both by Re

and M atoms in this case. Accordingly, the structure of the Re_3Nb has shown that the $24g_1$ site shares both Re and Nb atoms [39].

Table 1.1: Structural parameters of the χ-phase in the A-B system [34]

Space group	$I\bar{4}3m$						
Wyckoff positions	x	y	z	CN	Structures		
					α-Mn	$Re_{24}Ti_5$	$Mg_{17}Al_{12}$
2a	0	0	0	16	A	A	A
8c	~ 0.317	x	x	16	A	A	A
$24g_1$	~ 0.357	x	~ 0.035	13	A	B	A
$24g_2$	~ 0.089	x	~ 0.282	12	A	B	B

Experimental confirmation of the precise site occupancy in the Re-M generally requires both x-ray and neutron diffraction data to be fully reliable, mainly on those systems where the Re and M atomic radii are very close in size. Such proximity of atomic sizes occurs in the Re_3W material, but even neutron diffraction studies do not unambiguously determine the various sites' occupancy; while the purely neutron diffraction data have supported that the 2a Wyckoff position is fully occupied by the Re atoms [40], the crystallographic study made by Zuev *et al.* [41] — with both neutron and synchrotron x-ray powder diffraction — has supported that Re and W atoms share the 2a site. In spite of being less robust evidence, x-ray diffraction data have also indicated the same full occupancy of the 2a site by the Re atoms in the $Re_{0.77}Mo_{0.23}$ material [42].

The next step is to discuss the stability of the χ-phase in the Re-M binary systems. As shown in Figure 1.4, the highlighted NCS crystal structure (χ-phase) is roughly centered at ~ 0.75 %at. Re, when M = Ta, Nb, Mo, or W. The homogeneity range of the NCS phase, however, is very distinct in these systems: it spans more than 15 at.% on Re-(Nb or Ta) diagrams while being less than 5 at.% at its widest range in the Re-W and Re-Mo systems. Another key difference in the phase diagrams is the NCS phase stability at high temperatures, melting congruently in the Nb and Ta system while it is decomposed into the σ and $h.c.p$ (Re) phases in the Re-W and Re-Mo diagrams. This peritectoid transformation in the Re-W system is very important in the discussion of the superconducting properties of the $Re_{1-x}W_x$ materials with $0.25 \leq x \leq 0.28$.

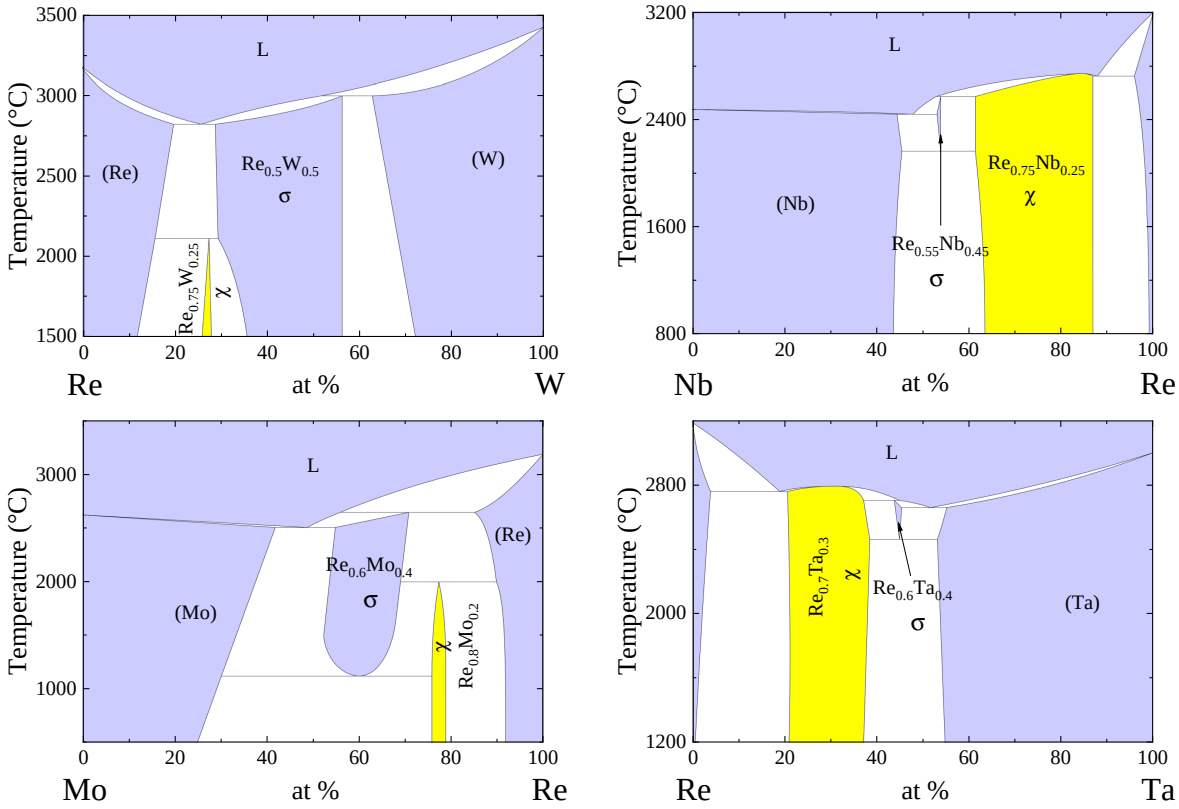

Figure 1.4: Phase diagrams of the binary Re-M (M = W, Nb, Mo, Ta) systems. Note the similarity of the diagrams with M being in the same group (W, Mo and Nb, Ta), mainly in the highlighted χ phase.

Considering the systems Re-M displayed in Figure 1.5, with M now being the group 4 transition metals Ti, Zr, and Hf, the NCS phase is now stoichiometric with the Re:M = 24:5 ratio. In the Re-Ti system, the NCS phase is indeed described as a line compound at the specific ratio of 24:5, as exhibited in the first diagram of Figure 1.5. Conversely, the α-Mn phase in both Hf and Zr systems has very similar features of the Nb and Ta phase diagrams, being shifted closer to the Re-rich side but with narrower solubility ranges. With this picture on the α-Mn phase stability in mind, the next step is to remind what has been published so far on the properties of the NCS materials above, specially those related to their superconducting states.

It is noteworthy that no agreement on the gap symmetry of the Re-based NCS materials has been reached yet, although the majority of the published data seems to point out to the conventional superconductivity direction. The occurrence of superconductivity in rhenium materials with α-Mn structures has been known since late 50's - early 60's, with studies from Blaugher and Hulm [43] and Matthias *et al.* [44] dealing with various intermetallic systems, being the rhenium systems among them. At the time of publishing those studies, no special attention was

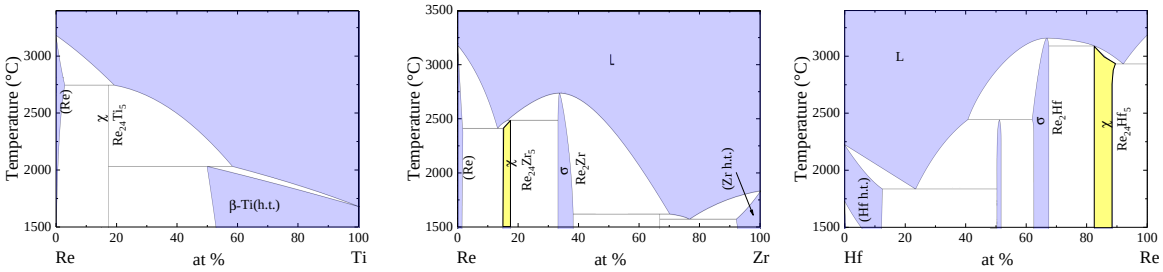

Figure 1.5: Re-M phase diagrams obtained by mixing rhenium with group 4 elements Ti, Zr and Hf. The Re-Ti system presents one of the prototypes structure of the χ phase in the $Re_{24}Ti_5$ line compound, which also appears in the Zr and Hf phase diagrams.

given to the NCS structure itself and the manuscripts focus was on establishing a relationship between the valence electrons concentration and superconductivity emergence. The authors have produced arc-melted samples of Re_3Mo; $Re_{0.82}Nb_{0.18}$; Re_3Ta and Re_3W, with superconductivity below T_Cs of 9.89; 8.89; 6.78 and 9.0 K, respectively. In fact, among the elements used to produce the materials, only Nb has a superconducting temperature close to those T_cs; the α-Mn $Re_{0.75}Mo_{0.25}$ compounds showed remarkable results due to the T_c's enhancement, increasing by almost an order of magnitude from those of the pure elements Re and Mo (1.7 and 0.9 K, respectively [45]).

In the rhenium-tungsten series, as-cast α-Mn Re_3W has been reported to superconduct below $\sim$ 9.0 K in the early studies [43]. The interest in this material has been renewed since the $CePt_3Si$ discovery, as a sizable spin-orbit coupling is expected to occur due to the heavy elements Re and W (Z = 75 and 74, respectively). However, in one of the first studies addressing the Re_3W NCS structure, the superconducting transition occurred at lower temperatures, with T_C = 7.4 K, after annealing the samples at 1500 °C [41]. Moreover, using magnetic penetration depth measurements, this study suggested a conventional nature of superconductivity in α-Mn Re_3W, fitting in a spin-singlet description. Another study reproduced the same critical temperature of about 7.4 K and also indicated isotropic s-wave superconductivity by point-contact spectroscopy [46]. The difference between the reported critical temperatures in this composition has been addressed by Biswas *et al.* [40], arguing that the material with a Re:W ratio of 3:1 has different crystal structures depending on the synthesis method employed: as-casted Re_3W would crystallize in the centrosymmetric Re-richer $h.c.p$ phase and the α-Mn Re_3W structure would

be achieved after annealing the as-cast samples at high temperatures (T > 1500 °C). Then, the superconducting $h.c.p$ centrosymmetric phase has the higher transition temperature of $\sim$ 9.0 K, while the NCS structure is associated with the lower transition at T = 7.4 K. In a following study, this group has also corroborated the conventional (BCS) character of superconductivity, exhibiting the preservation of the time-reversal symmetry in the NCS Re_3W state [47].

In the Re-Nb system, older studies indicated that the maximum T_C among the compounds spanning the α-Mn solubility range is at the $Re_{0.82}Nb_{0.18}$ composition, with T_C close to 9 K [43, 48]. This optimal composition for superconductivity was confirmed by a more recent study on $Re_{1-x}Nb_x$ ($0.13 \leq x \leq 0.38$) polycrystalline samples [37], which also suggested a single conventional gap with unusually high upper critical fields, agreeing with another data on $Re_{0.82}Nb_{0.18}$ [49]. It is at this composition that the one of the few α-Mn single crystals studies have been conducted [50]. The superconducting properties of the single crystal $Re_{0.82}Nb_{0.18}$, however, have suggested multiple superconducting gaps, specially at the point-contact spectroscopy measurements [51] — similarly to the case of MgIrB cited in the previous section. On the other hand, another study reported that superconducting tunnel junctions made with $Re_{0.82}Nb_{0.18}$ polycrystalline films displayed conventional, single gap spectroscopic results [52]. In addition, another property of the $Re_{0.82}Nb_{0.18}$ material is the occurrence of spontaneous magnetic fields within the superconducting state, indicative of unconventional superconductivity due to a time-reversal symmetry breaking scenario [53]. Nonetheless, this latter feature does not seem to be related to the NCS crystal structure alone, as the isostructural Re_3W and Re_3Ta materials do not exhibit any spontaneous magnetic field. One suggestion to explain the data has been pointed to the high rhenium concentration in $Re_{0.82}Nb_{0.18}$, since the time reversal symmetry breaking has even been observed in the elemental, pure Re [53, 54].

Regarding the superconducting properties, materials belonging to the Re-Ta system seem to be the lesser-studied until the completion of the present work. On the oldest published results side, only data in materials having the Re:Ta atomic ratio close to 3:1 have been explored [43, 48], whose maximum T_c occurred near 6.8 K. Other studies dealing with compounds in the Ta richer region, being solid solutions with Ta bcc structure, were also reported in the 70's [55]. A pair of recent studies have discussed the superconducting properties of some materials

almost spanning the full homogeneity range of the α-Mn phase in this system. A detailed study on polycrystalline samples of Re_3Ta has revealed that the superconductivity below T $\sim$ 4.7 K is described by an isotropic s-wave model [56], although its critical temperature to Fermi energy ratio (T_c/E_F) is close to the values showed by others unconventional superconductors. Additionally, another study has concluded that the superconducting critical temperature is enhanced to $\sim$ 8.0 K by increasing the rhenium concentration up to $\sim$ 84.5 at% in the $Re_{5.5}Ta$ compound [57]. In the $Re_{5.5}Ta$ material, nodeless isotropic superconducting gap has also been suggested as well as a rather high upper critical field, a result very similar to the Re-rich $Re_{0.82}Nb_{0.18}$ polycrystalline sample [37].

All of the $Re_{24}Ti_5$, Re_6Zr and Re_6Hf superconducting states break the time reversal symmetry, and have also presented otherwise conventional properties [58–64].

Not much information on the Re-M-N (with both M and N being either Nb, Ta, W, and/or Mo) ternary systems are available in the literature, specially regarding the superconducting properties of solid solutions having the NCS α-Mn phase. Considering additional transition metal elements in the alloying, a recent study on high-entropy alloys has concluded that some $Re_x(HfTaWIr)_{1-x}$ and $Re_y(HfTaWIr)_{1-y}$ samples (with $0.8 \leq x \leq 0.6$ and $0.75 \leq y \leq 0.6$) are NCS superconductors having the α-Mn atomic structure [65].

On the phase stability discussion in the ternary systems Re-M-N, the experimental investigation made by Tregubov *et al.* [66] on Re-Ta-W has indicated that the α-Mn structure is preserved throughout the whole range of substitution when temperatures as high as 1500 °C are considered, as displayed in Figure 1.6(b) by the yellow solid solutions phase field. The same seems to occur in the Re-Nb-W system, according with its ternary phase diagram at 2000 °C retrieved from reference 67, in which the α-Mn phase is believed to extend continuously between the two binary systems (Re-Nb and Re-W).

Our work fills the gap on superconductivity emerging in the ternary alloys Re-Ta-W and Re-Nb-W with NCS structures by conducting a systematic experimental study on the superconducting properties of the Re-based NCS α-Mn solid solutions $Re_3(Ta,Nb)_xW_{1-x}$, in which the W atom is partially substituted by Nb or Ta atoms. In this case, it is expected that the partial atomic substitution not only affects the α-Mn phase stability, but also alters the strength of the

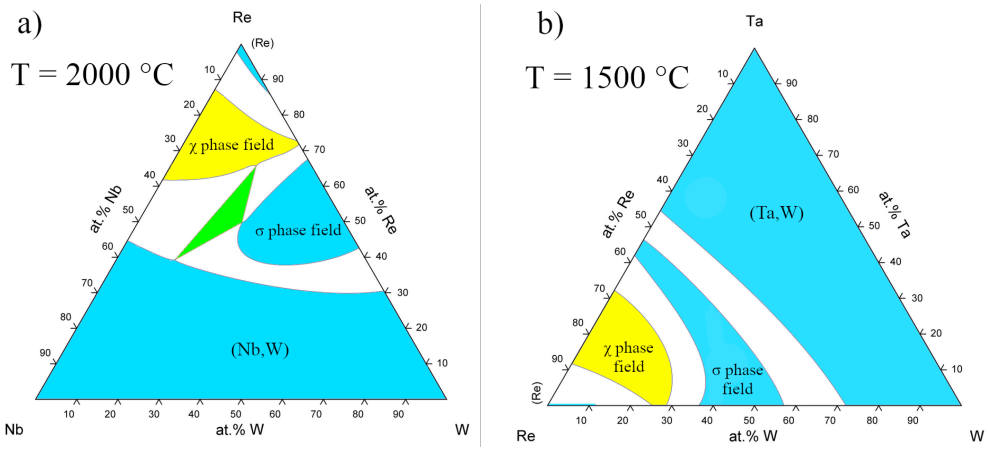

Figure 1.6: Ternary phase diagrams of the Re-Ta-W and Re-Nb-W systems at T = 1500 and 2000 °C, respectively. The α-Mn phase stability region is highlighted in yellow in both diagrams.

anti-symmetric spin-orbit coupling (ASOC). Additionally, this work also highlights some novel superconducting properties arising even in the parent compounds Re_3W, Re_3Ta, and Re_3Nb not contemplated in the previously reported studies.

Chapter 2

Background

The Ginzburg-Landau formalism captures the macroscopic phenomena associated with superconductivity. The main results of the GL theory used throughout this manuscript are presented in section 2.1, consisting of a very brief introduction of the theory.

Many-body quantum theory is suitable to the microscopic description of superconductivity, since it captures the simultaneous interaction among many electrons. Additionally, the grand canonical ensemble also seems to be a good choice, given the fluctuation of the total particle number in this description. The BCS theory can be regarded in three different levels: (i) as a general description of the pair's condensate and with no mention whatsoever to the pairing mechanism; (ii) the electron-phonon interaction is the underlying mechanism to pairs formation; and (iii) weak pair potential and an isotropic superconducting gap in the momentum space, as it is the case treated in the original BCS paper [4]. In this chapter, the section 2.2 deals with the case (iii), describing materials that are known as conventional superconductors. The more general case (i) of unconventional superconductors is briefly discussed in section 2.3 by relaxing some of the approximations. The relationship between unconventional superconducting properties and the absence of an inversion center is then presented in section 2.4, indicating how unconventional properties (i) may arise in that case.

The effect of the magnetic field on the superconducting properties is considered in the final part of this chapter. The suppression of the SC state by the external field is mentioned in section 2.5. Some results and models of the vortex matter arising in type-II superconductors are discussed in the final section 2.6, which first introduce the peak effect phenomenology.

2.1 Ginzburg-Landau theory

In GL theory of superconductivity, the two component, complex pseudowave-function Ψ is treated as the order parameter in the framework of the Landau theory of phase-transitions. In this description of superconducting phenomena, the movement of charged fluids must be considered, leading to the two intertwined characteristic length scales in the GL theory: the London penetration depth λ_L and the coherence length ξ_{GL}. The first length scale sets the distance a magnetic field penetrates into the superconductor, prevented to further occur by the Meissner effect, while the second is related to the extension on which the amplitude fluctuations of the order parameter are not negligible. Then, GL theory is well suited to describe spatially inhomogeneous superconductors, like the type-II superconductivity, being able to capture the general macroscopic behavior of these materials. This is to say that, on length scales larger than the coherence length, the internal structure of the order parameter is irrelevant. Furthermore, the GL theory is also the starting point for a more general analysis of thermal fluctuations around the mean-field theory.

The main idea of the Landau theory of phase transitions is to concentrate in the region of small order parameter $\Psi(x)$, which is very close to the critical temperature. If $\Psi(x)$ varies slowly in space within this region, the gauge-invariant expansion of the superconducting free energy f is [68]

$$f = \frac{\hbar^2}{2M}\left|(\nabla - \frac{ie^*}{\hbar}\vec{A})\Psi\right|^2 + r|\Psi|^2 + ur|\Psi|^4 + \frac{(\nabla \times \vec{A})^2}{2\mu_0}, \tag{2.1}$$

where M is the effective mass of the superconducting electrons, $\hbar$ is the Planck constant and e^* is the charge of the superconducting carriers. Both M and e^* are twice the respective bare electron values in a Cooper pair when the free electron model is used. The free energy in Equation 2.1 is then minimized by calculating the variations of the order parameter and the vector potential $\vec{A}$, resulting in the GL differential equations. The minimization of f by the

vector potential variation leads to

$$\begin{aligned} \frac{\nabla \times \vec{B}}{\mu_0} &= \vec{j}(x) \\ \vec{j}(x) &= -i\frac{e^*\hbar}{2M}(\Psi^*\nabla\Psi - \Psi\nabla\Psi^*) - \frac{e^{*2}}{M}|\Psi|^2\vec{A}. \end{aligned} \tag{2.2}$$

The second relation is achieved by minimizing f in relation to the order parameter

$$r\Psi(x) + u|\Psi(x)|^2\Psi(x) - \frac{\hbar^2}{2M}(\nabla - \frac{ie^*}{\hbar}\vec{A})^2\Psi(x) = 0. \tag{2.3}$$

The Meissner effect can be directly derived from Equation 2.2, which basically is nothing more than the Ampere law. For simplicity, the Ψ fluctuations are restricted to its phase φ, leading to

$$\nabla \times (\nabla \times \vec{B}) = \mu_0 \nabla \times \vec{j} = -\mu_0 \frac{|\Psi|^2 e^{*2}}{M}\vec{B}. \tag{2.4}$$

Therefore, the property of excluding magnetic fields arises explicitly in Equation 2.4 by using the complex representation of $\Psi(x)$ as $|\Psi|e^{-i\varphi(x)}$:

$$\begin{aligned} \nabla^2\vec{B} &= \frac{\vec{B}}{\lambda_L^2} \\ \lambda_L^2 &= \frac{M}{\mu_0|\Psi|^2e^{*2}}. \end{aligned} \tag{2.5}$$

The local density of superconducting electrons n_s is given by $|\Psi|^2$ in the GL theory. Then, Equation 2.5 identifies the characteristic length scale λ_L as the same to that proposed in the London theory. In addition to capture the London theory predictions, the GL theory is also able to treat the spatial variation of $|\Psi|^2$ and the nonlinear Ψ effects due to strong fields.

The second length scale, ξ_{GL}, emerges in a direct way if there are no fields present in the problem. In this case, Ψ can be real ($\Psi \rightarrow |\Psi|$) and Equation 2.3 results in a non-linear differential equation for Ψ. The solution of the linearized version of Equation 2.3 results in a Ψ that exponentially decays in space, and whose correlation length is given by:

$$\xi_{GL}(T) = \sqrt{\frac{\hbar^2}{2Mr(T)}} \propto \sqrt{\ell\xi_0}\left(1 - \frac{T}{T_C}\right)^{-1/2}, \tag{2.6}$$

where ℓ is the electronic mean free path and ξ_0 is the BCS coherence length. The last proportionality in Equation 2.6 only holds for dirty type-II superconductors[†], which is the case of the Re-based materials. Then, ξ_{GL} governs the range of amplitude fluctuations of Ψ in space.

The condensation energy is calculated as the free energy difference between the normal and SC states. In the normal state (Ψ = 0 , $\vec{B} = \mu_0\vec{H}$), the free energy $f_n = -\mu_0 H^2/2$ is given by Equation 2.1. In absence of magnetic fields and $\nabla\Psi$, Equation 2.1 results in f_{sc} = - $r^2/2u$. At the critical field H_C these two energies must be equal, then

$$\mu_0 H_C = \sqrt{\mu_0 \frac{r^2}{u}}. \tag{2.7}$$

The temperature dependence of the critical field H_C(T) comes from the parameters r(T) and u(T). These, in turn, are set by using the empirical approximation of $\lambda_{GL}^{-2} \propto (1 - t^4)$, leading to $r(T) \propto (1 - t^2/1 + t^2)$ and $u(T) \approx$ constant [3]. Then,

$$\mu_0 H_c(T) \propto \frac{1 - t^2}{1 + t^2} \rightarrow \mu_0 H_c(T) = \mu_0 H_c(0) \frac{1 - t^2}{1 + t^2}, \tag{2.8}$$

is the approximate temperature dependence of the critical field.

The GL theory is also used to estimate another intrinsic parameter that suppress superconductivity: the depairing (or pair-breaking) critical current J_0. In short, J_0 represent the current at which the kinetic energy of the superconducting carriers equals the Cooper pairs binding energy. In this description, the superfluid velocity is generated by the twisted phase of the order parameter and the external field:

$$\vec{v}_s = \frac{\hbar}{M}\left(\nabla\varphi - \frac{e^*\vec{A}}{\hbar}\right), \tag{2.9}$$

with the associated current density given by

$$\vec{j} = e^*|\Psi|^2\vec{v}_s. \tag{2.10}$$

[†]dirty SC materials have ℓ and ξ of about the same order of magnitude. In contrast, clean superconductors exhibit $\ell \gg \xi$.

The current density is then defined by the $|\Psi|$ value.

As response of strong fields or currents, the order parameter assumes an optimum value, being constant everywhere in the superconductor. The minimization of the free energy in Equation 2.1 is conducted to find the optimum $|\Psi|$, considering that the fluctuations in $|\Psi|$ are negligible. Then, the optimum value of the order parameter is

$$|\Psi|^2 = |\Psi_\infty|^2 \left[1 - \left(\frac{\xi M v_s}{\hbar}\right)^2\right], \tag{2.11}$$

$|\Psi_\infty|$ is the order parameter infinitely deep within the superconductor, where it is screened from surface fields or currents. The superconducting current density is found by inserting the $|\Psi|$ given by Equation 2.11 back in Equation 2.10. The critical current J_0 is then the maximum value attained by $|\vec{j}|$, which is calculated when $\partial j/\partial v_s = 0$. Therefore, the depairing current density from the GL theory is:

$$J_0 = \frac{\hbar}{3\sqrt{3}\mu_0 e^* \lambda_L^2 \xi_{GL}}. \tag{2.12}$$

These are the main results from the GL theory that are used in the next chapters of this study. The theory is highly more complete than the overview presented above and provides many more insights in the SC properties. In spite of being initially treated as a phenomenological theory, the GL theory was shown to be a limiting case of the BCS theory by Gorkov in what is sometimes called the GLAG (Ginzburg-Landau-Abrikosov-Gorkov) theory. In this broader description, the $|\Psi|$ is, in fact, closely related to the BCS SC gap parameter, explained below.

2.2 BCS theory

Leon Cooper has shown that, in the low temperature limit, two electrons with energies close to the Fermi level form a bound pair if an arbitrary small attractive potential exists between the electrons, leading to the so called Cooper pairs [69]. Therefore, the ground state of a metallic material would be composed of Cooper pairs if there is any electronic interaction taking place among electrons confined to a thin energy shell near the Fermi surface. The superconductivity emerges as a condensation process of these Cooper pairs, which are bosons overlapping in

a single quantum state. The seminal BCS paper [4] has put forward the description of the superconducting phenomena by stating that its macroscopic wave function can be represented by superposition of many coherent states.

The following description of the conventional BCS microscopic theory of superconductivity is a short and mixed version of those presented in Refs. 3 and 70, where the reader can found a more detailed description.

The BCS variational approach starts with the following wave function

$$|\psi_{BCS}\rangle = \prod_{\vec{k}} \left(u_{\vec{k}} + v_{\vec{k}} c^{\dagger}_{\vec{k},\uparrow} c^{\dagger}_{-\vec{k},\downarrow} \right) |0\rangle, \tag{2.13}$$

where the $c^{\dagger}_{\vec{k},s}$ ($c_{\vec{k},s}$) operator creates (annihilates) an electron with momentum $\vec{k}$ and spin s, $u_{\vec{k}}$ and $v_{\vec{k}}$ are related to the probability of having bound or unbound electrons states, respectively. The state $|0\rangle$ denotes an electron vacuum, or Fermi sea, with $|u_{\vec{k}}|^2 + |u_{\vec{k}}|^2 = 1$. These coherent states of Cooper pairs have lower energies than the bare Fermi gas. Considering the relevant scattering processes in the BCS theory as those of particle pairs with opposite spins and vanishing total momentum, the many body Hamiltonian in the second-quantization formalism takes the form

$$\mathscr{H}_{BCS} = \sum_{\vec{k},s} \xi_{\vec{k}} c^{\dagger}_{\vec{k},s} c_{\vec{k},s} + g \sum_{\vec{k},\vec{k'}} c^{\dagger}_{\vec{k},\uparrow} c^{\dagger}_{-\vec{k},\downarrow} c_{-\vec{k},\downarrow} c_{\vec{k},\uparrow}, \tag{2.14}$$

where the single particle energy $\xi_{\vec{k}}$ is measured from the chemical potential, with $\xi_{\vec{k}} = \epsilon_{\vec{k}} - \mu = \hbar^2(\vec{k} - \vec{k_F})^2/2m_e$ in the free electron approximation. The first term of the Hamiltonian then denotes the kinetic energy accounting for the band structure of the metal. The second term describes the two-electron interaction, with g representing a structureless electronic interaction for the moment.

Given the enormous number of particles involved in the macroscopic phenomena, the fluctuations of the number operator around its average should be regarded as just small corrections. Then, the application of the mean field theory is equivalent to use the parameter $\Delta = -g \sum_{k'} \langle c_{-\vec{k},\downarrow} c_{\vec{k},\uparrow} \rangle$ to describe the pairing interaction in Equation 2.14. After a suitable basis transformation (known as Bogoliubov-Valatin transformation) such as $c_{\vec{k},\uparrow} = u^{*}_{\vec{k}} \gamma_{\vec{k},0} + v_{\vec{k}} \gamma^{\dagger}_{\vec{k},1}$,

the diagonalized form of Equation 2.14 is

$$\mathscr{H} = E_0 + \sum_{\vec{k},s} E_{\vec{k}} \gamma^{\dagger}_{\vec{k},s} \gamma_{\vec{k},s}, \tag{2.15}$$

in which $E_{\vec{k}}$ defines the quasi-particle energy spectrum as

$$E_{\vec{k}} = \sqrt{\xi^2_{\vec{k}} + \Delta^2}. \tag{2.16}$$

The so-called "gap equation" is obtained by calculating the number operator $\langle c_{-\vec{k},\downarrow} c_{\vec{k},\uparrow} \rangle$ in the new basis and inserting it back in the gap parameter definition:

$$\begin{aligned} \Delta &= -g \sum_{k} \frac{\Delta}{2E_{\vec{k}}} tanh\left(\frac{E_{\vec{k}}}{2k_B T}\right) \Longrightarrow \\ \Longrightarrow \frac{1}{gN_0} &= -\int_{-\epsilon_c}^{\epsilon_c} d\xi \frac{1}{2(\xi^2+\Delta^2)^{\frac{1}{2}}} tanh\left(\frac{(\xi^2+\Delta^2)^{\frac{1}{2}}}{2k_B T}\right). \end{aligned} \tag{2.17}$$

In the last equality, the discrete summation over $\vec{k}$ has been replaced by the continuum integral over $\xi = |k - k_F|/2m$ by considering the density of states $N(\xi)$ around $d\xi$. This procedure leads to a integral with logarithmic divergence at $\xi \to \pm\infty$ limits. In order to avoid this divergence, the introduction of an energy cutoff ϵ_c is a useful approximation, corresponding to a characteristic energy scale in which the attractive interaction g is effective. This energy scale is solely set by the electrons close to the Fermi level, resulting in a ϵ_c much smaller than the Fermi energy or the band width. In other words, the scattering g can be defined in the following way:

$$g = \begin{cases} g, & \text{if } |\xi| \leq \epsilon_c \\ 0, & |\xi| > \epsilon_c \end{cases} \tag{2.18}$$

i.e., with g having a finite value only within a narrow energy range in the vicinity of the Fermi surface. The last step to get the right hand side of Equation 2.17 is to substitute the density of states $N(\xi)$ by its constant value at the Fermi level N_0, as $N(\xi)$ is not expected to vary much in the $|\xi| \leq \epsilon_c$ energy interval.

The zero temperature superconducting gap Δ_0 is then calculated by setting the low temper-

ature limit in the gap equation 2.17 ($T \to 0 \implies tanh(E/kT) \to 1$). Therefore, the integral acquires an analytical form and solving for Δ_0 leads to:

$$\Delta_0 = \frac{\epsilon_c}{sinh(-(gN_0)^{-1})} \approx 2\epsilon_c e^{-\frac{1}{gN_0}}, \tag{2.19}$$

where the weak-coupling approximation ($gN_0 \ll 1$) has been used to find the final result. In a similar manner, the critical temperature can also be calculated by the gap equation. Then, T_C is defined as the temperature where the gap closes ($\Delta(T_C)$ = 0), restoring the normal metal behavior. Using $\Delta = \Delta(T_C)$ in Equation 2.17 leads to

$$k_B T_C = \frac{2e^{\gamma_{EM}}\epsilon_c e^{-\frac{1}{gN_0}}}{\pi}, \tag{2.20}$$

being γ_{EM} the Euller-Mascheroni constant. Comparing equations 2.19 and 2.20, the following ratio in the weak-coupling scheme is obtained:

$$\frac{\Delta_0}{k_B T_C} \approx \frac{\pi}{e^{\gamma_{EM}}} = 1.764. \tag{2.21}$$

One consequence of the weak-coupling approximation is that it is possible to express physical quantities cutoff-free.

The quasi-particle occupation numbers $f_{\vec{k}}$ are determined by the energies $E_{\vec{k}}$, which are fixed once $\Delta(T)$ has been calculated by Equation 2.17. Therefore, the superconducting electronic entropy can be calculated using the non interacting fermion gas model

$$S_{es} = -2k \sum_k (1 - f_k) ln(1 - f_k) + f_k ln(f_k).$$

Then, the specific heat C_{es} of a superconductor is:

$$\begin{aligned} C_{es}(T) &= T\frac{dS_{es}}{dT} \\ &= -\frac{2}{T}\sum_k \frac{\partial f_k}{\partial E_k}\left(E_k^2 - \frac{T}{2}\frac{d\Delta^2}{dT}\right) \end{aligned} \tag{2.22}$$

There are two contributions in the electronic specific heat: one coming from the normal state

electrons and another originated by the temperature dependence of Δ. By setting Δ = 0, the normal state specific heat is obtained

$$C_n(T) = -\frac{2N_0}{T}\int_{-\infty}^{\infty} d\xi\ \frac{\partial f_k}{\partial \xi}\ \xi^2 \approx \frac{2\pi^2 k_B^2}{3} N_0 T = \gamma_n\ T. \tag{2.23}$$

Both contributions are exponentially small in the low temperature limit (T $\ll$T$_C$), where the thermal energy k$_B$T is much lower than the minimum excitation energy Δ_0. In this limit, the gap magnitude is saturated at Δ_0 and the quasi-particle density of states dominates the specific heat

$$\begin{aligned} C_{es}(T) &\overset{T \to 0}{=} \int dE\ N(E)\ E\ \frac{df(E)}{dT} \\ &\approx N_0 k_B \left(\frac{\Delta_0}{k_B T}\right)^2 \sqrt{2\pi k_B T \Delta_0} e^{-\Delta_0/k_B T}, \end{aligned} \tag{2.24}$$

where the thermally activated behavior is due to the presence of the gap in the energy spectrum, just like a semiconductor. As will be discussed in the next section, this result holds only if the gap is an isotropic function in the momentum space, i.e., $\Delta_{\vec{k}} = \Delta_0$ (or equivalently: $V_{\vec{k},\vec{k}'}$ = g).

The fermionic quasi-particle excitations created by $\gamma^{\dagger}_{\vec{k},s}$ operators are in a one to one correspondence with the normal electrons created by the operators $c^{\dagger}$. Thus, the number of superconducting states around $dE_{\vec{k}}$ must be equal to the number of normal electrons around $d\xi_{\vec{k}}$, leading to the equality $N_s(E_{\vec{k}})dE_{\vec{k}} = N_n(\xi_{\vec{k}})d\xi_{\vec{k}}$. Assuming that $N_n(\xi_{\vec{k}}) \sim N_0$ again, it follows

$$\frac{N_s(E_{\vec{k}})}{N_0} = \frac{d\xi_{\vec{k}}}{dE_{\vec{k}}} = \begin{cases} \frac{E_{\vec{k}}}{(E_{\vec{k}}^2 - \Delta^2)^{1/2}}, & \text{if } E > \Delta \\ 0, & E \leq \Delta \end{cases} \tag{2.25}$$

The same result is obtained by considering that the density of excited states is defined as:

$$N(E) = 2\sum_{\vec{k}} \delta(E_{\vec{k}} - E), \tag{2.26}$$

with $E_{\vec{k}}$ being the quasi-particle spectrum. Then, this density of states is evaluated in the momentum space ($\sum_{\vec{k}} \rightarrow \int d^3k$) by using the kinetic energy distribution $\xi_{\vec{k}}$ in k-space over an

spherical Fermi surface

$$\begin{aligned} N(E) &= N_0 \int \frac{d\Omega_{\vec{k}}}{4\pi} \int d\xi \; \delta(\sqrt{\xi^2 + |\Delta|^2} - E) \\ &\overset{*}{=} N_0 \int \frac{d\Omega_{\vec{k}}}{4\pi} \int d\xi \; \frac{\delta(\xi - \xi_0)}{|\xi/\sqrt{\xi^2 + |\Delta|^2}|_{\xi=\xi_0}} \\ &= N_0 \int \frac{d\Omega_{\vec{k}}}{4\pi} \frac{E}{\sqrt{E^2 - |\Delta|^2}}, \end{aligned} \tag{2.27}$$

where $\xi_0 = \sqrt{E^2 - |\Delta|^2}$ is the root of the function $h(\xi)$ appearing as the argument of the first delta distribution in Equation 2.27 ($h(\xi) = \sqrt{\xi^2 + |\Delta|^2} - E$) . As both the gap function Δ and Fermi surface do not depend on the momentum's direction, the last angular integral is the unity, resulting in the same density of states described in Equation 2.25. Nonetheless, this second method of calculating the density of excited states is valuable when the anisotropic superconducting gap is treated in the following section.

*The identity $\delta(h(x)) = \frac{\delta(x-x_0)}{|h'(x_0)|}$, with $h(x_0) = 0$, has been used.

2.3 Unconventional Superconductivity

Before moving on to the generalization of the conventional BCS theory, some symmetry aspects of the pair wave-function is discussed. Since the Cooper pairs' center of mass is at rest, a general expansion of the interaction potential $V_{\vec{k},\vec{k'}}$ can be done by considering the spherical harmonics $Y_{l,m}$ [71]

$$V_{\vec{k},\vec{k'}} = V(\vec{k} - \vec{k'}) = \sum_{l=0}^{\infty} -V_l \sum_{m=-l}^{l} Y_{l,m}(\hat{k}) Y_{l,m}(\hat{k'}). \tag{2.28}$$

Therefore, the energy of the two electrons (with momentum $\vec{k}$ and $\vec{k'} = -\vec{k}$) bound state is a function of the orbital angular momentum of the attractive interaction V_l. Critical temperatures are not the same in superconducting states with different orbital momentum Cooper pairing. From Equation 2.28, the parity of the Cooper pair's orbital wave-function $\psi_l(\vec{k})$ is

$$\psi_l(-\vec{k}) = (-1)^l \psi_l(\vec{k}). \tag{2.29}$$

The total wave-function of the pair is described by a product between the orbital and spin ($\chi(s, s')$) components, such that its symmetry must respect the Pauli's exclusion principle upon particle permutation

$$\psi_l(-\vec{k})\chi(s, s') = -\psi_l(\vec{k})\chi(s', s). \tag{2.30}$$

To comply with Equation 2.30, the wave-function's spin component must be anti-symmetric (symmetric) under particle exchange if its orbital part is an even (odd) function. Spin wave-functions of two half-spin particles are built upon the eigenstates α and β of the operators s^2 and s_z [†] with

$$\alpha = \begin{pmatrix} 1 \\ 0 \end{pmatrix} = |\uparrow\rangle; \quad \beta = \begin{pmatrix} 0 \\ 1 \end{pmatrix} = |\downarrow\rangle.$$

The anti-symmetric spin eigenfunction of the pair is the spin-singlet pair (S = s_1 + s_2 = 0)

$$\chi(s, s') = \alpha_s \beta_{s'} - \beta_s \alpha_{s'} = |\uparrow \ \downarrow\rangle - |\downarrow \ \uparrow\rangle = \begin{pmatrix} 0 & 1 \\ -1 & 0 \end{pmatrix} = i\sigma_y,$$

[†]recall that $s_z = \frac{\hbar}{2}\begin{pmatrix} 1 & 0 \\ 0 & -1 \end{pmatrix}$.

which can only be coupled with even orbital states $\psi_l, l = 0, 2, \ldots$. The conventional case fits here, where it is called "s-wave " superconductors by having the rotationally symmetric $l = 0$ orbital momentum state. Nonetheless, the unconventional d-wave superconductivity ($l = 2$) must also only be coupled to the spin-singlet state. On the other hand, the spin-triplet state (S = 1) is symmetric under particle exchange, and has three (2S+1) eigenstates, related to the spin projections on s_z = -1,0,1

$$\chi(s, s') = \begin{cases} \alpha_s \alpha_{s'}, s_z = 1 \\ \alpha_s \beta_{s'} + \beta_s \alpha_{s'}, s_z = 0 \\ \beta_s \beta_{s'}, s_z = -1, \end{cases}$$

Then, the general triplet pair wave function can generally be written as a linear combination of the eigenstates above

$$\begin{aligned} \psi(\vec{k})\chi(s, s') &= \psi_{1,1}(\vec{k})\alpha_s\alpha_{s'} + \psi_{1,0}(\alpha_s\beta_{s'} + \beta_s\alpha_{s'}) + \psi_{1,-1}(\vec{k})\beta_s\beta_{s'} \\ &= \begin{pmatrix} \psi_{1,1} & \psi_{1,0} \\ \psi_{1,0} & \psi_{1,-1} \end{pmatrix} = \begin{pmatrix} -d_x(\vec{k}) + id_y(\vec{k}) & d_z(\vec{k}) \\ d_z(\vec{k}) & d_x(\vec{k}) + id_y(\vec{k}) \end{pmatrix} = i(\vec{d}(\vec{k}) \cdot \vec{\sigma})\sigma_y \end{aligned} \tag{2.31}$$

where $\psi_{a,b}$ stands for the orbital component with $l = a$ and $s_z = b$. In this case a must be an odd number ($l = 1, 3, ...$), meaning that each of the orbital components $\psi_{a,b}$ has the required symmetry under particle exchange.

The momentum dependent electron interaction $V_{\vec{k},\vec{k'}}$ is used to generalize the BCS theory, maintaining the condition of an attractive interaction with a vanishing total momentum. In this description, the scattering matrix element $V_{\vec{k},\vec{k'};s_1,s_2,s_3,s_4} = \langle -\vec{k}, s_1; \vec{k}, s_2|\hat{V}| - \vec{k'}, s_3; \vec{k'}, s_4\rangle$ represents the interaction strength between electrons having initial momenta $\vec{k}$ and $\vec{k'}$. The spin degree of freedom s_i can assume two values in conventional electrons, α or β (which were written in the $|\uparrow\rangle, |\downarrow\rangle$ eigenbasis in the previous section). According with the anti-commutation

rules for fermionic particles, the identities

$$V_{\vec{k},\vec{k'};s_1,s_2,s_3,s_4} = -V_{-\vec{k},\vec{k'};s_1,s_2,s_3,s_4} = -V_{\vec{k},-\vec{k'};s_1,s_2,s_3,s_4} = V_{-\vec{k},-\vec{k'};s_1,s_2,s_3,s_4}$$

must also hold. Rewriting Equation 2.14 with the new potential yields

$$\mathscr{H}_{BCS} = \sum_{\vec{k},s} \xi_{\vec{k}} c^{\dagger}_{\vec{k},s} c_{\vec{k},s} + \frac{1}{2} \sum_{s_1,s_2,s_3,s_4} \sum_{\vec{k},\vec{k'}} V_{\vec{k},\vec{k'};s_1,s_2,s_3,s_4} c^{\dagger}_{\vec{k},s_1} c^{\dagger}_{-\vec{k},s_2} c_{-\vec{k'},s_3} c_{\vec{k'},s_4}. \tag{2.32}$$

Proceeding in a similar way as the original BCS case, the generalized gap function Δ now depends both on momentum $\vec{k}$ and spins (s, s'):

$$\Delta_{\vec{k};s,s'} = -\sum_{\vec{k'};s_3,s_4} V_{\vec{k},\vec{k'};s,s',s_3,s_4} \langle c_{-\vec{k},s_3} c_{\vec{k},s_4} \rangle. \tag{2.33}$$

The gap function is closely related to the Cooper pair's wave function and the above results on symmetry aspects also apply here: the momentum dependence of the gap function is solely defined by the symmetry of the pairing interaction; i.e., $\Delta_{\vec{k}}$ must be even in the singlet state and odd in the triplet state. In other words, the gap function must obey the rules:

$$\Delta_{\vec{k};s_1,s_2} = -\Delta_{-\vec{k};s_2,s_1} = \begin{cases} \Delta_{-\vec{k};s_1,s_2} = -\Delta_{\vec{k};s_2,s_1}, \text{ singlet configuration (even in k)} \\ -\Delta_{\vec{k};s_1,s_2} = \Delta_{\vec{k};s_2,s_1}, \text{ triplet configuration (odd in k)} \end{cases} \tag{2.34}$$

It is useful to represent the gap function in spin space, through the α and β states as a basis, yielding a 2x2 complex matrix

$$\hat{\Delta}_{\vec{k}} = \begin{pmatrix} \Delta_{\vec{k},\alpha\alpha} & \Delta_{\vec{k},\alpha\beta} \\ \Delta_{\vec{k},\beta\alpha} & \Delta_{\vec{k},\beta\beta} \end{pmatrix},$$

whose symmetry rules defined in Equation 2.34 is expressed as

$$\hat{\Delta}_{\vec{k}} = -\hat{\Delta}^{T}_{-\vec{k}}.$$

Using this general description, the spin singlet pairing is recovered by considering a null scattering potential between electrons with the same spin projection (therefore $\Delta_{\vec{k},\alpha\alpha} = \Delta_{\vec{k},\beta\beta} = 0$), and only a scalar function $\psi(k)$ is required to describe the momentum dependence of $\Delta(k)$. The conventional BCS description is just a particular case of this scalar function, in which $\psi(k) = g$ is a constant. In contrast, the superconducting gap parameter of the triplet state needs a vector function $\vec{d}(\vec{k})$ (the same defined in Equation 2.31) to fully describe its symmetry. In close analogy to what has already been discussed , the gap functions are

$$\begin{cases} \hat{\Delta}_{\vec{k}} = i\psi(\vec{k})\hat{\sigma_y} \rightarrow |\Delta_k|^2 = \frac{1}{2}tr(\hat{\Delta}_{\vec{k}}\hat{\Delta}^*_{\vec{k}}) = |\psi(\vec{k})|^2 & \text{(spin singlet)} \\ \hat{\Delta}_{\vec{k}} = i\left(\vec{d}(\vec{k})\cdot\hat{\vec{\sigma}}\right)\hat{\sigma_y} \rightarrow |\Delta_k|^2 = \frac{1}{2}tr(\hat{\Delta}_{\vec{k}}\hat{\Delta}^*_{\vec{k}}) \overset{\ddagger}{=} |\vec{d}(\vec{k})|^2 & \text{(spin triplet)} \end{cases} \tag{2.35}$$

Regardless of the particular gap symmetry, four-dimensional vector operators $\mathrm{C}^\dagger_{\vec{k}}$ are used to write Equation 2.32 in a more compact notation, while a generalized unitary Bogoliubov transformation $\mathrm{C}_{\vec{k}} = \hat{U}_{\vec{k}}A_{\vec{k}}$ is used to diagonalize the BCS Hamiltonian in this four-dimensional basis. Then, Equation 2.32 reads as

$$\mathscr{H} = \sum_{\vec{k}} A^\dagger_{\vec{k}}\hat{E}_{\vec{k}}A_{\vec{k}} + K = E_0 + \sum_{\vec{k};s} E_{\vec{k}}a^\dagger_{\vec{k},s}a_{\vec{k},s},$$

with

$$\hat{E}_{\vec{k}} = \begin{pmatrix} E_{\vec{k}}\hat{\sigma}_0 & 0 \\ 0 & -E_{\vec{k}}\hat{\sigma}_0 \end{pmatrix}.$$

The ground state energy is E_0 ($= K - 1/2\sum_{\vec{k}} E_{\vec{k}}$) and the energy spectrum of the elementary excitations,

$$E_{\vec{k}} = \sqrt{\xi^2_{\vec{k}} + |\Delta_{\vec{k}}|^2}, \tag{2.36}$$

has an energy gap following the definition of Equation 2.35. Note that the operators $a^\dagger_{-\vec{k},\alpha}$ are the generalization of the quasi-particle $\gamma^\dagger$ operators used in the previous section. The gap

‡This equality holds for the unitary states. Note that $\hat{\Delta}_{\vec{k}}\hat{\Delta}^*_{\vec{k}} = |\vec{d}(\vec{k})|^2\hat{\sigma}_0 + i(\vec{d}\times\vec{d}^*)\cdot\hat{\vec{\sigma}}$. Non-unitary pairing states are the cases where $(\vec{d}\times\vec{d}^*) \neq 0$.

equation can again be recovered by writing down explicitly the Equation 2.33 in the $a^{\dagger}_{-\vec{k},\alpha}$ basis:

$$\begin{aligned}\Delta_{\vec{k};s_1,s_2} &= -\sum_{\vec{k'};s_3,s_4} V_{\vec{k},\vec{k'};s_1,s_2,s_3,s_4}\frac{1-2f(E_{\vec{k'}})}{2E_{\vec{k'}}}\Delta_{\vec{k'};s_3,s_4} \\ &= -\sum_{\vec{k'};s_3,s_4} V_{\vec{k},\vec{k'};s_1,s_2,s_3,s_4}\frac{\Delta_{\vec{k'};s_3,s_4}}{2E_{\vec{k'}}}\tanh\left(\frac{E_{\vec{k'}}}{2k_BT}\right).\end{aligned} \tag{2.37}$$

In this way, the self-consistent gap equation of each type of spin-pairing is obtained by using Equation 2.35 to explicitly write down $\Delta_{\vec{k}}$.

Some properties of the unconventional superconductors can be predicted using the gap equation 2.37. Actually, these superconducting properties are the main goals of this section, with its results serving as the foundations for the discussion of some experimental results in later chapters of this work. As a simple example, considering the anisotropic effects in the spin-singlet pairing (by setting $\psi(\vec{k}) = \Delta\ f(\vec{k})$ with $|f(\vec{k})| \leq 1$), the above relations imply that

$$\begin{aligned}&\frac{\Delta_0}{k_BT_C} \geq 1.764 \\ &\left.\frac{C-C_n}{C_n}\right|_{T=T_C} \leq 1.43,\end{aligned}$$

even in the weak-coupling limit. The above quantities are no longer universal and become dependent both on the gap and Fermi surface anisotropy. The specific heat superconducting jump being smaller than the BCS value of 1.43 is a direct result from the low energy excitations in anisotropic superconductors. It is noteworthy that the superconducting jump is also affected by strong coupling corrections (not discussed here), enhancing its values to well above the BCS prediction.

Given the excitation spectrum in Equation 2.36, the density of quasi-particle states is defined by Equation 2.26[§], which depends on the angular dependence of $\Delta_{\vec{k}}$ in the momentum space. If this gap has nodes (a set of $\vec{k}$ values such that $\Delta_{\vec{k}} = 0$), the density of states is then sensible to the topology of these gap nodes. This is due to the constrain $|E| > |\Delta_0|$ not being required anymore, and the otherwise prohibited sub-gap states (quasi-particles with energies below Δ_0)

[§]just replace Δ for $\Delta_{\vec{k}}$.

contributes to $N(E)$ in the $E \to 0$ limit. In fact, some of the unconventional superconducting states do have gap nodes. In the He^3 A-phase state, the gap function $\Delta_{\vec{k}} = \Delta_0 sin(\theta)$ has axial symmetry with point nodes along k_z direction, located at the north and south poles of the Fermi surface. Then the density of states in this case,

$$\begin{aligned} N(E) &= N_0 \int_0^{\pi} \int_0^{2\pi} \frac{\sin(\theta)}{4\pi} d\theta d\varphi \frac{E}{\sqrt{E^2 - \Delta_0^2 \sin^2(\theta)}} \\ &= N_0 \frac{E}{\Delta_0} \int_{-1}^{1} dx \; Re\left(\frac{1}{\sqrt{x^2 + [(E/\Delta_0)^2 - 1]}}\right) = N_0 \frac{E}{\Delta_0} \ln\left(\left|\frac{1 + \frac{E}{\Delta_0}}{1 - \frac{E}{\Delta_0}}\right|\right), \end{aligned} \tag{2.38}$$

also vanishes continuously in the low energy limit ($E \to 0$), with the density of the low lying energy excitations contributing quadratically to $N(E)$ (in the $x \sim 0$ approximation, $ln((1 + x)/(1 - x)) \to 2x$).

Superconducting gaps with line nodes are another important class of node topology. Such states can be realized by the spin-singlet "d-wave" superconductors, whose gap symmetry is believed to occur in the cuprate's superconductivity. In this case, $\psi(\vec{k}) = \Delta_0 \frac{(k_x^2 - k_y^2)}{|k_F|^2}$, meaning that the gap function vanishes at $k_x = \pm k_y$ lines, just like the atomic orbital $d_{x^2-y^2}$. A simple parametrization $\psi(\vec{k}) = \Delta_0 cos(\theta)$ is used as a model to describe the density of states of line nodes topology, since nodes are present when θ crosses the $k_x - k_y$ plane. The calculation of the density of states in this model yields

$$\begin{aligned} N(E) &= N_0 \int_0^{\pi} \int_0^{2\pi} \frac{\sin(\theta)}{4\pi} d\theta d\varphi \frac{E}{\sqrt{E^2 - \Delta_0^2 \cos^2(\theta)}} \\ &= N_0 \frac{E}{\Delta_0} \int_{-1}^{1} dx \; Re\left(\frac{1}{\sqrt{(E/\Delta_0)^2 - x^2}}\right) = N_0 \frac{E}{\Delta_0} \begin{cases} \frac{\pi}{2}, \; |E| < \Delta_0 \\ \arcsin\left(\frac{\Delta_0}{E}\right), \; |E| \geq \Delta_0, \end{cases} \end{aligned} \tag{2.39}$$

making it clear that a finite density of quasi-particle states also appears below the gap energy. This contribution, however, vanishes linearly in the low energy limit.

The above power laws in the energy dependence of the density of states in the low temperature limit ($N(E) \propto E^n$) provide further insight on the thermodynamics properties. In this limit,

Equation 2.24 determines the superconducting specific heat

$$C_{es}(T) \propto \int dE E^n \frac{E^2}{k_B T^2} \frac{1}{cosh^2(E/2k_B T)} \propto T^{n+1}, \tag{2.40}$$

whose temperature dependence is fundamentally different from the conventional s-wave case. The low lying energy excitations created at the gap nodes still contributes to $C_{es}(T)$ in the low temperature limit, resulting in the electronic specific heat vanishing less dramatically with temperature than the exponential decrease expected in nodeless isotropic superconducting gap. As Equation 2.40 indicates, the behavior of the $C_{es}(T)$ in the gap symmetry with line (point) nodes follows a T^2 (T^3) power law. More generally, similar results in other thermodynamic quantities also follow from the density of states of nodal superconductors. Table 2.1 lists the expected temperature dependence of some quantities in superconducting materials having line or point nodes.

Table 2.1: Temperature dependence of some thermodynamic properties in the low temperature limit.

Quantity	Point nodes	Line nodes
Specific heat and thermal conductivity	T^3	T^2
London penetration depth	T^2	T
Knight Shift NMR	T^5	T^3

2.4 Noncentrosymmetric Superconductivity

According to Anderson's theorems [72, 73], the formation of Cooper pairs relies on both the time reversal and inversion key symmetries, regardless of the global symmetries broken upon entering the superconducting state. Then, deviations from usual Cooper pairing are expected if one or both of these key symmetries are missing [74] — which is exactly the case of the NCS family of SC, lacking the the inversion symmetry. In principle, a superconductor having no spatial inversion symmetry would allow for a superconducting state without a definite parity [75], mixing both the even and odd parity channels discussed in the last section. This is in stark contrast with a superconducting crystal possessing the inversion symmetry, in which the

orbital component of the Cooper pairs' wave-function do have a definite parity [6]. Therefore, superconducting states within NCS structures could then exhibit novel physical properties arising from the spin singlet/triplet mixture, in addition to those considered in odd or even channels alone.

The anti-symmetric spin-orbit coupling (ASOC) is the essential microscopic feature to describe the Cooper pairing arising in NCS systems. This interaction is proportional to $\vec{S} \cdot (\nabla U(\vec{r}) \times \vec{P})$ (with $\vec{S}$, $U(\vec{r})$, and $\vec{P}$ being the single electron spin, lattice potential, and the momentum operator, respectively), and the absence of inversion symmetry is directly related to the term $\nabla U(\vec{r})$ [76]. This is to say that the intrinsic electrical field $\vec{E}$ within a NCS structure — proportional to $\nabla U(\vec{r})$ — is translated to an effective magnetic field $\vec{B}_{eff}$ created by electronic movement induced by $\vec{E}$. The $\vec{B}_{eff}$ couples to the spin degree of freedom of single electrons, resulting in an effective spin-orbit interaction, which is described by the vector $\vec{\gamma}_{\vec{k}}$ in the following.

In order to understand how the ASOC affects the superconducting properties of a NCS material, the discussion starts by recalling some normal state properties when both time-reversal $\mathcal{T}$ and inversion $\mathscr{I}$ symmetries are present. In this case, it is well known that the electronic states at a given momentum $\vec{k}$ are doubly degenerate: the state $|\vec{k}, \alpha\rangle$ has the same energy as the $\mathscr{I}\mathcal{T}\,|\vec{k}, \alpha\rangle = |\vec{k}, \beta\rangle$ state. Additionally, these two states are also degenerate with the states at $-\vec{k}$, since $|-\vec{k}, \alpha\rangle = \mathscr{I}\,|\vec{k}, \alpha\rangle$ and $|-\vec{k}, \beta\rangle = \mathcal{T}\,|\vec{k}, \alpha\rangle$ [73]. A close analogy with the description of a spin-1/2 particles follows from the above properties: a two-component wave-function is required to specify any state at momentum $\vec{k}$ [77]. Therefore, a pseudo-spin basis is formed by the $|\vec{k}, \alpha\rangle$ and $|\vec{k}, \beta\rangle$ states, enabling the construction of single particle operators from the Hermitian operators σ_i, resembling the usual Pauli-matrices [77, 78].

Using the Pauli-matrix like Hermitian operators σ_i, the general normal state Hamiltonian

$$\mathscr{H} = \sum_{\vec{k},s} \xi_{\vec{k}} c^{\dagger}_{\vec{k},s} c_{\vec{k},s} + \sum_{s_1,s_2} \sum_{\vec{k}} \vec{\gamma}_{\vec{k}} \cdot \{c^{\dagger}_{\vec{k},s_1} \vec{\sigma}_{s_1,s_2} c_{\vec{k},s_2}\} \tag{2.41}$$

has the following transformations under time-reversal and inversion operations

$$\mathcal{T}\mathscr{H}\mathcal{T}^{\dagger} = \sum_{\vec{k},s} \xi_{-\vec{k}} c^{\dagger}_{\vec{k},s} c_{\vec{k},s} - \sum_{s_1,s_2} \sum_{\vec{k}} \vec{\gamma}_{-\vec{k}} \cdot \{c^{\dagger}_{\vec{k},s_1} \vec{\sigma}_{s_1,s_2} c_{\vec{k},s_2}\}$$

$$\mathscr{I}\mathscr{H}\mathscr{I}^{\dagger} = \sum_{\vec{k},s} \xi_{-\vec{k}} c^{\dagger}_{\vec{k},s} c_{\vec{k},s} + \sum_{s_1,s_2} \sum_{\vec{k}} \vec{\gamma}_{-\vec{k}} \cdot \{c^{\dagger}_{\vec{k},s_1} \vec{\sigma}_{s_1,s_2} c_{\vec{k},s_2}\}.$$

The conservation of the time reversal symmetry means that $\mathscr{H} = \mathcal{T}\mathscr{H}\mathcal{T}^{\dagger}$, leading to $\xi_{\vec{k}} = \xi_{-\vec{k}}$ and $\vec{\gamma}_{\vec{k}} = -\vec{\gamma}_{-\vec{k}}$, while the inversion symmetry requires that $\xi_{\vec{k}} = \xi_{-\vec{k}}$ and $\vec{\gamma}_{\vec{k}} = +\vec{\gamma}_{-\vec{k}}$ [74]. Thus, $\vec{\gamma}_{\vec{k}}$ = 0 if both symmetries are preserved in the system and the single particle Hamiltonian 2.41 is reduced to the diagonal form $\xi_{\vec{k}}\sigma_0$.

Considering now that the inversion symmetry is broken, the constraint on the spin-orbit parameter γ is that it must be anti-symmetric in k-space, as $\vec{\gamma}_{\vec{k}} = -\vec{\gamma}_{-\vec{k}}$ must hold. In this way, the spin-orbit interaction

$$\mathscr{H}_{ASOC} = \vec{\gamma}_{\vec{k}} \cdot \vec{\sigma}$$

is also anti-symmetric. In this broken inversion symmetry description, the quasi-particles energies obtained from Equation 2.41 become $E_{\vec{k},\lambda} = \xi_{\vec{k}} + \lambda|\gamma_{\vec{k}}|$, with λ = $\pm$ 1. The diagonalization of the Equation 2.41 results in the so-called helicity basis — composed by the $|\vec{k},+\rangle$ and $|\vec{k},-\rangle$ states and denoted by the band index λ — and have been obtained after a suitable Bogoliubov transformation such as [74]

$$c_{\vec{k},s} = \sum_{\lambda=\pm} u_{s,\lambda}(\vec{k}) a_{\vec{k},\lambda}. \tag{2.42}$$

The quasi-particles energies confirm the lifting of the pseudo-spin degeneracies at each $\vec{k}$, but remain not disturbed in the time-reversed pair of states $\vec{k}$ and - $\vec{k}$. Therefore, this lifting indicates that the ASOC fix the single-particle's pseudo-spin direction, inducing $\vec{k}$-dependent spin quantization axis which removes the SU(2) symmetry [75] — no longer allowing for pseudo-spin rotations [78].

Before moving on to the superconducting case, note that the basic form of the anti-symmetric spin-orbit coupling $\vec{\gamma}_{\vec{k}}$ depends upon the space group of the crystal as well as the pseudo-spin representation related to the single-particle states. Therefore, Table 2.2 shows the detailed form of some $\vec{\gamma}_{\vec{k}}$ obtained through small momenta $\vec{k}$ expansions preserving the point group

and pseudo-spin symmetry requirements.

Table 2.2: Momentum dependence of the anti-symmetric spin-orbit coupling allowed in some crystal systems.

Point group $\mathscr{G}$	$\vec{\gamma}_{\vec{k}}$
O	$\gamma_0\vec{k}$
$\mathbf{T}_d$	$\gamma_0[k_x(k_y^2-k_z^2)\hat{x}+k_y(k_z^2-k_x^2)\hat{y}+k_z(k_x^2-k_y^2)\hat{z}]$
$\mathbf{C}_{4\nu}$	$\gamma_\perp(k_y\hat{x}-k_x\hat{y})+\gamma_\parallel k_xk_yk_z(k_x^2-k_y^2)\hat{z}$

The point group $\mathscr{G}$=**O** is related to the symmetry of cubic systems, as it is the case of the $Li_2(Pd,Pt)_3B$ NCS superconducting family, while the tetragonal point group $\mathbf{C}_{4v}$ is relevant in the heavy-fermion superconductors $CePt_3Si$ or $Ce(Pt,Rh)Si_3$. Usually, the parallel component is negligible in a tetragonal 2d system, giving rise to the well-known Rashba ASOC — often used to illustrate some of the results presented in this section. The full tetrahedral point group $\mathbf{T}_d$ has the proper crystal symmetry to treat the materials discussed in this work, as the crystal structure of the Re-based NCS superconductors is described by this space group.

Moving on to the superconducting state description, as the ASOC splits the electronic bands in normal state, the pairing in NCS materials includes single-particle states of both helicity bands ($\lambda = \pm$). Therefore, this description is actually very similar to the two band problem, introduced soon after the original BCS study [79], but with the bands involved having no spin degeneracy. The general BCS Hamiltonian for this two-band case, including only the electron-electron interaction, is

$$\mathscr{H} = \sum_{\vec{k},\lambda} \xi_{\vec{k},\lambda} a^\dagger_{\vec{k},\lambda} a_{\vec{k},\lambda} + \sum_{\vec{k},\vec{k}'} \sum_{\lambda_1,\lambda_2,\lambda_3,\lambda_4} V_{\lambda_1,\lambda_2,\lambda_3,\lambda_4}(\vec{k},\vec{k}') a^\dagger_{\vec{k},\lambda_1} a^\dagger_{-\vec{k},\lambda_2} a_{-\vec{k}',\lambda_3} a_{\vec{k}',\lambda_4}, \tag{2.43}$$

with $\xi_{\vec{k},\lambda}$ being the energy dispersion of the split bands measured relative to the chemical potential μ. It seems reasonable that the energy scale associated with the ASOC E_{ASOC} strongly exceeds the superconducting energy scale k_BT_C. In this limit $k_BT_C < E_{ASOC}$, pairing between the different $\pm$ bands would require states far from the Fermi surface, a very unlikely event in the BCS picture. Therefore, only intraband pairing is considered, meaning that four band index λ_i in Equation 2.43 reduces to only two: $\lambda = \lambda_1, \lambda_2$ and $\lambda' = \lambda_3, \lambda_4$. Proceeding similarly as in

the previous sections, the gap function of the band λ can be defined as

$$\Delta_{\vec{k},\lambda} = -\sum_{\vec{k}',\lambda'} V_{\lambda,\lambda'}(\vec{k},\vec{k}')\langle a_{-\vec{k}',\lambda'} a_{\vec{k}',\lambda'}\rangle, \tag{2.44}$$

leading to the Bogoliubov quasi-particle spectrum $E_{\vec{k},\lambda} = \sqrt{\xi^2_{\vec{k},\lambda} + \Delta^2_{\vec{k},\lambda}}$.

It is well established that the Cooper pairing is favored between the time reversed states having the same single-particle energy. In the helicity basis, although not lifting the degeneracy between the time reversed states, the time reversal operation in NCS systems introduces a non-trivial phase factor $t_\lambda(\vec{k})$, i.e. $\mathcal{T}\,|\vec{k},\lambda\rangle = t_\lambda(\vec{k})\,|-\vec{k},\lambda\rangle$. This phase factor plays a key role in Equation 2.43, since it is translated into the relation $\mathcal{T} a^\dagger_{\vec{k},\lambda} = t_\lambda(\vec{k}) a^\dagger_{-\vec{k},\lambda} = \tilde{a}^\dagger_{\vec{k},\lambda}$ ($\mathcal{T} a_{\vec{k},\lambda} = t^*_\lambda(\vec{k}) a_{-\vec{k},\lambda} = \tilde{a}_{\vec{k},\lambda}$) — defining $\tilde{a}^\dagger_{\vec{k},\lambda}$ as the raising operator for the time-reversed partner of $|\vec{k},\lambda\rangle$ [75]. Defining $\Delta_{\vec{k},\lambda} = t_\lambda(\vec{k})\tilde{\Delta}_{\vec{k},\lambda}$, with

$$\tilde{\Delta}_{\vec{k},\lambda} = -\sum_{\vec{k}',\lambda'} \tilde{V}_{\lambda,\lambda'}(\vec{k},\vec{k}')\langle \tilde{a}_{-\vec{k}',\lambda'} a_{\vec{k}',\lambda'}\rangle, \tag{2.45}$$

such that $\tilde{V}_{\lambda,\lambda}(\vec{k},\vec{k}')$ represents the pairing interaction between time-reversed states $|\vec{k},\lambda\rangle$ and $\mathcal{T}\,|\vec{k},\lambda\rangle$, the gap function $\tilde{\Delta}_{\vec{k},\lambda}$ transforms according to one of the irreducible representations of the crystal group. Then, the Bogoliubov quasi-particle spectrum becomes

$$E_{\vec{k},\lambda} = \sqrt{\xi^2_{\vec{k},\lambda} + \tilde{\Delta}_{\vec{k},\lambda}\tilde{\Delta}^\dagger_{\vec{k},\lambda}}. \tag{2.46}$$

Finally, the relation between the results obtained in the band description and the original pseudo-spin basis is given below. In the pseudo-spin basis, a general gap function, having both even and odd channels, can be written as

$$\hat{\Delta}(\vec{k}) = [\psi(\vec{k})\sigma_0 + \vec{d}(\vec{k})\cdot\vec{\sigma}]i\sigma_y \tag{2.47}$$

with the pseudo-spin singlet and triplet gap functions $\psi(\vec{k})$ and $\vec{d}(\vec{k})$, respectively [¶]. This gap function can also be recovered from Equation 2.45 through the inverted Bogoliubov transfor-

[¶] recall the discussion presented in section 2.3, specifically on the spin components of the pair' wave-function, such as the matrix in Equation 2.31.

mation, so that $\Delta_{\vec{k},s_1,s_2} = \sum_{\lambda} t_\lambda(\vec{k}) u_{\lambda s_1}(-\vec{k}) u_{\lambda s_2}(\vec{k}) \tilde{\Delta}_{\vec{k},\lambda}$. Using the known form of coefficients $u_{\lambda s}$ and phase factor $t_\lambda(\vec{k})$ [‖] results in the following matrix representation the gap function

$$\hat{\Delta}(\vec{k}) = \sum_{\lambda} \frac{1}{2}[\sigma_0 + \lambda \hat{\gamma}_{\vec{k}} \cdot \vec{\sigma}] i\sigma_y \tilde{\Delta}_{\vec{k},\lambda}, \tag{2.48}$$

where $\hat{\gamma}_{\vec{k}} = \vec{\gamma}_{\vec{k}}/|\vec{\gamma}_{\vec{k}}|$. The comparison between the matrix elements of Equation 2.47 and Equation 2.48 yields

$$\begin{aligned} \psi(\vec{k}) &= \frac{1}{2}\{\tilde{\Delta}_{\vec{k},+} + \tilde{\Delta}_{\vec{k},-}\} \\ \vec{d}(\vec{k}) &= \frac{1}{2}\{\tilde{\Delta}_{\vec{k},+} - \tilde{\Delta}_{\vec{k},-}\}\hat{\gamma}_{\vec{k}}, \end{aligned} \tag{2.49}$$

meaning that the pseudo-spin gap functions — the scalar $\psi(\vec{k})$ as well as the vector $\vec{d}(\vec{k})$ — are composed of pairing occurring in both split $\pm$ bands. Additionally, Equation 2.49 also reveals that the odd component $\vec{d}(\vec{k})$ must be parallel to the spin-orbit coupling parameter $\gamma_{\vec{k}}$. Then, the mixed-parity gap functions are obtained by combining the odd and even pseudo-spin channels in Equation 2.49:

$$\tilde{\Delta}_{\vec{k},\lambda} = \psi(\vec{k}) + \lambda\{\hat{\gamma}_{\vec{k}} \cdot \vec{d}(\vec{k})\}. \tag{2.50}$$

This is a direct manifestation of the inversion symmetry absence; without this symmetry the superconducting state is unable to distinguish between odd and even parity [75].

It is valuable at this point to make some important statements. It is readily seen from Equation 2.49 that if both bands have the exactly same gap magnitude $\tilde{\Delta}_{\vec{k},\pm} = \tilde{\Delta}_{\vec{k}}$, the superconducting state resembles a spin-singlet system — this statement can also be reversed: if the odd-parity spin-triplet is absent in the superconducting state, both bands have the same gap magnitude. But this is not the complete picture emerging from this model. As $\tilde{\Delta}_{\vec{k},\lambda}$ is related both to pairing interaction between time-reversed states and to the anomalous averages $\langle \tilde{a}_{-\vec{k},\lambda} a_{\vec{k},\lambda} \rangle$, the spin singlet-triplet mixture is (un)realized only when two requirements are (un)met:(i) unequal $\tilde{\Delta}_{\vec{k},\pm}$; and (ii) sizable spin-orbit coupling $|\gamma|$ to split the normal electron bands $E_{\vec{k},\pm}$. One consequence of this fact is the possibility of a NCS superconductor with $\tilde{\Delta}_{\vec{k},+} = \tilde{\Delta}_{\vec{k},-}$ ($\vec{d}(\vec{k}) = 0$) still having some spin-triplet-like property, depending on the $\vec{\gamma}_{\vec{k}}$ magnitude in relation to the Fermi energy

[‖] The spin-orbit parameter γ defines both the coefficients and the phase factor.

[77].

Another key feature extracted from Equation 2.50 is that the interplay of the momentum dependent even and odd states could lead to gap nodes in $\tilde{\Delta}_{\vec{k},\pm}$. These nodes would be present only if the odd parity state is sizable in relation to the even parity one. Note that such nodes are not related to the singlet or triplet gap structure alone, but would arise at definite momentum values $\vec{k}'$ in which $\psi(\vec{k}') = -\lambda\{\hat{\gamma}_{\vec{k}'} \cdot \vec{d}(\vec{k}')\}$. These gap nodes have experimentally been suggested to occur in both Li_2Pt_3B and BiPd NCS materials, as shown in Figure 2.1, illustrating the momentum dependence of both d-wave and NCS gaps ($\Delta_{\vec{k},-}$ and $\Delta_{\vec{k},+}$) for comparison.

To gain some insight on the meaning of the above results, it is instructive to consider the case of a Rashba-type ASOC. Table 2.2 provides the momentum dependence of the coupling parameter $\vec{\gamma}_{\vec{k}}$ in this case, in which the parallel component $\gamma_{\parallel}$ will be ignored to simplify the calculations. Once $\vec{\gamma}_{\vec{k}}$ is known, the coefficients $u_{\lambda s}$ are set and enable the split band states $|\vec{k}, \pm\rangle$ to be written in the pseudo-spin eigenbasis

$$|\vec{k}, +\rangle = \frac{1}{\sqrt{2}}(|\vec{k}, \alpha\rangle + ie^{i\phi_{\vec{k}}} |\vec{k}, \beta\rangle); \quad |\vec{k}, -\rangle = \frac{1}{\sqrt{2}}(ie^{-i\phi_{\vec{k}}} |\vec{k}, \alpha\rangle + |\vec{k}, \beta\rangle), ^{**} \tag{2.51}$$

with the azimuthal angle of $\vec{k}$ represented by $\phi_{\vec{k}}$. As mentioned before, the spin-quantization axis is $\vec{k}$-dependent in NCS systems; the phase factor $ie^{\phi_{\vec{k}}}$ rotates the pseudo-spin direction in the $k_x - k_y$ plane. This feature can be visualized in Figure 2.2, where the split Fermi surfaces in the plane k_z = 0 are depicted by the rough blue and red lines and the spin axes are tangent to the Fermi surface in each band. Then, using Equation 2.51 to write down the conventional, singlet state in the helicity basis yields

$$\begin{aligned} |\psi_s\rangle = |\vec{k}; S = 0, s_z = 0\rangle &= \frac{1}{\sqrt{2}}[|\vec{k}, \alpha\rangle |-\vec{k}, \beta\rangle - |\vec{k}, \beta\rangle |-\vec{k}, \alpha\rangle] \\ &= \frac{i}{2\sqrt{2}}[-e^{-i\phi_{\vec{k}}} |\vec{k}, +\rangle |-\vec{k}, +\rangle + e^{i\phi_{\vec{k}}} |\vec{k}, -\rangle |-\vec{k}, -\rangle], \end{aligned} \tag{2.52}$$

supporting that the singlet state is composed of pairs anti-parallel pseudo-spins in both helicity bands, as illustrated by the dashed lines connecting the relevant pseudo-spin within the same

**the factor $ie^{\pm i\phi_{\vec{k}}}$ is the non-trivial phase factor $t_\lambda(\vec{k})$ in the Rashba ASOC, such that $\mathcal{T} |\vec{k}, \pm\rangle = ie^{\pm i\phi_{\vec{k}}} |-\vec{k}, \pm\rangle$.

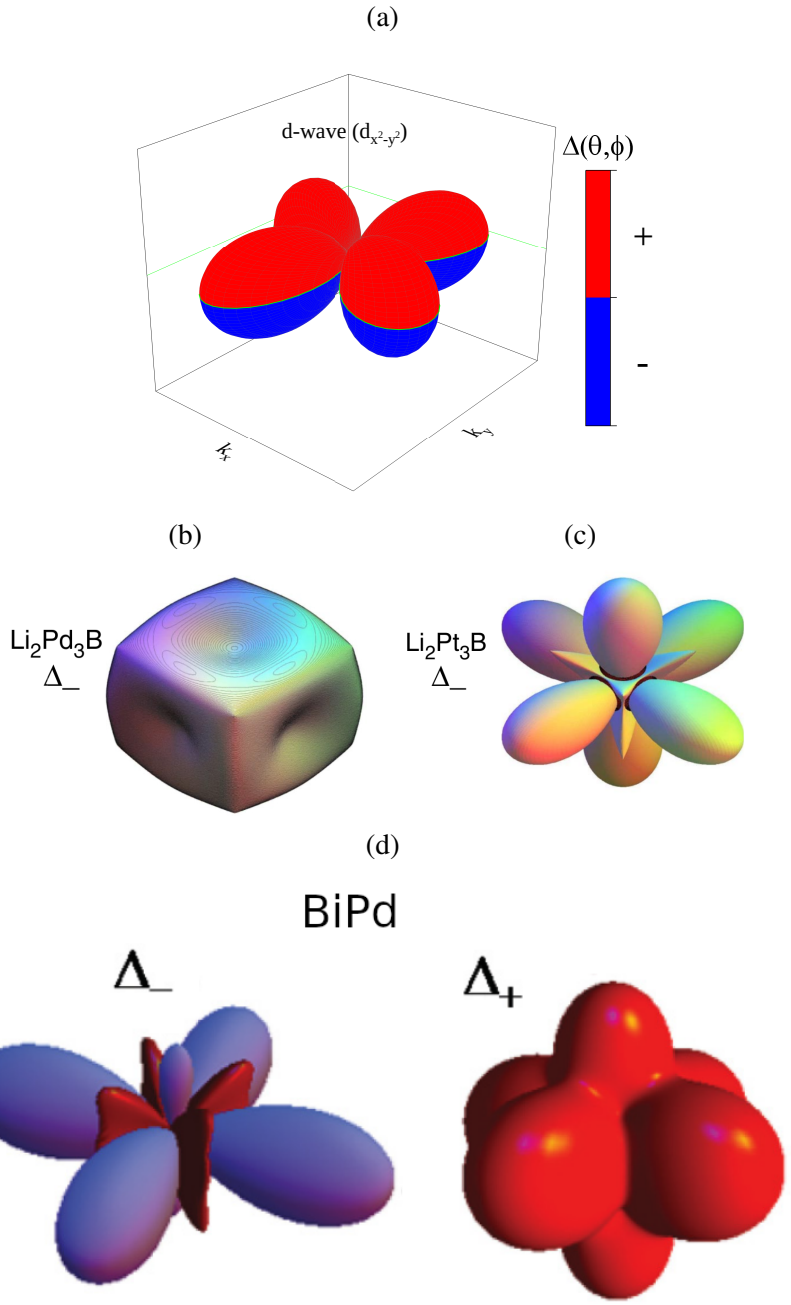

Figure 2.1: Three dimensional plots of the superconducting gaps. (a) represents a general d-wave gap symmetry only. (b) and (c) are the suggested momentum-dependence of the spin-split gap function Δ_- of the superconductors Li_2Pd_3B and Li_2Pt_3B, respectively (adapted from [10]). In this case, there are no gap nodes in (b) while the circle-like black lines represents the nodes in (c). (d) BiPd's gap functions Δ_- and Δ_+ [13].

band λ in Figure 2.2.

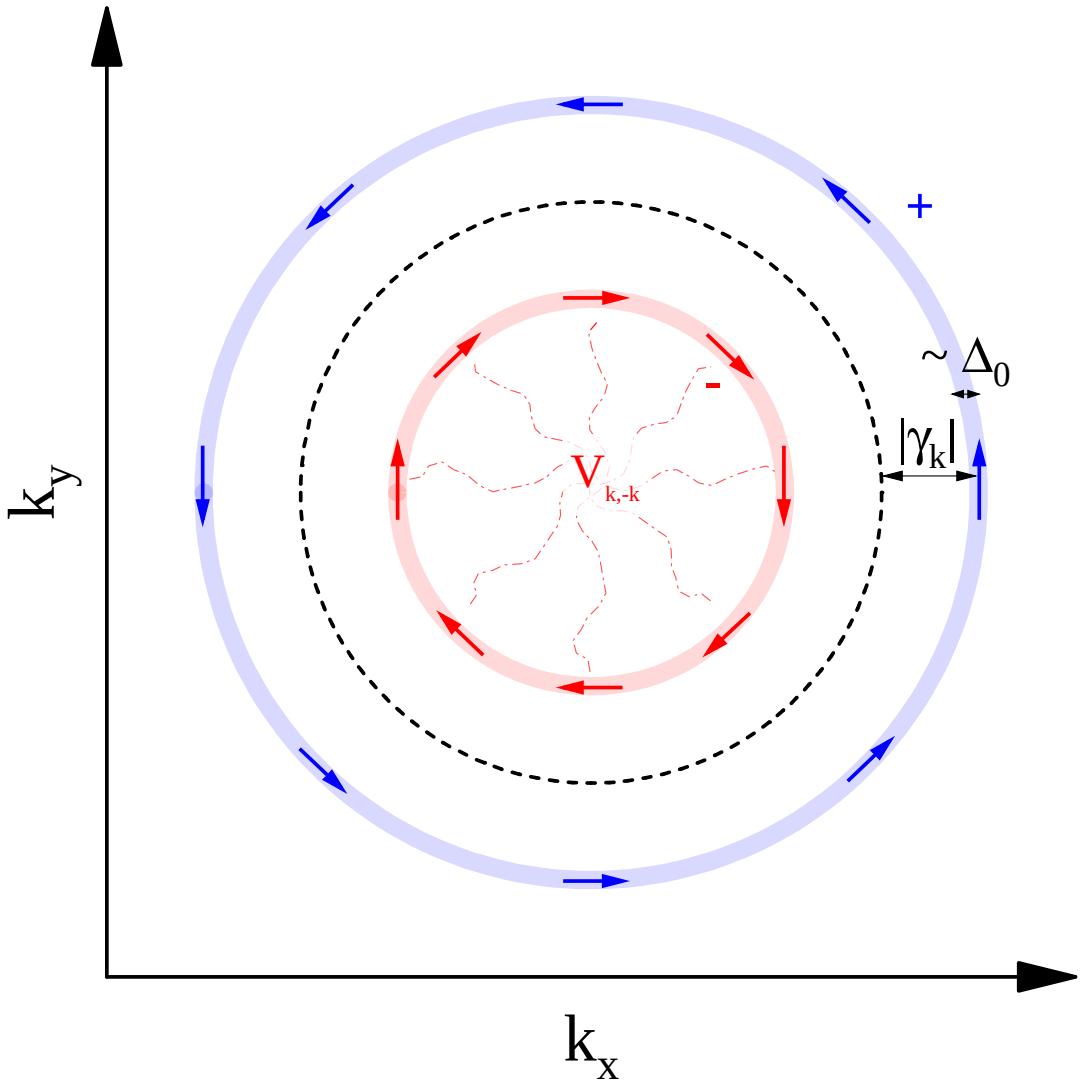

Figure 2.2: The cross section of a simple Fermi surface of nearly free electrons is represented by the black dashed line. The spin-split plus + and minus - bands are depicted by the smeared blue and red lines, respectively. The energy of the spin-orbit parameter $|\vec{\gamma}_{\vec{k}}|$ is larger than the superconducting energy scale defined by Δ_0, illustrated by the lines' thickness, suppressing any possible pairing between the electrons in different bands.

2.5 Critical Fields

There are various kinds of pair-breaking mechanisms capable of suppressing the superconducting properties of a given type-II superconductor [3]. Among those, the magnetic field induced pair-breaking processes have been experimentally probed in this work and are one of the main contributions considered here. Commonly, these magnetic pair-breaking processes are treated as coming from two independent and simultaneous contributions. The first is the Pauli-paramagnetic term related to the Zeeman energy acting on the Cooper's pairs under an external magnetic field. The other is the orbital pair-breaking contribution arising from the supercurrents exceeding the superconducting gap energy scale.

The upper critical field arising only from the Pauli contribution is known as the Pauli paramagnetic-limiting field H_P. This contribution sets a magnetic field threshold beyond which the Cooper pairs are broken due to the electronic band spin polarization, arising from the Zeeman interaction. Then, in the low temperature limit, $H_P(0)$ is set to occur at the exact energy balance between the Zeeman and the superconducting condense energies [75, 80]

$$H_P(0) = \frac{\sqrt{2}\Delta_0}{g\mu_B\sqrt{1-\frac{\chi_s}{\chi_n}}}, \tag{2.53}$$

with g as the electronic gyro-magnetic ratio, μ_B the Bohr magneton, and the spin susceptibility in the superconducting (normal) state χ_s (χ_n). According to Equation 2.53, a non-continuous, first order transition is expected to occur at $H_P(0)$. The linear relationship $H_P(0)$ = 1.86 (T K^{-1}) $\times$ T$_C$ is commonly employed to estimate $H_P(0)$ in s-wave superconductors. This estimate is a reliable one only if some restrictions are valid [81]: Δ_0 is calculated in the weak coupling BCS approximation ($\sim$ 1.764 k_BT_C), g = 2 for bare electrons, and the fact that the spin singlet Cooper pairs do not have any contribution on spin susceptibility (χ_s = 0 in the T $\rightarrow$ 0 limit). Note, however, that $H_P(0)$ is proportional to Δ_0 and inversely proportional both to g and the spin susceptibility ratio χ_s/χ_n . Therefore, many-body interactions would potentially enhance $H_P(0)$, by increasing the ratio between Δ_0 and T_C in a strong-coupling picture as well as reducing the Landè g-factor g [75, 81, 82]. The strong-coupling effects on $H_P(0)$ can be captured by the α-model, using the α parameter to account for the renormalization of

the weak-coupling BCS values [83] — section 4.2.2 describes how this value can be obtained from the experimental data. Then, the α-model leads to a paramagnetic critical field $H_P(0)$ now estimated by

$$H_P(0) = \frac{\alpha}{1.764}\frac{k_B T_C}{g\mu_B} \approx \frac{\alpha}{1.764} 1.86\ T_C. \tag{2.54}$$

On the other hand, the NCS structure affects $H_P(0)$ differently: the limiting field could be increased indefinitely, depending on the magnetic field direction. As NCS superconductors can exhibit an admixture of singlet-triplet pairings, two scenarios may arise here [75]: (i) $H_P(0)$ diverges if the magnetic field is applied perpendicular to $\vec{d_k}$, since the $\chi_s \rightarrow \chi_n$ when T $\rightarrow$ 0 in this case; and (ii) $H_P(0)$ is not affected if the magnetic field is parallel to $\vec{d_k}$. This hypothesis seems to be corroborated by the anisotropic critical fields observed in the NCS $CePt_3Si$ single crystals [84].

The orbital critical field component is due to the overlap of the normal-state vortex cores when the magnetic flux density has reached a critical value. This picture is well described by the GL theory, relating the critical field value with the superconducting coherence length ξ_{GL} as

$$H_{c2}^{orb}(T) = \frac{\phi_0}{2\pi\xi_{GL}^2}, \tag{2.55}$$

with ϕ_0 being the quantum of magnetic flux. The temperature dependence of $H_{c2}^{orb}(T)$ is given by the GL formula in Equation 2.8, adapted for the upper critical field [††]. It has been proposed that impurities alters the orbital field in NCS superconductors, enhancing or decreasing it depending on the major component of the gap function [85]. The orbital critical field is also altered by anisotropic corrections in the superconducting gap as well as multiple gaps or bands scenario [86].

A very useful approximation including the above contributions to the pair-breaking problem is the Werthammer, Helfhand, and Hohenberg (WHH) model [87], which describes the temperature dependence of the reduced critical field $\overline{h} = 4H_{c2}/(\pi^2 dH_{c2}/dT)_{T_c}$ of a dirty su-

[††] $H_{C2} = \sqrt{\kappa} H_C$ in the GL formalism.

perconductor by the implicit relation

$$ln\left(\frac{T_c}{T}\right) = \left(\frac{1}{2} + i\frac{\lambda_{SO}}{\nu}\right)\Gamma\left(\frac{1}{2} + \frac{\overline{h} + \frac{\lambda_{SO}}{2} + i\nu}{2\frac{T_c}{T}}\right) + \left(\frac{1}{2} - i\frac{\lambda_{SO}}{\nu}\right)\Gamma\left(\frac{1}{2} + \frac{\overline{h} + \frac{\lambda_{SO}}{2} + i\nu}{2\frac{T_c}{T}}\right) - \Gamma\left(\frac{1}{2}\right), \tag{2.56}$$

where $\nu = \sqrt{(\alpha_M \overline{h})^2 + (\lambda_{SO}/2)^2}$, α_M is the Maki-parameter, λ_{SO} spin-orbit scattering and, Γ is the digamma special function. The purely orbital critical field is recovered from Equation 2.56 by fixing α_M = 0; in this case, it is estimated to be $\sim 0.693\ T_c(dH_{c2}/dT)_{T_c}$. The WHH model, however, has considered only the conventional s-wave superconducting state. Therefore, some extensions of the WHH model have been proposed to account for anisotropic pairing and/or multigap features [86, 88].

2.6 Vortex Matter

Still before the microscopic description of the BCS theory, Abrikosov was able to explain the Shubnikov phase of some superconducting alloys by using the concepts of superconducting vortices and type-II superconductivity (or superconductors of the second kind) [89]. In his picture, the vortices are created by the diverging nature of charged superfluid velocity around special sites — often related to defects —, in close analogy to the superfluid helium II. Therefore, a normal state is favored around the vortex core due to the increased Cooper pairs energy by the superfluid divergence; this normal state is expected to extend over a certain characteristic length, resulting in a normal vortex core with radius ξ. In other words, the internal vortex structure is such that the superconducting order parameter rises from zero to unity over the coherence length [90].

Type-II superconductors support the creation of superconducting vortices, consequently inducing trapped magnetic flux within the SC material [68]. In its lowest-energy configuration, each vortex carries a single superconducting flux quantum. This is a direct consequence from the external magnetic field not penetrating the (type-II) material homogeneously, resulting in a

magnetic flux that is quantized [‡‡] in units of the superconducting flux quantum:

$$\begin{aligned} \Phi &= n\Phi_0 \\ \Phi_0 &= \frac{hc}{2e} = 2.08\ 10^{-7}\ Wb, \end{aligned} \tag{2.57}$$

with h as the Planck constant, c the light speed, and e the electron charge. In terms of GL theory, this quantization is a direct result of a single-valued superconducting order parameter [3]. The region spanned by the supercurrent circulation required to generate one superconducting quantum flux sets the another characteristic length [90], the magnetic penetration depth λ.

Upon entering the superconducting volume, the various individual magnetic flux lines arrange in a configuration known as vortex lattice (or flux-line lattice FLL). A magnetic field gradient ensures there is a repulsive interaction between two vortices with the same direction, falling off exponentially at large distances but varying logarithmically at small intervortices spacings [3]. A visual representation of this interaction is illustrated in Figure 2.3(a)-(b). Then, this inter-vortex interaction alone, in absence of any force preventing vortex motion, sets the triangular array of the vortex lattice as the more stable static structure, since it has the lowest energy configuration. The hexagonal nature of the FLL has been confirmed by various experimental studies. Shown in Figure 2.3(d) is the vortices configuration obtained by Hess *et al.* [91] through scanning tunneling microscope (STM) measurements.

As of the conventional atomic lattice, the flux-line lattice could also undergo a melting transition by altering thermodynamic variables such as temperature. In this case, raising the system temperature induces thermal vibrations of the flux lines away from the otherwise ideal, rigid Abrikosov lattice. Nonetheless, such a melting transition is obscured when using the mean-field theory to treat conventional superconductors, since the magnitude of the order parameter vanishes only in the vicinity of T_c in those materials; descriptions taking into account the fluctuation of the order parameter (or fluctuation effects) are able to capture the melting picture. Although believed to be a true thermodynamic transition, discontinuously destroying the long-range "crystalline" order, the FLL melting would be difficult to observe in thermodynamic measurements, such as specific heat. This is due to a much larger entropy change by the mi-

[‡‡] Actually, the physical quantity quantized here is the fluxoid.

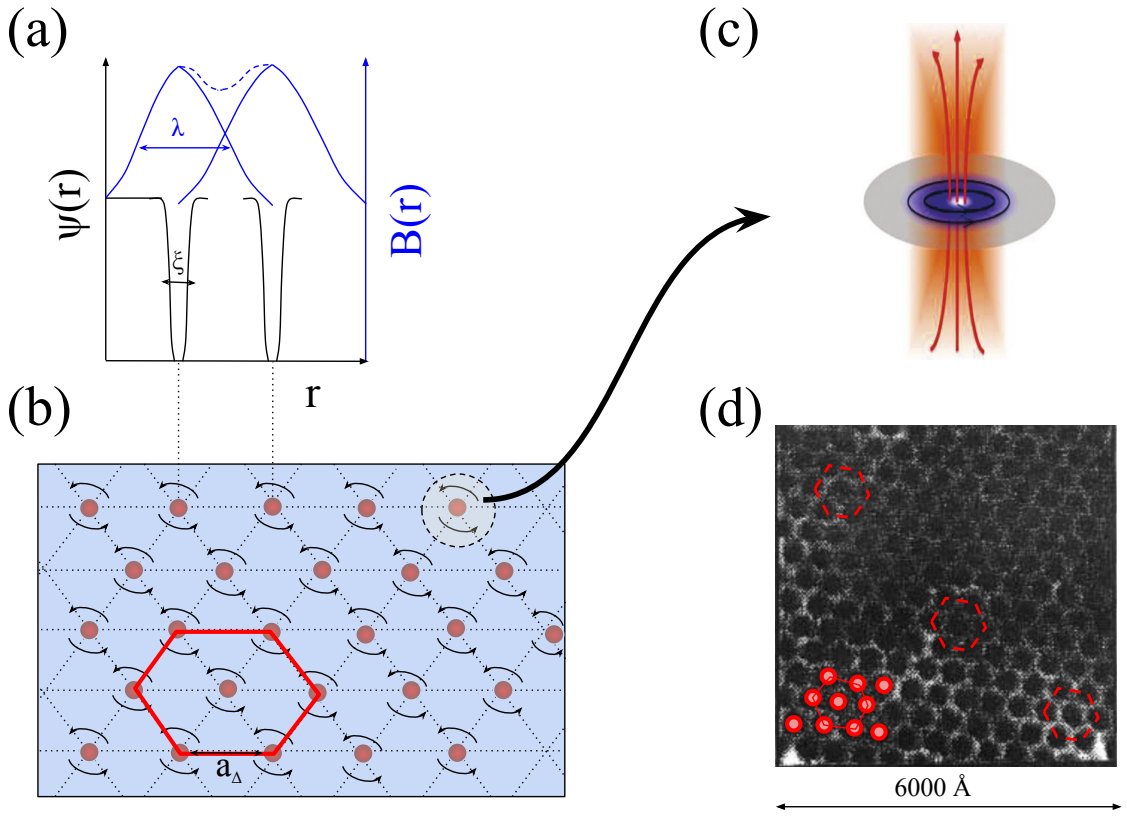

Figure 2.3: Illustrations of the Flux line lattice. (a) Order parameter and magnetic field spatial distributions between two flux-lines. (b) Triangular vortices array forming a hexagonal configuration. (c) Representation of a single flux-line in each site of the FLL, adapted from [68]. (d) STM picture of the SC vortices in $NbSe_2$, figure adapted from [91]

croscopic electronic degrees of freedom occurring in a SC transition, masking the more modest entropy change associated with the vortex ordering [3].

2.6.1 Pinning Phenomena

According to the above description, a perfect SC material in the mixed state would dissipate energy when excited by an electric field, since the current flow would exert a Lorentz force F_L on the flux vortices

$$F_L = J \times B. \tag{2.58}$$

Then, the vortices would move, creating a voltage drop in the superconductor and also generating heating effects. As real materials have microstructural defects such as impurities, crystal defects, and second phase precipitates, the movement of vortices is prevented by the interaction with those crystal imperfections. Such a mechanism is known as flux pinning due to its ability

to pin the vortices to fixed locations. Therefore, the net pinning force acts to exactly counterbalance the Lorentz force and depends essentially on the particular material's microstructural parameters and the local value of the magnetic field [92, 93].

There are different regimes in response to external excitations depending on the strength of the pinning forces within a superconductor. In the weak pinning forces approximation, the vortices would move freely if the Lorentz force overwhelms the pinning forces, but would also experience a viscous flux flow caused by a dragging force. According to the Bardeen-Stephen model [94], due its normal core, the moving vortices will cause a flow resistance ρ_{ff}

$$\frac{\rho_{ff}}{\rho_N} \propto \frac{H}{H_{c2}}, \tag{2.59}$$

proportional to the reduced field value, where ρ_N is the normal resistivity of the material.

For the case of hard superconductors, exhibiting strong pinning forces, the critical state model is widely accepted to predict some of its properties. Upon changing the external current or field, the critical state model assumes that shielding currents are induced on the sample's surface until a maximum value is reached. Then, this maximum current density, the critical current J_c, is attained when the Lorentz force on flux lines is balanced by pinning forces due to inhomogeneities; field penetration starts to occur beyond this critical current value. In the simplest case (Bean model), where J_c is assumed to be field independent [95], the net result is such that the current density is either everywhere equal to the J_c or zero. In general, J_c may depend on the flux density [96] and local microstructure [93].

Different experiments could be explained by using this critical state description since the model reduces the variables to a single property of the material, the critical current J_c. The hysteric magnetization features arising when cycling hard superconductors in an external field can be roughly captured by the Bean model. Another example is the description of the thermomagnetic instabilities arising from the competition between the thermal and magnetic diffusities. In this case, any disturbance of the critical state, such as a constant magnetic field sweep, potentially leads to flux redistributions in order to lower the instantaneous overall energy configuration and restore the critical state. These flux redistributions are the mechanisms behind the spectacular vortex avalanches, or flux jumps, known to take place in some hard superconductors

and also occur in some Re_3M samples studied here.

The avalanche-like events are connected to the unstable configuration of the vortices in the critical state, and its triggering occurs by a local thermal fluctuation coupled with the temperature dependence of J_c. Then, an initial increase of T (δT_i) would lead to a decrease of the critical current density ($J_c \downarrow$), subsequently releasing heat and creating another thermal gradient (δT_f) leading to cycles of the type $\delta T_i \Rightarrow J_c \downarrow \Rightarrow \delta T_f$ [97]. The relation between δT_i and δT_f defines whether the process will go on indefinitely or not: the critical state of the superconductor would be stable against the local thermal fluctuation only if $\delta T_f < \delta T_i$, while the avalanche-like flux jumps would then occur in the case of $\delta T_i < \delta T_f$. Those flux jumps could occur in a complete manner, i.e., the avalanche only stops when the temperature of the material is above T_c, or in a partial way, where the flux redistributions lead the sample to the unstable equilibrium once again; additionally, the magnetic moment of the sample can even be reversed during a giant flux jump [98].

Although some general features can be understood by the microscopic details of vortex motion, a macroscopic point of view is more suited to further discuss the vortex motion in presence of pinning. This is due to the inter-vortex mutual repulsion preventing the individual motion of a vortex within the lattice, inducing the flux movement to occur in bundles when the pinning force is exceeded by the overall driving force. Including the effect of temperature in the vortex motion problem results in the thermally activated flux creep, where bundled flux lines are capable to tunnel between adjacent pinning sites depending on the thermal energy provided to the system [99, 100]. Additional types of superconducting response when the vortex motion is treated collectively are considered and discussed below.

2.6.1.1 Collective pinning

No overall pinning could exist in a perfect vortex configuration consisting of a rigid FLL with randomly distributed pinning centers [93]. This is a direct consequence of the summation problem, as any flux line would interact with an equal number of pinning sites adding up or opposing to the Lorentz force, effectively leading to a zero net force. As the real FLL is not strictly rigid, it would acquire some kind of elasticity or plasticity in response to external excitations. Then,

deviations from the ideal hexatic Abrikosov lattice are expected to occur as the flux lines tend to pass through the more favorable pinning sites. In doing so, the system distorts the lattice in order to better conform the pinning forces while still minimizing the total lattice energy. The shape of an isolated elastic flux line is illustrated in Figure 2.4 [101].

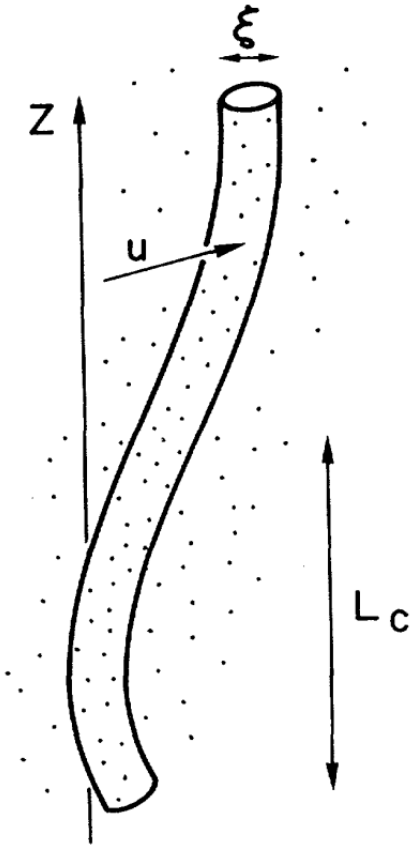

Figure 2.4: Distorted flux line in a randomly pinning potential induced by the point-like impurities (black dots). Figure adapted from [101].

In Nb alloys, for instance, the FLL is very soft mainly because of the large magnetic penetration depth λ, as the shear modulus of the FLL is $c_{66} \sim \lambda^{-2}$, and the tilt modulus $c_{44} \sim (1 + k^2/\lambda^2)$ become very small for short distortion wavelengths $2\pi/k \ll \lambda$ [102]. In layered high-T_C superconductors this softness is further enhanced by the pronounced anisotropy which strongly increases the penetration depth for electrical current densities J along the c-axis of these (nearly uniaxial) materials and may even cause a decoupling of two-dimensional vortex lattices within the Cu-O layers. A combination of thermal fluctuations and softening may melt the FLL and cause thermally activated depinning of the flux lines in 3D superconductors or two-dimensional 'pancake vortices' in layered compounds.

As long as the lattice distortions are small, on the order of ξ, the elastic continuum approximation is still valid to describe the FLL [103]. In this elastic description, Larkin and Ovchinnikov propose a theory treating the collective pinning for the case of randomly distributed weak disorder, acting as point-like pinning centers. This collective pinning model assumes that there is no long range order present in the FLL. Instead, the sample volume is subdivided into correlation volumes V_c within which short range order exists and the FLL is assumed to be almost periodic. Each vortex segment within V_c, set by the longitudinal L_c and transversal R_c pinning lengths, is then pinned independently, leading to a finite critical current density when balancing the Lorentz force against the pinning force acting on these individual segments [101]. A schematic view of the FLL composed by those correlation volumes is exhibited in Figure 2.5

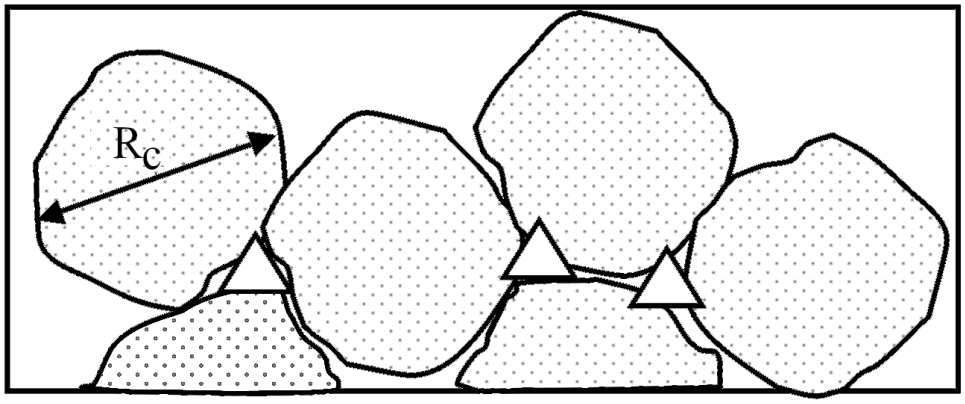

Figure 2.5: Illustration of the Larkin's description of the flux line lattice with collective pinning. In a simple (and not complete) description, the FLL is subdivided in crystallites with R_C as the characteristic Larkin length. Figure adapted from [103].

The random pinning forces adds in similar manner as random walk, and using the statistical summation of pinning forces results in a net pinning force proportional to $N^{1/2}$, whereas $N = nV_C$ is the total number of pinning centers in V_c and n is the density of pinning centers. Defining f_p as the pinning force per unit volume, the total pinning force $F_p = f_p N^{1/2}$ is opposing the Lorentz force (= $J_C V_c B$) when the maximum critical current density is flowing in a superconductor at equilibrium, leading to

$$J_C = \frac{f_p n^{1/2}}{B V_c^{1/2}} = \frac{n^2 f_p^4}{2 B c_{44} c_{66}^2 \xi^3}. \tag{2.60}$$

The right hand side of Equation 2.60 uses the value of V_c in terms of the pinning lengths L_c and

R_c, calculated by minimizing the elastic free-energy in a 3D distorted lattice [3, 102]. Then, $V_c \rightarrow \infty$ for a perfectly ordered lattice, hence $J_c \rightarrow 0$. On the contrary, V_c is finite for a disordered FLL and therefore the critical current density is non-zero.

According to Equation 2.60, a softer, less rigid FLL will have a larger critical current, and this is one of the main points when discussing the peak effect in the next section. Nonetheless, as the results given above are based on an effective elastic response of the FLL, the collective pinning theory is expected to breakdown at (or in the vicinity of) the melting temperature, where the shear modulus $c_{66} \rightarrow 0$.

The absence of long range order, however, was not confirmed by experimental studies on neutron diffraction (for instance, in conventional Nb) at the time, which strongly suggested an ordered vortex phase in the mixed state. Then, it has generally been agreed that disorder leads to a glass state with diverging barriers, pinning, and loss of translational order. One of those states is the vortex-glass phase that may occur with vanishing resistivity and long-range phase coherence [105], in contrast to the short-range coherence volumes in Larkin theory. By revisiting the weak random pinning problem, some authors argued that other glassy phase, the Bragg-glass, exists deep within the superconducting state [106, 107]; its dynamical properties are glass-like but it also retains a quasi-long range order, with diverging Bragg peaks, and perfect topological order (absence of dislocations) [103]. Furthermore, a transition from the quasi-ordered Bragg glass to a more disordered vortex-glass has also been proposed [107], what sometimes is called as the order-disorder transition of the vortex lattice. This solid to solid transformation is considered to arise due to a sudden proliferation of dislocations into the Bragg glass phase.

2.6.1.2 Peak effect PE

Ubiquitous in nearly all varieties of type-II superconductors, the peak effect is a sharp anomaly in which the field or temperature dependence of the critical current J_c is peaked. In conventional superconductors, this peak usually occurs close to the normal phase boundary, being already noted in some early 1960's studies [108], when Abrikosov ideas still were not fully appreciated. It is expected that J_c decreases monotonically with increasing temperature or magnetic field.

However, in the peak effect region and under certain circumstances, increasing magnetic field, electric current density, and temperature actually enhances the superconducting state.

The peak effect anomaly was one of the problems that Larkin and Ovichinikov (LO) addressed when proposing their theory on collective pinning. In light of what has been discussed so far, the PE can be related to a sudden increase of the pinning forces acting on vortices, but the mechanism and nature of such increase is still in debate. The LO result came as to corroborate the earlier ideas of Pippard [109], who advocated that a softening of the shear stiffness of the FLL might lead to the steep increase of $J_c(B)$ near the upper critical field, where c_{66} vanishes quadratically as $(H\text{-}H_C)^2$. More recent views put forward by some authors propose that the order-disorder transition between the complex vortex-matter, such as the Bragg to vortex-glass transition, induces the peak effect; such description is illustrated in Figure 2.6 [110], in agreement with contemporary phenomenological theories on the subject matter [111]. Another cause of the peak effect would be related to thermal fluctuations [112, 113]. Therefore, it seems that there is not a single mechanism to universally explain the PE, as this general effect could encompass a large set of interrelated phenomena in which the interplay between thermal fluctuations and intrinsic material disorder is the main ingredient.

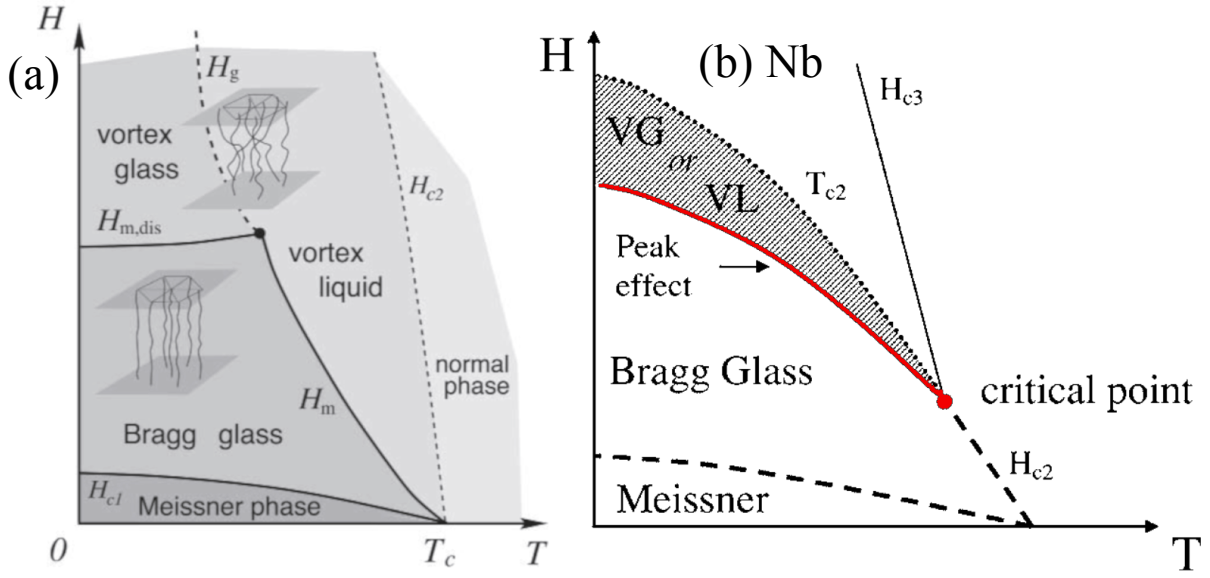

Figure 2.6: (a) General phase diagram of a type-II superconductor [114]. (b) Suggested Niobium superconducting phase diagram including the order-disorder transition from the Bragg to the Vortex glass phases. The peak effect would be induced at this boundary line. Figure adapted from [110].

Only the elastic description of the FLL have been considered so far. The elastic model is

effective in describing the weakly pinned FLL; but even in those weakly pinned systems the interaction is substantially enhanced as the peak effect emerges. Then, a proper description of stronger pinning interactions would consider plastic responses from the vortex lattice, permanently distorted by the stronger pinning centers, creating FLL defects. Not surprisingly, numerous studies point towards the correlation between the peak effect and sample disorder [115–117], which would potentially induce a breakdown of the FLL elastic response as disorder grows.

The plasticity picture is more evident in the dynamic response of the vortex lattice, i.e., when the vortices begin to move. This movement occurs when the critical current threshold is exceeded, leading to depinning of the flux lines. In the elastic depinning, the vortex system may move coherently through meandered channels along the principal axis of the FLL [118], as those channels are the best compromise between the elastic forces and the static disorder still experienced by the moving system [103]. On the other hand, near the threshold depinning, the plastic flow is characterized by the breaking and eventually reforming of bonds between neighboring vortices during flow [119] and some of the FLL regions can remain pinned while other parts of the system flow [103].

Shown in Figure 2.7 is the dynamical phase diagram of a sample exhibiting the peak effect, whose boundary lines F_p, F_{pl}, and F_{cr} are related to the pinned solid $\rightarrow$ elastic flow, pinned solid (or liquid) $\rightarrow$ plastic flow, and elastic $\rightarrow$ plastic flow dynamical transitions, respectively. In this particular sample, the authors argue that plastic flow of the flux-line lattice dominates the intermediate regime, being accompanied by qualitative changes in the I-V curves related to tearing of the FLL [120]. This intermediate regime is precisely where the peak effect occurs.

From a phenomenological point of view, the peak effect can manifest itself in various properties of a superconductor material. These include electrical transport, A.C. susceptibility, D.C. magnetization, and eventually thermodynamic properties [110, 121]. Then, shown in Figure 2.8 is a collection of experimental results in various systems exhibiting the peak effect. The critical current density J_c of a MoGe thin film [122] in Figure 2.8(a) declines monotonically before starting to increase at the peak effect region (highlighted in yellow). Field dependent electrical resistivity of the same sample is also shown in Figure 2.8(b), having a resistance minimum just

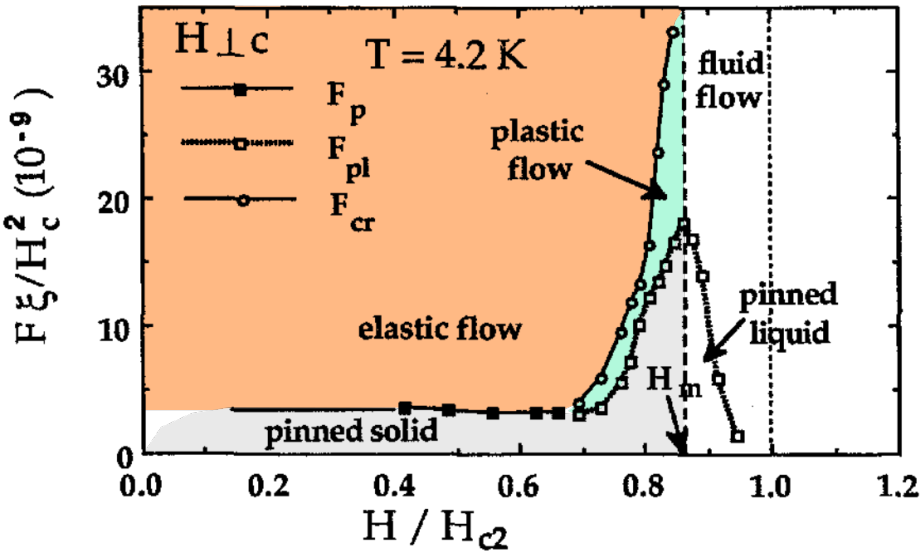

Figure 2.7: Dynamical phase diagram exhibiting the driving force versus the magnetic field response of a $NbSe_2$ sample exhibiting the peak effect, readily visible by the peaked shape of the boundary lines. Figure adapted from [120].

below the mean field transition at H_{c2}. In D.C. magnetization M(H) measurements, a bump close to H_{c2} usually is the signature feature of the PE, as exemplified in Figure 2.8(c). The PE also induces a minimum in the A.C. magnetic susceptibility χ at fields just before the transition to the normal state (Figure 2.8(d)), very similar to the ρ(H) results. The magneto-caloric signature of the peak effect is exhibited both in Nb and Nb_3Sn data, where clear peaks are readily seen in Figure 2.8(e) and Figure 2.8(f).

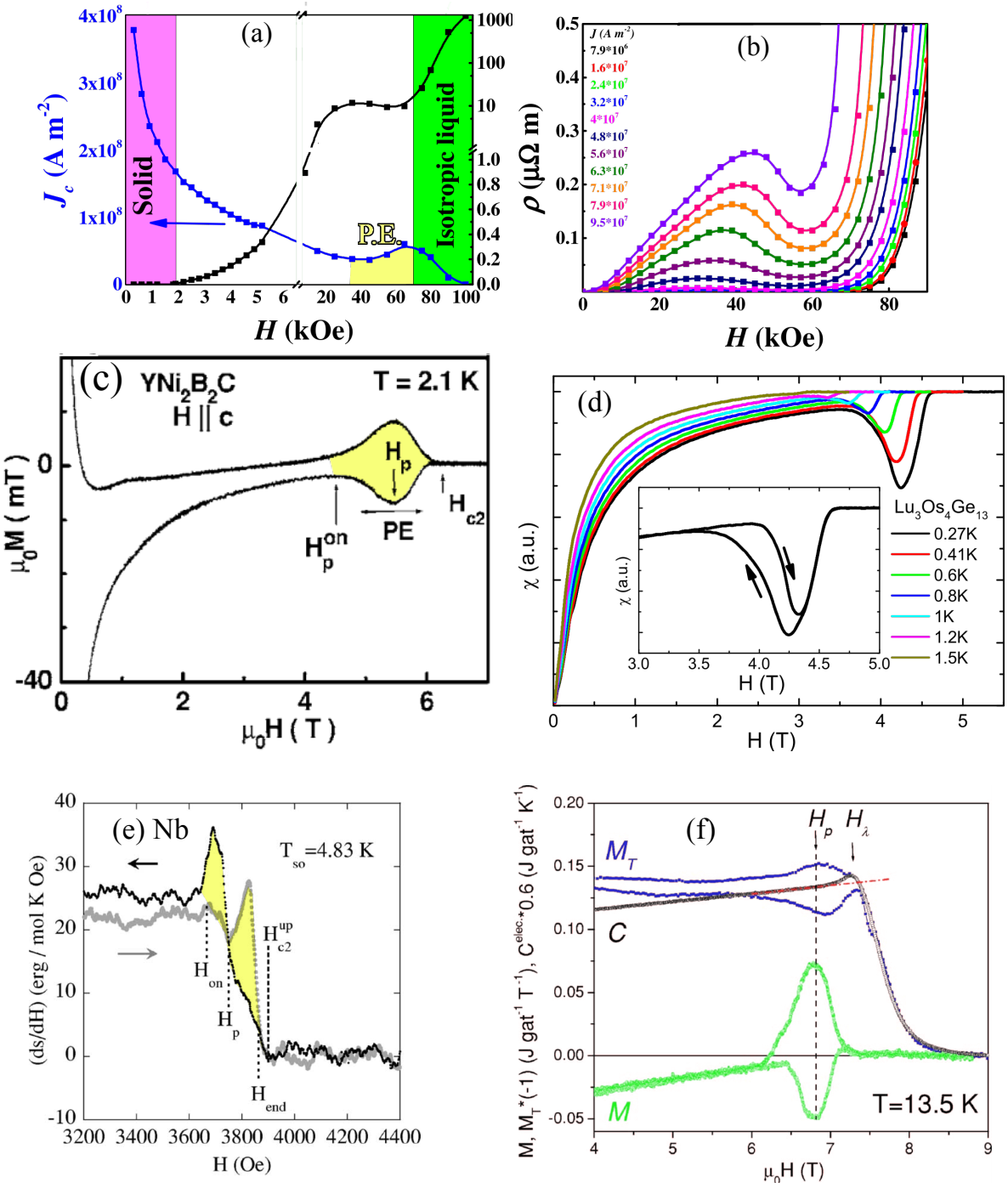

Figure 2.8: Various measurements of superconducting materials with the peak effect. (a) and (b) are the measurements of the magnetic field dependence of the critical current and electrical resistivity, respectively [122]. (c) Magnetization data of the borocarbide superconductor YNi_2B_2C exhibiting a characteristic peak near H_{c2} [123]. (d) Magnetic susceptibility curves with minima associated with the PE, with the irreversibility between the heating and cooling curves shown inset [124]. (e) Peaks seen in the magneto-caloric effect of a Nb sample [110]. (f) Comparison among various Nb_3Sn results: magneto-caloric, magnetization and specific heat measurements taken across the peak effect occurring at H_p [121].

A material prone to instability and flux jumps when the flux gradient is very steep may display the peak effect in the critical current curve [90]. In the case of the Re_3M materials studied

here, both the flux jumps and the peak effect were observed in our polycrystalline samples, whose pinning strength has not been anticipated to lie in the weak limit due to the samples' inherent disorder. As far as (roughly) similar sample properties goes — but not considering the NCS features in our samples — the study on the peak effect arising in a polycrystalline V-Ti alloy is of great interest to the discussion made here [125], as well as the published works on the Nb_3Sn compound [121, 126]. The first suggests that the local order-disorder Bragg glass transition in microcrystalline domains may be the cause of the peak effect while the latter ascribe the peak effect as arising in response to its not so weak thermal fluctuations. These different mechanisms are certainly related to the stark contrast between the basic SC properties of the V-Ti alloys and the Nb_3Sn compounds. To the best of our knowledge, no experimental evidence, or even a theoretical suggestion, of the peak effect emerging in NCS SC materials have been discussed up to this date. Then, it remains unclear whether the lack of inversion symmetry could be related with the peak effect in the Re_3M samples.

Chapter 3

Experimental Techniques

This chapter deals with the experimental part of this manuscript and its purpose is to present the methods of production and characterization of the superconducting polycrystalline samples. The temperature range used in this experimental study has been rather wide, spanning the high temperature side ($\sim$ 3000 K) in the synthesis and heat treatments as well as the low temperature (down to 100 mK) to characterize the Re_3M superconducting specimens. Cryogenic liquids are required to study matter at low temperatures, enabling the study of superconducting materials in cryogenic environments. The brief overview presented below describes the experimental apparatuses used in the various characterizations; a more detailed description of the instruments can be found in the manufacturers' manuals and/or in the specialized literature.

3.1 Synthesis of polycrystalline samples

3.1.1 Arc-melting

An arc melting furnace was used to mix the refractory metals Re (99.9 %at.), W (99.9 %at.), Nb (99.99 %at.), and Ta (99.99 %at.), since the lower melting point in this set is $\sim$ 2500 $^\circ$ C. This furnace is composed of a central chamber housing a movable electrode and whose base works as the bottom electrode. The bottom electrode is made of a water cooled 2.5 cm thick cooper plate. The chamber is connected both to pumping and high purity Ar (99.999 %at.) lines, enabling the purge of atmospheric gases from the chamber's volume. The electrodes are

connected to a high voltage power supply.

In order to mix stoichiometric pieces of high purity metallic elements, care must be taken in reducing the partial oxygen pressure inside the chamber. This is done by pumping the chamber down to pressures $\sim$ 20 mTorr, closing the pumping line, refilling the chamber with pure Ar up to atmospheric pressure, and repeating this cycle three or more times. Additionally, a piece of Ti (much larger than the typical sample's size) is also placed close to the mixture of the elements to be melted together, working as an oxygen getter.

The arc is created under the Ar atmosphere and, before heating the mixture, the Ti piece is melted to absorb any remaining oxygen. After half a minute, the arc is moved to the surroundings of the mixture of elements, in order to heat them slowly. When the mixture is glowing dimly, the arc is immediately redirected to it, and the mixture melts together after a few seconds. Depending on the sample's composition, it may be required to increase the power of the power supply, and consequently the temperature, to fully melt the constituents. After approximately one minute of melting, the power is shut down abruptly and the sample is cooled rapidly by the thermal contact with the water-cooled cooper base. The melting order Ti $\rightarrow$ mixture is repeated two or more times in this position. Then, the unpowered top electrode is used to flip the sample, placing the sample's base pointing upward. The sample then is remelted and the procedure is repeated several times (at least three more times) to improve the homogeneity of the samples. In its final form, the sample is a spherical metallic button with approximately 4 millimeters of diameter (for samples with 1 gram).

The final step is to check if any weight variation occurred in the melting procedure, which could cause deviations in the desired stoichiometry. All the samples produced in this work had only negligible mass loss, less than $\sim$ 0.5 %wt. of the initial mass, as expected for mixing refractory elements with high boiling points at atmospheric pressure. Samples subjected to these steps are referred as as-cast (AC) samples.

3.1.2 Heat treatments

Following the initial arc-melted production, the AC samples were annealed at 1100 or 1700 °C, depending on different experimental setups. This procedure was conducted in order to promote

a higher degree of homogeneity to the AC specimens. Only a few samples were exposed to heat treatments in both temperatures, while the vast majority of the samples studied here underwent a single heat treatment step (see Table 3.1). The samples mass were carefully recorded before and after each heat treatment, ensuring that no contamination or diffusion took place during the treatments.

In the lower temperature heat treatments, the samples were heated to 1100 °C during 10 days — which is the maximum temperature in this setup's temperature range. To conduct this heat treatment, pieces of the samples were first wrapped in Nb foils, forming bundles. These bundles were placed in a quartz tube, subsequently sealed with a slightly positive pressure of ultra pure Ar gas. Then, the quartz tube was heated inside a commercial muffle furnace from Lindberg, whose temperature was limited to 1100 °C in order to preserve the inert Ar atmosphere inside the quartz tube.

Higher temperatures heat treatments were obtained with a homemade vacuum furnace, not limited by the quartz 1200 °C threshold. The samples were placed directly on top of a high purity Mo platform, heated by the power delivered by its current source, while the furnace temperature was continuously monitored by a pyrometer and the main sample chamber was kept at pressures below $\sim$ 10 μTorr. This type of heat treatment was conducted by our collaborators at the Escola de Engenharia de Lorena, using dwelling times of 8-10 and 20 hours.

Table 3.1: Selected samples subjected to one or both annealing procedures.

Sample	1100 °C - 10 days	1700 °C (hours)
Re_3W *	✗	30
Re_3Ta	✓	10
Re_3Nb	✓	10
$Re_3Ta_{0.1}W_{0.9}$	✓	10
$Re_3Nb_{0.1}W_{0.9}$	✓	10
$Re_3Ta_{0.25}W_{0.75}$	✓	10
$Re_3Nb_{0.25}W_{0.75}$	✗	10
$Re_3Ta_{0.5}W_{0.5}$	✗	10
$Re_3Nb_{0.5}W_{0.5}$	✗	10

*This sample has been subjected to two rounds of heat treatments at 1700 °C, totaling 30 hours at that temperature.

3.2 Physical characterizations

3.2.1 X-ray Diffraction

Structural properties of the Re_3M samples have been analyzed by X-ray diffraction (XRD) measurements. In short, this type of technique enables the study of the atomic arrangement of a sample by placing it along the direction of the X-ray beam. This beam is diffracted by the sample's ordered electronic cloud, since the distance between crystallographic planes d_{hkl} is of the same magnitude of the incident wavelength λ. This process is illustrated in Figure 3.1(a), which is a very simple sketch of the phenomenon. An X-ray detector is placed in the direction of the diffracted beam, in the Bragg-Brentanno geometry.

Constructive superposition of the diffracted beams occurs at specific angles θ_{hkl} associated with d_{hkl} by the Bragg-law:

$$2d_{hkl}sin(\theta_{hkl}) = n\lambda,$$

where n is simply an integer. Therefore, X-ray diffractograms are obtained by sweeping the scattering angle 2θ, defined as the angle between the incident and diffracted beams, and have well defined peaks at θ_{hkl} corresponding to various d_{hkl} of a given atomic ordering. The elastic scattering occurring in the diffraction process can also be visualized in the reciprocal lattice — the Fourier transform of the real space lattice. In the reciprocal space, the diffraction condition is written as **k'**= $(\mathbf{k} + \mathbf{G})^2 = \mathbf{k}^2$, with **G** being a reciprocal lattice vector [1]. This fact is illustrated in Figure 3.1(b) in which the Ewald sphere define all the possibles **k'** participating in the diffraction process, represented by the orange circles.

The Bruker D8 - Discovery diffractometer was the commercial apparatus used to conduct the XRD measurements, property of the Departamento de Física Aplicada of this Institute. The unit operated in the θ-2θ (or Bragg-Brentanno) geometry, as displayed in Figure 3.1(a). The X-ray source was a cooper tube driven by a current of 30 mA and V = 40 kV, resulting in the radiation's wavelength of λ = 1.5406 Å(Cu K_{α_1}). A Ni CuK_β-filter has been placed before the detector to decrease the yield of some artifact peaks. Typically, the angular sweeping was between the 15 $\leq 2\theta \leq$ 120 ° range during the runs, with 0.05 ° as the angular step size. Additionally, some set of data have also been obtained with 0.02 ° step to resolve some otherwise superimposed

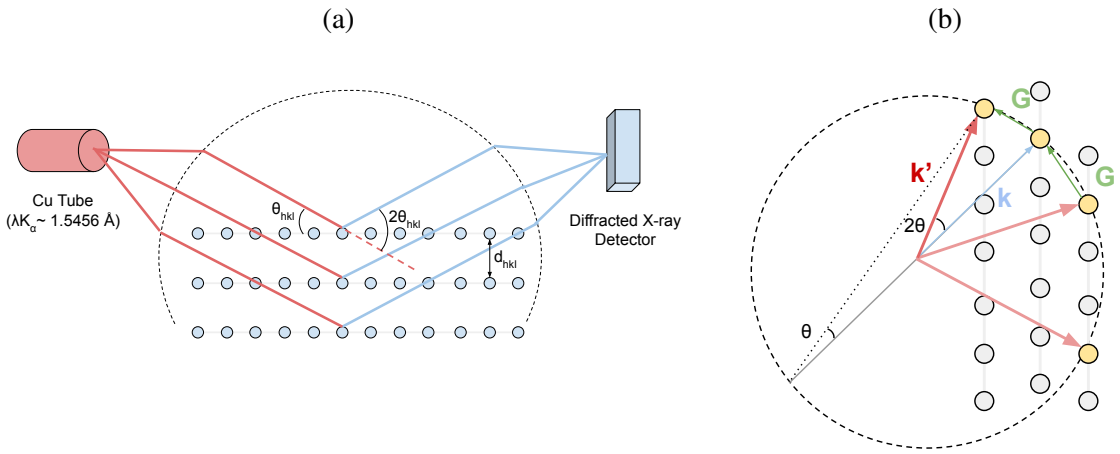

Figure 3.1: (a) Schematic representation in real space of the diffraction process during the angular scans. (b) Reciprocal space analogue of the diffraction process, where all the reciprocal lattice points lying on the Ewald sphere (dashed circle) contributes to the total elastic scattering.

reflections. All the samples were irradiated during at least two seconds in each step.

In general, the samples were measured by using its powders. Nonetheless, it was not possible to crush some of the as cast specimens with a conventional steel mortar. For these samples, the XRD measurements were conducted in the sample's surface, which was carefully sanded and cleaned. Due to small surfaces, however, the results of these measurements contained elevated levels of background, but the main peaks were clearly seen.

Powdered samples were obtained by crushing small pieces of the sample until reaching a fine powder. This powder was attached on the sample support (a conventional glass slide) using vacuum grease (silicon grease). Then, the glass slide was coupled to the sample holder of the equipment.

Rietveld refinements were conducted in raw powder XRD data to extract structural parameters of each specimen. This refinement method employs directly the profile intensities obtained from the step-scanning measurements of the powder diagram and uses a least-squares refinement procedure [127, 128]. In this way, various parameters are simultaneously optimized to calculate a diffractogram that matches the observed powder diagram. These parameters include sample's specific ones, such as the lattice parameters; those related to the experimental set-up itself, such as the background noise; and also the ones influenced both by the instrument and sample, as it is the case of the peaks shapes. The software FULLPROF [129] automates the fitting procedure and was used to conduct the refinements of the NCS Re_3M materials by using the

atomic coordinates shown in Table 1.1 and the nominal Re:M atomic ratios in each Wyckoff site.

3.2.2 Magnetic Properties Measurement System - MPMS

The MPMS, equipment from Quantum Design Inc., is equipped with a continuous Helium-gas-flow cryostat to control the temperature of the sample between 2-300 K, cooling it by flowing the cold He gas over its surface. Two reservoirs are used in this cryostat, with the liquid helium reservoir nested inside the outer reservoir filled with liquid nitrogen (LN_2). The outer reservoir works as a radiation shield, suppressing the helium evaporation promoted by the external radiation (which travels through the evacuated space separating the room temperature from the helium reservoir) [130]. As the boiling of LN_2 produces vibrations, the outer LN_2 reservoir has been replaced by a super-insulation layer as the radiation shield in more moderns cryostats.

Shown in Figure 3.2 is the experimental setup used to deliver the cooling power to the sample space. The liquid helium bath is thermally isolated from the sample chamber by the vacuum sleeve. A variable impedance is used to introduce liquid helium into the cooling annulus, which is in thermal contact with the sample chamber. The liquid helium is vaporized by the gas heater upon entering at the bottom of the cooling annulus. This gas is pumped and its temperature is set both by the power to the gas heater and the flow-rate [131]. By turning off the chamber heater, the sample space can be quickly cooled, achieving rates of -10 K/min when the unit is operating in the cooling mode.

The external magnetic field is provided by a superconducting magnet (also embedded in the helium bath) attached on the sample probe (highlighted in Figure 3.2(a)), as exhibited in Figure 3.2(b). Additionally, the **S**uperconducting **Qu**antum **I**nterference **D**evice (SQUID) detection coils are also assembled together with the magnet. The sample's magnetic moment detection is described in the following.

3.2.2.1 Magnetization M(T)

In this system, a SQUID is used to probe the magnetic flux within the sample, proportional to the sample's magnetic moment. In short, the quantum interference of tunneling Copper pairs at

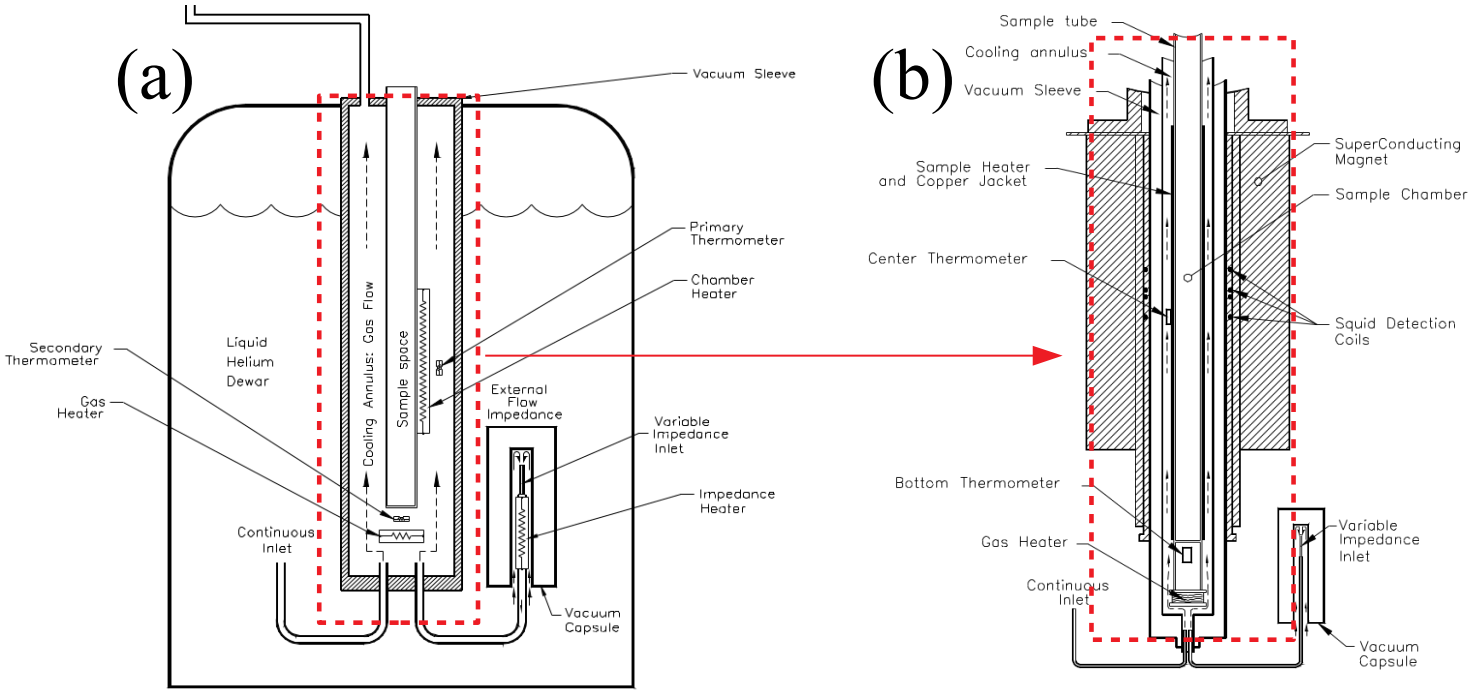

Figure 3.2: Continuous gas flow cryostat. Adapted from the MPMS' manufacturers manual.

both identical Josephson junctions induces a periodic electrical resistance across the device — known as D.C. SQUID [132]. This electrical signal is then translated to magnetic flux values multiples of the quantum magnetic flux $\phi_0 = h/2e$ = 2.07 x 10^{-17} Wb. The external field can be created by applying alternate current (A.C.) or direct current (D.C.) excitations in the magnet.

In the D.C. measurement process, the magnetic moment of the sample is probed by moving it along the pickup coils, connected to the SQUID, while an external D.C. magnetic field is applied. The superconducting coils used as pickup coils are mounted in a second order gradiometer configuration to suppress the inherent noises of the inductive technique. The voltage signals read by the SQUID are used to fit a magnetic dipole model, leading to the recorded value of sample's magnetic moment.

Tiny pieces of Re_3M samples (with masses ranging $10 \leq m \leq 500$ mg) were placed inside a gelatin capsule fixed in a plastic straw, both having negligible magnetic signals compared with sample's response. The straw was then coupled to a sample rod, inserted in the cryostat, and had its z-axis position controlled by a motor, moving the sample along the pickup coils.

Two common methods of measurements were employed: (i) Zero-Field Cooled (ZFC); and (ii) Field-Cooling (FC). In the ZFC method, the sample was first cooled down to the lowest temperature in zero applied magnetic field, usually down to 2 K, then the external magnetic field H_{DC} was turned on at this temperature, and the measurements were conducted by heating the samples from the superconducting to the normal state. In the FC mode, the sample was cooled from the normal state down to the lowest temperature under the applied magnetic field, and the data was acquired during this cooling step. The ZFC measurement resulted in maximum field exclusion from the sample, in a state close to the Meissner state when sufficiently low H_{DC} was applied — both H_{DC} = 5 and 20 Oe were used in the measurements, and they were found to be close to the H_{c1} values of the Re_3M materials. In contrast, the external magnetic penetration was enhanced in the FC mode. The ZFC and FC D.C. magnetization curves M(T) studied in this work were obtained in the temperature interval of 2$\leq$ T $\leq$ 15 K. The estimated SC volume fractions, using the ZFC data at the lowest temperature of measurement ($\sim$ 2 K) and assuming the density of all NCS Re_3M samples varying from 17 to 21 g cm^{-3}, were found to be between 100 - 300 %. These estimates did not take into account the corrections arising from

the demagnetization factors.

In the A.C. measurement mode, the sample's magnetic response is time-dependent, enabling the study of the dynamics of the magnetic properties of superconductors. The inductive method now is a time-dependent differential technique in which a modulated magnetic field is applied to the sample through a primary coil and the response is then measured with the secondary (pickup) coil already mentioned. Considering only low frequencies and magnetic fields, the induced sample's A.C. magnetic moment is proportional to the A.C. susceptibility χ_{AC} = dM/dH. In general, however, the sample's response to the A.C. stimulus is not in phase with the excitation and the measurements yield two quantities: the in-phase χ' and out-of-phase χ" components of χ_{AC}. Usually, χ' follows the D.C. magnetization while the χ" component is related to dissipative processes, such as eddy currents in metallic materials and losses in type II superconductors [133].

3.2.3 Physical Properties Measurement System - PPMS

Three different PPMS systems were used in this work, being two of them the latest Dynacool model. The vast majority of the experimental data was obtained in the Dynacool system located at Departamento de Física dos Materiais of this Institute, which is equipped with a 9-T superconducting magnet. Additionally, some experiments under $9 \leq$ H $\leq$ 14 T magnetic field range were performed in other 14-T Dynacool system, property of the Laboratório Nacional de Nanotecnologia (LNNano). Thermal conductivity data were obtained in a PPMS-Evercool through our collaboration with Prof. Milton Torikavichili, San Diego State University, USA.

Regarding the low temperature operation, the closed-cycle two-stages pulsed tube (PT) cryocooler is the PPMS Dynacool's core system. A Gifford–McMahon (G–M) cryocooler type is used in the PPMS, meaning that the pressure change is produced by a compressor and pressure oscillations are created by a rotary valve. This cryocooler contains the Cryomech's PT410-RM cold head, which delivers 31.5 W at the first stage ($\sim$ 45 K) and 0.9 W at the second stage (4.2 K) of cooling power when coupled with the CP289C helium compressor. A basic outline of the PT cryocooler operation principle is given below, followed by a description of how the PPMS utilizes the cold head to control the temperature down to 1.8 K.

The main idea to produce refrigeration in this type of mechanical refrigerator is to use the gas compression–expansion cycle; the expansion stage produces cooling since the work done on the fluid by compression is rejected to the surroundings [130]. In the PT case, both the smooth periodic pressure variation and working gas displacement in the pulse tube are used to produce the cooling effect [134]. The main components of a GM-type (single stage) PT cryocooler are regenerators (regenerative heat exchanger), heat exchangers, pulse tubes, and reservoirs volumes, as pictured in Figure 3.3. The pulse tube is a simple hollow tube connected to the room temperature helium reservoir by an orifice (or a flow impedance, inertial tube), in the so-called orifice pulse tube cooler (OPTC) configuration.

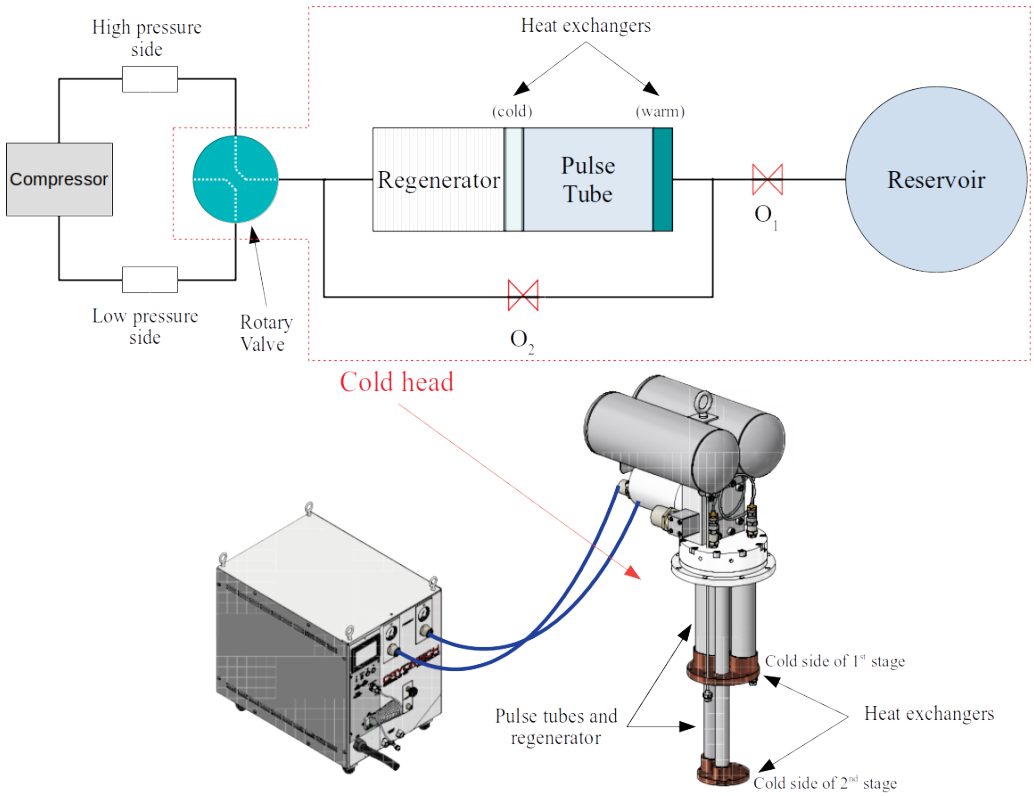

Figure 3.3: The top diagram exhibits the main components of an OPTC. The bottom of the figure exhibits the real drawing of the PT410 cold head and the CP289 compressor from Cryomech.

The regenerator often contains porous materials, usually magnetic compounds with high heat capacity, and is connected at its cold end to the pulse tube by a (cold) heat exchanger. As regenerators are used as “cold storage” or heat reservoir, their heat capacity at the lowest operation temperature must be higher than the helium gas stream [130].

By making use of its two-stage PT crycooler mounted inside a high purity helium gas at-

mosphere, the PPMS is able to finely control the sample's temperature. A diagram with the components of the PPMS' cryostat cooled both by the 1st and 2nd stages is exhibited in Figure 3.4. This cryostat is more sophisticated than the MPMS' one, since much development has been done in the low temperature area during the two decades separating these systems. Only the main components of the PPMS' cryostat are discussed here, since its full theory of operation requires more than a couple of paragraphs. The helium gas condenses on the cryocooler's second stage and falls on the bottom of the cryogenic tank (bucket), which is thermally connected to a metal plate (4 K plate) having solid thermal links with some of the cryostat's components — such as its 9 (or 14) Tesla superconducting solenoid. Typically, the system operates with only $\sim$ 150 ml of liquid helium inside the bucket. The (main) radiation shield, cooled by the first stage, and the vacuum case are used to create the required thermal isolation between parts of the cryostat at different temperatures.

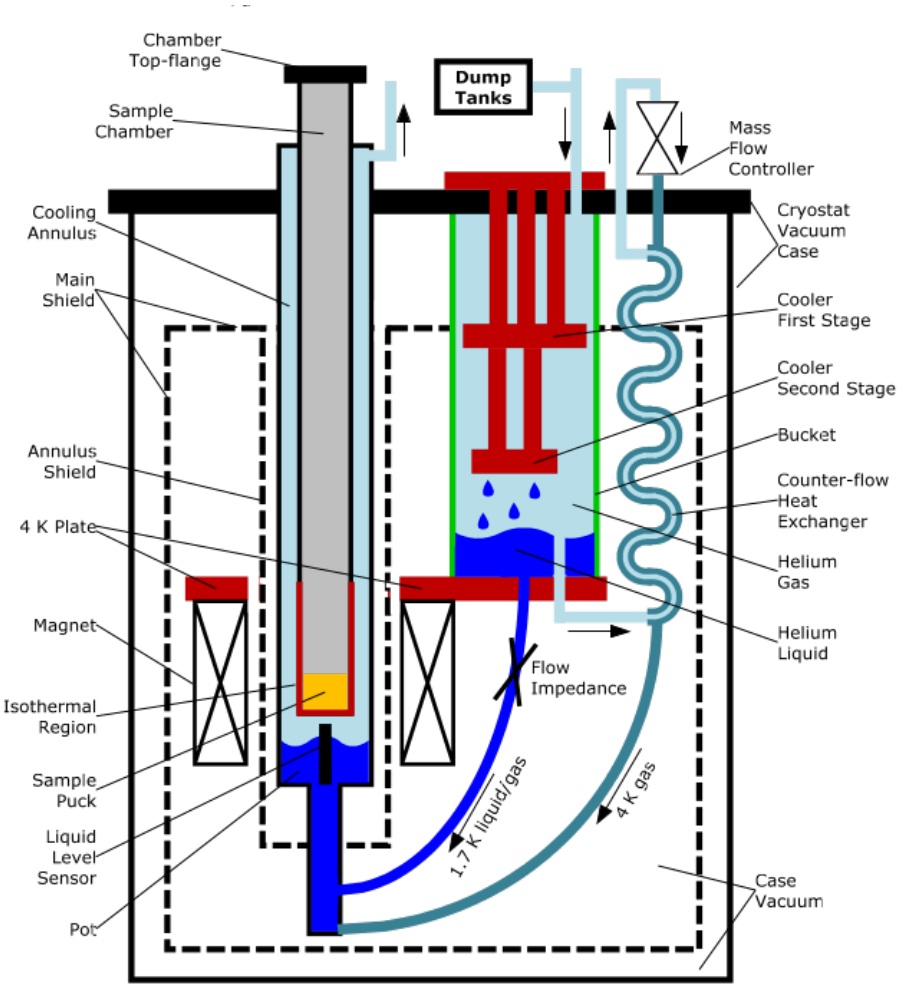

Figure 3.4: Main components of the PPMS Cryostat. See the main text for an overview of its operation principle.

3.2.3.1 Dilution Refrigerator

A separate probe containing the dilution refrigerator insert is need to achieve the lowest temperature limit of the system, enabling measurements to be done in temperatures down to 50 mK. The dilution cooling mode is used to conduct measurements in the $0.05 \leq T \leq 1$ K range while measurements within $1.1 \leq T \leq 4$ K range are achieved by using the evaporative cooling mode.

Considering the dilution cooling mode, the latent heat of mixing of the two helium isotopes (^{3}He and ^{4}He) is used to cool a small portion of the system down to mK window. The helium mixture used in this option has a ^{3}He concentration x_3 higher than ~ 6.6 %at., meaning that the liquid mixture separates into two phases when cooled below 0.87 K [134]. These two phases are called diluted and concentrated phases, where the dilute phase consists of mostly ^{4}He with about 6 % ^{3}He and the concentrated phase is almost pure ^{3}He. Then, the cooling in a ^{3}He-^{4}He dilution refrigerator is achieved by transferring ^{3}He atoms from the almost pure ^{3}He phase to the diluted, mostly ^{4}He containing phase.

A closed ^{3}He circulation cycle is used to keep the chamber with the diluted and concentrated phases (mixing chamber) at the lowest operation temperature. The main components to produce the ^{3}He closed-cycle are illustrated in Figure 3.5, whose operation principle is briefly discussed below [134, 135].

Firstly, the gas mixture is liquefied in the condenser (not shown in Figure 3.5), which is maintained at the PPMS base temperature, close to 1.8 K. The now liquid ^{3}He will flow down through a flow impedance into the still heat exchanger, located inside the still at a temperature of about 0.6 K, then through the concentrated side of the counter-flow heat exchanger, cooling the liquid even further before entering at the top of the mixing chamber (the concentrated side). As the still operates like a distillation chamber, evaporating almost pure ^{3}He, the osmotic pressure drives ^{3}He up the dilute side of the counter-flow heat exchanger from the mixing chamber into the still. Then, the ^{3}He atoms in the concentrated phase are pushed to cross the phase boundary. In this way, the ^{3}He concentration in the dilute phase of the mixing chamber will stay constant because ^{3}He atoms are continuously crossing the phase separation boundary line from the concentrated to the dilute phase, producing cooling due to the latent heat of mixing. Pumping continuously on the still using a turbo pump backed by a diaphragm pump cools the

still to about 0.6 K. Then, the pumped ^{3}He gas exiting the diaphragm pump is circulated back and reliquefied in the condenser, repeating the cycle.

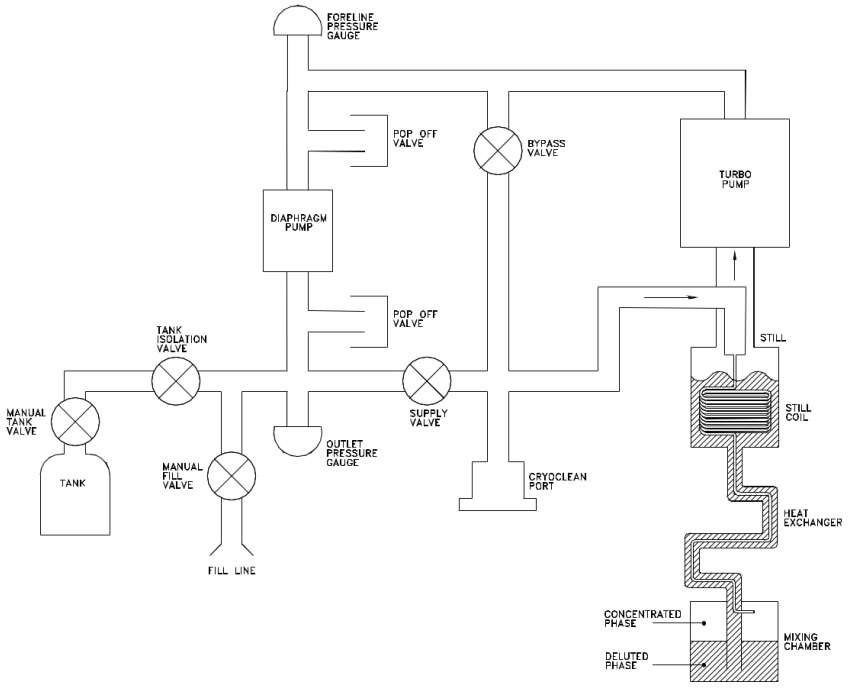

Figure 3.5: Diagram with main components of the DR probe insert. Figure adapted from the manufacturer's manual.

A thermal standoff between the mixing chamber and sample stage allows the sample to be heated up to 1.1 K even though the mixing chamber must stay below about 0.6 K in order to maintain dilution cooling. Control of the sample stage temperature is achieved by heating both the sample stage and the still. The still temperature set point is determined by the sample set point.

In the evaporative cooling mode, the system runs with mostly ^{4}He in circulation with the helium liquid level down in the mixing chamber. In order to achieve this mode of operation, the liquid ^{3}He must be distilled from the mixture and stored in the tank, leaving nearly pure ^{4}He to circulate. The turbo pump is used to pump through the heat exchanger, effectively providing the cooling power in the mixing chamber. Returning ^{4}He gas is then reliquefied in the condenser, which is maintained at 2.5 K by the PPMS sample chamber.

3.2.3.2 Electrical resistivity ρ

The PPMS Electric Transport Option was used to measure the temperature and magnetic field dependence of the electrical resistance of our Re_3M samples.

The electrical resistance was measured by the conventional 4 probes method, where four wires are attached to the sample. The A.C. excitation current flows through the sample by the external leads, while the inner leads are used to measure the potential drop. Ideally, if only resistive loads are present in the sample + leads system, the voltage signal is in phase with the current signal, and only a small phase angle should be read by the phase detection device.

The roughly parallelepipeds-shaped Re_3M were obtained by cutting the samples with the help of a Buehler low speed diamond saw. In general, the sample dimensions were in the size range of 2-4 x 1-3 x 0.2-0.5 mm^3 (Length x Width x Thickness). In order to obtain samples suited to the 4-probe method, the samples' surface were carefully sanded in various steps, increasing the grit sizes in each step until the finer 1200-grit emery paper was reached. Two types of electrical contact between the samples and PPMS' sample puck were done, depending on the particular sample: a combination of Cu wires with silver epoxy (epotek HE150) or gold wires with silver paste were attached to the sample's surface. The silver epoxy contacts needed to dry at $\sim$ 120 ^{o}C or more over at least 30 minutes. The contacts made with the silver epoxy were mechanically more reliable than the ones produced with the silver paste. In spite of being much more fragile, the silver paste contacts had lower contact resistance. All samples had its characteristic curves IxV taken at room temperature to ensure the linear, ohmic response to the excitation; if this was not the case, the electrical contacts were done once or even twice again.

The distance between the inner voltage leads l_V must be known in order to compute the resistivity of the sample. Considering the typical sample's dimensions and its misaligned silver trails (see Figure 3.6(a)), a caliper was not the proper tool to measure l_V. To circumvent this problem, the software ImageJ was used to calculate l_V from a picture of the sample by a millimetric scale taken at the top of a conventional microscope. In this way, it was possible to obtain l_V by the analysis of the gray-scale profile from a line passing through both contacts, as exhibited in Figure 3.6. This profile is shown in Figure 3.6(b), where the baseline refers to the sample's surface and the clear steep rise of the gray-scale value indicates the silver contact on

the sample surface; then, l_V was obtained as the distance between the peaks. The calibration of the software using the scale image yielded l_V in the millimeter scale, whose values agreed with the rough estimates made using the caliper. The distance between the voltage leads is then defined as the smallest l_V value obtained through various lines crossing the contacts.

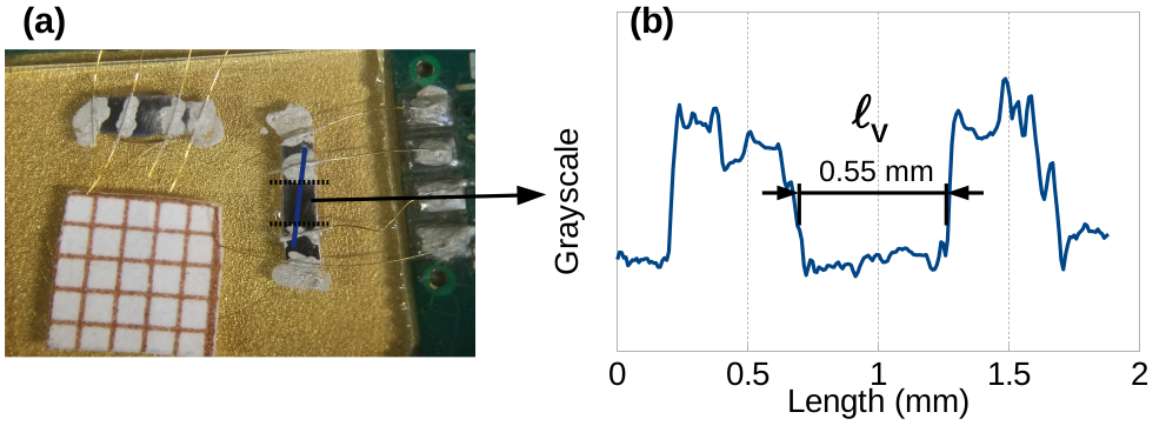

Figure 3.6: (a) Picture of two samples with gold wires attached with silver paste. (b) The gray-scale profile of the line drawn on (a) is used to determine the l_V value in mm.

3.2.3.3 Heat capacity

One of the thermal properties measured in this work is the heat capacity c_p(or specific heat C_p) of the samples through the PPMS' Heat Capacity option. Basically, this module keeps track of the sample temperature while a heat pulse is applied in the system. By controlling the magnitude of the heat pulse, the heat capacity of the system can be calculated by the so-called relaxation method. In order to mount the sample on the sample holder, the sample is placed on puck's sapphire platform, with a small layer of apiezon N grease. The cross section of this sample holder is shown in Figure 3.7, indicating the main parts of the heat capacity experimental setup.

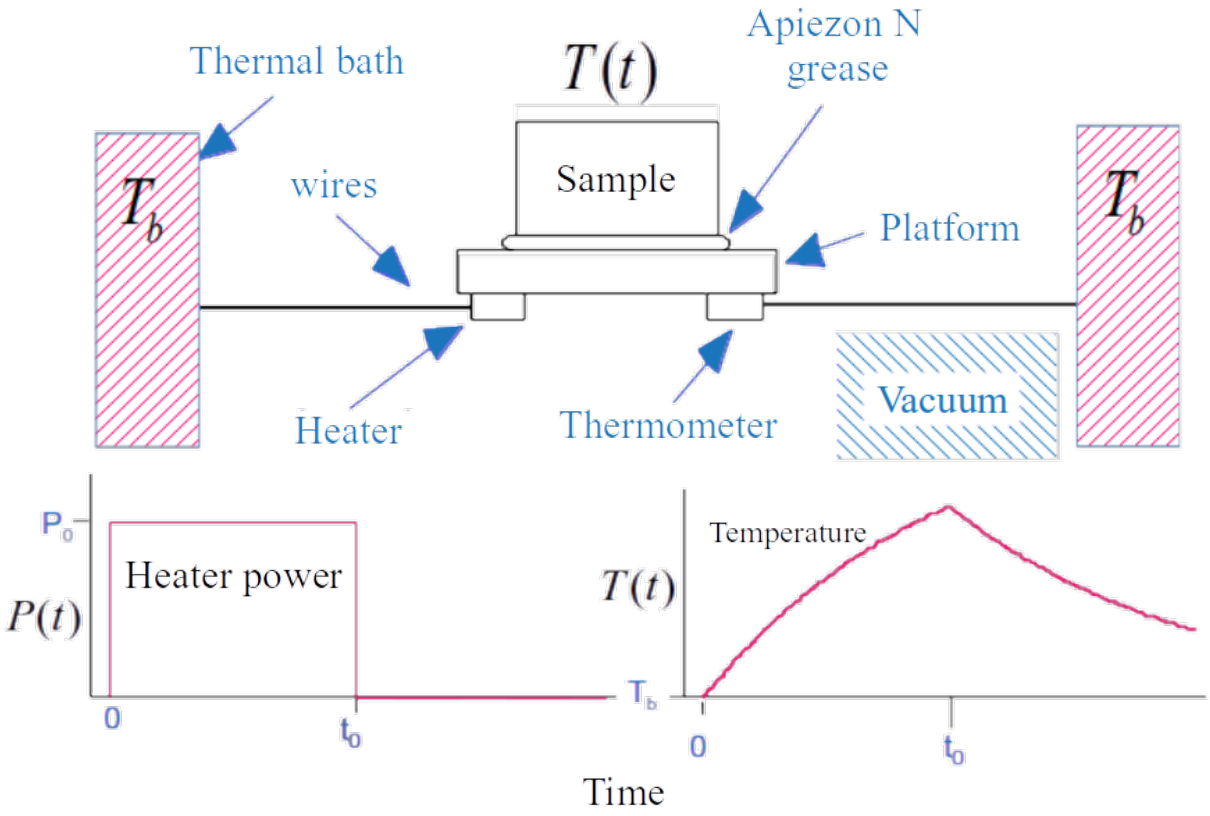

Figure 3.7: Main components of the heat capacity measurement, figure adapted from the manufacture's manual. The bottom plots are the time profile of the power on heater and the temperature read by the thermometer.

In general, this measurement is conducted as follows: the heat pulse is created by turning the power on the RuO_2 heater located underneath sample's platform. This increases the system temperature, as indicated by the bottom part of Figure 3.7, until the heat pulse is over. After that, the system is allowed to cool while its temperature is still monitored. The total heat capacity

(c_{total} = c_{sample} + $c_{platform}$) is obtained by fitting T(t) using the thermal relaxation model:

$$c_{total}\frac{dT(t)}{dt} = P(t) - K_w(T(t) - T_b)$$
$$T(t) = \begin{cases} T_{heat}(t) & = \frac{P_0\tau_1(1-e^{-\frac{t}{\tau_1}})}{c_{total}} + T_b,\ 0 \leq t \leq t_0 \\ T_{cool}(t) & = \frac{P_0\tau_1(1-e^{-\frac{t_0}{\tau_1}})e^{-\frac{(t-t_0)}{\tau_1}}}{c_{total}} + T_b,\ t \geq t_0 \end{cases},$$

with T_b as the base temperature and K_w as the thermal conductance of the weak link to the thermal bath (supporting wires). The first relaxation time constant $\tau_1 = c_{total}/K_w$ is related to the time required for the system platform + sample achieve the thermal equilibrium. Previously knowing the addendum heat capacity $c_{platform}$ enables the calculation of c_{sample} from c_{total}. In order to simulate the effect of a poor thermal contact between the sample and platform, another time constant is introduced in the 2τ-model:

$$\begin{aligned} c_{sample}\frac{dT_s(t)}{dt} &= -K_g(T_s(t) - T_p(t)) \\ c_{platform}\frac{dT_p(t)}{dt} &= P(t) - K_w(T_p(t) - T_b) + K_g(T_s(t) - T_p(t)) \end{aligned},$$

with the sample temperature $T_s(t)$ different from the platform temperature $T_p(t)$, and the thermal conductance between platform and sample K_g is needed to solve the model. Then, a second time constant τ_2 due to additional internal relaxation times is used to describe the grease + sample system, whose typical value is only a tiny fraction of τ_1 [136]. As the system automates the fitting procedure to obtain the heat capacities with both models above, it records only the value obtained from the best fit.

Small sample's surfaces (< 3x3 mm^2) were prepared by cutting and carefully sanding pieces of the Re_3M specimens. The flat surfaces were placed on the sapphire platform, which was previously coated with a thin layer of Apiezon N grease in order to hold the samples tightly and optimize the thermal contact between the sample and platform. The sample holder was then covered with a radiation shield and coupled with the main system where the actual measurements were performed.

3.2.3.4 Thermal conductivity κ

Thermal conductivity κ is a measure of the heat conduction along a material, usually coming both from phonons and electrons. To probe this property, measurements need to be conducted in a similar fashion as in the heat capacity: under a thermally isolated environment while the sample's temperature difference is recorded. The PPMS Thermal Transport Option (TTO) was used to conduct this type of measurement in some of our samples, in the temperature range between $2 \leq T \leq 100$ K and under magnetic fields up to 9 Tesla.

In the experimental setup, a heat load is introduced in the sample through a heater in thermal contact with the sample. Then, the temperature difference along the sample is monitored by the two cernox thermometer connected at the sample ends (hot (T_H) and cold (T_C) thermometers). A non-linear fitting procedure is conducted in the $\Delta T = T_H - T_C$ vs time data, yielding the short and long relaxation times τ_1 e τ_2 used to calculate κ at a given temperature T. A prototypical sample mounted on the TTO's sample holder is shown in Figure 3.8, highlighting the main components of the measurements apparatus.

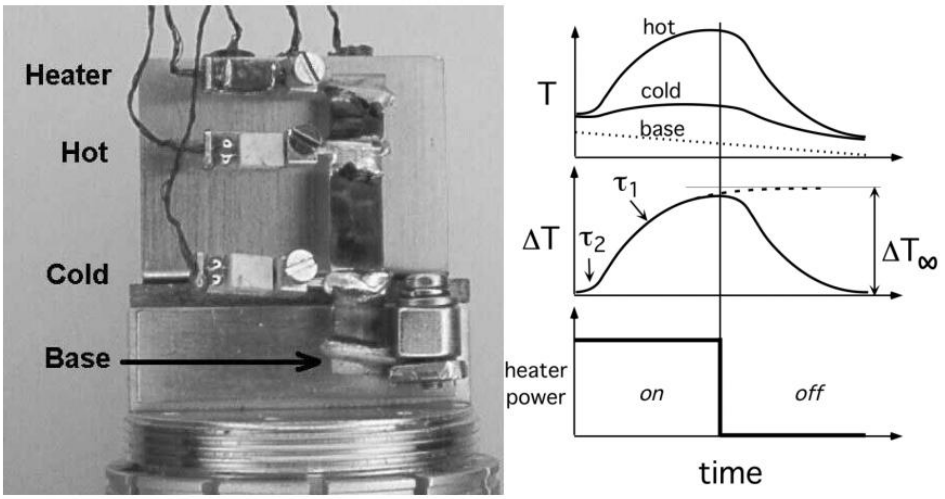

Figure 3.8: Picture of an experimental apparatus analogous to the one used to conduct our measurements of thermal conductivity (left hand side of the figure). The schemes on the right side are the time dependent power dissipated on the sample, temperature difference along the sample, and power applied to the system. Figure taken from reference 137.

Chapter 4

Results

The experimental results presented and discussed in this chapter are a summary of our findings and do not include the data obtained in every single sample synthesized. The summary is built from a careful data selection among nearly third Re_3M samples in order to illustrate several superconducting features occurring across the Re_3M family of compounds. From the data, it seems that the superconducting state of Re_3M materials can be classified as conventional in nature, i.e., the suggestion of a triplet pairing symmetry does not seem to be corroborated by the experimental results described hereafter. This, by no means, implies that a simple superconducting system emerges from the experimental results; in fact, novel superconducting phenomena in the NCS Re-based materials arise in the magnetic phase diagrams and in their vortex matter.

To explicitly discuss the novel phenomena and correlate them with the NCS structure, this chapter has been organized as: first, the synthesis of the materials and its structural properties are presented, giving a particular emphasis on the single α-Mn phase Re_3W material production; after that, the superconducting ground states of the parent compounds Re_3W, Re_3Ta, and Re_3Nb and the solid solutions $Re_3Ta_{0.5}W_{0.5}$ and $Re_3Nb_{0.5}W_{0.5}$ are discussed separately; closing our results are the magnetic field dependence of the Re_3M superconducting properties, which culminate in the various superconducting phase diagram and also leads to the peak effect observed in nearly all the samples.

4.1 Synthesis and structural properties of the Re_3M materials

On the production side, tables 4.1 and 4.2 summarize the compositions of all polycrystalline samples synthesized throughout this study. The second column of each table exhibits the mass ratios between the mixture of elements before melting (M_b) and the resulting AC samples after melting (M_a), indicating very low levels of mass loss during the melting procedure. The mass change after heat treatments is displayed in the third column by the AC (M_{AC}) and heat treated (M_{HT}) mass ratio of each sample, suggesting that no sample contamination occurred over the entire annealing time.

Table 4.1: Samples in the Re-W system

Sample	M_b/M_a	M_{HT}/M_{AC}
$Re_{0.9}W_{0.1}$	0.999	1.00
$Re_{0.82}W_{0.18}$	0.99	1.00
$Re_{0.75}W_{0.25}$ *	0.998	1.00
$Re_{0.735}W_{0.265}$	0.999	1.00
$Re_{0.727}W_{0.273}$	0.999	1.00
$Re_{0.72}W_{0.28}$	0.999	1.00
$Re_{0.667}W_{0.33}$	0.991	1.00
$Re_{0.5}W_{0.5}$	0.997	1.00

Table 4.2: Solid Solutions $Re_3(Ta,Nb)_xW_{1-x}$

Sample	M_b/M_a	M_{HT}/M_{AC}
Re_3Ta	0.999	1.00
Re_3Nb	0.998	1.00
$Re_3Ta_{0.1}W_{0.9}$	0.999	1.00
$Re_3Nb_{0.1}W_{0.9}$	0.999	1.00
$Re_3Ta_{0.25}W_{0.75}$	0.994	1.00
$Re_3Nb_{0.25}W_{0.75}$	0.999	1.00
$Re_3Ta_{0.5}W_{0.5}$	0.999	1.00
$Re_3Nb_{0.5}W_{0.5}$	0.993	1.00

Before discussing the Re_3M compounds, the results obtained in all $Re_{1-x}W_x$ samples will be considered. These results may shed light on the α-Mn phase nucleation at compositions close to Re_3W.

Shown in Figure 4.1 is the phase diagram populated with the $Re_{1-x}W_x$ samples synthesized in the Re-W system (x is the W atomic fraction with values of 0.1, 0.18, 0.25, 0.265, 0.273, 0.28, 0.33, and 0.5) and subsequently annealed at 1700 °C. According to the phase diagram, at 1700 °C, some compositions are located in single phase fields (χ and σ), others in two phase (white) regions, and two of them (x = 0.1 and 0.33) very close to phase boundaries. Although the equilibrium phase diagram Re-W used here is the more recent version [138], it should be noted that the diagram is by no means flawless; the well-delineated phase boundaries could be

*sample #1. Other three samples with this composition have been synthesized and exhibited similar mass ratios.

a bit off from the experimental situation.

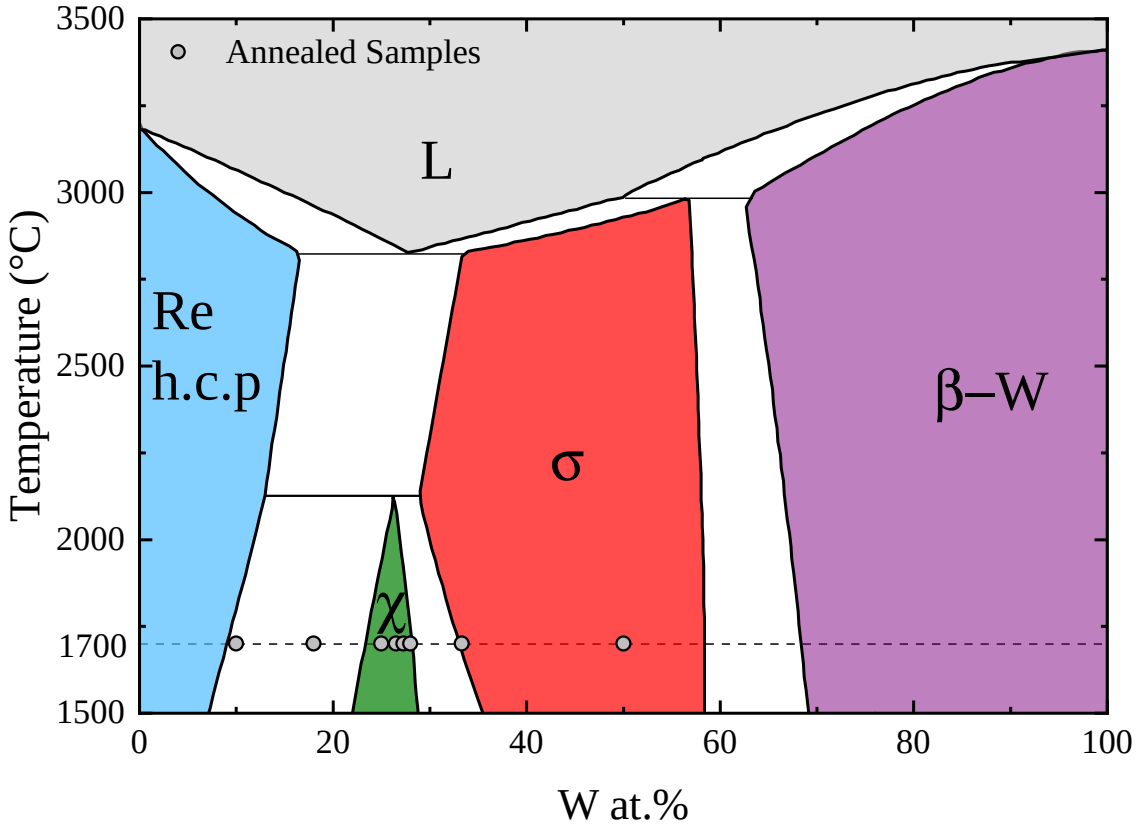

Figure 4.1: Re-W equilibrium phase diagram [138] with all the compositions synthesized in this system. The samples are expected to be in the various phase fields after the annealing procedure at 1700 °C.

It is noteworthy to mention that the rhenium-rich ($x < 0.33$) AC samples could not been crushed with the steel mortar, reproducing the mechanical properties of the elemental Re AC sample. Thus, the reminiscent ductility of the rhenium-rich materials seems to be coming from the $h.c.p.$, Re-like phase. In contrast, crushing all the remaining AC samples was a straightforward task, being them solid solutions or parent compounds. These facts, combined with the phase diagrams and the XRD results presented below, suggest that the Re-$h.c.p.$ structure is present in some AC samples.

The comparison of all XRD results obtained in the Re-W AC samples is exhibited in the top panel of Figure 4.2. By increasing the tungsten content x from 0.1 to $\sim$ 0.33 in the $Re_{1-x}W_x$ system, the individual diffractograms evolve from rhenium h.c.p-like structures (bluish bottom diagrams) to also hexagonal, but more intricated, σ-like structures (reddish top diagrams), pass-

ing through multi-phase materials with Re:W ratio close to 3:1 — probably having a mixing between those two phases.

The central, black diffractogram in Figure 4.2(a) (Re_3W AC sample) is a representative multi-phase diagram of the $Re_{1-x}W_x$ AC samples, with x comprehended between 0.25 and 0.28. In that diagram, the main diffraction peaks occur in the angular range $35 \leq 2\theta \leq 45$ °, matching the most intense peaks of both σ and h.c.p phases. In addition, the intensity of the main peaks can potentially be enhanced due to artifacts coming from preferential reflections of certain atomic planes when directly measuring the sample's surfaces. Thus, it is not possible to extract the exact phase composition of the Re_3W AC sample from its XRD data. This is true not only in the Re_3W AC specimen, but also in the $Re_{1-x}W_x$ AC samples with $0.25 \leq x \leq 0.28$ (XRD scans not shown). As will be shown below, the main diffraction peak of the NCS structure occurs at $2\theta \sim 40°$, blurring even more any determination of the Re_3W AC composition based solely on X-ray data. Therefore, a minor α-Mn NCS phase can not be ruled out in these AC materials.

In the hypothesis of the Re_3W (x = 0.25) AC material being comprised of two phases, all of the XRD data from $Re_{1-x}W_x$ AC system can be understood by evoking the Re-W equilibrium phase diagram. In the usual description, the rapid cooling from the liquid state, after melting, freezes the samples in its current thermodynamic state, with the AC materials retaining the high temperature structure in the process. Then, the AC samples with $x \geq 0.33$ and ≤ 0.10 are single phase materials, as those compositions fall in the single h.c.p or σ phase fields at high temperatures. Additionally, the $Re_{0.82}W_{0.18}$ AC sample is a potentially single $h.c.p$ phase material, even though this composition does not cross any single phase field in the whole temperature range below the liquidus line in Figure 4.2(b). This strongly suggests that the solubility limit of W into the Re $h.c.p$ structure at high temperatures is larger than the one present in the Re-W phase diagram here considered.

The above description needs other considerations to account for the samples within the χ-phase solubility range. In this case, an additional difficulty lies on knowing whether the frozen high temperature structure would be above or below the peritectoid temperature at 2125 °C, transforming the phases $h.c.p + \sigma$ into the desired χ phase. Ideally, one expect that

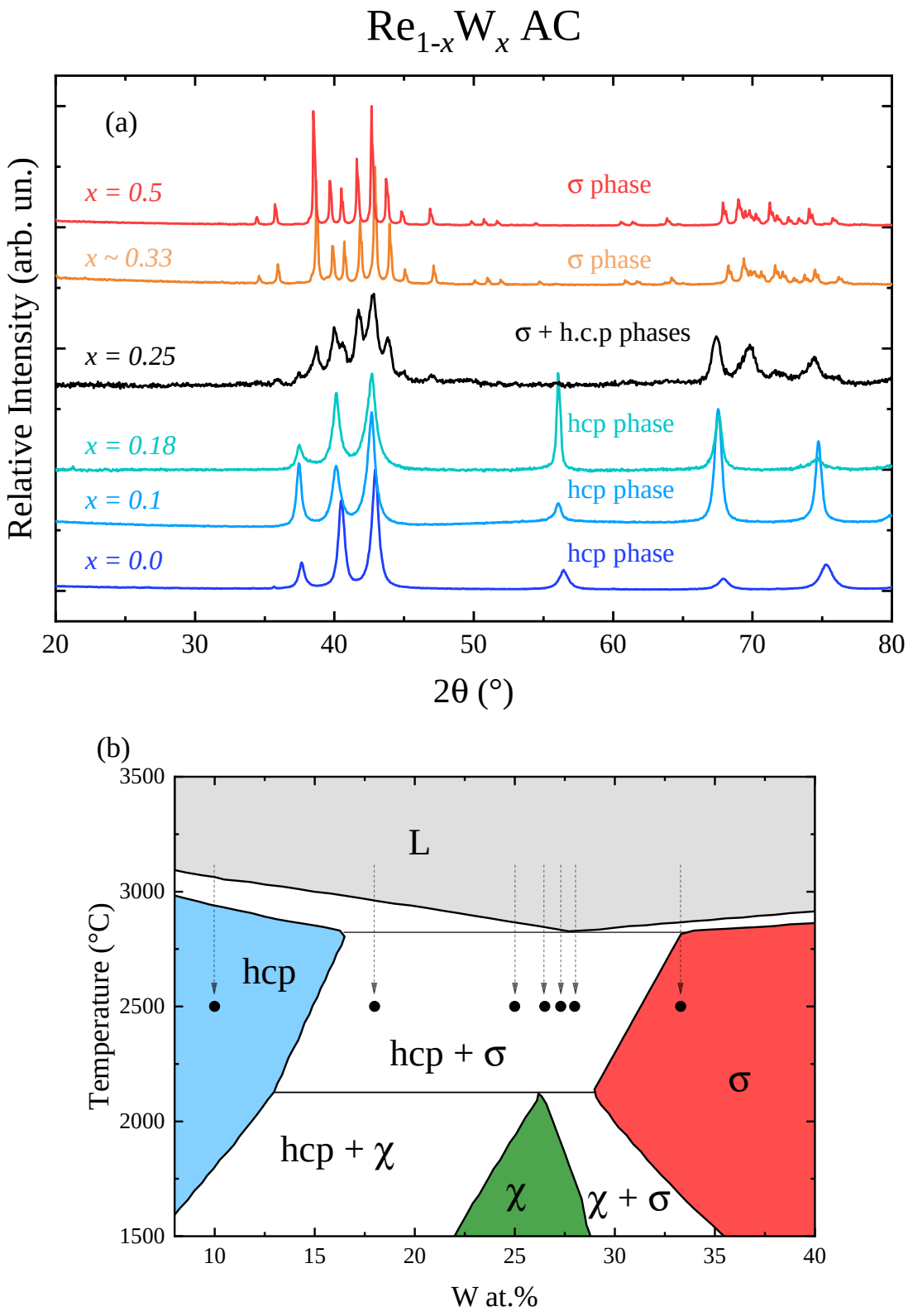

Figure 4.2: (a) X-ray diffraction data for some Re-W AC samples produced in this work. (b) Enlarged view of the Re-W phase diagram [138] in the region 5 $\leq$ W at.% $\leq$ 40.

cooling the sample rapidly enough would completely avoid the two-phase field $h.c.p + \sigma$ during cooling. But this is not the case seen in the XRD data; a more accurate description should include the close proximity of the eutectic point at $\sim$ 26 %at. W ($L \rightarrow h.c.p + \sigma$ at T $\sim$ 2825 °C) and the $Re_{1-x}W_x$ (0.25$\leq$ x $\leq$ 0.28) liquidus lines. Therefore, the high-temperature atomic structures frozen in those as-cast materials are very likely mixtures of the $h.c.p$ and σ phases, as illustrated by the black points in Figure 4.2(b). Then, the dashed arrows are visual representations of the cooling mechanisms described above, using an arbitrary temperature (both above the peritectoid and below the eutectic temperatures) in which the atomic structures are locked during the cooling procedure.

The XRD results obtained in the powdered annealed samples are displayed in Figure 4.3. It is clearly seen that the overall shape of the $Re_{1-x}W_x$ (0.25$\leq$ x $\leq$0.28) diffractograms (grayish central diagrams) are radically different from its AC counterparts, while only subtle changes occur in the $Re_{0.82}W_{0.18}$ and $Re_{0.67}W_{0.33}$ samples. In the materials with Re:W close to 3:1, the small number of intense Bragg peaks reflects the high symmetry of the unit cell — which now can be described as having the cubic NCS α-Mn symmetry. Therefore, the peritectoid reaction $h.c.p + \sigma \rightarrow \chi$ is essential to obtain single α-Mn materials in the Re-W system, in a similar manner as what has been discussed in the Re-Mo system [42].

Figure 4.3 also indicates that some otherwise not present reflections are now seen in the diffractograms of the annealed $Re_{1-x}W_x$ (x = 0.1, 0.18, and 0.67) materials. These new reflections match the most intense α-Mn Bragg reflections, as indicated by the dashed vertical lines. In these samples, the peritectoid reaction also occurs by heating them to 1700 °C, driving the materials to the two phase field and resulting in the loss of the somewhat pure AC diffractograms.

A more descriptive diffractogram is shown in Figure 4.4, capturing the main features of all α-Mn single phase materials produced in the Re-W system. All experimental Bragg reflections have been indexed by the corresponding crystalline planes of the α-Mn b.c.c. structure. The Bragg planes are indicated by the numbers in parenthesis beside the main peaks and also by green marks below the experimental points.

Rietveld refinement of the XRD data provides further information on the NCS structure

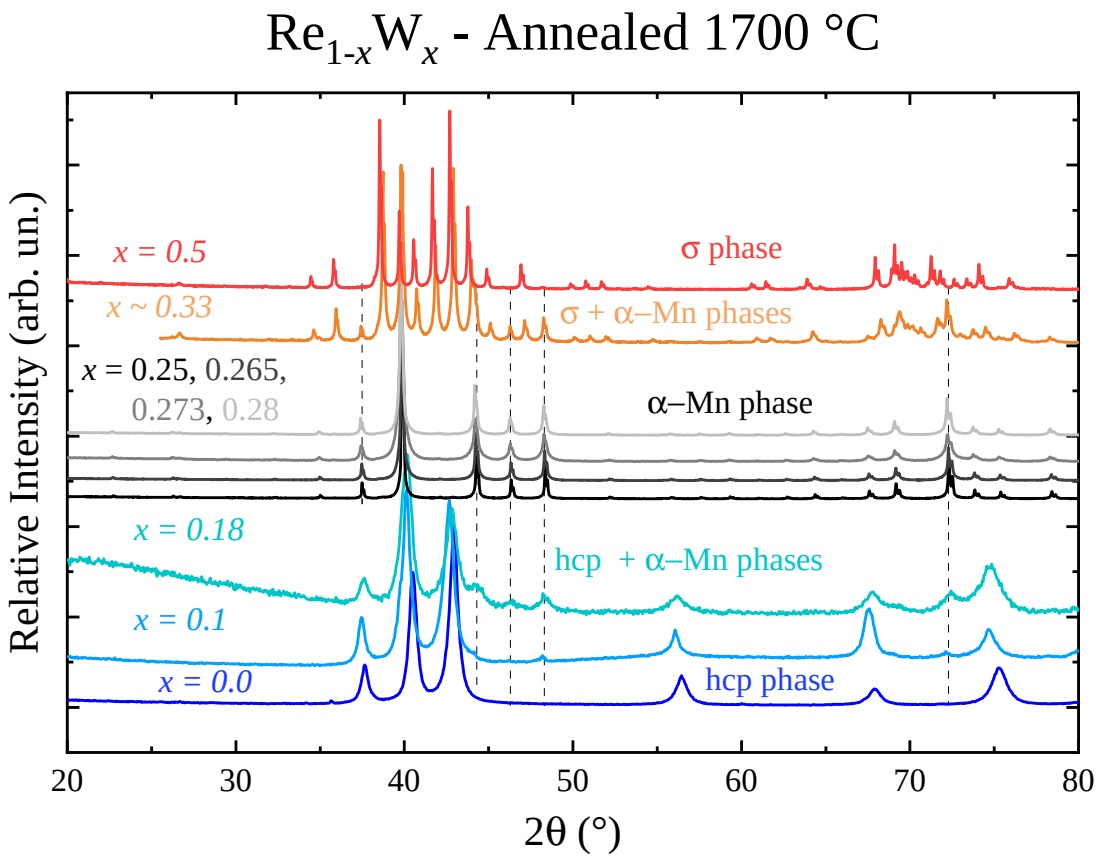

Figure 4.3: Comparison of the annealed Re-W samples XRD data. The dashed line is a guide to the eyes to highlight the spurious peaks associated with the χ phase arising in the samples after the heat treatment, indicating multi-phase materials.

[127]. The red line in Figure 4.4 is obtained by refining the data using the space group $I\bar{4}3m$ (with the help of FULLPROF software [129]), and exhibits good agreement with the experimental dataset (open black circles). A more precise data fitting is challenging due to the atomic occupations in each Wyckoff sites: distinguish between Re and W atoms is not a straightforward task when using commercial X-ray diffractometer, as discussed above in section 1.3.1 (see page 12). For our purpose, which is to ensure the single-phase character of the materials, the XRD refinement is a reliable procedure to extract the lattice parameters and compare them among the produced materials; the various lattice parameters obtained through the Rietveld refinements are presented in tables 4.4 - 4.5 at the end of this chapter (see page 143 onwards).

The results in the Re-Ta and Re-Nb systems were the opposite of the Re-W system: the α-Mn NCS structure could be produced directly from melting in materials with atomic ratio Re:M of 3:1. Accordingly, the three powder Re_3Ta diffractograms shown in Figure 4.5 are almost identical with each other, being the Re_3Ta sample in its AC or in any of its annealed forms. The

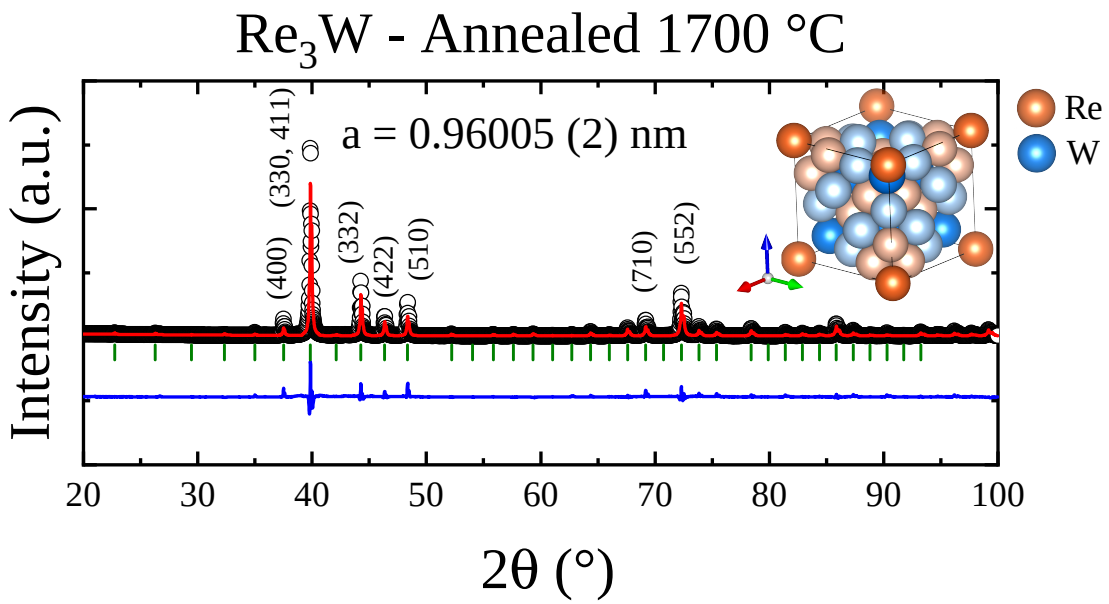

Figure 4.4: Annealed Re_3W diffractogram alongside with the the Rietveld refinement results obtained by using the α-Mn structure. The illustration of the NCS Re_3W cubic unit cell is also shown.

logarithmic scale on the y-axis highlights the various α-Mn low intensity Bragg peaks that are otherwise masked in the linear scale. It is possible to correlate each of the minor reflections directly to the NCS α-Mn structure in all three diagrams, as indicated by the vertical green bars below the curves.

Sample crystallinity is usually improved after heat treatments, resulting in sharper reflections in the annealed samples diffractograms. However, the shape of the Re_3Ta reflections among AC and annealed samples did not show major differences. The reflections shown in Figure 4.5(b) have roughly the same full width at half maximum when compared among the samples. Moreover, high K_{α_2} reflections in all of them were measured, suggesting that the AC material already possess a high degree of homogeneity. Although not directly shown here, the same features were observed in the Re_3Nb specimen.

The XRD results acquired in the solid solutions $Re_3(Ta,Nb)_xW_{1-x}$ specimens are discussed below. Shown in Figure 4.6(a) is the comparison of all XRD results of Re-Ta-W AC samples, suggesting that the α-Mn phase is stabilized, provided that $x \geq 0.25$.

The sample having the smallest Ta concentration, with $x = 0.1$, exhibited only a subtle change from the parent Re_3W AC diagram. Then, the overall $Re_3Ta_{0.1}W_{0.9}$ AC diagram still retains the features of a multi-phase material. By increasing the Ta content up to $x = 0.25$,

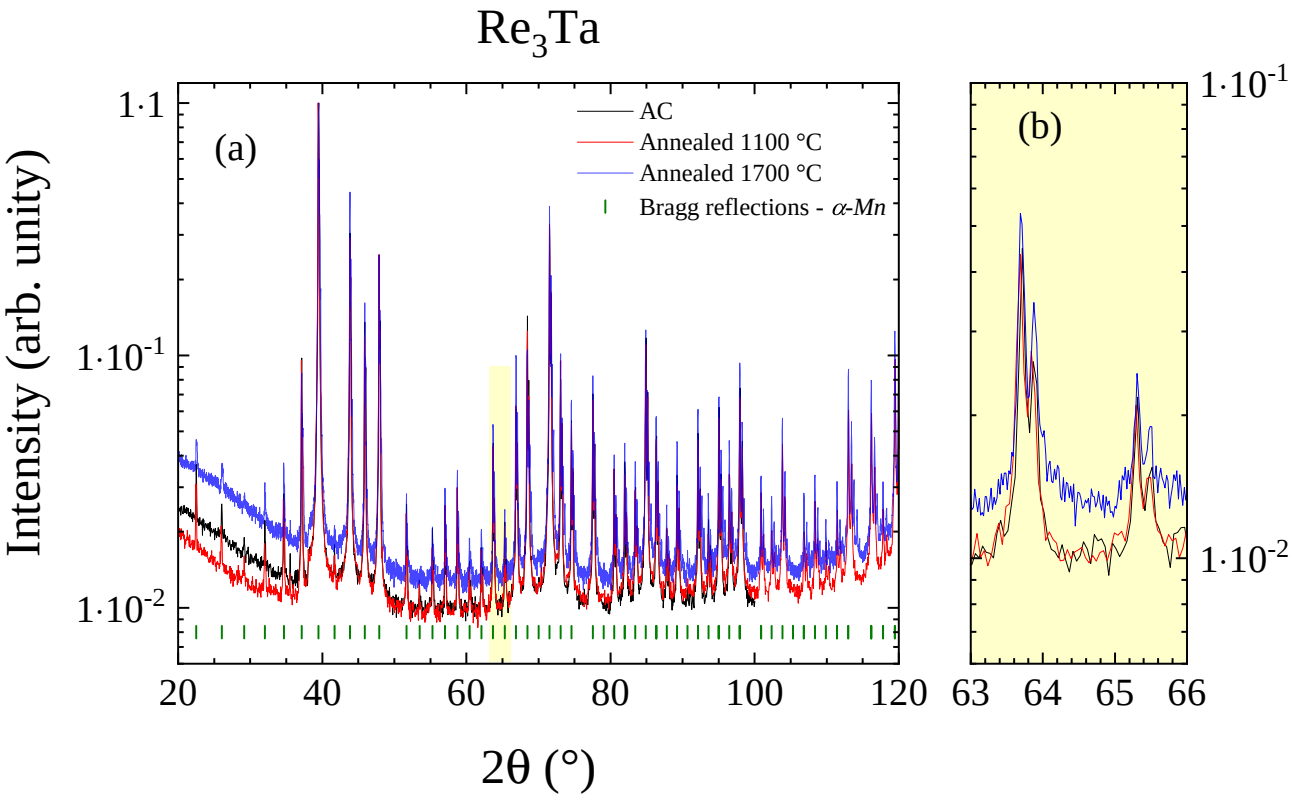

Figure 4.5: Diffractograms of different forms of Re_3Ta sample in log scale: AC (black line), annealed at 1100 (red line) and 1700 °C (blue line). (b) Enlarged view of the angular region $63 \leq 2\theta \leq 66$ °; the K_{α_2} reflection is clearly split from the main peak as expected for a material with high degree of crystallinity.

the AC sample could easily be crushed and a more substantial change of the pattern is noted (see Figure 4.6(a) for comparison). The $Re_3Ta_{0.25}W_{0.75}$ AC sample has a similar diffractogram to the Re_3Ta's one, displayed once more in the bottom of the Figure 4.6 as a guide to the eyes. A very small reflection not pertaining to the NCS crystal structure was also detected in the $Re_3Ta_{0.25}W_{0.75}$ diffractogram, although the chosen scale does not make it clear, being marked with an asterisk in Figure 4.6(a). The angular position of this spurious reflection is close to the angles where the maximum peak occurs in both the $h.c.p$ and σ phases, as well as in the Re_3W and $Re_3Ta_{0.1}W_{0.9}$ AC samples. Thus, the presence of this tiny peak is a strong indication that the atomic substitution of $x = 0.25$ has not been sufficient yet to completely suppress the $h.c.p$ or σ phases formation directly from melting. By increasing the Ta content even further until reaching equal amounts of Ta and W, the $Re_3Ta_{0.5}W_{0.5}$ AC diagram shows that its crystal structure acquires a single α-Mn phase, not having any spurious reflection and being very similar to the Re_3Ta and the annealed Re_3W samples, aside from the small shifts in the peaks angular position.

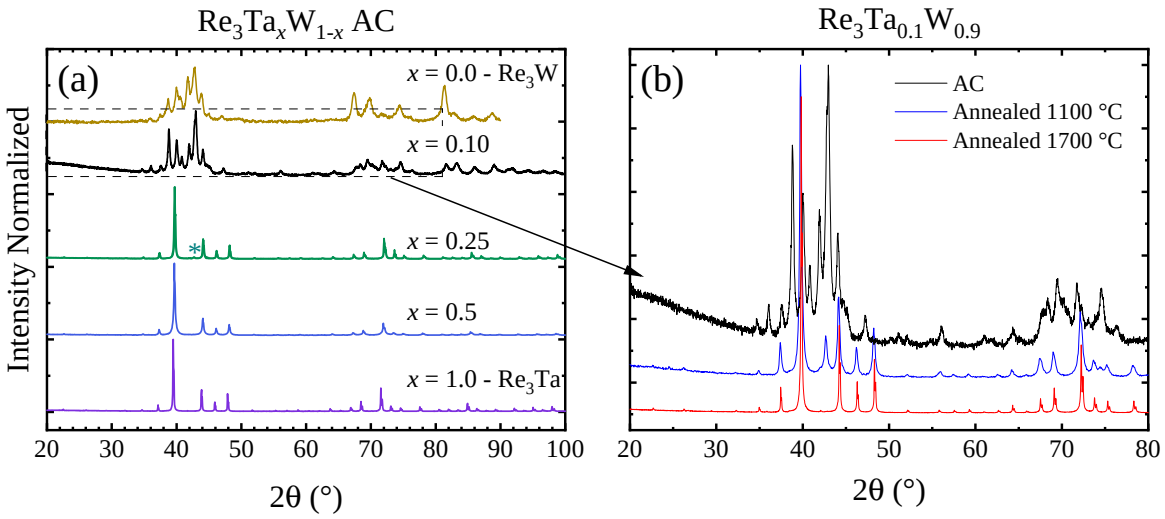

Figure 4.6: (a) XRD results obtained in the AC samples of the $Re_3Ta_xW_{1-x}$ series. (b) Effect of the heat treatments on the $Re_3Ta_{0.1}W_{0.9}$ sample. A single NCS α-Mn phase is obtained only through annealing the sample at temperatures close to 1700 °C, a behavior similar to the one found in the parent compound Re_3W.

The effect of heat treatments on the structural properties of the $Re_3Ta_{0.1}W_{0.9}$ sample is shown in Figure 4.6(b). After 10 days of heat treatment at 1100 °C, the corresponding diagram (blue curve in Figure 4.6(b)) indicates that the NCS α-Mn phase is almost stabilized and is fairly similar to the ones presented by the pristine NCS samples, being the only difference a spurious peak at $2\theta \sim 43$ °. This is very similar to the $Re_3Ta_{0.25}W_{0.75}$ AC compound and signalizes that the NCS phase formation was not complete after this heat treatment. Such a spurious peak is not observed after annealing both $Re_3Ta_{0.1}W_{0.9}$ and $Re_3Ta_{0.25}W_{0.75}$ samples at 1700 °C, as shown by the red curve in Figure 4.6(b).

The samples produced in the Re-Nb-W ternary system ($Re_3Nb_xW_{1-x}$, $0.1 \leq x \leq 0.5$) share the overall features discussed above in the Re-Ta-W system: samples with low concentration of Nb ($x \sim 0.1$) require annealing at 1700 °C to yield single NCS materials, while those with $x \geq 0.25$ are single crystalline exhibiting rather sharp Bragg peaks even in its AC forms. In this Nb system, reflections other than the NCS ones are only present in the $Re_3Nb_{0.1}W_{0.9}$ AC diffractogram, while the AC $x = 0.25$ diagram agrees with a single NCS phase material.

4.2 Superconducting properties

This part of the study is split into two major portions: (i) the superconducting phenomena are first established in the parent compounds Re_3W, Re_3Ta, and Re_3Nb, representatives of the NCS materials in binary Re-M (M = W, Ta, and Nb) systems; in (ii) the NCS $Re_3(Ta,Nb)_xW_{1-x}$ solid solutions are considered and its SC properties are discussed together with the parent compounds, specially with the annealed Re_3W material.

4.2.1 Parent Compounds Re_3W, Re_3Ta, and Re_3Nb

This section is devoted to introduce and discuss the superconducting properties of the parent compounds. Firstly, the properties of the $Re_{1-x}W_x$ materials, with $0.25 \leq x \leq 0.28$, are discussed in some detail. Next, the Re_3Ta and Re_3Nb SC properties are displayed and briefly examined.

The discussion in the Re-W samples includes the results of both AC and annealed materials. In fact, distinct SC features emerge depending on the particular sample type in this system. The discussion of these features is then conducted in light of what has already been published in this family of compounds.

Although short, the Re_3Ta and Re_3Nb data discussion summarizes the general SC properties seen across the whole NCS solubility range in Re-Ta and Re-Nb systems. For a more in-depth discussion of superconductivity in the two materials, the reader is invited to gain information provided in references 56 and 37.

4.2.1.1 Re-W system

The superconducting properties of the Re-W samples have been probed by temperature and magnetic field dependent D.C. and A.C. magnetization, electrical resistance, heat capacity, and thermal conductivity measurements. All samples in the Re-W system showed superconducting transitions.

Given the uncertainty in the structural composition of some AC samples, their superconducting states could, in principle, be used as a characterization tool. However, the precise

correlation between each individual SC transition and a thermodynamic phase is not straightforward. A classification scheme using T_C's of the AC samples does not settle the problem: both the σ and $h.c.p.$ phases have particular compositions matching the T_C of the Re_3W AC material.

A visual data summary (of $Re_{1-x}W_x$, $0.25 \leq x \leq 0.28$ samples) is displayed in Figure 4.7. In short, Figure 4.7 shows two kinds of SC resistive transitions: (i) broad ones, with a slightly bumpy structure, beginning above T = 9 K in AC materials, and (ii) sharp, featureless transitions in the NCS annealed samples close to T = 7.7 K. It is argued that (i) is probably due to inherent inhomogeneity in AC samples; and (ii) is related to samples with high degree of homogeneity. The heat capacity data clearly show jumps associated with superconducting transitions, and the AC data exhibit two jumps for each material. The low temperature jump in AC samples occurs at T $\sim$ 6.7 K, regardless of the particular sample W %at. concentration *x*, while both the temperature position and the shape of the high temperature jump are sensitive to slight changes in *x*. Then, the AC samples are probably composed of two distinct superconducting phases. Moreover, the bulk SC properties are also demonstrated by the temperature dependent D.C. magnetization curves. The large difference in the diamagnetic signal between the ZFC and FC modes strongly suggests that these samples are hard type-II superconductors.

Representative curves of the temperature dependent resistivity ρ(T) in both AC and annealed forms are shown in Figure 4.8 for the $Re_{0.75}W_{0.25}$ sample. Unsurprisingly, both curves suggest conventional metal behavior as its slopes dρ/dT are positive, but almost negligible when compared to ordinary metals. According to Figure 4.8, the resistivity of the $Re_{0.75}W_{0.25}$ AC specimen is higher than its annealed counterpart over the entire temperature $1.8 \leq T \leq 300$ K range. In contrast, the data of all others $Re_{1-x}W_x$ (not shown) indicate that the annealed samples with NCS structures are more resistive than their AC forms in the whole T range studied. Additionally, the room temperature resistivity of the $Re_{0.75}W_{0.25}$ AC sample is a few times higher than others AC samples. Then, the unusually enhanced resistivity of the $Re_{0.75}W_{0.25}$ AC sample could be due to extrinsic factors, such as a minor crack on the sample surface.

Regarding the low temperature data, the T $\rightarrow$ 0 extrapolation of $\rho(T)$ sets the residual resistivity ρ_0, which is approximated by the $\rho(T)$ immediately above the superconducting transition.

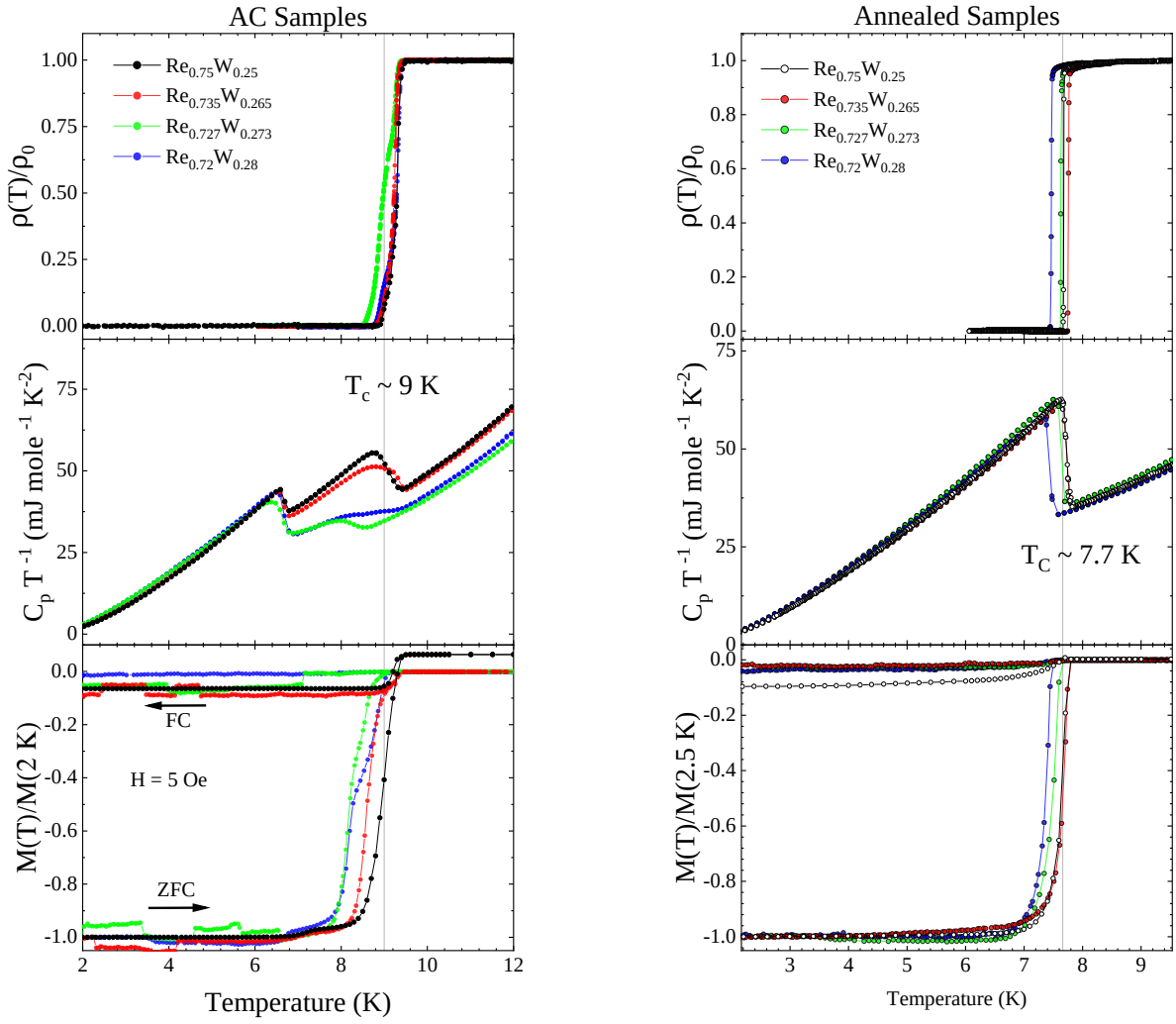

Figure 4.7: Superconducting data summary of the AC (left) and annealed (right) $Re_{1-x}W_x$ samples. The top panels exhibit the temperature dependent normalized resistivity. Specific heat data are shown in the middle panels. The bottom panels are temperature dependent D.C. magnetization under H = 5 Oe, using both the ZFC and FC protocols.

The value of ρ_0 decreases after the annealing procedure, reflecting an increased degree of homogeneity in the annealed material. The residual resistance ratio (RRR) is the ratio of room temperature resistivity to ρ_0 and is commonly used as a probe of the sample's purity; usually, single crystalline metallic samples exhibit RRR values as high as few thousands [139]. In the Re-W AC samples, however, the RRRs values were found to lie in the 1.3 - 1.5 range. Although the latter values are very small for metallic materials, they still are significantly higher than the common RRRs obtained in all single α-Mn materials of about 1.1 - 1.15, being they solid solutions or parent compounds.

In all NCS materials, the absolute value of ρ_0 remains in the few hundred $\mu\Omega\, cm$, suggesting that the major part of $\rho(T)$ in all temperatures comes from impurities. In this picture, the highly

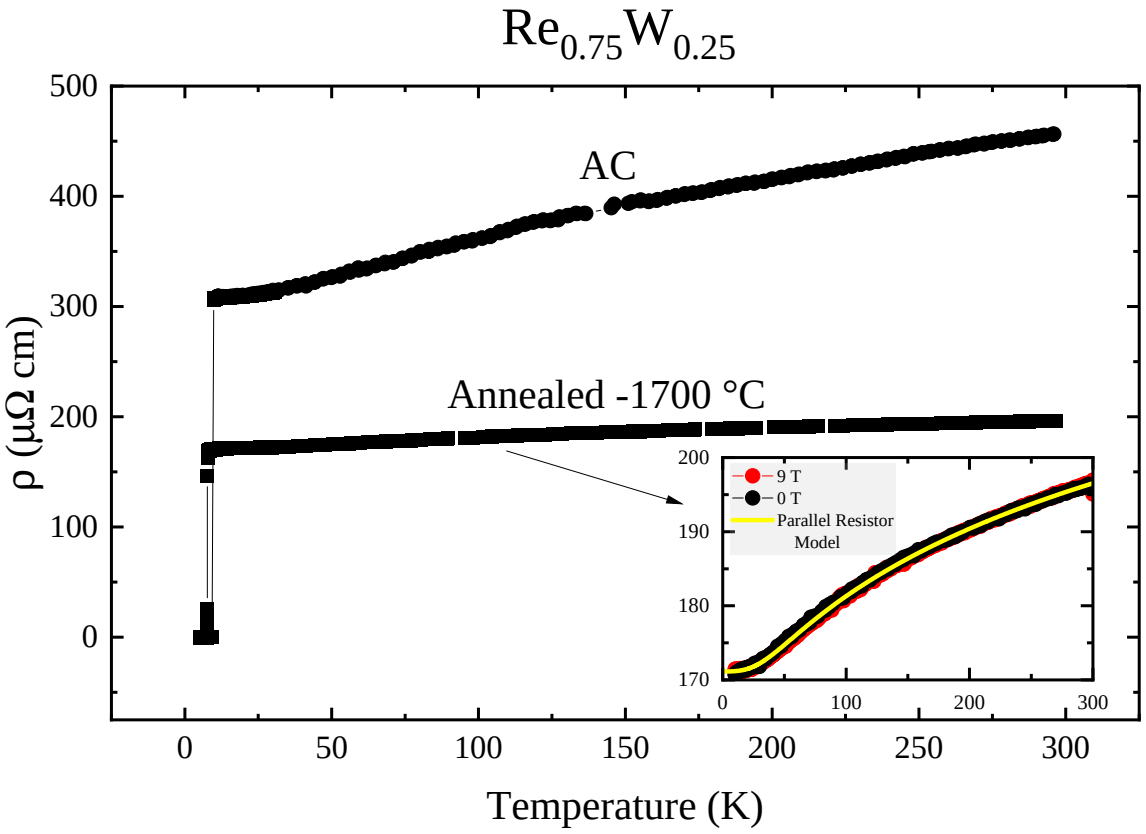

Figure 4.8: Temperature dependence of the electrical resistivity obtained in AC and annealed $Re_{0.75}W_{0.25}$ samples. The parallel resistor model was used to fit the annealed sample data, as shown in the inset of the figure — see the main text for details.

packed α-Mn crystalline structure, very susceptible to site's disorder, potentially leads to an almost T-independent electronic mean free path, and consequently, to the small RRR values of the α-Mn NCS materials. This hypothesis agrees with all reported ρ(T) data in materials having the α-Mn structure [65, 140–143], specially those based in rhenium [57]. Accordingly, the α-Mn phase exhibits the higher ρ_0 among all the phases in the Re-Mo system [42].

The normal-state data of the annealed sample show good agreement with the parallel resistor model, as shown in the inset Figure 4.8. Such a model utilizes the Boltzmann scattering theory to calculate the electrical resistivity of metals, treating the electrons semi-classically [144]. The sublinear T-dependence of ρ(T) at high temperatures (T > 150 K) indicates a trend in ρ(T) towards a saturation value ρ_{sat}, much similar to the behavior seen in Nb_3Sn [145, 146], in pure α-Mn metal, and others 3d and 5d metals [144]. According to a simple picture, this T-independent ρ_{sat} could be related to a lower limit of the electronic mean free path (the Mott-Ioffe-Regell limit); this lower limit, then, would be comparable to the interatomic spacing within

the crystalline structure [147]. Therefore, the parallel resistor model captures these features by stating that the sample's conductivity can be well described by the sum of the ideal and saturated conductivity in the following manner [148]:

$$\begin{aligned} \frac{1}{\rho(T)} &= \frac{1}{\rho_{sat}} + \frac{1}{\rho_{ideal}(T)} \\ \rho_{ideal}(T) &= \frac{\rho_0}{1-\rho_0/\rho_{sat}} + C\left(\frac{T}{\theta_{D\rho}}\right)^n \int_0^{\theta_{D\rho}/T} \frac{x^n}{(e^x-1)(1-e^x)}dx, \end{aligned} \tag{4.1}$$

where $\theta_{D\rho}$ is the Debye temperature, *n* is the Wilson scattering parameter, and C is a multiplicative constant in resistivity unities. The normal-state data was fitted using Equation 4.1, resulting in the yellow line in the inset of Figure 4.8, and yielding the values: ρ_{sat} = 227 $\mu\Omega\ cm$; ρ_0 = 170 $\mu\Omega\ cm$; $\theta_{D\rho}$ = 185 K, C = 852 $\mu\Omega\ cm$; *n* = 3 was fixed during the fitting procedure. This procedure was conducted in all NCS Re_3M samples and resulted in ρ_{sat} values in the $\sim$ 130 - 300 $\mu\Omega\ cm$ resistivity range. The published resistivity saturation value of others NCS Re-based materials [42, 63, 149] are comparable to the results found here, suggesting a common origin for the saturation in these NCS materials.

In order to explicitly show the differences in the resistive superconducting transition of the AC samples, Figure 4.9 compares the normalized resistivity of the various $Re_{1-x}W_x$ samples produced in the $0.25 \leq x \leq 0.28$ range. Two features of this comparison are clearly noted: (i) two different $Re_{0.75}W_{0.25}$ (#1 and #2) samples have distinct critical temperatures ($\sim$ 9.3 and 9.5 K) and transition widths (0.5 and 0.15 K, respectively); and (ii) a bump in the resistance drop can be seen in all samples, a feature more pronounced in the $Re_{0.727}W_{0.273}$ data. Those observations are consistent with a picture of inhomogeneous AC $Re_{1-x}W_x$ samples: in this picture, the $Re_{0.75}W_{0.25}$ #2 sample being the more homogeneous among the materials. It should be noted that this sample has been synthesized in a different arc-melting furnace than the others.

On the other hand, the data comparison among the annealed samples shown in Figure 4.7 indicates sharp transitions, confirming the single phase character and high homogeneity, as suggested by the XRD data.

Moving on to the specific heat $C_p(T)$ data of the Re-W samples, the $C_p(T)$ values were obtained by the product between the measured heat capacity and the nominal molecular weight

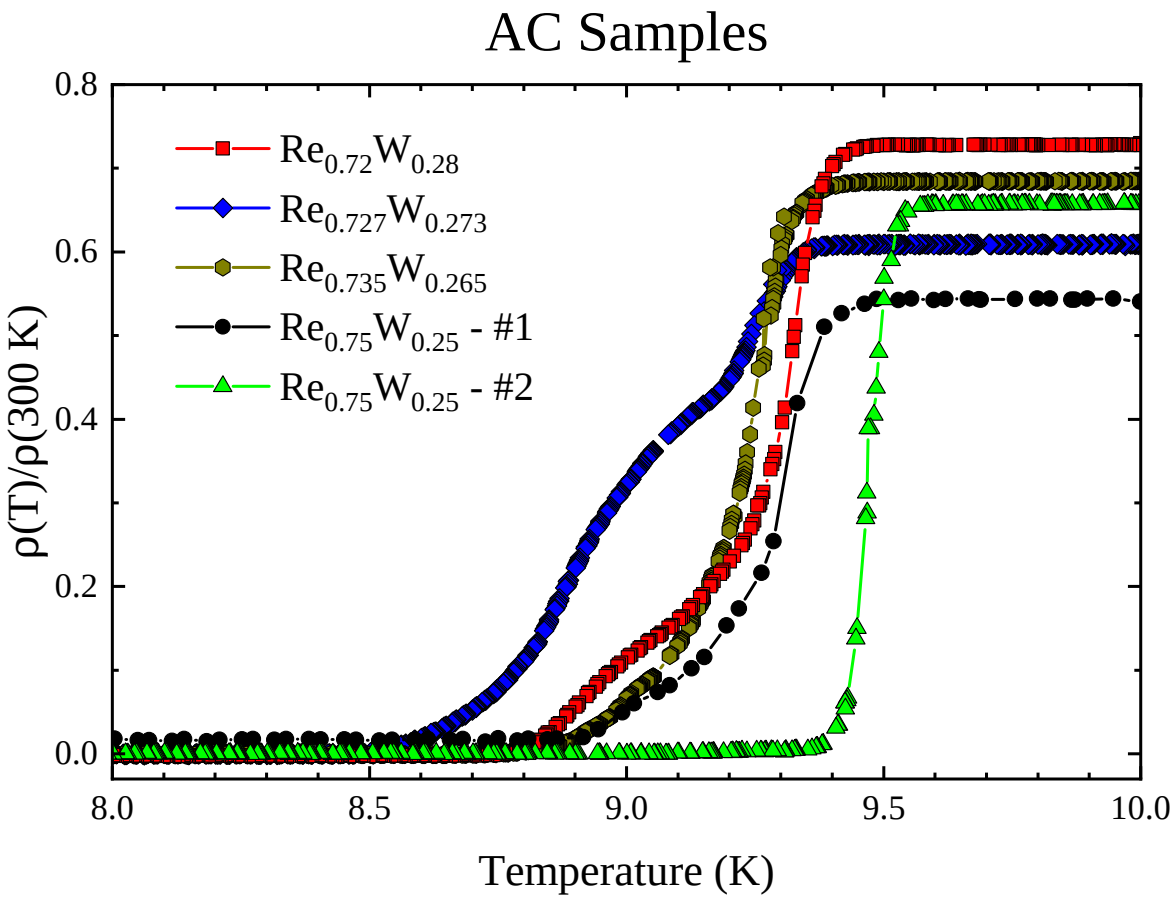

Figure 4.9: Comparison of the normalized resistivity of AC samples $Re_{1-x}W_x$ with $x \sim 0.25$ near the transition temperature.

of the various Re_3M samples (considering 4 atoms in each formula unit). The high temperature $C_p(T)$ (T > 20 K) results are not shown here, but they agree with the published data found in others NCS Re-based materials [150]. Then, shown in Figure 4.10 is the low temperature $C_p(T)$ data of a representative sample in both its AC and annealed forms.

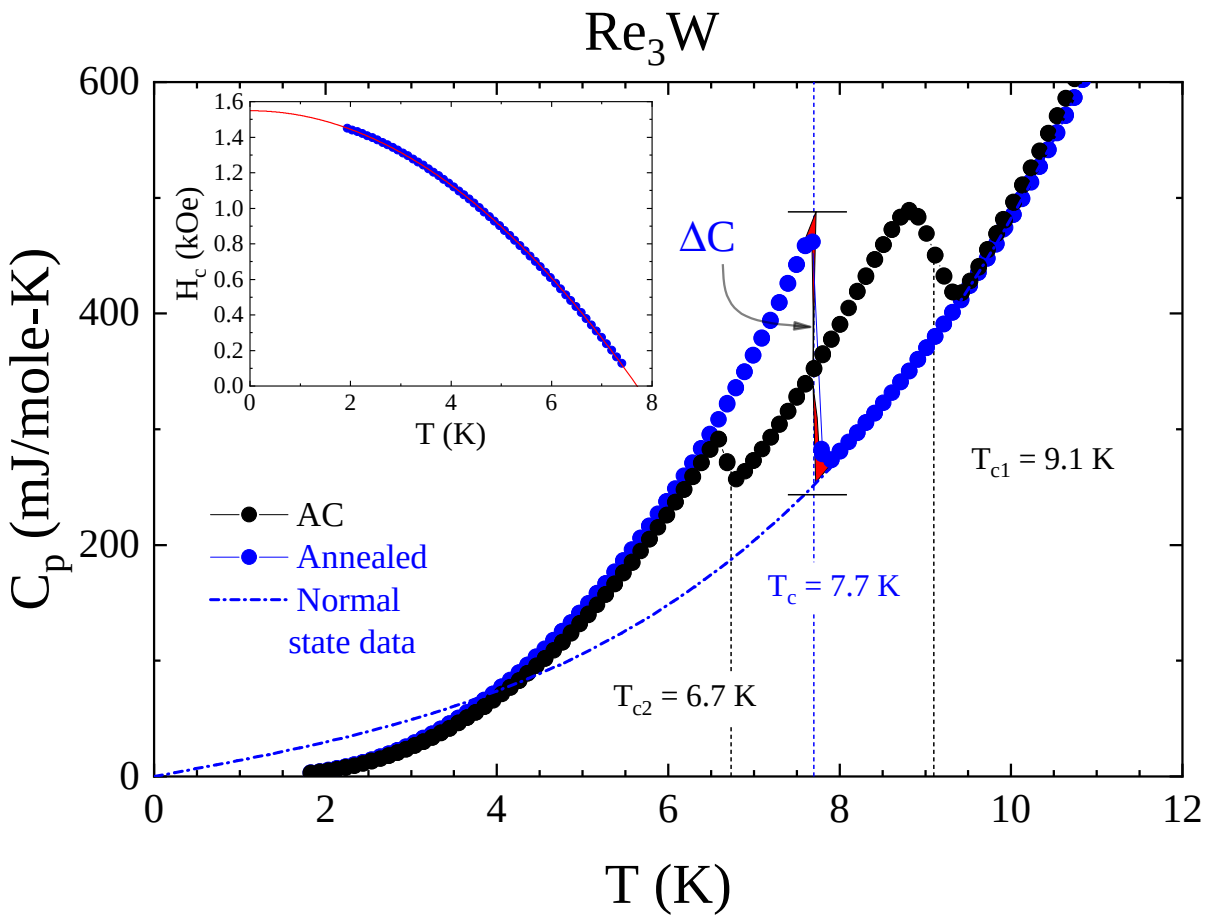

Figure 4.10: Low temperature specific heat data. The results obtained in the Re_3W AC material are show in black solid data points while the blue points represent the measured annealed sample. The figure's inset shows the temperature dependent thermodynamic critical field H_C of the annealed Re_3W sample, obtained through integration of its C_p(T) data.

The C_p vs T data for the NCS single phase Re_3W (blue circles) show a jump centered near 7.7 K, a feature consistent with the opening of a superconducting energy gap. In contrast, the C_p vs T data for the AC Re_3W sample, also shown in Figure 4.10 by the black circles, display two peaks corresponding to the SC transitions of different phases, clearly identified near 6.7 and 9.1 K, as indicated by the vertical dashed lines.

This double peak structure is certainly related to the multiphase structure suggested in the XRD data. Then, assuming that the XRD data is not capable of precisely set the sample's

composition, the question that arises here is: which SC transition corresponds to which atomic structure? By comparing the AC Re_3W data with the results obtained for the single phase AC materials $Re_{0.9}W_{0.1}$, $Re_{0.667}W_{0.333}$, and $Re_{0.5}W_{0.5}$ (not shown here), it is strongly suggested that the superconducting transition occurring in the higher temperature is due to the phase with the $h.c.p$ structure while the jump at T_{C2} would be produced by a secondary σ phase with composition in the range $0.5 < \%$ at.Re < 0.66. This hypothesis is partially corroborated by the results described in Ref. 40, where the authors have argued that the $\sim$ 9 K SC transition in the AC Re_3W comes from the $h.c.p$ (CS) phase, but no secondary phase is mentioned in their study. Evidence of the double peak structure in Re_3W specific heat data have also been discussed in another study [151], but no mention on the origin of the lower temperature peak was made.

In general, a fairly simple and common analysis is used to extract some of the materials parameters by using the $C_p(T)$ data at low temperatures. The specific heat can be described by $C_p(T) = C_{en}(T) + C_{latt}(T)$, where $C_{en}(T)$ and $C_{latt}(T)$ are the electronic and the lattice (phonons) components, respectively. The electronic term is $C_{en}(T) = \gamma_n T$, where γ_n is the Sommerfeld electronic contribution. The phonon term can be written as $C_{latt}(T) = \beta_1 T^3 + \beta_2 T^5$, where the T^3 term is the Debye low temperature approximation and the T^5 term accounts for non-harmonicities. Therefore, an extrapolation of the annealed Re_3W data from the normal state down to T = 0 K, represented by the dashed line in Figure 4.10, was obtained by fitting the 7.8 < T < 12 K data* with a model considering the electronic and lattice contribution to $C_p(T)$. This procedure yielded γ_n = 17.1 mJ mole^{-1} K^{-2}, β_1 = 2.5 mJ mole^{-1} K^{-4}, and $\beta_2 \sim 6{\cdot}10^{-4}$ mJ mole^{-1} K^{-6}. The order of magnitude of γ_n suggests that these are weakly-correlated NCS materials, as commonly reported in Re-based materials [78]. The γ_n values of all samples are displayed in tables 4.4-4.7.

In C_p data, T_C is defined by the entropy conservation construction since rounded jumps are commonly seen in the data. In this construction, T_C = 7.7 K is calculated by equalizing the C_pT^{-1} vs. T areas immediately above and below the jump of the annealed Re_3W; the procedure is illustrated in Figure 4.10 by the shaded regions (in red color) near the SC jump, even though the y-axis is presented in C_p unity. Using linear extrapolations both from SC and

*The fitting procedure was also conducted in the dataset obtained under H = 9 Tesla, which suppresses the superconducting state down to $\sim$ 3 K, but no significant difference in the extrapolated values was observed.

normal states towards the T_C line, it is now possible to estimate the SC jump magnitude $\Delta C \approx$ 220 mJ mole^{-1}K^{-1}. The comparison of ΔC with the normal state specific heat value ($\gamma_n T_C$) leads to the ratio $\frac{\Delta C}{\gamma_n T_C} \sim 1.67$, slightly above the BCS weak-coupling value of 1.43.

Additionally, the thermodynamic critical field H_C was also estimated directly from the specific heat results. The following relations have been used to obtain the critical field [152]:

$$\begin{aligned} \frac{\mu_0 H_c^2}{2}(T') &= \Delta F = \Delta U(T') - T\Delta S(T') \\ \Delta U(T') &= \int_{(T')}^{T_c} C_s - C_n dT \\ \Delta S(T') &= \int_{(T')}^{T_c} \frac{C_s - C_n}{T} dT. \end{aligned} \tag{4.2}$$

Each H_C(T) blue point in the inset of Figure 4.10 was calculated by conducting the numerical integrations of the specific heat data at each temperature using the annealed Re_3W curve. Then, the zero-temperature $H_C(0)$ = 1.53 kOe could be estimated by extrapolating H_C(T) using a mean field model, with

$$H_C(T) = H_C(0)\left[1 - \left(\frac{T}{T_C}\right)^2\right]. \tag{4.3}$$

The results obtained here are in agreement with the values reported in literature for the $Re_{0.82}Nb_{0.18}$, Re_6Zr, and Re_3Ta materials [49, 56, 150], whose $H_C(0)$'s were found to lie in the 0.6 - 1.3 kOe range. The results of the mean field model is also shown by the continuous line in the inset of Figure 4.10.

4.2.1.2 Re_3Ta and Re_3Nb

Regarding the NCS superconductivity arising in the Re-Ta and Re-Nb systems, the discussion is restricted to the data comparison shown in Figure 4.11, since they are very similar to those exhibited by the Re-W NCS samples considered above.

The results of the annealed Re_3Ta are shown in the left hand side of Figure 4.11 while the right hand side displays the results from the annealed Re_3Nb sample; the results of their AC forms did not present any deviation from the annealed samples data. The main difference between the Re_3Ta and Re_3Nb samples is on the SC transition observed in the specific heat data: while a steep jump is seen Re_3Ta, having the T_C = 4.75 K estimated by the conservation of the entropy (represented by the faded gray line), the Re_3Nb sample has a wide SC transition, spanning $\sim$ 1 K and resulting in a T_C of about 6.2 K. Nonetheless, the onset of superconductivity at 6.7 K in C_p(T) data matches the half of resistance drop in the $\rho(T)$ curve. Lastly, bulk SC is indicated by the temperature dependent A.C. susceptibility curves shown in the bottom panels, in agreement with their D.C. magnetization results (not shown).

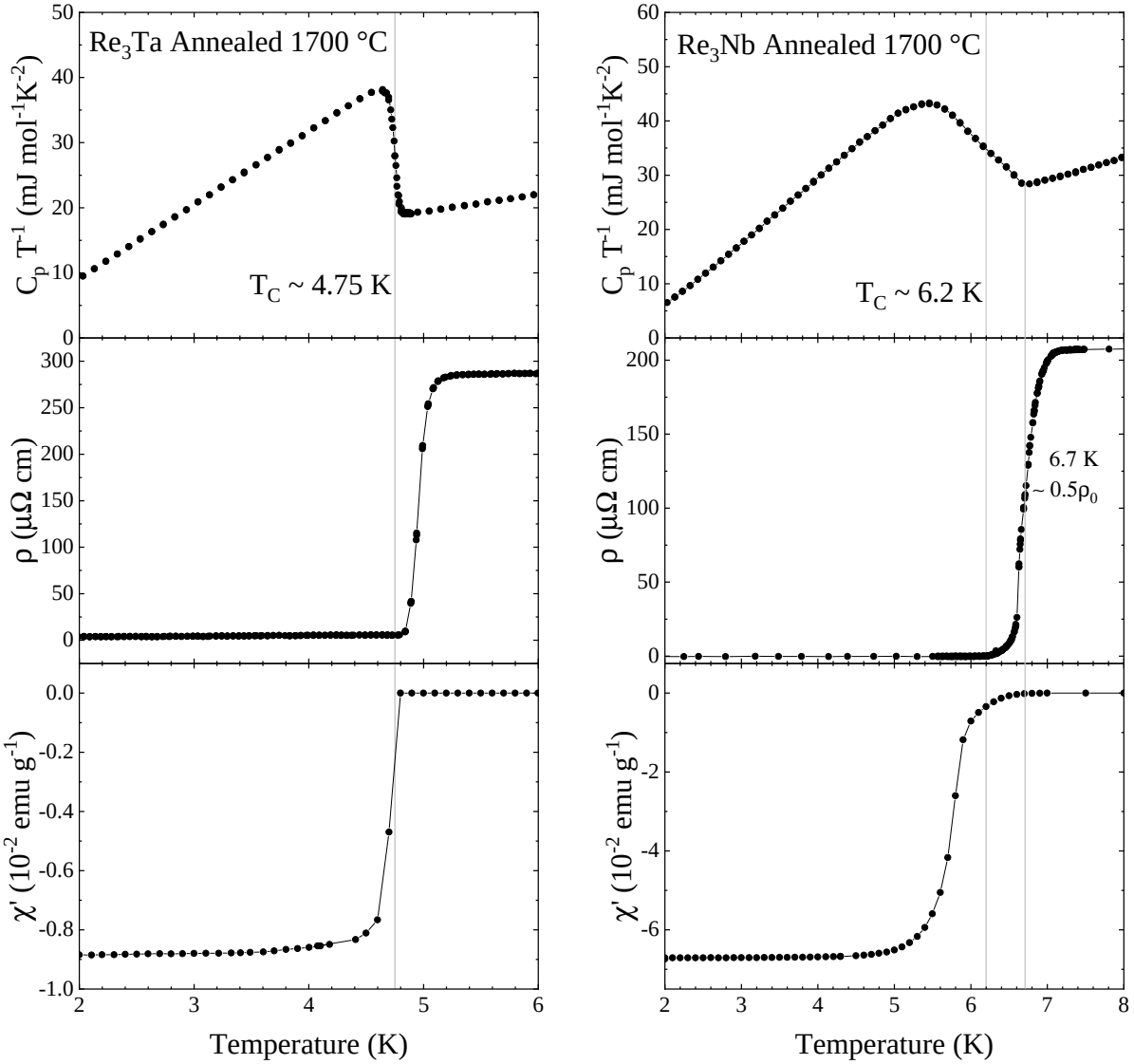

Figure 4.11: SC data summary of the Re_3Ta (left) and Re_3Nb (right) parent compounds. The vertical faded gray lines represent the T_C value obtained through the specific heat data.

4.2.2 Re-W-(Nb,Ta) Solid Solutions

The SC properties of Re_3M solid solutions are discussed in this section; this discussion is conducted mainly from the results obtained in the AC $Re_3Nb_{0.5}W_{0.5}$ and $Re_3Ta_{0.5}W_{0.5}$ specimens, since these results contain all features exhibited by the $Re_3(Nb,Ta)_xW_{1-x}$ samples in general. The only effect of the annealing on the $Re_3(Nb,Ta)_{0.5}W_{0.5}$ samples is to diminish any compositional disorder, resulting in sharper SC transitions. Therefore, the annealing does not invalidate any of the general trends indicated below for the AC solid solutions samples at the x = 0.5 composition.

For the discussion of superconductivity in solid solutions, the starting point is the temperature dependent resistivity of the solid solutions. These results are plotted along with those of the annealed Re_3W sample in Figure 4.12. In the normal state data, T > 10 K, the temperature dependence is essentially the same in all curves; therefore, the parallel resistor model also describe the solid solutions reasonably well.

The partial W substitution increases the residual resistivity, as clearly noted in the main panel of Figure 4.12. Such an increase in single crystalline materials could have two main origins: (i) compositional fluctuations arising in the AC samples and (ii) impurities induced by the partial substitutions, breaking the long-range order symmetry and increasing the average density of electronic scattering centers. The results on the annealed solid solutions samples, however, yield very similar ρ_0 values to those of the AC specimens. This suggests that the contribution (i) is only marginal and that (ii) determines the normal state data in Figure 4.12.

On the superconducting state, the inset of Figure 4.12 shows an expanded view of the $6 \leq T \leq 9$ K region and focuses on the three superconducting transitions. By defining T_C at the transition midpoint ($\rho(T_C) = 0.5\ \rho_0$), the parent compound T_C ($\sim$ 7.7 K) is almost insensitive to the Nb substitution, but the Ta solid solution's T_C is clearly decreased to 7.3 K. The solid solution transition widths (ΔT_C) are unsurprisingly wider than the parent compound due their inherent enhanced disorder. Small compositional fluctuations on local Re:W/Nb content could possibly lead to the high SC transition's onset in AC $Re_3Nb_{0.5}W_{0.5}$ sample ($\sim$ 7.8 K). As a result of the annealing, the onset of the SC resistive transitions is suppressed to lower temperatures, effectively sharpening the transitions.

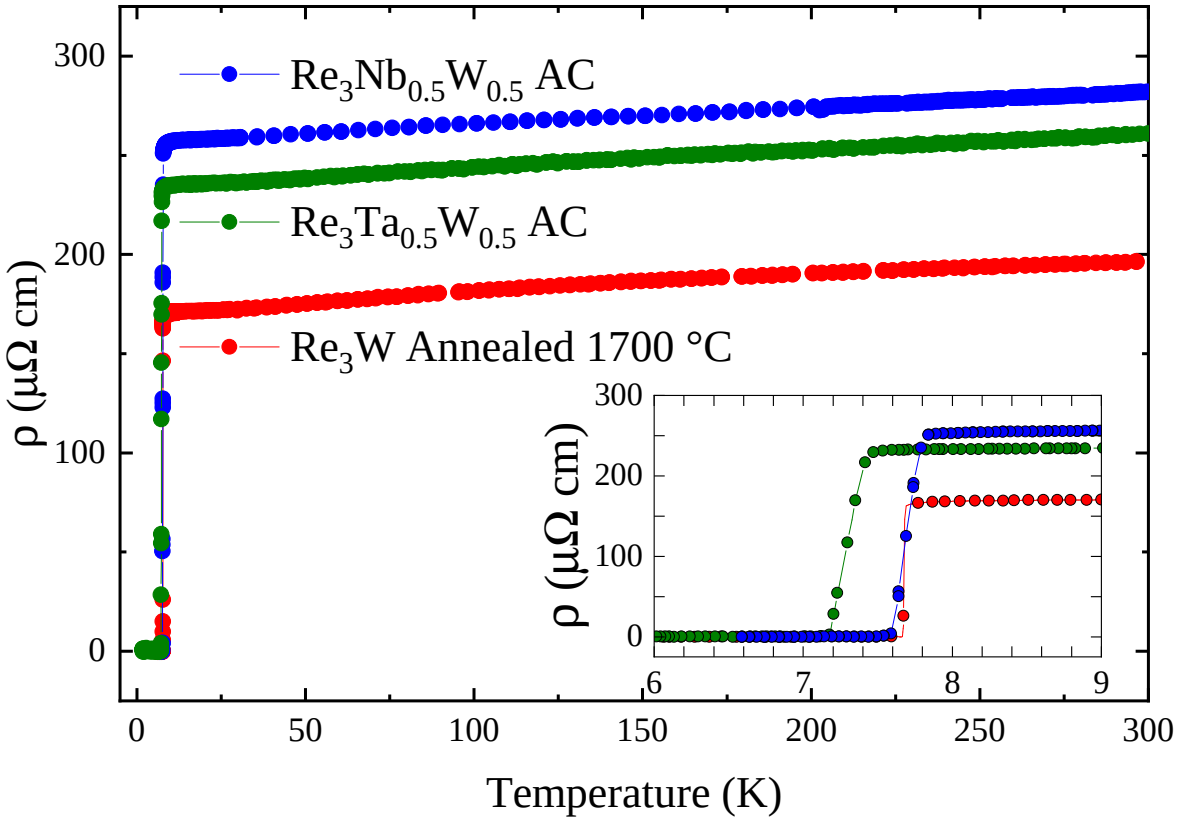

Figure 4.12: Comparison of the temperature dependent resistivity among the NCS materials: as cast solid solutions $Re_3Nb_{0.5}W_{0.5}$ and $Re_3Nb_{0.5}W_{0.5}$, and annealed parent compound Re_3W. The low temperature data is shown in the inset, in order to clearly see the transitions to the zero resistance state.

Further probing of the $Re_3(Nb,Ta)_xW_{1-x}$ superconducting properties was carried out by means of heat capacity and thermal conductivity measurements. The low temperature specific heat of the C_p of the $Re_3Nb_{1-x}W_x$ and $Re_3Ta_{1-x}W_x$ AC samples are plotted in Figure 4.13.

From Figure 4.13(a), both SC jumps evolve smoothly with the systematic substitution of W by Ta. By using a small substitution of x = 0.1, the clear double peak structure of the parent compound is strongly suppressed, but two superconducting transitions still remain in the data (light green pentagons). The high temperature transition is spread over a large T range and does not exhibit a well-defined jump-like feature, probably signalizing the low volumetric fraction of this SC phase. In a picture where the high T_c SC phase is due to a $h.c.p$ phase, the peak suppression suggests that the formation of the $h.c.p$ phase is partially prevented by this level of Ta content. On the other hand, in the lower temperature transition, the substitution effect is just to diminish its T_c from 6.7 to 6.6 K when x is increased from 0.0 to 0.1, respectively. By further

increasing the Ta concentration, no double transition is noted in the $Re_3Ta_{0.25}W_{0.75}$ AC sample. Its single transition, however, extends over 0.4 K and has a small feature rounding the topside of the specific heat jump, suggestive of a non-homogeneous material. Finally, a single, quasi-discontinuous jump preceded by a well-behaved normal metallic state is seen in the results of $Re_3Ta_{0.5}W_{0.5}$ as cast sample (dark green triangles). Considering only materials with the NCS α-Mn structure, the T_C trend is as expected: it is shifted to lower temperatures as the Ta content (x) increases, ultimately reaching the Re_3Ta at the other end of the series, whose data are shown by the darker green diamonds data points in Figure 4.13(a).

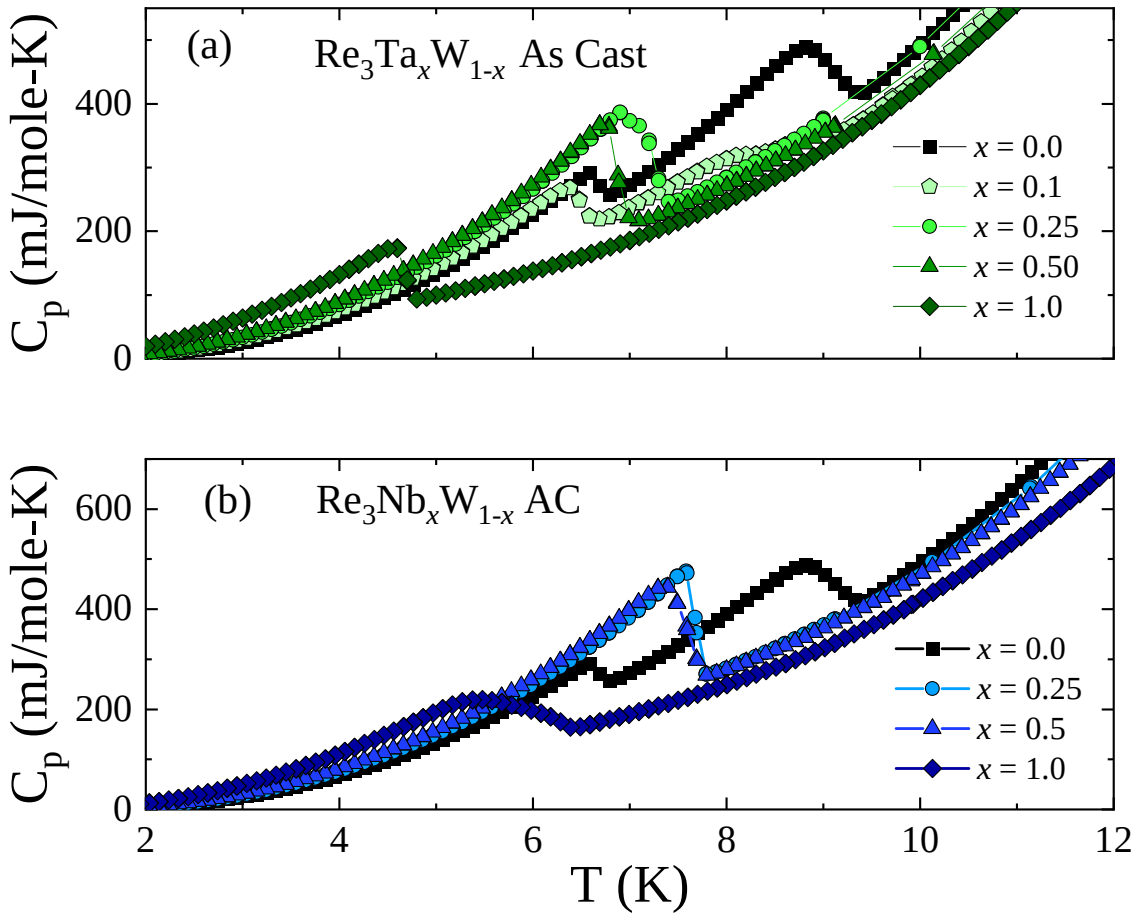

Figure 4.13: Temperature dependence of the specific heat at low T (< 12 K) of the (a) $Re_3Ta_{1-x}W_x$ and (b) $Re_3Nb_{1-x}W_x$ AC samples.

The results obtained in the AC $Re_3Nb_{1-x}W_x$ system are shown in Figure 4.13(b) and exhibit profound similarities with the Re-Ta-W system. In order to produce a clearer figure, the $Re_3Nb_{0.1}W_{0.9}$ AC data is omitted, but it has the same qualitative behavior as the $Re_3Ta_{0.1}W_{0.9}$ AC described above. In the Re-Nb-W system, even though the NCS T_c's are also shifted to

lower values by increasing *x*, the superconducting state is more robust against the W substitution: T_c is lowered as little as 0.1 K from *x* = 0 to 0.25 and even less in the 0.25 - 0.5 substitution range. In fact, the onset of superconductivity in C_p(T) seems to occur at the same temperature in both $Re_3Nb_{0.25}W_{0.75}$ and $Re_3Nb_{0.5}W_{0.5}$ AC samples. The SC jump width, however, is different in these otherwise identical curves, being wider in the composition *x* = 0.5.

The Sommerfeld constant γ and the Debye temperature $\theta_D = (12\pi^4 RN/5\beta_1)^{\frac{1}{3}}$ are calculated by using again the Debye model to describe the low temperature C_p(T), in the normal state above T_c. In θ_D formula R = 8.314 J mol^{-1} K^{-1} is the gas constant, N = 4 atoms in the formula unit, and β_1 is the slope of the C_p/T vs T^2 curve. The extracted values of γ and θ_D of each sample in the Re-(Ta,Nb)-W systems are displayed in tables 4.6 and 4.7.

Having the θ_D value, the electron-phonon coupling constant λ_{ep} can be estimated using the inverted McMillan equation [153]:

$$\lambda_{ep} = \frac{1.04 + \mu^* ln(\theta_D/1.45T_c)}{(1 - 0.62\mu^*)ln(\theta_D/1.45T_c) - 1.04}, \tag{4.4}$$

with the Coulomb pseudopotential μ^* = 0.13, as commonly used in alloys of transition metals. The λ_{ep} estimates throughout all the samples studied here are within the 0.6-0.8 range (see tables 4.6 and 4.7 in page 144), indicating moderate electron coupling, and in close agreement with the published values of other NCS Re-based systems [49, 61, 149].

Changing the focus to the SC state in the specific heat results, the superconducting electronic specific heat C_{es}(T) was estimated by subtracting the lattice contribution (obtained from the Debye model) from the zero-field data, i.e., $C_{es}(T) = C_p(T) - C_{latt}(T)$. Then, the temperature dependent C_{es}(T) can directly be compared to the weak-coupling BCS results. Displayed in Figure 4.14 are the plots of $C_{es}(T)(\gamma_n T)^{-1}$ *versus* the reduced temperature T/T_C (= *t*) obtained through the results of the annealed Re_3W, $Re_3W_{0.5}Ta_{0.5}$ AC, and $Re_3W_{0.5}Nb_{0.5}$ AC samples. The data for the three samples all but completely overlap, suggesting a universal behavior; additionally, no sign of unconventional superconductivity seems to be emerging due to the partial W substitution in these series.

Furthermore, the C_{es}(T) data could be fitted very well to an extension of the BCS theory, known as the alpha-model. This model accounts for the strong coupling superconducting pair-

ing and is based upon re-scaling the α = Δ_0/k_BT ratio [83], an otherwise universal quantity in the BCS weak-coupling limit [4]. Then, a model of independent fermionic excitations can be used to calculate C_{es}(T):

$$\frac{C_{es}(T)}{\gamma_n T} = \frac{3\alpha^3}{\pi^2 t^3} \int_{-\infty}^{\infty} f(\epsilon)[1 - f(\epsilon)]\{y^2 + \delta^2 - \frac{d\delta^2}{dT}\}dy, \tag{4.5}$$

where f(ϵ) is the Fermi-Dirac function with $\epsilon^2 = \Delta_0^2(y^2 + \delta(T)^2)$, $y = \xi/\Delta_0$ is the rescaled quasi-particle energy measured relative to Fermi energy, and δ(T) = 1.76 tanh(1.82[1.018(T_C/T - 1)]$^{0.51}$) is the approximate formula for the temperature dependence of the gap function obtained by self-consistently solving the gap equation in the weak-coupling limit [154].

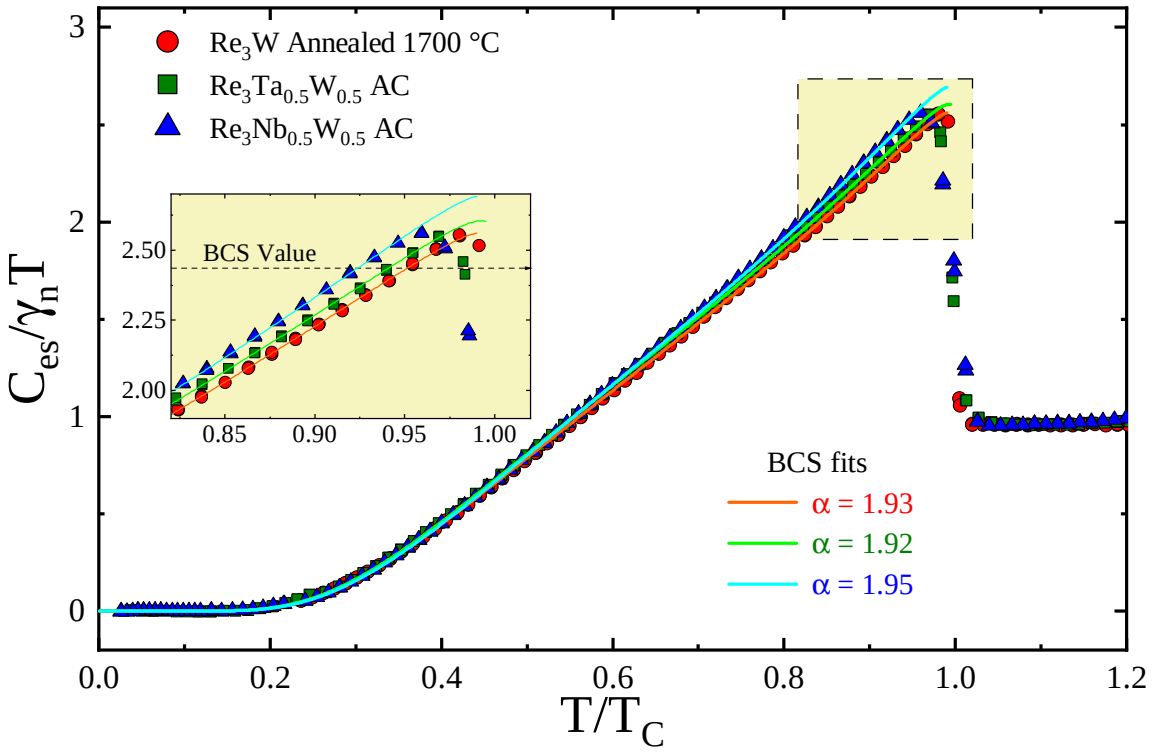

Figure 4.14: Specific heat electronic contribution in the superconducting state (C_{es}(T)) of the $Re_3Nb_{0.5}W_{0.5}$ AC, $Re_3Nb_{0.5}W_{0.5}$ AC, and annealed Re_3W samples. The dashed lines are the α-model data fitting results for each sample.

Temperature dependent thermal conductivities (κ) of the AC materials Re_3W, $Re_3W_{0.5}Ta_{0.5}$, and $Re_3W_{0.5}Nb_{0.5}$, as well as annealed Re_3W are displayed in the inset of Figure 4.15. κ(T) drops monotonically in all samples below 50 K, and downturns with higher slopes occur below 20 K. Clear upturns near T_C can be identified in the annealed Re_3W, $Re_3Ta_{0.5}W_{0.5}$, and

$Re_3Ta_{0.5}W_{0.5}$ AC samples, suggesting that this is a feature of the NCS phase.

The thermal conductivity is typically described as $\kappa = \kappa_e + \kappa_p$, where κ_e is the electronic contribution, and κ_p is due to phonons. The steeper downturns below 20 K suggest that they are mostly due to the suppression of phonons modes [63, 155]. To test this hypothesis, κ_e has been estimated from the Wiedemann-Franz relation $\kappa_e(T) = L_0 T\ \rho(T)^{-1}$, where $\rho(T)$ is the sample resistivity and $L_0 = 2.45\ 10^{-8}\ W\Omega K^{-2}$ is the Lorenz number. Then, κ_e/κ ratios were found to be lower than 0.2 in the 2-50 K temperature range, indicating that the electronic contribution to $\kappa(T)$ is rather small. Similar weak electronic contributions have also been observed in isostructural $Re_{24}Ti_5$ and Re_6Zr polycrystalline specimens [61, 63], suggesting that this maybe a characteristic of the α-Mn phase, in light of the electronic mean free path in these materials being of the order of the lattice parameters. The magnitude of $\kappa(T)$ decreases with the substitution of Ta or Nb for W, consistent with an increase in disorder scattering due to the partial substitutions.

The normal state behavior of $\kappa(T)$ in all samples follow similar trends. However, two types of behavior appear in the superconducting state, as seen in Figure 4.15. In the case of the annealed Re_3W and AC $Re_3W_{0.5}Ta_{0.5}$, $\kappa(T)$ begins to rise immediately below T_c, peaking at 2-3 K below T_c, and start to drop again. To a much lesser extend this is the behavior shown by the AC $Re_3W_{0.5}Nb_{0.5}$ as well. In the AC Re_3W sample data, the features at T_c and below are not observed, suggesting that they are due to the NCS α-Mn structure. Previous thermal conductivity studies in Re-based materials have also shown features near T_c. While $\kappa(T)$ for $Re_{24}Ti_5$ does not exhibit any marks near T_c [61], $\kappa(T)$ for Re_6Zr begins to rise $\approx$ 1 K below its T_c = 6.7 K and peaks near 4.5 K [63]. In spite of the different behaviors, the $\kappa(T)$ data indicate that phonons are the major heat carriers in the superconducting state, since the electronic contribution to the superconducting thermal conductivity $\kappa_{es}(T)$ rapidly decreases due to the formation of Cooper pairs, entities that, in principle, do not carry heat [156].

In order to understand these different behaviors in $\kappa(T)$ data, the conventional picture of SC is used as starting point. In this picture, the lattice conductivity increases below T_C due to the reduction of electron-phonon scattering, resulting in an increase in the phonon mean free path l_{ps}. The $\kappa(T)$ enhancement upon cooling continues until the phonon density starts to decrease,

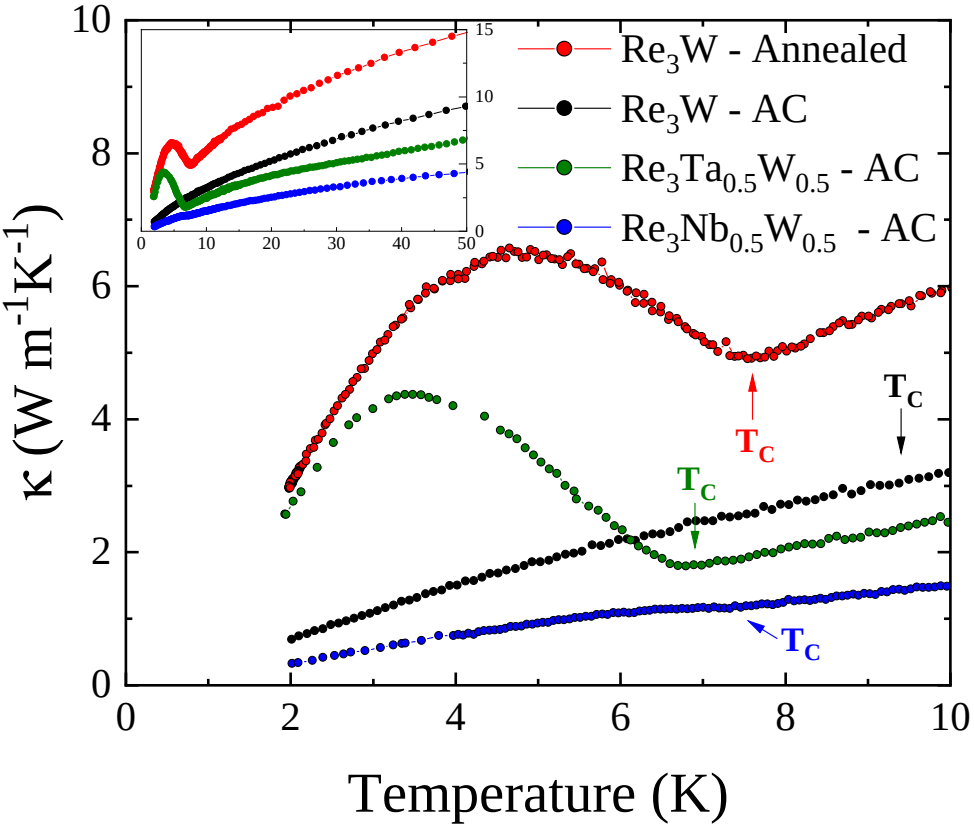

Figure 4.15: Low temperature thermal conductivity κ(T) of selected samples.

causing κ(T) to peak and drop again [157].

In light of the different peak magnitude in the κ(T) data below T_C for the three NCS single phase samples of Figure 4.15, it is instructive to consider possible phonon scattering mechanisms, specifically the ones that limit the phonon mean-free path l_{ps} at low temperatures; e.g., impurities, point-defects, dislocations, and sample's size [158]. In comparison, the effect of disorder on phonon scattering in the κ(T) data for superconducting $V_{1-x}Ti_x$ was sizable, and the thermal transport is dominated by electrons in the normal state [159]. Furthermore, the huge peak of κ_s(T) in niobium carbides is completely suppressed by increasing the carbon vacancy density, as the composition is tweaked from $NbC_{0.97}$ to $NbC_{0.77}$ [160]. These studies posit a picture in which more disorder leads to lower and more spread κ_s(T) peaks. With regard to the size effect, Morton *et al.* have shown that κ_{es}(T) is limited by grain boundary scattering in polycrystalline Nb_3Sn [161], and various studies on single crystalline superconductors suggested κ(T) is limited by sample's size at low temperatures [20, 162]. Therefore, it is plausible

to consider that site disorder and grain size should contribute to the phonon scattering in the superconducting state of the NCS Re_3M samples, and the occurrence (or lack thereof) of peaks in κ(T) data reflects the strength of such scattering mechanism.

4.3 Magnetic field dependence of the superconducting properties

Almost all of the data exhibited above were characterized in the absence of magnetic fields. In general, the SC state is suppressed by external magnetic fields, whose effects on the Re_3M SC properties are of particular interest in this study. Having said that, below is a discussion on the general trend seen throughout most of our field-dependent data. Particular features of some representative samples are exhibited and discussed in the following, leaving the broader discussion of SC phase diagrams to the section 4.3.2.

In the context of as-cast materials, various ρ(T,H) curves are shown in Figure 4.16 for the $Re_{0.735}W_{0.265}$ AC sample. It is noteworthy that the XRD results of this AC specimen suggested a two phase material — probably a mixture of the $h.c.p$ and σ phases — whose both of the phases superconducts at low temperatures. At the zero field curve, the SC transition width spans more than 0.3 K, indicating a high degree of inhomogeneities in the material. The SC transitions widen as the external magnetic field is increased, but the widening does not occur in an evenly manner: shoulder-like features are observed when the sample is approaching the zero-resistance state. These features are subtle in the low-field regime (H < 1 T) but become clearly noticeable at the curve obtained at 2 Tesla. At higher values of the magnetic field, the feature seems to evolve from the bottom to the middle of the resistive transition, being marked by a cusp in the transition's slope.

The origin of these features is not completely understood, but they are certainly associated with the two-phase character of the materials. As it will be discussed in the next sections, the results shown in Figure 4.16 could be related to two different mechanisms: (i) a proximity (or even a Josephson) effect between the two phases, and (ii) unusual vortex dynamics enhanced by the inherent inhomogeneities present in Re-W AC samples.

Shown in the top panel of the Figure 4.17 is the temperature dependent normalized resistivity of the annealed $Re_{0.75}W_{0.25}$. In contrast to the case in the AC samples, the magnetic field acting in the annealed material simply produces an even broadening of the superconducting transition. In order to compare the transitions among the various fields, the 10, 50, and 90 % drops from

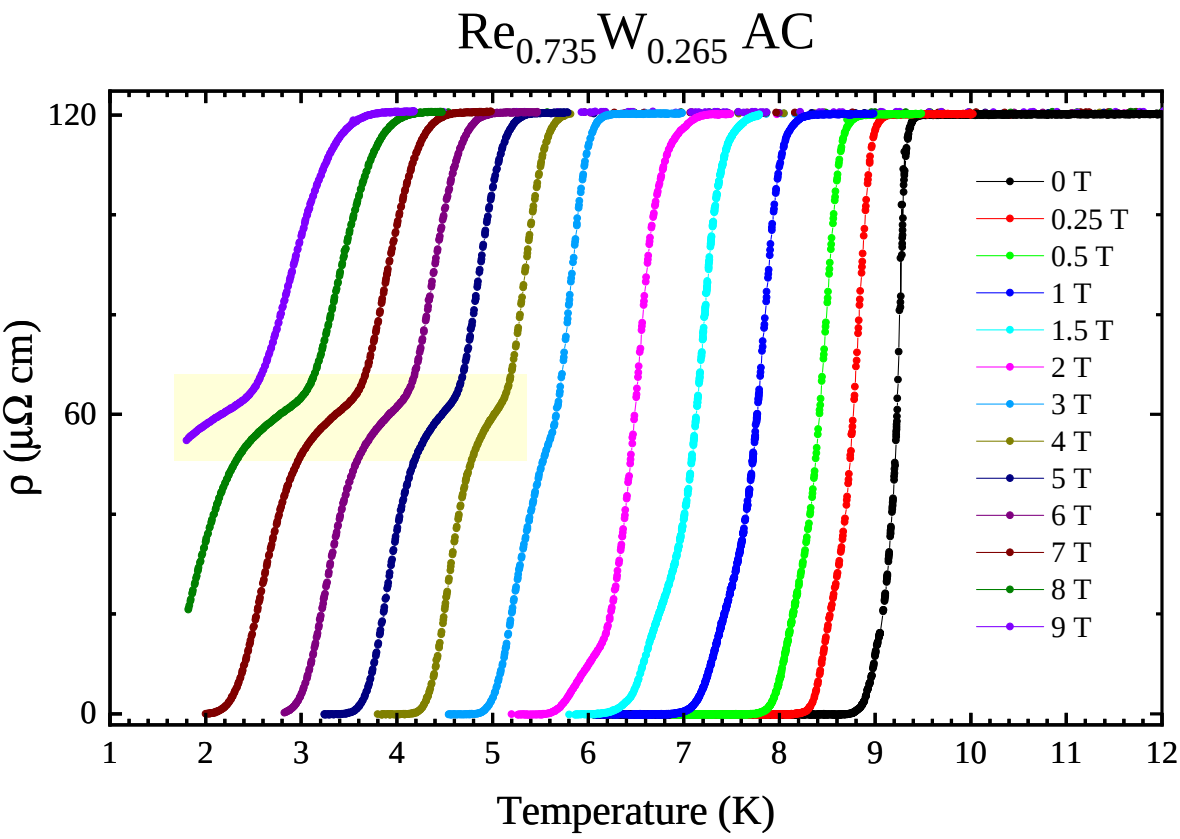

Figure 4.16: Temperature dependent resistivity $\rho(T, H)$ of the as cast $Re_{0.735}W_{0.265}$ sample under various applied magnetic fields H. The A.C. excitation was 0.5 mA (J $\sim$ 250 mA cm^{-2}).

the normal state are represented by the dashed lines in Figure 4.17. A partial sharpening of the SC transitions develops in the presence of magnetic fields, becoming systematically less pronounced as the fields become stronger; this is clearly seen by comparing the top transition half (90-50% lines) to the bottom (10-50% lines) one. As a reference, the data obtained in the same sample in its AC form is also presented in the bottom panel of the Figure 4.17. In this case, the magnetic field dependence of the ρ drop exhibits slope changes close to the $0.9\rho_0$ line, in accordance with the aforementioned $Re_{0.735}W_{0.265}$ AC results.

The same Re_3W samples have also been measured by ramping the magnetic field at fixed temperatures, but using A.C. excitations about 20 times smaller than the R vs T described above. These isothermal magneto-resistance curves are exhibited in Figure 4.18, with the minimum temperature of measurement being as low as 0.1 K. As of the R vs T data, sharper sections of the SC transitions occur in the low resistance region of the curves. This is particularly clear in the T = 3 K curve (blue), where the data points have a much lower density in the $\rho < 40$ $\mu\Omega$ cm region than in the rest of the transition. In the lower temperature curves, however, the sharpening

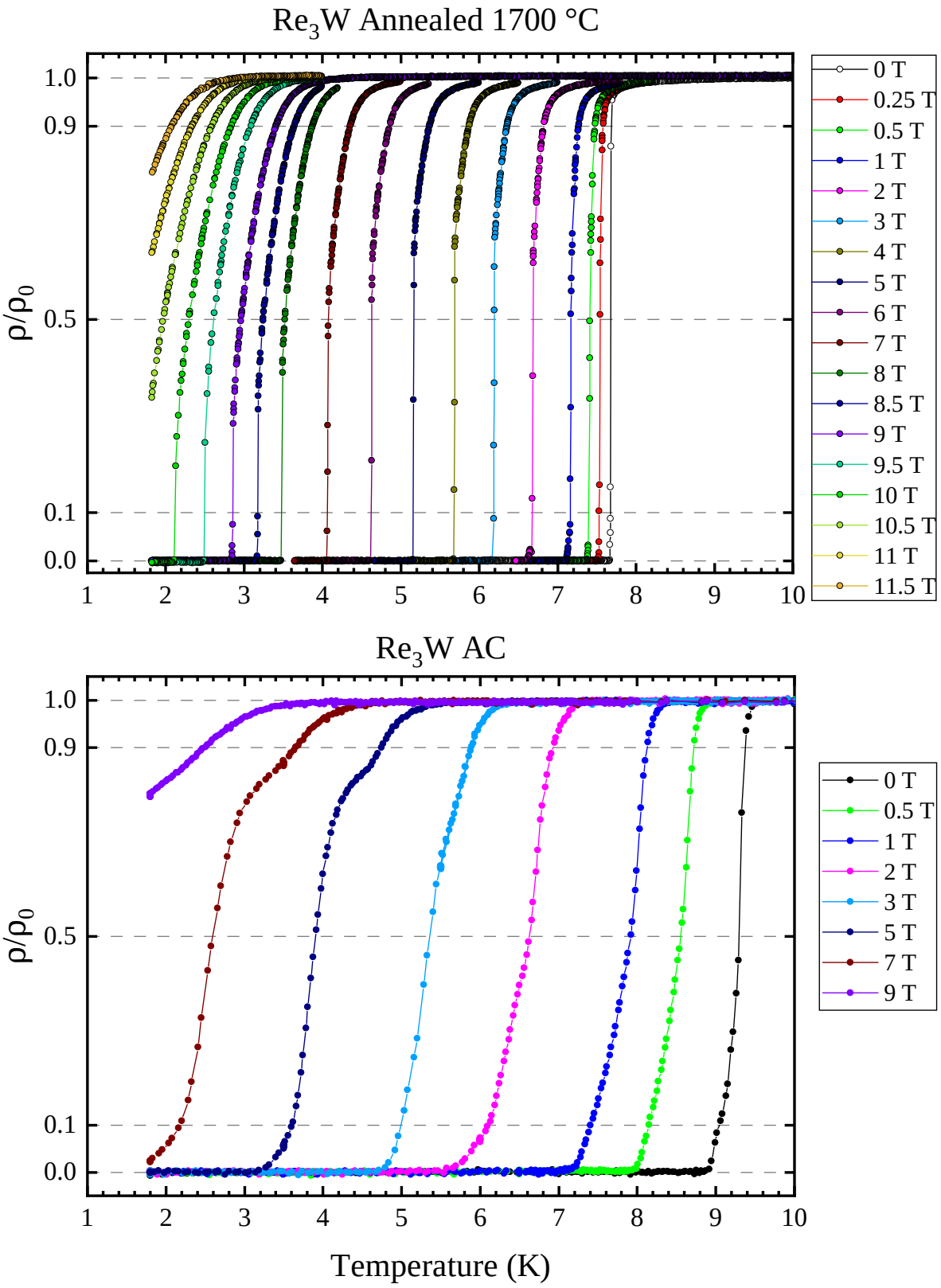

Figure 4.17: Magnetic field dependence of the resistive superconducting transition of $Re_{0.75}W_{0.25}$ material in its both as-cast and annealed forms. The resistivity values were normalized by the residual resistivity ρ_0 obtained slightly above the zero-field transition. The A.C. excitation current used here was 0.5 mA ($J_{AC} \sim 100$ and 55 mA cm^{-2} for the AC and annealed samples, respectively).

trend evolves to a two step transition as the temperature is decreased down to T = 100 mK. Each step has a distinct T-dependence: in the first transition step, below the ρ(H) = 60 $\mu\Omega$ cm solid line, no significant broadening occurs in response to temperature changes, while the second step slowly leans toward a plateau as the temperature decreases. In the lowest temperatures curves, $\rho(H)$ remains almost constant in the plateau before rising again toward the normal state resistance.

The two step transition is not an artifact of the measurement related to some temperature stability issue; the magnetic field ramp was slow enough (10 Oe/s) to ensure a very stable sample temperature, monitored during the whole experiment and better than 1% at the lowest temperature of 100 mK. In fact, the Re_3W ρ vs H curves obtained in temperatures lower than 1 K are very similar in shape to the ρ vs T curves presented in Figure 4.16. Nonetheless, the latter curves are believed to be related to two superconducting phases while all of the annealed Re_3W results strongly suggest a single α-Mn phase specimen.

Usually, a resistive two-step SC transition in single phase specimens might be related to thermal fluctuations of the order parameter, and the first and second steps would be associated to the coherent motion and annihilation of the Cooper pairs, respectively. This view would result from a granular superconductor, with a given local superconducting volume being independent from the remaining of the sample's volume upon entering the superconducting state. As the annealed Re_3W sample is proven be homogeneous, single phase material, its high degree of disorder could, in principle, induce these incoherent superconducting volumes within the material. In spite of that, the development of a resistance plateau only at very low temperatures can not be described by this picture.

To the best of our knowledge, similar evolution of the ρ(H,T) curves has not been reported in the literature yet. However, the peak effect, discussed in more detail in section 4.3.3, is a key feature to consider in this context. As the A.C. drive current (50 μA) was lowered to its minimum level in the $\rho(H)$ measurements, it is possible that some feature related to the peak effect would only arise in the low temperature and high field region — as it is the case of the resistance plateau. Additionally, in these low temperature ranges, other types of vortex dynamics could appear as well, such as the quantum vortex tunneling in the exotic two-dimensional

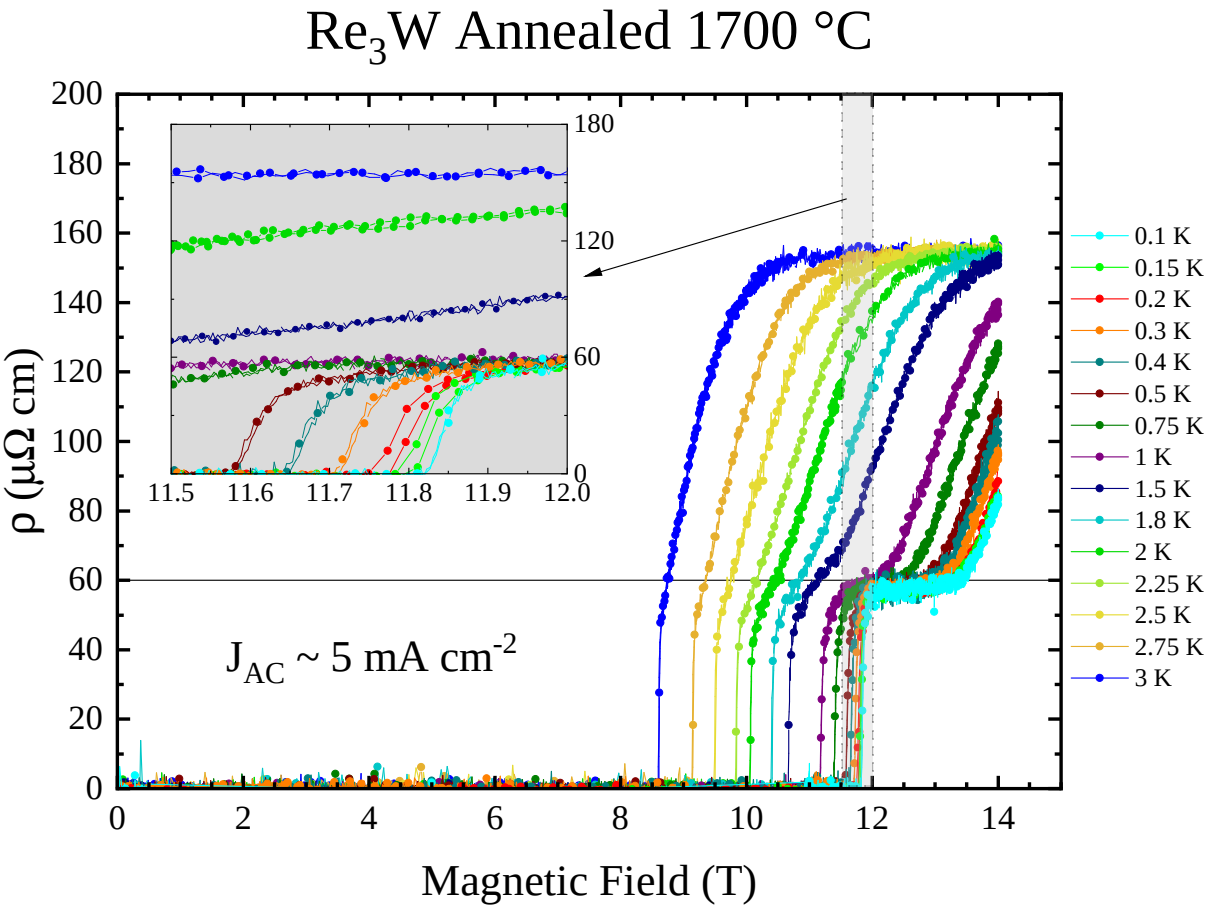

Figure 4.18: Re_3W magnetic field dependent resistivity measured at low temperatures with the dilution refrigerator. The isothermal curves at the lowest temperatures were obtained by using a low level of the A.C. excitation, in order to produce a voltage signal just above the measurement sensitivity.

materials called “anomalous metals” [163–165].

More usual, conventional SC to normal transitions are seen in the magneto-resistance curves of the annealed $Re_3Nb_{0.5}W_{0.5}$ sample. Shown in Figure 4.19 are the low temperatures $\rho(H)$ curves obtained with low A.C. drive. This material does not exhibits two-step transition or a discontinuous change in $d\rho/dH$ even at the lowest temperature measured. Instead, increasing the magnetic field strength leads to a normal state in a more ordinary way. Among the few samples studied in low temperatures (T < 1.8 K) and high magnetic fields (up to 14 T), only the annealed Re_3W displayed the two step transition discussed here.

On the magnetic field dependent specific heat curves C_p(T,H), two representative data are exhibited in Figure 4.20. Clear discontinuities are noted in all curves under magnetic fields up to 9 Tesla, being possible to calculate the critical temperatures in each field value by employing the entropy conservation construction — represented again by the light yellow areas in the 9 T

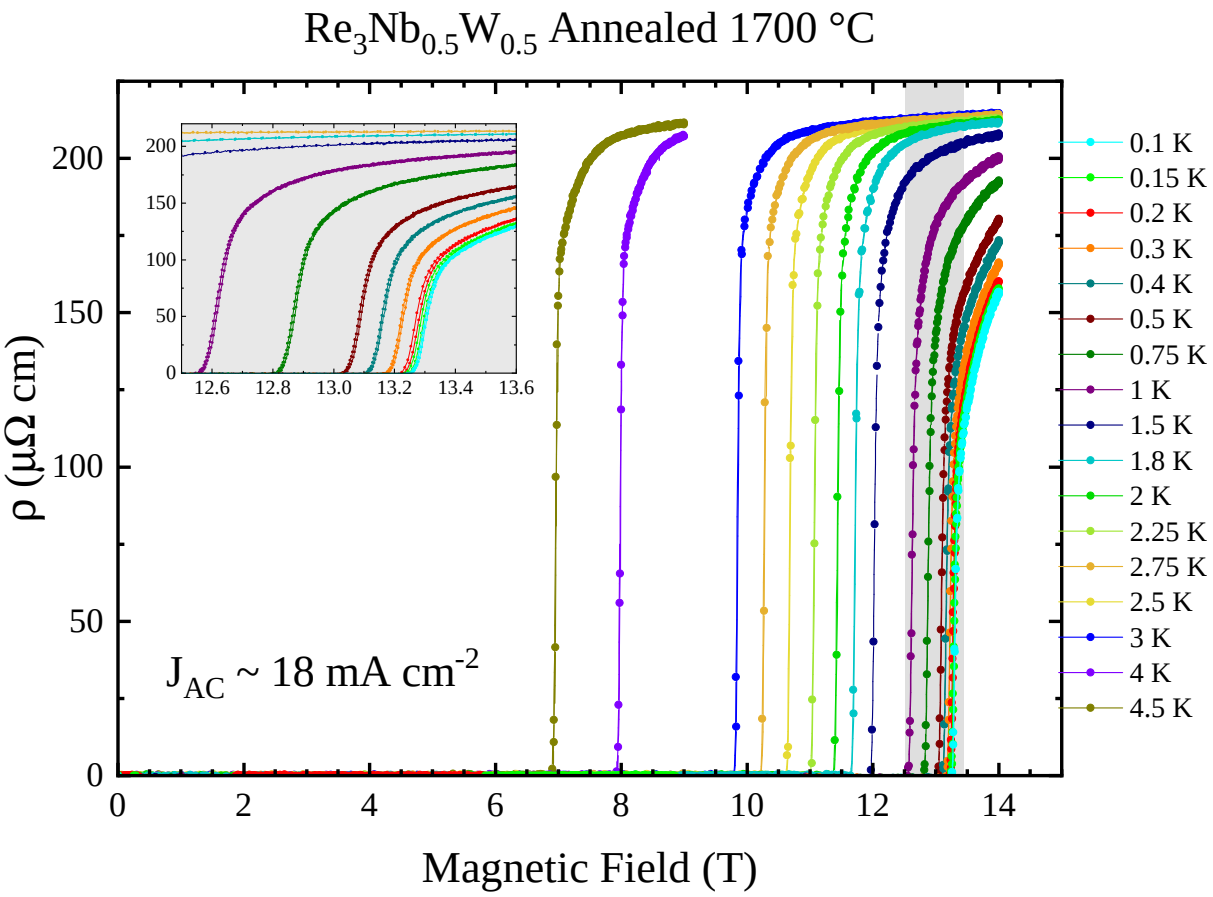

Figure 4.19: Isothermal magneto-transport data of the annealed $Re_3Nb_{0.5}W_{0.5}$ sample at low temperatures.

curves in both set of data.

A prominent peak-like feature is noted on the final stage of the specific heat jumps and is marked by the arrows in Figure 4.20. In comparison with the solid solutions results, the feature seems to be more pronounced in single phase Re-W samples. According to Lortz *et al.* [121], very similar peaks arising in Nb_3Sn would be related to thermal fluctuations due to its intermediate value of the Ginzburg number $G_i \sim 10^{-7}$ [126]. In that case, G_i is not so small as the ones observed in conventional low T_C superconductors but also not as large as those reported in high-T_C superconductors. In fact, this is also the case for the Re_3M samples, whose G_i is of order of $\sim 10^{-7}$, and thermal fluctuations could lead to the small peaks seen near the critical temperatures. The calculation of G_i in Re_3M materials is postponed to the section 4.3.3 and its results are presented in tables 4.6 and 4.7. Another mechanism that would lead to a peak close to the superconducting jump is associated with type-I superconductivity, whereas

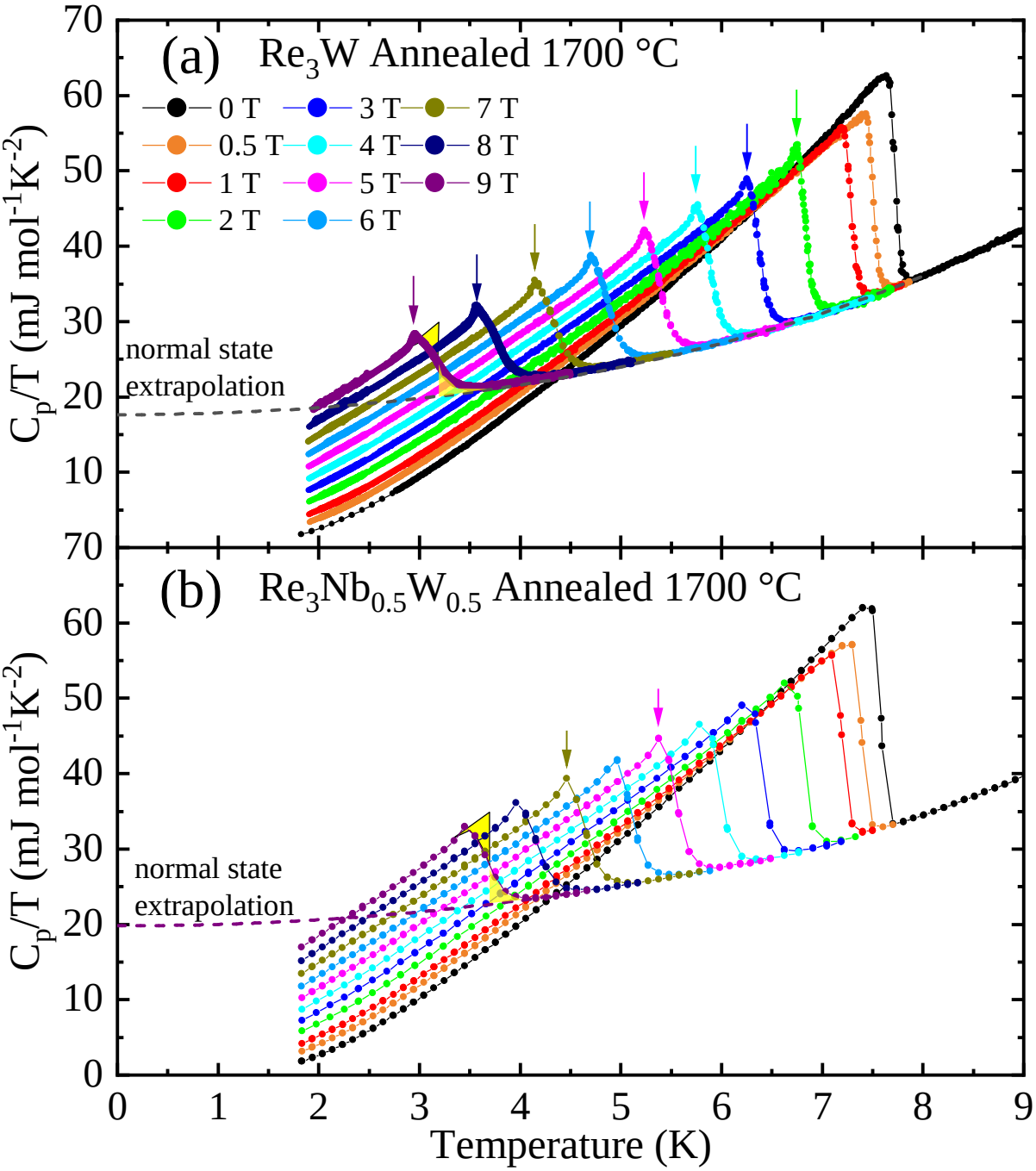

Figure 4.20: Magnetic field and temperature dependence of the total specific heat of the annealed (a) Re_3W and (b) $Re_3Nb_{0.5}W_{0.5}$ samples.

the latent heat could induce a specific heat peak [166]; a hypothesis of type-I SC in our samples is not considered, as it strongly opposes the results obtained in D.C. or A.C. magnetization measurements — i.e., large difference between ZFC and FC signals, deviation of the Meissner state in very low fields on M(H) curves, and sizable out-of-phase component of $\chi_{A.C.}$.

Specific heat measurements using the dilution refrigerator probe have also been conducted by sweeping the temperature while maintaining a fixed magnetic field. These data could, in

principle, yield information on the superconducting gap symmetry [167, 168], as briefly mentioned in section 2.3 (see page 34). Shown in Figure 4.21 are the low temperature SC specific heat results obtained for the $Re_3Nb_{0.5}W_{0.5}$ and $Re_3Ta_{0.5}W_{0.5}$ samples in their AC form. Deep in the superconducting state, a drastic enhancement in the C_{es} magnitude is clearly seen already at the field strength of 1 Tesla, being more than ten times larger than the zero field C_{es} data.

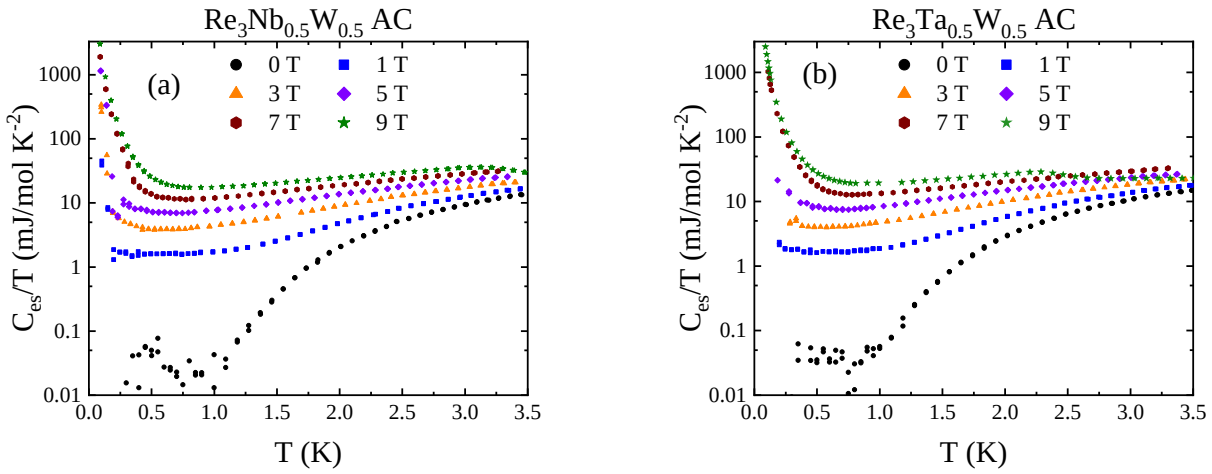

Figure 4.21: Magnetic field dependence of the low temperature electronic specific heat data obtained with the dilution refrigerator probe. Data shown are from the as cast solid solutions (a) $Re_3Nb_{0.5}W_{0.5}$ and (b) $Re_3Ta_{0.5}W_{0.5}$ samples.

In Figure 4.21, the magnitude of $C_{es}T^{-1}$ rises rapidly at the lowest temperatures, with the rate of change depending on the particular magnetic field strength. In the H = 9 T curves, the $C_{es}T^{-1}$ values have almost three orders of magnitude of enhancement during the measurements. These ingredients suggest a multi-level Schottky anomaly, probably induced by the interaction of the rhenium nuclear moments in the Re_3M samples and its crystal field. Accordingly, the results exhibited in Figure 4.21 are very similar to the pure rhenium measurements, both from the literature [169, 170] and from a pure sample. This nuclear contribution in the specific heat has also been reported in other rhenium-rich samples [37, 56, 171]. As a reliable discussion of the gap symmetry in those samples requires the precise value of the residual quasi-particle density of states in each magnetic field at the lowest temperature, the Schottky anomaly prevent us from gaining any information on the superconducting symmetry with the present set of data — even if one tries to subtract the nuclear contribution using a suitable data fitting procedure.

Magnetic field dependent thermal conductivity κ(T) has also been studied during this work. The overall behavior of κ(H,T) is very similar to the zero field curves, with the bump in κ(T)

occurring for a few NCS samples. The subtraction of the normal state contribution from the total κ(T) leads to the $\Delta\kappa(T)$ presented in Figure 4.22 for the $Re_3Ta_{0.5}W_{0.5}$ AC sample under various magnetic fields. The broad peaks seen in all curves seem to be related to the competition between the phononic and quasi-particle contributions, as discussed in the zero field data κ(T) previously. But this competition is not expected to yield the approximately field independent κ(T) maxima represented by the dashed line in Figure 4.22, as the magnetic field certainly changes the relative weight of the quasi-particle contribution at a given temperature.

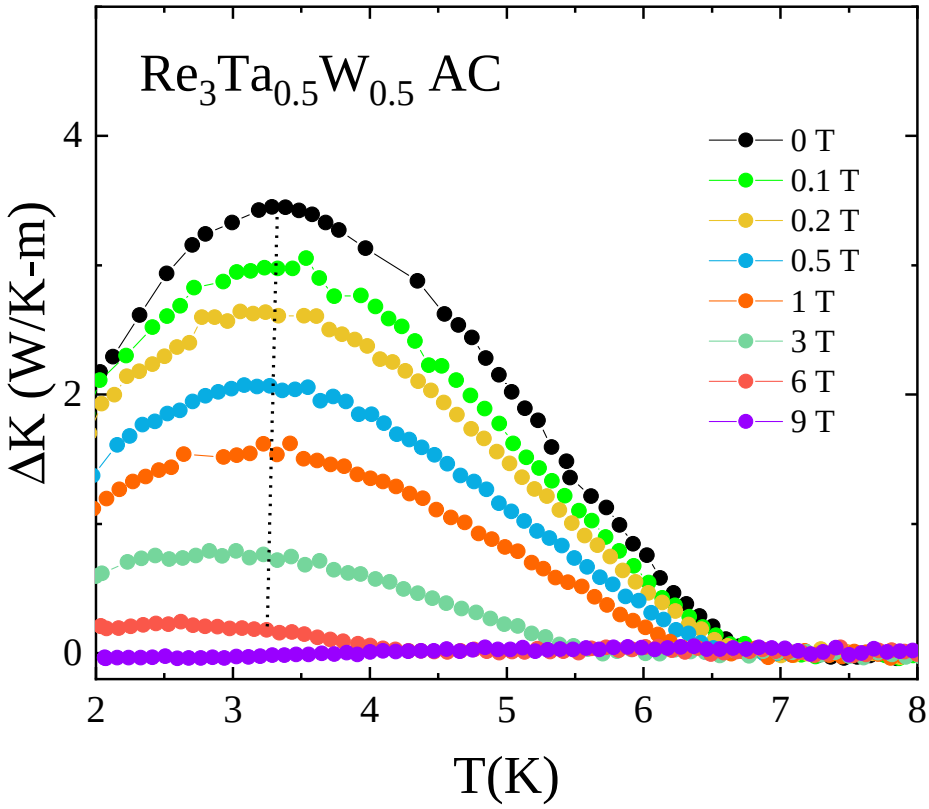

Figure 4.22: Temperature dependence of the superconducting thermal conductivity ΔK (T) under various external magnetic fields.

4.3.1 D.C. Magnetization M(H)

4.3.1.1 Flux jumps

The aim of this section embraces the discussion of the magnetic properties of the Re_3M samples, focusing on the magnetic field dependent D.C. magnetization M(H) measurements. One of the main magnetic properties is related to the flux jump phenomena. In this way, the mag-

netic properties of the annealed Re-W samples are compared with those of their respective AC forms, as the occurrence of flux jumps in M(H) data seem to be correlated with multiphase specimens. Moreover, these magneto-thermal instabilities are closely related to the nature of the flux pinning leading to the critical state in hard type-II superconductors. Thus, it is believed that the results discussed in this section, combined with those discussed in section 4.3.3, point to a not so usual flux dynamics in this set of samples.

Relaxation of the metastable critical state through a jump of the magnetic flux, $\Delta\Phi_{av}$, is described by a combination of Maxwell's and the heat balance equations [98]. Often, jumps occur during a magnetic field sweep and are avalanche-like phenomena, meaning that a sizable reduction of the diamagnetic signal could suddenly occur while the external magnetic field is being ramped (up or down) — as the avalanche embraces a partial, localized portion of the sample's volume, only a reduction of the superconducting magnetic signal is observed.

Shown in Figure 4.23 are the isothermal magnetization curves of the AC and annealed forms of $Re_{0.727}W_{0.273}$, representative of all Re-W materials with Re:W ratio close to 3:1. The data of the AC sample at T = 2 K (black points) have many discontinuities in the low field region ($\sim -0.7 \leq \mu_0 H \leq 0.7$ T), which are the flux jumps, before reaching a more stable curve at higher magnetic fields; the jumps occur in any direction of the field sweep. Conversely, the NCS annealed samples do not shown any discontinuity in the whole field range, as depicted in Figure 4.23(b).

In the AC sample, there is not a single flux jump at temperatures closer to T_C (see the magenta curve at 7 K in Figure 4.23(a)), suggesting that both phases within the material must be in their superconducting state for the triggering of the magneto-thermal instabilities in the low field region. In fact, flux jumps in the AC $Re_{0.727}W_{0.273}$ were found to first appear in temperatures below 6 K. For comparison, the 7 K curve of the annealed sample is also shown in more detail at the inset of Figure 4.23(b), having essentially the same field dependence as the 2 K curve.

In addition to the flux jumps occurrence, a marked contrast between the AC and annealed M(H) results is noted in the reversibility of the curves: at T = 2 K, the magnetization of the annealed sample remains reversible from $\sim$ 0.6 T up to 9 T while the magnetic reversibility of

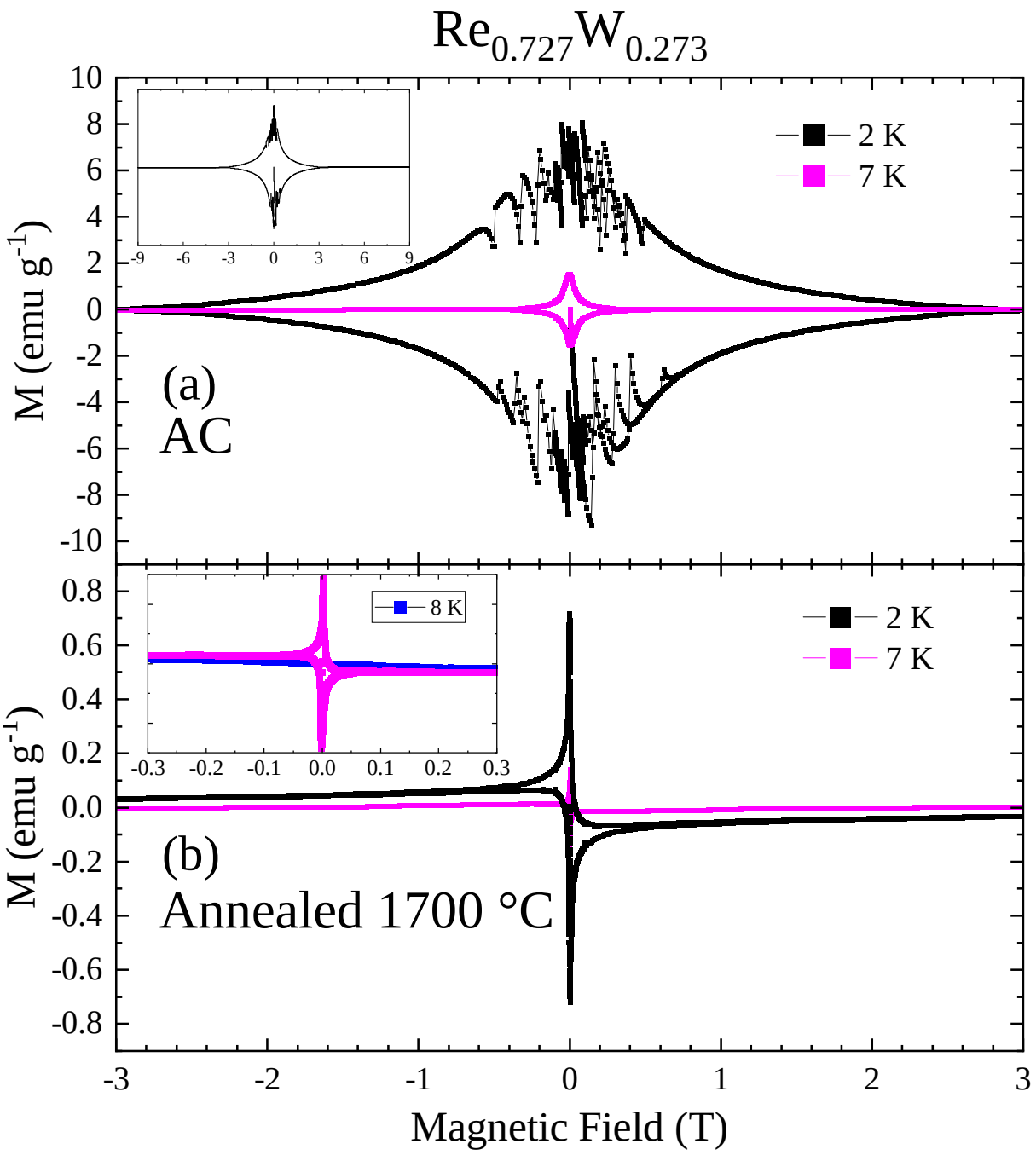

Figure 4.23: Isothermal magnetization curves of the as cast (a) and annealed (b) $Re_{0.727}W_{0.273}$ samples obtained by ramping the magnetic field with a sweep rate of 50 Oe/s.

the AC sample only begins at fields larger than 3.5 T. Such a difference in M(H) loops points to a scenario where the flux pinning is stronger in the AC sample, as already expected from its inherent inhomogeneities. Therefore, the sudden redistribution of the magnetic flux line lattice during the avalanche process is more likely to occur in less pure samples, with stronger flux pinning.

To test the dynamical features of the flux jumps instabilities, the measurements at the lowest

temperature (2 K) have been repeated using slower field sweep rates (dH/dt). Then, Figure 4.24 compares the 2 K magnetization curves obtained by sweeping up and down the magnetic field using dH/dt = 10 and 50 Oe s^{-1}. Flux jumps were still observed when using lower rates, but they are slightly shifted to higher magnetic fields and decrease in number over the entire M-H scan. These rate-dependent flux jumps seem to corroborate the magneto-thermal instability hypothesis.

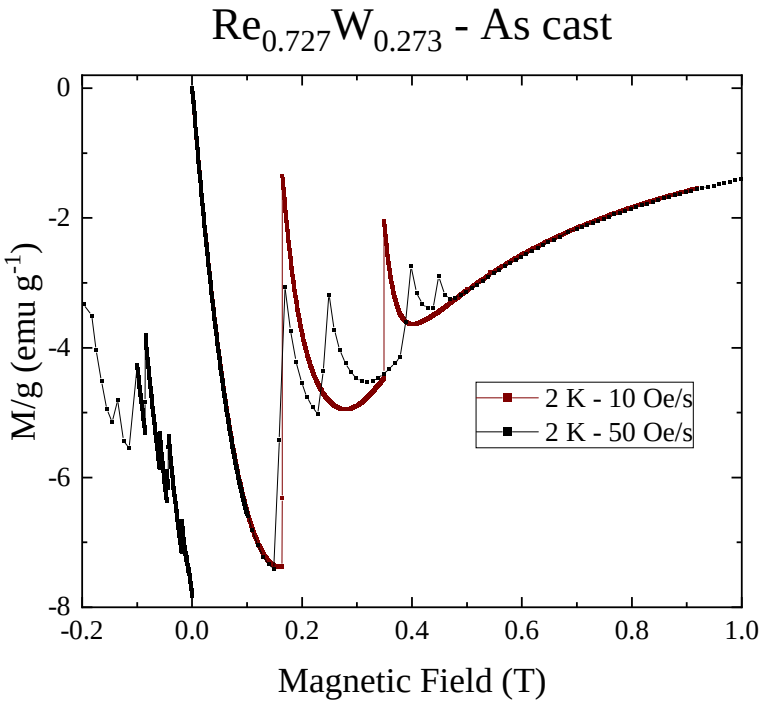

Figure 4.24: Magnetization curves M(H) at T = 2 K with two different sweeping rates.

It is noteworthy that all the magnetization M(H) results of the annealed solid solutions samples in the Re-Ta-W and Re-Nb-W systems did not exhibit any flux jump and have very similar curves to the ones shown in Figure 4.23(b). However, flux jumps were also observed in the $Re_3Ta_{0.25}W_{0.75}$ AC sample, which was shown to have a tiny amount of a secondary phase. In this way, the absence of jumps in M(H) scans could be considered as an indicator of the overall sample purity and sample composition.

4.3.1.2 Critical Fields

It is common to estimate the lower critical field $H_{c1}(T)$ from the magnetization data by the initial portions of the M(H) scans. This is usually made by calculating the deviation ΔM of the low

field M(H) data from the ideal diamagnetic linear contribution of M(H) when the sample is in the purely Meissner state. Therefore, the magnetic field of the first ΔM(H) point exceeding the threshold value set as 0.05 emu g^{-1} was considered to be the H_{c1}(T) at a given temperature.

The ideal linear contribution M_{ideal}(H) is extrapolated by fitting the M(H) data in the lowest field region. Hence, in order to have enough experimental points in this region, the measurements have been conducted by ramping the magnetic field in the $0 \leq H \leq 500$ Oe range using a field rate as low as 3 Oe/s. These curves have been used to extract the M_{ideal}(H) data, giving the means to calculate $\Delta M = M(H) - M_{ideal}(H)$ at each temperature.

Using the annealed Re_3W as an example, the results of the linear fitting and their respective H_{c1}(T) values are shown in Figure 4.25. The method results in partially consistent H_{c1}(T) values throughout the entire temperature range when deviations of $\sim$ 15 Oe are included, as indicated by the scattered data in Figure 4.25(b). This error in H arises both from the remnant magnetization of a 9 T superconducting magnet and the threshold value used in ΔM. The H_{c1}(T) data fit to the mean field model yields the blue line in Figure 4.25(b), leading to a satisfactory agreement between the data exhibited here and those from study conducted by Biswas *et al.* [40] (dashed light blue line).

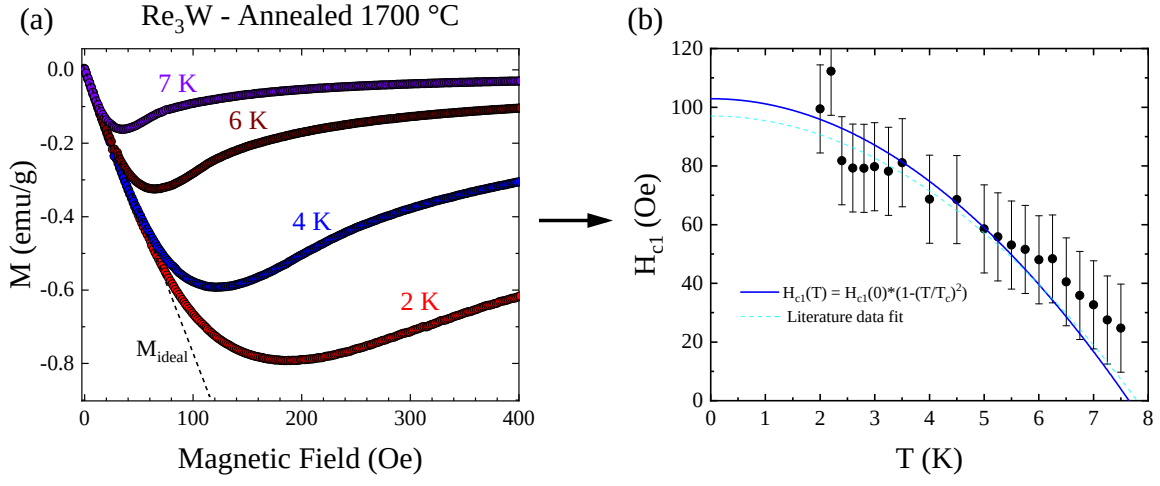

Figure 4.25: (a) Low-field magnetization curves of the annealed Re_3W sample at selected temperatures (2, 4, 6, and 7 K). (b) Lower critical field H_{c1}(T) obtained from various M(H) curves.

On the other hand, the estimates of the upper critical field H_{c2}(T) from the magnetization data in the annealed samples are conducted as follows: first, the paramagnetic region of M(H) curve is identified by comparing its slope with a M(H) curve obtained at $T > T_C$; second, two

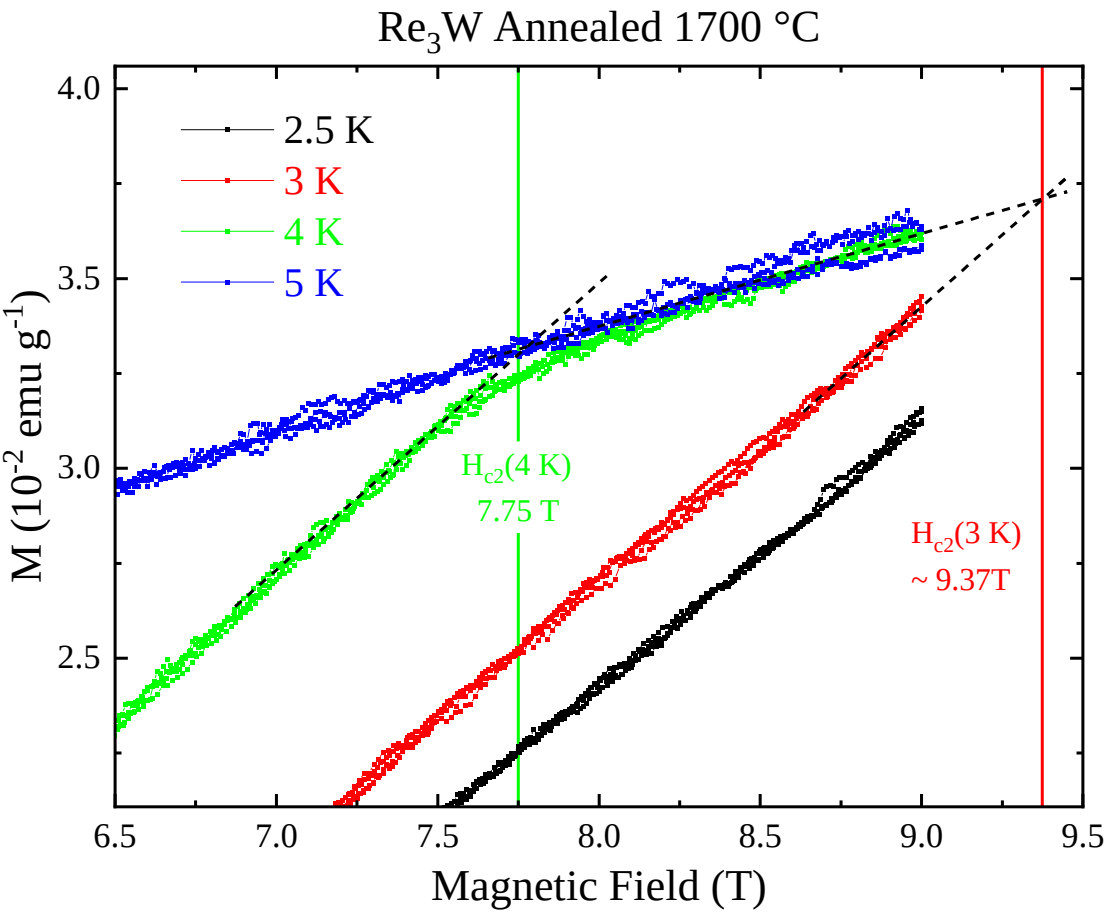

Figure 4.26: Examples of the upper critical field estimates through the isothermal M(H) data.

straight lines are used to extend both the SC and normal states; the last step is to find the field where the two extrapolated lines cross, resulting in the H_{c2}(T) value. Figure 4.26 exhibits an example of this procedure in two M(H) curves of the annealed Re_3W sample. However, the estimated H_{c2}(3 K) value is slightly less reliable than the higher temperature ones, since it was not possible to reach the normal state at temperatures T = 3 K or below. As shown in the next section, the values of H_{c2}(T) obtained in M(H) curves are in good agreement with those extracted from resistivity and specific heat measurements.

4.3.2 Superconducting phase diagrams

The phase diagrams discussed in this section have mainly been built by setting the critical field (or temperature) through the 50% resistance drop criterion in the resistivity data. This criterion has been largely used to extract the averaged mean field description of H_{c2}(T). When considering annealed samples, the $H_{c2}(T)$ (or $T_c(H)$) data obtained through this method almost overlap with those results from specific heat or magnetization; one exception to that is the annealed Re_3Nb results presented in Figure 4.11. In contrast, the estimate of the phase boundary by the 50% resistance drop in multi-phase specimens, which mainly are AC materials, is somewhat dubious as it is not possible to ensure which superconducting phase is first leading the sample to the zero resistance state. This is due to the percolative nature of the resistive transition, in which a small amount of a superconducting phase within a metallic matrix can drive the whole system to the zero resistance state.

Regardless of those caveats in the AC Re-W results, the 50% resistance drop has still been used to roughly calculate their H_{c2} values. From the joint analysis of H_{c2}(T) among all Re-W AC samples, it is argued that the superconducting phase diagrams of some AC Re-W materials are composed of two contributions. The hypothesis is that these samples are composed of $h.c.p$ and σ-like structures, which are both superconducting phases.

Shown in Figure 4.27 are the estimated $\mu_0 H_{c2}$ values for the $Re_{0.727}W_{0.273}$, $Re_{0.90}W_{0.10}$, and $Re_{0.50}W_{0.50}$ as cast samples (blue circles, green triangles, and orange circles, respectively), delineating their SC-normal boundary lines. In a two-phase material picture, the abrupt slope change occurring in the $Re_{0.727}W_{0.273}$ data at $H^* \sim 1.5$ T, not present in the other curves, probably signalizes that T_C is almost the same in both phases at this particular magnetic field; therefore, H^* marks a crossover behavior, where the lower T_C phase at low fields becomes the phase with the higher T_C in fields above H^*. Such a description seems to be corroborated by the results obtained in the $h.c.p$ ($Re_{0.90}W_{0.10}$) and σ ($Re_{0.50}W_{0.50}$) phases prototypes: the $h.c.p$ phase has the higher T_C ($h.c.p.$ = 7.52, σ = 6.56 K) but also a smaller slope $|dH/dT_c|$ ($h.c.p. \approx$ 0.6 and $\sigma \approx 0.8$ T K^{-1}) value, resulting in a crossing of the line boundaries taking place at a particular field $H^* \sim 2$ T.

According to that description, in a generic material composed of both $Re_{0.90}W_{0.10}$ and

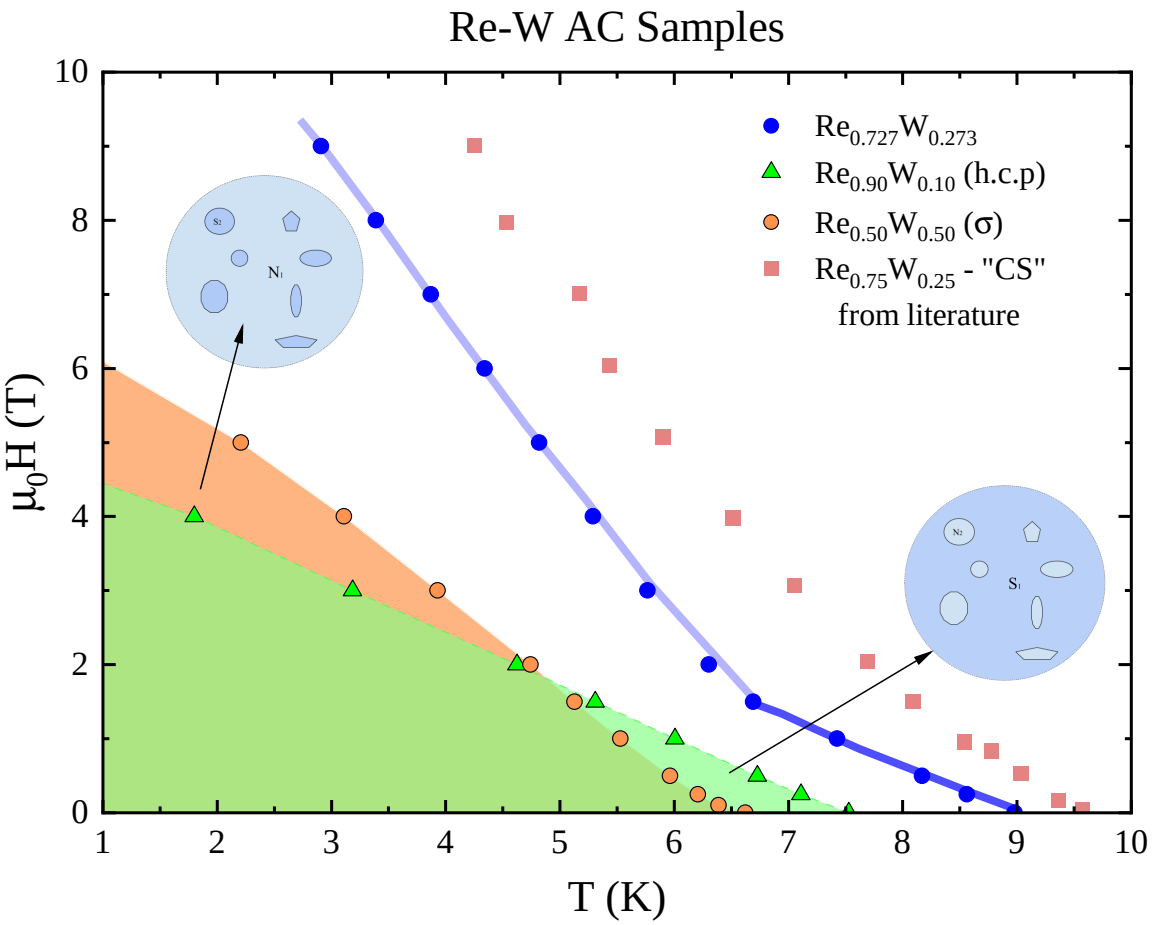

Figure 4.27: SC phase diagrams of as cast $Re_{0.90}W_{0.10}$, $Re_{0.5}W_{0.5}$, and $Re_{0.727}W_{0.273}$ samples. The experimental points of the centrosymmetric, as cast Re_3W material were retrieved from reference 40.

$Re_{0.50}W_{0.50}$ phases, there will be two regions in the phase diagram where one of the superconducting phases has been suppressed by the external field while the other is still superconducting; these regions are highlighted in light green and orange in Figure 4.27. Additionally, simplistic representations of each region's volume are illustrated in the figure, indicated by the black arrows. At these regions, the Josephson or proximity effect coupling between the SC islands probably occurs and, depending on the particular micro-structure and relative volume fractions, causes a resistance plateau in the R vs T data [172, 173], much like what has been exhibited in Figure 4.16. Regarding the $Re_{0.727}W_{0.273}$ sample, it still is not evident which of its phase has the higher T_C, since both $h.c.p$ and σ phases have a particular composition ($Re_{0.82}W_{0.18}$ and $Re_{0.67}W_{0.33}$, respectively) with T_c as high as ~ 9 K.

Also shown in Figure 4.27 is the published data of a Re_3W AC specimen (faded red squares), which is described to be a single ($h.c.p.$) phase material [40]. By comparing these results with

the present study, it is suggested that the upward curvature of the H_{c2}(T) near T_C = 9.6 K could be a hint of the phase coexistence. Nonetheless, instead of having an abrupt slope change in the $H_{c2}(T)$ line, the slope of their data (as well as in other samples in this study) seems to be affected differently by the field; when compared to the blue curve in Figure 4.27, the slope evolves more gradually from milder to steeper behaviors as the reduced temperature is diminished. This picture can be induced by a secondary phase that has a minor SC volume fraction.

Despite being single phase materials, some NCS samples have shown unusual low temperature trends in the phase diagrams, specially the annealed parent compounds Re_3W and Re_3Ta. On the other hand, the $Re_3Nb_{0.5}W_{0.5}$ material indicates a more conventional phase diagram in the low T limit. The diagrams of the parent compounds Re_3W and Re_3Ta are exhibited in Figure 4.28 while the results of the solid solutions $Re_3Nb_{0.5}W_{0.5}$ and $Re_3Ta_xW_{1-x}$ are shown in Figure 4.28. In the following, their individual features are described separately.

The estimated upper critical field H_{c2} boundary line of the Re_3W annealed sample is shown in Figure 4.28(a), whose data points have been extracted from the electrical resistance, magnetization, and specific heat measurements. The results in the various experiments are in good agreement among each other, indicating fairly similar field dependence of the superconducting transition. This converging nature of the H_{c2} results reinforces the bulk character of the SC and is commonly observed in all the (single-phase) NCS Re-based samples but it is only shown here for the sample Re_3W as an example. Moreover, there is also internal consistency in the H_{c2} values obtained both from ρ vs T and ρ vs H measurements, represented by the circles and square data points, respectively.

In order to extract the upper critical field at zero temperature $H_{c2}(0)$ of the NCS Re_3W, two models have been used to fit the H_{c2}(T) data : the Werthamer-Helfand-Hohenberg (WHH) method and the Ginzburg-Landau (GL) equation 2.7 (see pages 45 and 21, respectively). Regarding the WHH model, its H_{c2}(T) expression has three variables (section 2.5): the Maki parameter α_M, the spin-orbit scattering parameter λ_{SO}, and the gradient at T_c. Using the initial slope and the asymptotic limit T $\rightarrow$ 0 of the WHH expression results in an approximate value of the orbital limiting field $H_{c2}^{orb}(0) = 0.693\, T_c\, |dH/dT_c|_{T_c}$ in dirty superconductors. Then, the Maki parameter can be calculated by the following relation:

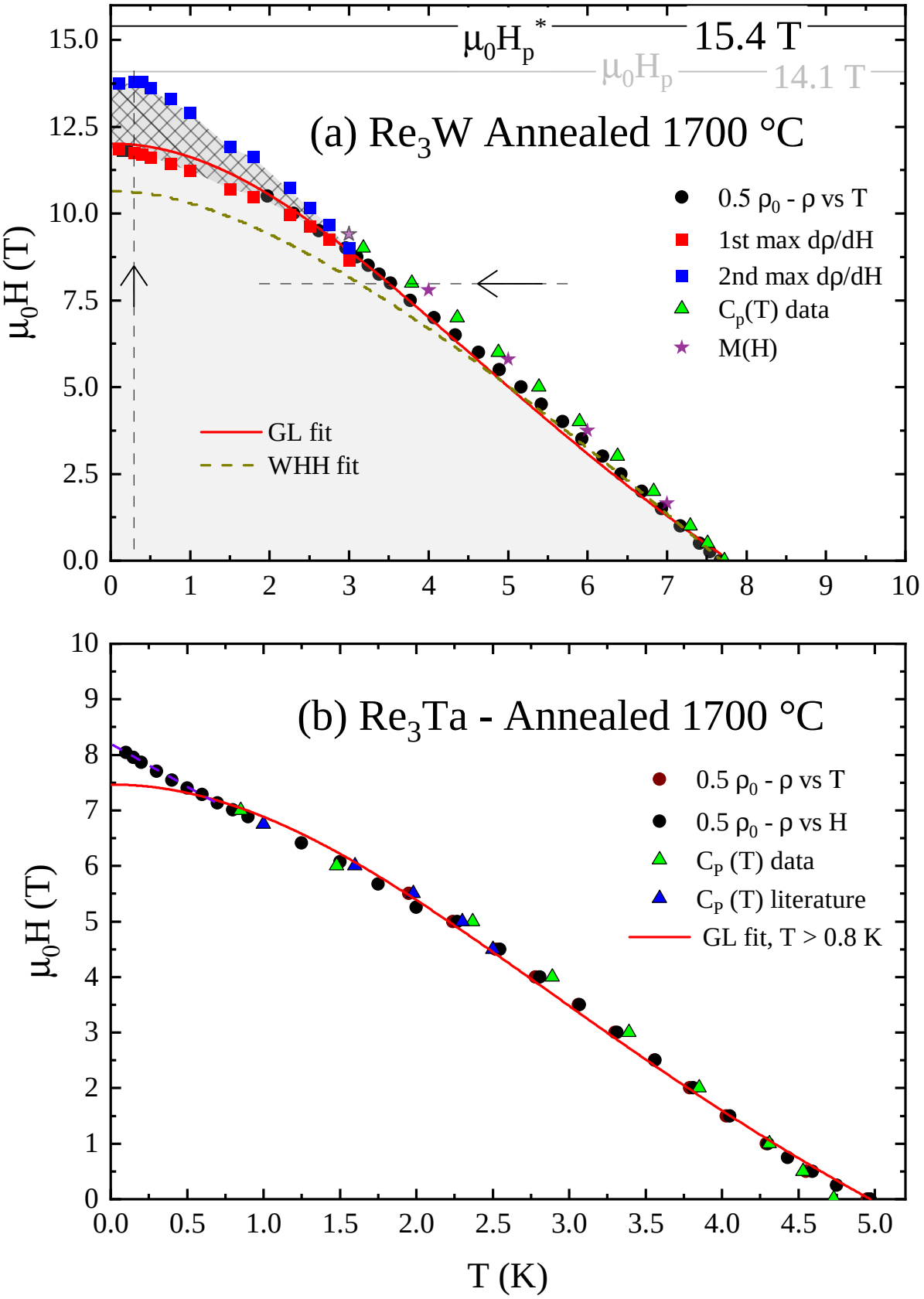

Figure 4.28: Phase diagrams of the annealed parent compounds.

$$\alpha_M = \sqrt{2}\frac{H_{c2}^{orb}(0)}{H_P^*(0)}, \tag{4.6}$$

with $H_P^*(0)$ being the renormalized Pauli limiting field due to the α-model used to fit the specific heat data (see Equation 2.53 in section 2.5); the horizontal lines in Figure 4.28(a) represent the Pauli limiting field before and after the renormalization. The value of α_M = 0.96 for the annealed Re_3W was obtained after using $\mu_0 H_{c2}^{orb}(0)$ = 10.6 T and $\mu_0 H_P^*(0)$ = 15.6 T, calculated with the values of T_C = 7.65 K, α = 1.93, and $|dH/dT_c|_{T_c} \simeq$ 2.0 T K^{-1}. Plugging this α_M value in the WHH equation, however, results in H_{c2}(T) curves that poorly describe the data, as it tended to underestimate the H_{c2}(T) experimental line when λ_{SO} is restrained to reasonable values lesser than 20.

The continuous and dashed (red and dark yellow) lines in Figure 4.28(a) are the results of best fitting procedure using GL and WHH methods, respectively. By comparing these results to the experimental data, the GL fit is considerably better suited to extrapolate the data in the T $\rightarrow$ 0 limit, leading to a $\mu_0 H_{c2}(0)$ of 12.0 T. The dashed line in Figure 4.28(a) clearly indicates that the WHH method, even when using α_M = 0 λ_{SO} = 0 to maximize its $H_{c2}(0)$ output, tends to underestimate the critical field at temperatures below 5 K. This inadequacy of the WHH model to account for the H_{c2}(T) line in the whole T range has already been observed in other Re-based NCS materials, such as some samples in the Re-Nb and Re-Ta systems [37, 56]. In contrast, the WHH method seemed reliable to describe the experimental data reasonably well in others Re-based NCS materials [58, 150], including the Re_3W material in Ref. 40.

There is a supposed difference between the H_{c2}(T) lines calculated through WHH method in this work and those present in Ref. 40. In our view, the data are equivalent and the difference is likely due to the T_C definition: while the authors of Ref. 40 used the onset T_C, the 50 % resistance drop criterion has been adopted here. These two types of T_C's lead to different values of the slope $|dH/dT_c|_{T_c}$ ($\simeq$ 2 and 2.3 T K^{-1}, $\approx$ 15 % of difference), and larger slopes cause stronger WHH $H_{c2}(0)$, better representing the experimental data. Nevertheless, as the fluctuation effects seem to be significant in the systems studied here, it is believed that the 50 % criterion is the proper way to analyze the mean-field behavior of H_{c2}(T), specially when fields at the same order of magnitude of $H_{c2}(0)$ are being used.

The key feature of the annealed Re_3W phase diagram seems to be at the low temperature and high field region. The ρ versus H results in this region suggest a splitting in the critical field line at $\approx$ 3 K; below this temperature, two peaks in the $d\rho/dH$ data are clearly resolved. Therefore, the temperature dependence of the peaks are shown by the red and blue squares in Figure 4.28(a). The hatched area between the two $d\rho/dH$ peaks is where the resistance plateau emerges, whose causes are currently under study and are possibly related to the peak effect phenomena otherwise absent in this particular sample. Moreover, quantum vortex tunneling has been suggested to induce a field quasi-independent resistance in some materials called "anomalous metals" [163, 165]; note, however, that this description is made for disordered bidimensional systems, in contrast with the bulk Re_3M samples studied here.

In the Re_3Ta case, whose phase diagram is shown in Figure 4.28(b), no splitting of the H_{c2}(T) line is observed, but another unusual feature emerges: a non-saturating, quasi-linear H_{c2}(T) at the lowest temperatures. Various situations could be related to this linear response, which has been observed in several families of SC materials [174–177], and some of them are briefly mentioned: (i) strong disorder; (ii) vortex lattice thermal fluctuations; and (iii) multiband superconductivity.

As far as (i) is concerned, Ren *et al.* suggest that strong disorder leads to the formation of superconducting "puddles", eventually resulting in quantum phase fluctuations, as observed in $AgSnSe_2$, a disordered 3D conventional superconductor [178]. Still in the strong disorder domain, (ii) is relevant in some amorphous indium-oxide films as the thermal fluctuations of the vortex-glass ground state give rise to a linear temperature dependence of H_{c2} (T) in the low T limit [179], where a quantum critical point (QCP) is believed to exist.

Alternatively to the disorder picture, the presence of multiple superconducting bands (iii) could, in principle, account for the finite slopes in H_{c2} (T) at low temperatures, as well as critical fields above the WHH predictions [88]. This picture has been discussed in the contexts of the two band superconductor $LuFe_3Si_5$ [180] and the Pauli-limited nickelates $Nd_{0.775}Sr_{0.225}NiO_2$ thin films [181].

Given the above scenarios, it is believed that, in the 3D Re_3M samples, the interplay of inherent disorder and unusual vortex dynamics could result in the linear behavior in Figure 4.28(b);

otherwise, the unusual feature in the Re_3Ta phase diagram could still be related to multiple superconducting bands, arising due to a particular Fermi level topology or even due to the NCS structure itself. Indeed, the quasi-linear temperature dependence of H_{c2} has also been observed in the NCS, strong spin-orbit coupled superconductor YPtBi [30, 182].

Qualitatively, the phase diagrams of the solid solutions are somewhat simpler than the parent compounds Re_3W and Re_3Ta and, consequently, the GL theory provides better description throughout the whole T range studied. An example of the solid solution samples is exhibited in Figure 4.29(a), whose resistance data could be obtained down to T = 100 mK. The trend toward H_{c2} saturation is more compelling in the $Re_3Nb_{0.5}W_{0.5}$ results, as the H_{c2} (T) slope progressively diminishes at low temperatures in a similar manner to what is expected from conventional superconductivity; yet, a reminiscent small, non-zero H_{c2} (T) slope is also noted in the experimental data below T = 1 K, as indicated by the dashed black line on top of the low T data.

Among all the samples studied here, the GL fit of the $Re_3Nb_{0.5}W_{0.5}$ data seems to be the most reliable one, as it could capture the overall shape of the experimental curve in this case. Disorder effects probably induce the $\mu_0 H_{c2}(0)$ enhancement from $\simeq$ 12 to $\simeq$ 13.7 T as the Nb substitution increases from x = 0.0 to 0.5 [85]. However, such proximity of $\mu_0 H_{c2}(0)$ to the renormalized Pauli field ($\mu_0 H_P^*(0) \simeq$ 15.5 T) may indicate a minor triplet component, although no other measurement supports this hypothesis. This is exactly the picture observed in the NCS, chiral superconductors $NbRh_2B_2$ and $TaRh_2B_2$: even though their $\mu_0 H_{c2}(0)$ values are substantially above the Pauli limit, all the remaining SC properties strongly indicate a conventional BCS scenario [183–185].

Lastly, Figure 4.29(b) shows a comparison of all phase diagrams built by the resistance data obtained in the Re-Ta-W system (for visual clarity, only T > 2 K data for the Re_3W are present in the figure). As the Ta content x is increased, the critical temperature gets lower and the $|dH/dT_c|_{T_c}$ slope becomes slightly steeper, achieving $\approx$ - 2.25 T K^{-1} in the $Re_3Ta_{0.5}W_{0.5}$ sample. These main features are also observed in the Re-Nb-W phase diagram (not shown). Then, the application of GL theory in the Re-(Ta,Nb)-W systems has led to the $H_{c2}(0)$ values shown in tables 4.6 and 4.7.

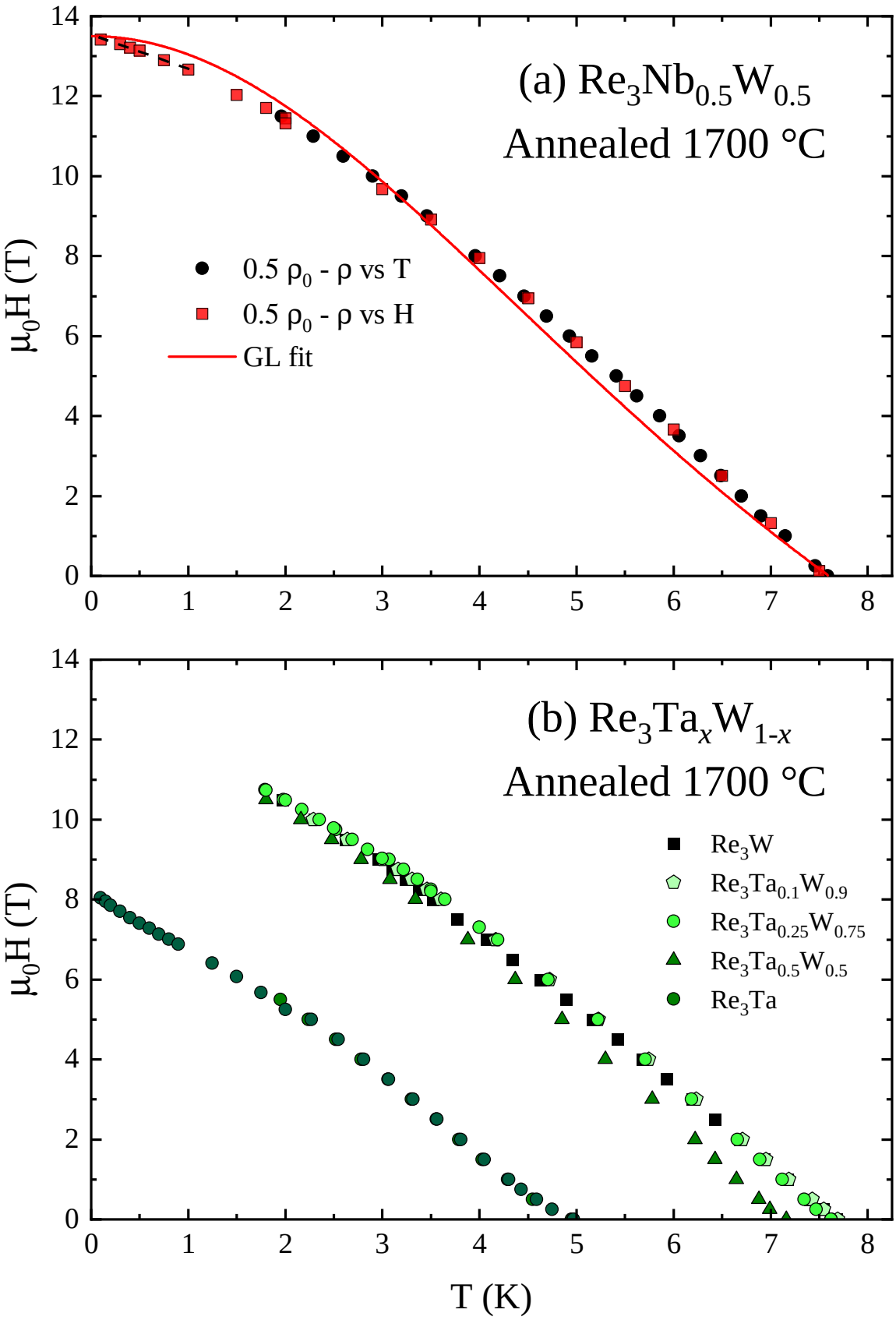

Figure 4.29: Phase diagrams of two solid solutions systems studied.

4.3.3 Peak effect

At the moment of writing this thesis, the PE superconducting phenomena are not completely understood; no agreement has been reached on the subject matter and some research programs are still pursuing the mechanism underlying the sudden critical current rise close to the H_{c2} boundary line in superconductors. In spite of lacking consensus on its nature, the PE emergence is certainly related to quenched disorder and thermal fluctuations [111], as briefly discussed in section 2.6.1.2 (see page 52). This interplay is, indeed, aligned with our findings: strong PE features were clearly observed in the solid solutions $Re_3(Ta,Nb)_xW_{1-x}$, where a high degree of disorder is expected due to the partial atomic substitution.

In a SC material in which both disorder and fluctuations effects are present, it is believed that the disorder potential is smoothed by thermal fluctuations, in addition to the flux creep enhancement due to fluctuations. In this scenario, both the quenched disorder and thermal fluctuations can be evaluated using the SC parameters: the characteristic lengths λ and ξ as well as the thermodynamic critical field H_c. Then, the ratio between the critical and depairing currents (J_C/J_0) is the most simply accessible phenomenological parameter describing the quenched disorder strength [101]. On the other hand, the strength of thermal fluctuations can be captured by the Ginzburg number G_i, defined as the ratio of thermal energy to the condensation energy associated with the coherence volume:

$$G_i = \frac{1}{2}\left(\frac{\mu_0 k_B T_C}{4\pi H_c^2(0)\xi^3}\right)^2 . \tag{4.7}$$

Under this circumstance, the PE might arise when a particularly optimal set of J_C/J_0 and G_i values is found in a given superconductor.

As shown in Table 4.3, the J_C/J_0 and G_i values of different kinds of SC materials are separated by orders of magnitude: while conventional, type-II low T_C (LTSC) materials usually have strong pinning ($J_C/J_0 \sim 10^{-1}$- 10^{-2}) and weak thermal fluctuations ($G_i \sim 10^{-8}$- 10^{-10}), the high temperature superconductors (HTSC) have weak pinning ($J_C/J_0 \sim 10^{-3}$) and large fluctuations ($G_i \sim 10^{-1}$ - 10^{-2}). Then, the LTSC and HTSC materials likely set the upper and lower bounds of the thermal fluctuation effects. Intermediate G_i values, in the $\sim 10^{-3}$ - 10^{-6}

range, have been observed in some low T_C materials, such as the $NbSe_2$ [120], as well as in MgB_2, and in the iron-based SC such as $Ba_{0.6}K_{0.4}Fe_2As_2$, and FeSe [186]. The G_i sorting of the SC materials in Table 4.3 places the NCS Re-based samples in an intermediate region, but closer to the LTSC side, where weak pinning forces dominate the flux flow dynamics. This seems to be consistent with the specific heat and magnetization results, being the small peak in C_p(T) and the rather low irreversible field in M(H) likely induced by thermal fluctuations in the Re_3M materials. A few others LTSC exhibiting the PE, such as $CeRu_2$ and $NbSe_2$, are also located in this intermediate region between the conventional LTSC and HTSC, implying that weak pinning coupled with non-negligible thermal fluctuations might be correlated with the PE occurrence.

Table 4.3: Quenched disorder and thermal fluctuations parameters for various types of superconducting materials.

Quantity	SC materials				
	LTSC	Re_3M	Re_6Hf [149]	2H-$NbSe_2$ [120]	HTSC
G_i	10^{-8}	10^{-7}	10^{-2}	10^{-4}	10^{-2}
$(J_C^M/J_0)^*$	10^{-1}	10^{-4}	—	10^{-6}	10^{-2}

To put the PE in the perspective of NCS materials, it has been proposed that unusual vortex states may appear within NCS SC materials [187–189], and these states could possibly introduce novel pinning phenomena when the time reversal symmetry is absent [190–193]. However, no clear correlation between the NCS structure and unusual vortex dynamics or states has experimentally been reported to the best of our knowledge; some recent experiments on nonreciprocal magneto-transport in the NCS superconductors seem to point toward this issue [194–196]. Although there is no clear sign of novel pinning phenomena in NCS Re_3M samples, other experiments on single crystalline materials would be desirable to test some hypothesis on this subject.

The peak effect has manifested itself in our measurements mainly by an unusual resistance minimum during the R vs H scans in single phase NCS materials. In some samples, the PE occurred so close to the $H_{c2}(T)$ boundary line that, instead of having a clear resistance minimum, the ρ(H) curve only exhibited a satellite feature in the mean-field transition. In other samples,

*J_C^M is the critical current density calculated from the magnetization data.

having enough separation between $H_{c2}(T)$ and the peak effect lines, reentrant superconductivity has been observed: increasing the external field effectively leads the sample back to the zero resistance state after the dissipation phenomena have first emerged.

The driving force strength, which is proportional to the modulation amplitude dI_{ac} in our measurements, has proven to be crucial for the experimental observation, and, therefore, for the emergence of the PE in the Re_3M samples. Moreover, the PE has even been detected when using A.C. current densities that were orders of magnitude below the typical J_c of hard superconductors: the maximum J_{AC} used in the measurements were a few tenths of A cm^{-2} while Nb and its solid solutions, for instance, have J_C as large as 10^4 - 10^5 A cm^{-2} [117, 197].

Four magnetic field dependent resistivity curves are shown in Figure 4.30, originated from the measurements of the $Re_{0.735}W_{0.265}$, $Re_3Nb_{0.5}W_{0.5}$, and $Re_3Ta_{0.5}W_{0.5}$ materials at a fixed temperature of T = 5.5 K and driven by $J_{AC} \sim 370$ mA cm^{-2}. The curves in the main panel of Figure 4.30(a) are restricted to the high field region, and the applied field in each sample is normalized by its respective mean field value ($h = H/H_{c2}$), calculated from the 50% resistance drop across the SC transition. All the resistivity curves are not monotonic during the transition from the superconducting to the normal state. Moreover, a dramatic and anomalous decrease in resistivity with increasing magnetic field occurs slightly below H_{c2} in all but one curve (AC $Re_3Nb_{0.5}W_{0.5}$). In these curves, a subsequent resistivity minimum is clearly observed in higher fields, being followed by a sharp rise of ρ(H) until reaching its normal-state value. In the $Re_{0.735}W_{0.265}$ data, however, the resistivity only begins to decrease at $h \sim 0.99$, being rapidly suppressed by the onset of the mean field transition. These observations strongly indicate that the PE is present in all the NCS samples studied through magneto-transport measurements, but in somewhat different ways.

Once the samples are in a state of low level of dissipation, each curve evolves to the mean field transition in a particular way: (i) in the $Re_3Ta_{0.5}W_{0.5}$ (green curve), $\rho(H)$ reaches a maximum and goes back to the dissipationless state before rising again to ρ_0, in the usual way; (ii) in the $Re_3Nb_{0.5}W_{0.5}$, a maximum in $\rho(H)$ also occurs, being followed by a decreasing resistivity down to a non-vanishing, low level value, and subsequently entering the mean field transition; (iii) $\rho(H)$ of the unsubstituted material $Re_{0.735}W_{0.265}$ (black curve) rises to a certain

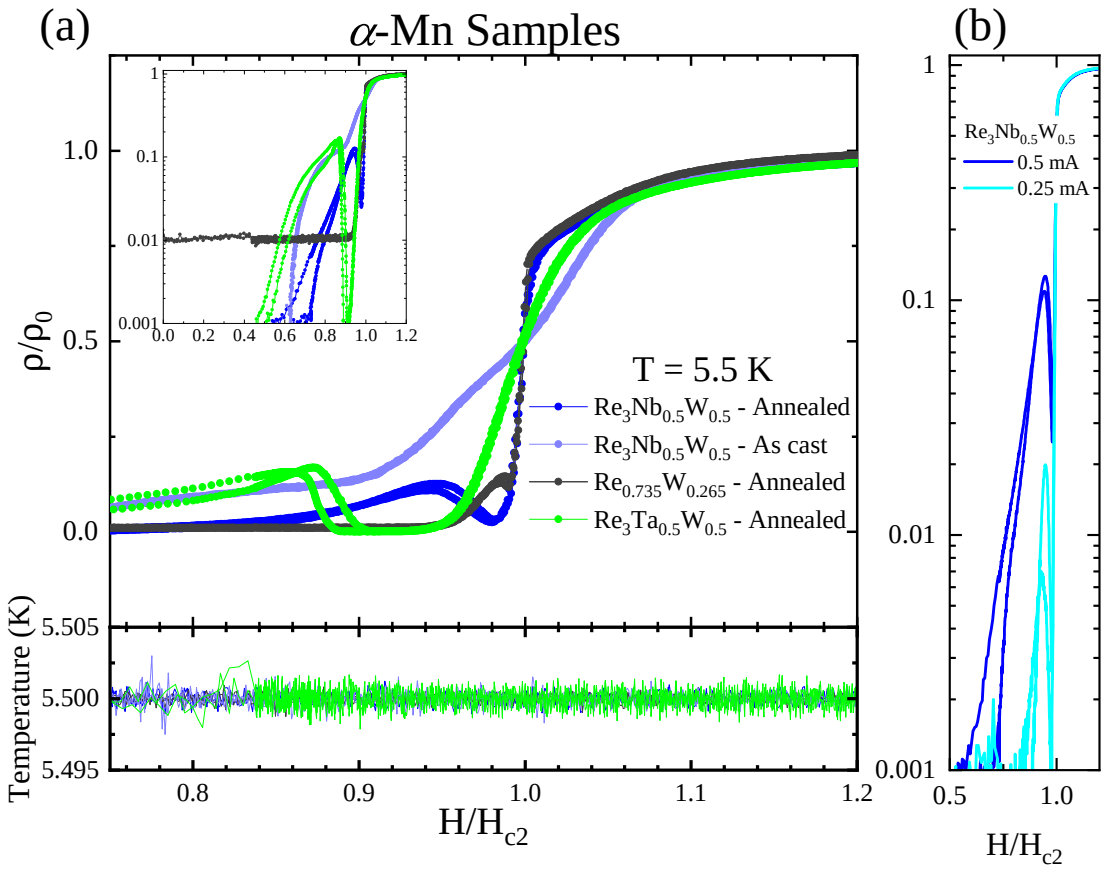

Figure 4.30: (a) Scans of the normalized resistivity close to the upper critical field; the reduced field H/H_{c2} is used to compare the annealed samples $Re_3Nb_{0.5}W_{0.5}$, $Re_3Ta_{0.5}W_{0.5}$ as well as the as cast $Re_3Nb_{0.5}W_{0.5}$ specimen. All curves were measured using J_{AC} in the 110 - 370 mA cm^{-2} range. The bottom panel shows the temperature stability at T = 5.5 K. (b) Comparison between two ρ(H) curves measured in the annealed $Re_3Nb_{0.5}W_{0.5}$ sample by applying different AC excitations (0.5 and 0.25 mA).

level, decreases just a little, and steeply rises again as soon as H_{c2} is approached; (iv) no negative slope is seen in the $Re_3Nb_{0.5}W_{0.5}$ AC data (light blue) along the field sweep, but a inflection point aligned with the resistance maximum of its annealed counterpart suggests that the same mechanism is already present, or even hidden, in the as cast specimen.

At this particular temperature of T = 5.5 K, the thermal depinning of the flux lines is evident even at h $\sim$ 0.75, as the resistivity of the annealed $Re_3Ta_{0.5}W_{0.5}$ and as cast $Re_3Nb_{0.5}W_{0.5}$ samples have already reached a sizable fraction ($\sim$ 10 %) of ρ_0. In contrast, the resistivity of the annealed $Re_3Nb_{0.5}W_{0.5}$ and $Re_{0.735}W_{0.265}$ samples begin to significantly increase ($\rho \sim 0.01\ \rho_0$) just above h $\sim$ 0.8 and 0.93, respectively. Shown in the inset of the Figure 4.30(a) is a more representative view of the difference among the curves, whose the ρ-axis is presented in logarithmic scale. It is clear that the thermal depinning is more likely to occur in lower fields in

the solid solution materials. This could be due to the combination of a relatively high reduced temperature (t $\approx$ 0.70, 0.72, and 0.8, for the $Re_{0.735}W_{0.265}$, $Re_3Nb_{0.5}W_{0.5}$, and $Re_3Ta_{0.5}W_{0.5}$ materials at T = 5.5 K, respectively), favoring thermal fluctuations, and an inherent high degree of disorder expected by the alloying in solid solutions.

As the results of the $Re_3Ta_{0.5}W_{0.5}$ material have revealed robust evidence for the PE, the following discussion is focused on this material. There is no loss in generality with that choice, as similar features have also been observed in the other α-Mn NCS specimens, but always less pronounced.

The resistive peak effect is also seen clearly in Figure 4.31 by varying T at constant H (2 Tesla) and fixed current densities ($\sim$ 100 $\leq$ J_{AC} $\leq$ 1200 mA cm^{-2}) as a sudden drop in resistance at a well defined temperature in each curve. Then, by using J_{AC} $\simeq$ 370 mA cm^{-2}, the resistance minimum is located at T_{min} = 6.0 K in the ρ vs T curve under H = 2 T while it occurs at H_{min} $\sim$ 2 T in the ρ vs H curve with T = 6 K (not shown), unambiguously implying that it has a unique location in the (H, T) phase space. The peak structure in the ρ vs T curves is only absent when the sample is excited by the lowest current level ($\sim$ 100 mA cm^{-2} and below) and begins to emerge, although restricted to the bottom section of the Figure 4.31, when the excitation current density is larger than $\sim$ 200 mA cm^{-2}. At slightly higher driving currents, a large irreversibility between the warming and cooling curves is observed, becoming systematically less pronounced as the current density keeps increasing.

In a simple picture, the $\rho(T)$ irreversibility can be understood as follows: upon entering the peak region by warming the sample, the measured voltage drop is significantly suppressed, indicating that flux motion has lowered or even stopped; when the sample is cooled again, the FLL remains in this strong pinned state over a small temperature range (0.1 K), which becomes narrower as the current is increased, before the flux motion start to rise again. Similarly, hysteric or irreversible features across the PE region have also been observed in the $NbSe_2$ and $CeRu_2$ superconductors [198, 199], with a strong dependence of measured quantities on the magnitude of the transport current.

The results displayed in Figures 4.30 and 4.31 are in agreement with an intricate depinning of the disordered flux lattice. Accordingly, some authors argue that the hysteresis observed

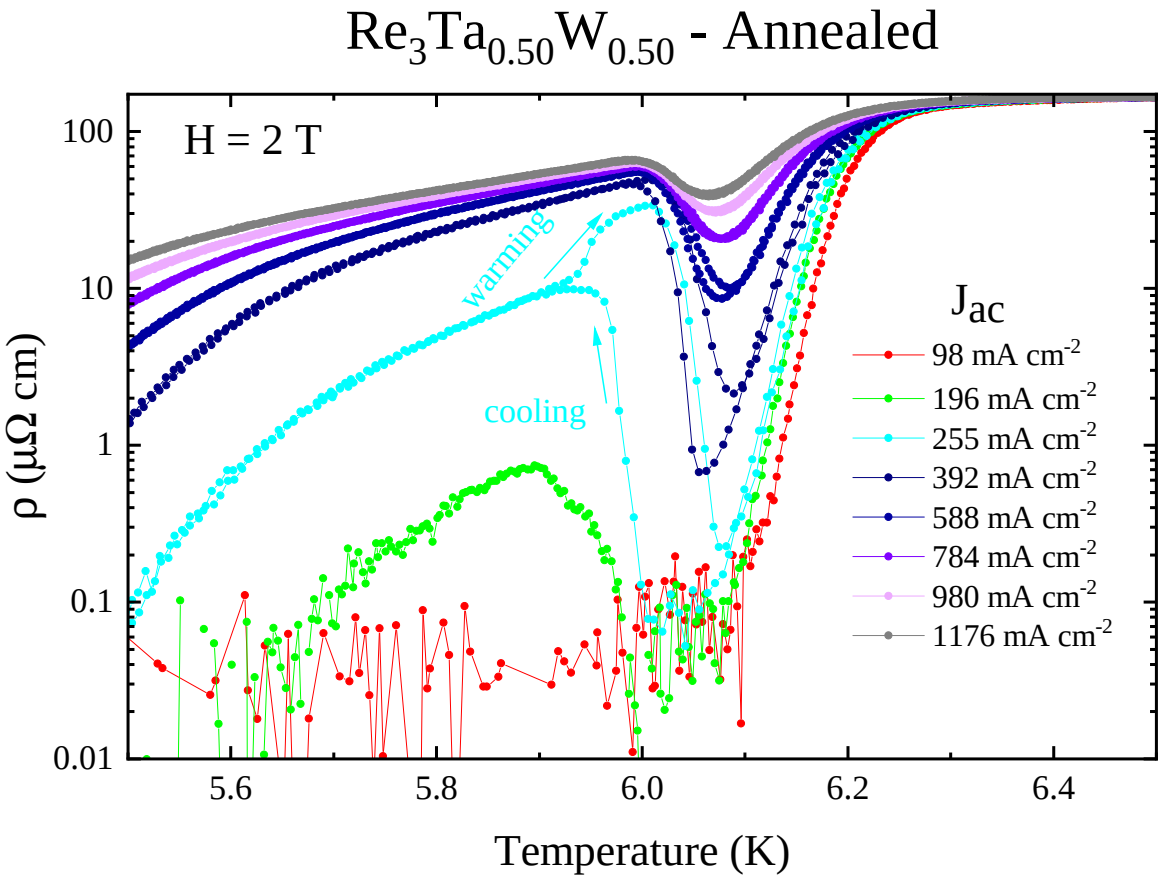

Figure 4.31: Temperature dependence of resistivity obtained with various current excitations. The data were measured both by warming and cooling the sample under the fixed magnetic field of 2 Tesla.

in transport measurements near the PE reflects a dynamic transition leading to depinning of the FLL in a two-step process [200]. In this description, the first step takes place when some fractions of flux lines are suddenly depinned and move in channels throughout the material, resulting in a plastic flow in which portions of the FLL remains pinned [198, 199]. Then, in the second step, a coherent movement of the FLL is only achieved when the current is raised above a critical value, as the number of available channels for vortices movement increases with I, becoming indistinguishable from the usual movement occurring in a weakly pinned phase. This two step depinning process has been suggested to occur in $NbSe_2$ and $CeRu_2$, in which metastable superconducting phases are believed to occur depending on the particular thermal history. In contrast, the reentrant superconducting glass $Fe_xNi_{1-x}Zr_2$ exhibits two stable phases for the same H and I pair over very long time scales, in addition to hysteric or irreversible behavior and two well-separated depinning phases [201].

In addition to the plastic flow picture, the dynamics of moving vortex states can also resemble elastic flow. The elastically flowing regime occurs at large flow velocities when all the vortices are moving almost uniformly and maintain their spatial correlations, resulting in elastic channels for vortices movement in the moving Bragg-glass phase [103, 202]. In this elastic description with low driving currents, there are large barriers separating the metastable states of the flux lines due to the quenched disorder [101], effectively creating the elastic channels for the FLL movement. In lower velocities, the picture of the coherent motion in elastic channels breaks down as defects appear in the FLL, decoupling the channels and resulting in the smectic glass picture. Such a smectic glass phase is layered in a sense that the vortices flow in channels and are correlated perpendicular to their flow, but uncorrelated along it. The channel structure, however, is still preserved and the smectic phase is also a moving glass phase. Both regimes, the moving smectic and the moving Bragg, were observed through decorations experiments by increasing the applied magnetic field [203, 204].

In the above context, in the low velocity side, the plastic flow emerges as a sudden proliferation of topological defects and dislocations. Then, the coherent vortex motion is completely destroyed and the vortex matter moves incoherently in the plastic flow regime [103, 205], not having well-defined channels as the other moving glass phases. The vortices movement is expected to be slow near the PE region, resulting in the plastic flow. Therefore, different parts of a very soft FLL move with different velocities in this region, and crossing it through field cooling or warming may not lead to the same response as there are not well-defined channels in this regime. In other words, the vortices movement that begins after the supercooled metastable state in FC measurements need not be the same as the stopping movement due to the superheated metastable state in the warming curve; thus, irreversibility effects are observed in the $\rho(T)$ curves.

In addition to the vortices movement picture, the irreversibility features may also be related to an inhomogeneous current distribution during the measurements in the PE region. The spatial current distribution throughout the material could lead to a current localization effect: the current flows through channels, which are fundamentally different than the channels of vortices movement, when the vortices flow has stopped or lowered due to the pinning enhancement in the

PE region. In this picture, the Josephon coupling between SC islands surrounded by a metallic matrix would create percolative pathways (the current channels) within the sample, decreasing the overall sample resistance and eventually leading to the zero resistance state.

In the scenario of the applied current flowing through channels, the Joule heating is not uniformly distributed over the sample; instead, the heating is concentrated in regions surrounding the current channels. This local heating provides additional thermal energy to the metastable vortex lattice, and due to the close proximity of PE to the boundary line, any disturbance of the local temperature could trigger the vortices movement once more. Therefore, the irreversibility between the cooling and warming curves in the PE region would signalize the randomness in the establishment of the percolative pathways of the current channels, which would not be the same in both curves. Furthermore, this scenario would explain the PE features arising in the unexpected low current density values: the real J could be orders of magnitude higher than those obtained by simply using the sample's dimensions perpendicular to the current flow; thus, the calculation must be carried out considering the effective area of the channels.

In order to further probe the PE in Re_3M materials, differential resistance (dV/dI) measurements have been carried out using various D.C. current bias superimposed to the dI_{ac} current modulation while the samples were maintained in fixed magnetic fields and temperatures. The dV/dI vs I curves are closely related to the I-V curves, being more useful to probe eventual non-linear responses.

Shown in Figure 4.32(a) are the field dependence of various dV/dI vs I curves, which were obtained using the modulation current dI_{ac} = 0.1 mA and at T = 6 K. The main panel of Figure 4.32(a) clearly shows the evolution of the dV/dI vs I curves as the magnetic field is increased. As expected, the response from the sample is highly non-linear (not ohmic) as soon as it begins to exhibit dissipation under magnetic fields, but becoming linear at larger values of the current bias I_{DC}, where the dV/dI values move toward saturation. Upon increasing magnetic field from 1 to 2 T, the differential resistance saturation is systematically driven to ever more smaller I_{DC} values. Then, this trend is reversed in magnetic fields above 2 T, signalizing that the sample has entered the PE region. By further increasing the magnetic field (H > 2.3 T), the low field behavior is recovered and the differential resistance curves move toward the normal-state value.

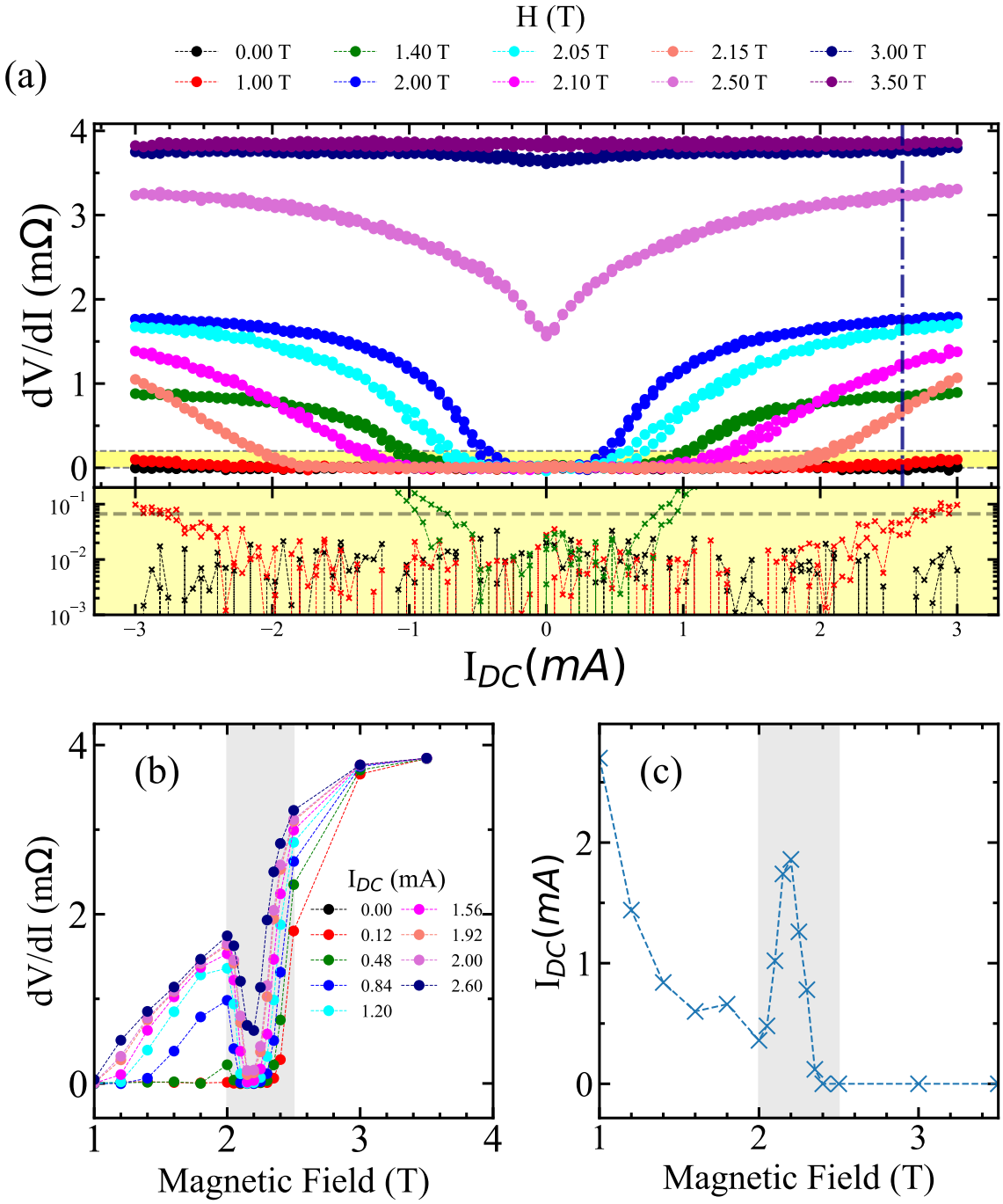

Figure 4.32: Results from the annealed $Re_3Ta_{0.5}W_{0.5}$ sample at T = 6 K and with dI_{AC} = 0.1 mA. (a) Differential resistance (dV/dI) versus the bias current (I_{DC}) curves obtained in various external magnetic fields. (b) Field dependence of dV/dI at various I_{DC}. (c) Field dependent critical current extracted from (a), see the main text for details.

To make the PE clear in the differential resistance measurements, various dV/dI values were gathered at several I_{DC} (= 2.6 mA in the dashed vertical line), resulting in Figure 4.32(b). The maxima in dV/dI followed by a drop to zero resistance state indicate the magnetic PE region at this particular temperature (6 K), represented by the region shaded in gray color.

It is also possible to estimate the field dependence of the critical current I_c(H) from the dI/dV vs I curves. In this estimate, I_c is set as the first current value in which the dV response exceeds a threshold value, defined as twice of the maximum dV measured in the zero field curve. A graphical representation of this estimate is exhibited in the logarithmic bottom panel of Figure 4.32(a), spanning the yellow region of the main panel: the critical current is at the point where the dV/dI curves crosses the dV/dI threshold value depicted by the black dashed line. Then, the I_c values of various curves obtained at fixed fields are shown in Figure 4.32(c). A sharp rise in I_c develops in the $2 \leq H \leq 2.5$ T region, unveiling the most direct peak effect feature, before it becomes essentially zero. Note, however, that this estimate of I_c is not conducted in the ordinary, usual way (i.e., using a voltage criterion in I-V curves, proportional to an electric field of 10^{-5}-10^{-8} V cm^{-1} [206]), but using a threshold value observed in the I-V's slope. This could, indeed, cast doubt in the magnitude of our I_c values, but not in its magnetic field dependence.

The comparison between the I_c(H) and ρ(H) curves is exhibited in Figure 4.33. The peak effect regions in each of these measurements agree remarkably well in all temperatures. This enables a qualitative explanation of the ρ(H) data in three steps: (i) only noisy ρ(H) values are measured at low magnetic fields, followed by the emergence of finite resistances as soon as the excitation current crosses the I_c(H) boundary line, inducing an elastic flow of the now depinned flux lines; (ii) this scenario continues until the PE region is reached, where the current excitation crosses the I_c(H) boundary line (having now a positive slope) again, and the resistance begins to decrease as the vortices movement is impeded by the flux pinning enhancement, effectively creating the conditions for the plastic flow; (iii) after leaving the PE region, a sharper increase in ρ as H rises to H_{c2} indicates the development of a usual, coherent flux flow until the normal state is finally attained.

Although the PE is doubtlessly observed in the electrical resistance measurements, the same is not true for the field dependent magnetization M(H) results. In the latter, it is also possible to estimate the critical current by using the Bean's model of the critical state [197, 206, 207]. The Bean model proposes that the critical current J_c^M is proportional to the magnetization difference ΔM between the upward ($M_\uparrow$, with dH/dt > 0) and the downward ($M_\downarrow$, dH/dt < 0) branches of

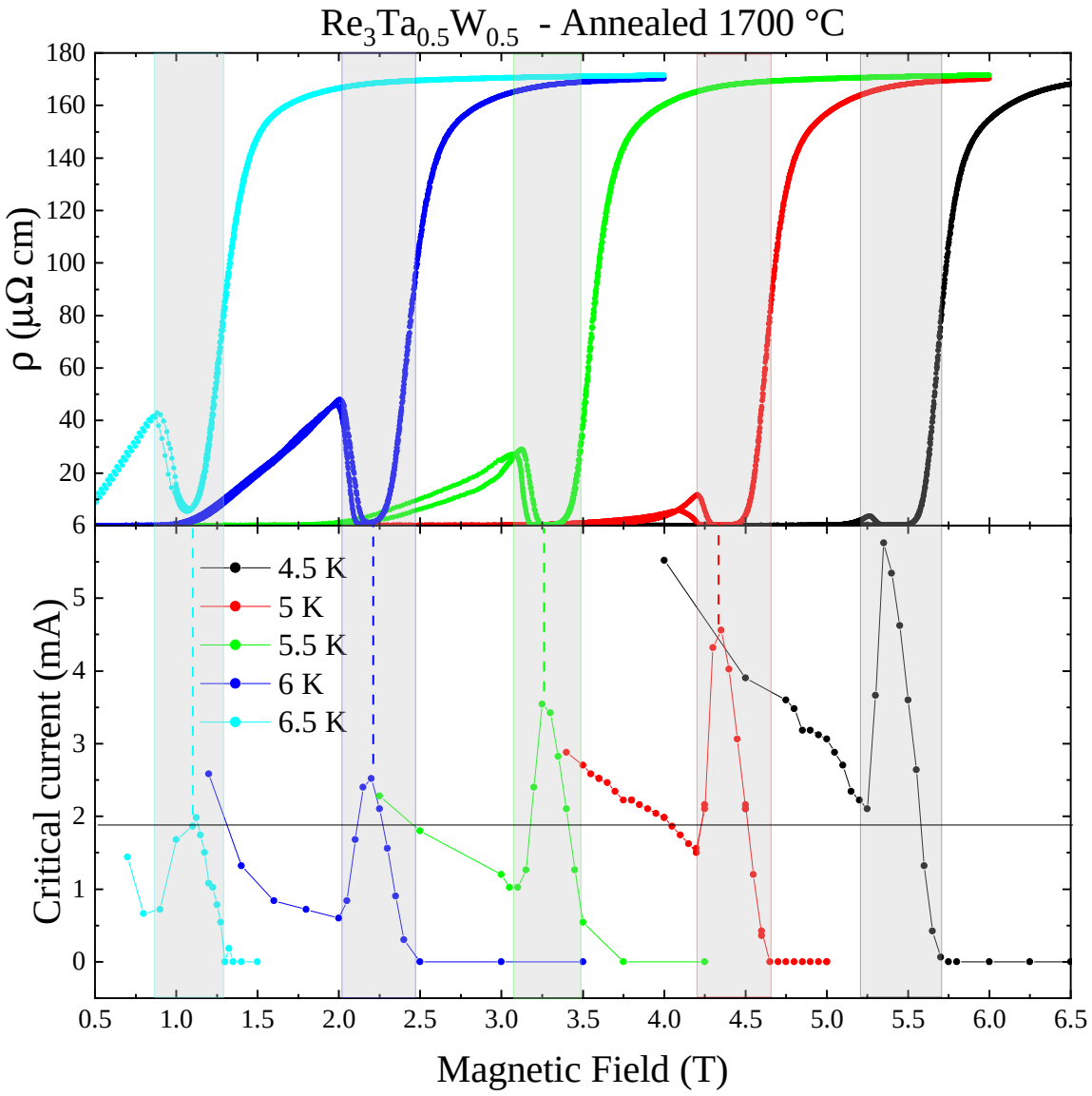

Figure 4.33: Comparison between the ρ(H) and I_c(H) curves at several temperatures.

the M-H hysteresis loops; then, any critical current enhancement due to the PE would lead to a departure from the ordinary splitting of the branches at fields close the upper critical field. At first glance, however, the M-H (T = 6 K) data displayed in Figure 4.34(a) do not show the expected clear splitting between the two branches near H_{c2} commonly observed in superconducting materials with the PE (see Figure 2.8(c) and (f) in page 56). A more careful data analysis in the $1.8 \leq H \leq 2.2$ T region (illustrated in yellow and expanded in the figure's inset) suggests a tiny, subtle difference between $M_{\uparrow}$ and $M_{\downarrow}$, as indicated by the red dashed ellipsis.

Therefore, shown in Figure 4.34(b) is the critical current,

$$J_c^M = \Delta M \left[\frac{3\pi}{4d_{grain}} \right], \tag{4.8}$$

exhibiting the characteristic J_c enhancement related to the PE over the 1.5 T < H < 2.2 T magnetic field interval. In Equation 4.8, d_{grain} is referred to the average crystallite size, introduced to account for the sample's polycrystalline nature and estimated as $d_{grain} \approx 50$ μm in the Re_3M materials (images not shown).

In Figure 4.34(b), the critical current density values obtained in the dV/dI vs I curves, J_c(H), are plotted (red line and points) alongside with the J_c^M obtained at the same temperature (T = 6 K). The comparison indicates a good agreement between the two estimates of the critical current magnitude; the value of J_c^M at its peak is only six times larger than the resistive peak value, a seemingly negligible difference given our limitations in calculating J_c by both methods. Nevertheless, although both curves share similar trends with the magnetic field, they are slightly shifted from each other: the J_c^M peak value occurs at H $\sim$ 2 T, which is precisely the field in which the resistive J_c starts to rise before reaching its peak at H $\sim$ 2.2 T. It should be noted that the results compared here were obtained by examining different properties: the magnetization probes the volumetric response while the electrical resistance is more sensible to surface or filamentary SC properties. In addition, the critical current estimates were obtained in two different pieces of the same annealed material and this could be related to the slightly different peak locations of tenths of Tesla. Thus, it might be the case in which the average pinning strength is not evenly distributed over the entire (annealed) sample.

Among all of the Re_3M samples studied, it was only possible to resolve completely the J_c^M peak in the annealed $Re_3Ta_{0.5}W_{0.5}$ sample, which appears to have the more pronounced peak effect in the series studied here. The search for a peak in the J_c^M(H) of other samples remained elusive, as a sizable ΔM could not be perceived in any visual or numerical analysis. At this point, it is not clear why the PE anomalies in the M-H scans should be so small, if any at all, in the remainder Re_3M samples. Similar findings have been reported for some $Ti_{1-y}V_y$ alloys [208]: clear J_c^M(H) peaks are observed in the $Ti_{60}V_{40}$ but become absent when y is decreased to 30 %at., although both alloys were found to exhibit a peak effect in magnetization below the

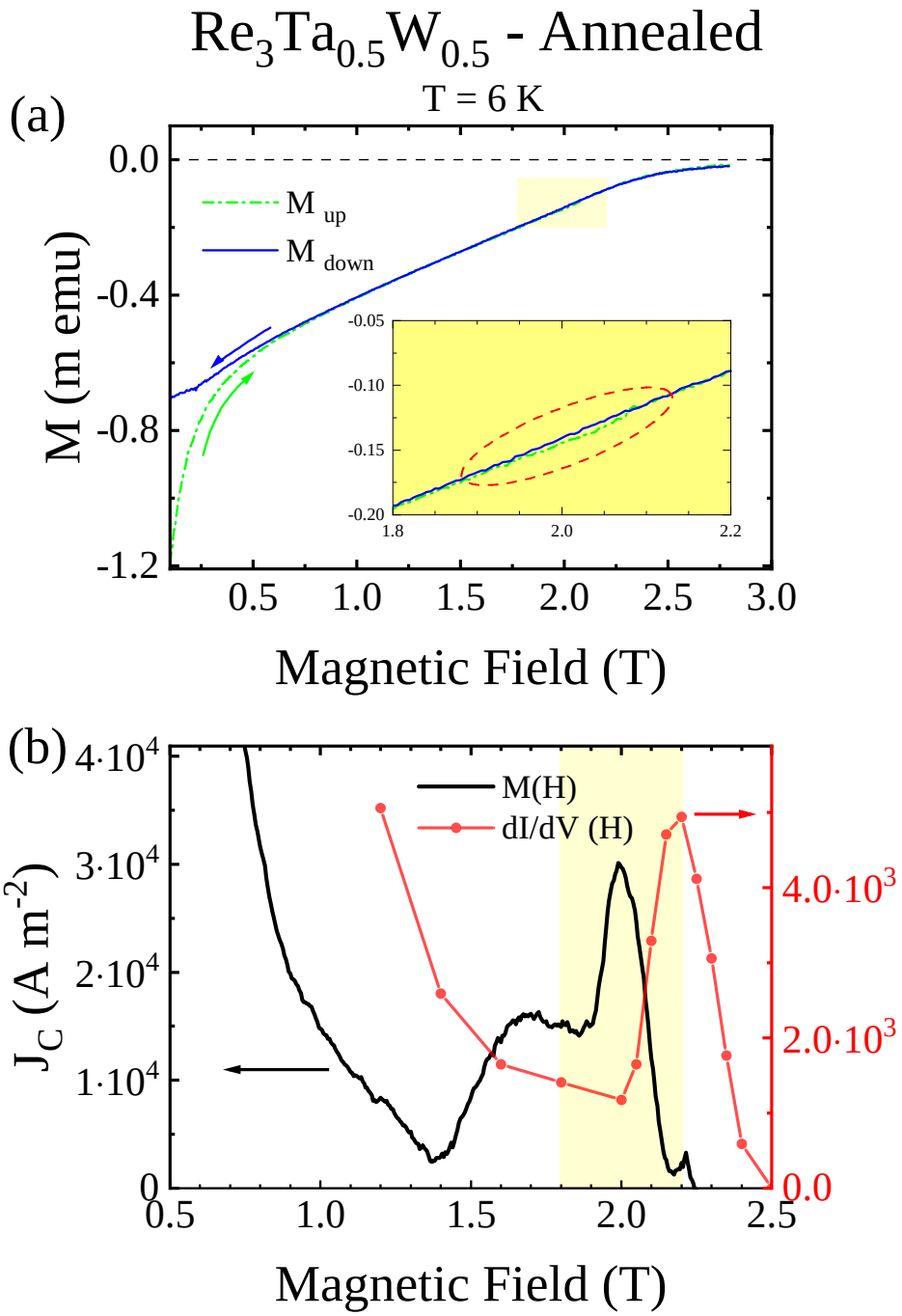

Figure 4.34: (a) First quadrant of the magnetization loop after subtraction of the normal-state paramagnetic contribution. Inset: expanded view of the highlighted area in the main panel. (b) Critical currents obtained by using the magnetic measurements (black line) and the resistive data (red line and points). The yellow shaded area spans the same field range as the inset in (a).

upper critical field.

A line in the HxT phase diagram is added by gathering the fields where the peak value occurs (H_P) in each I_{DC} vs H curves at constant T. Then, shown in Figure 4.35 is the updated phase diagrams for the annealed $Re_3Ta_{0.5}W_{0.5}$ and $Re_3Nb_{0.5}W_{0.5}$ samples, with the PE line

accompanying the H_{c2}(T) line over the major part of the (H,T) phase space.

Recently, the PE line has been found to lie in the vicinity of the mean field boundary line in a vanadium single crystal while its order-disorder transition occurs deep in the mixed state. The authors, then, have argued that the order–disorder transition and the peak effect are not necessarily related in this material, being the PE on the edge of the regime where thermal fluctuations dominate [112]. Similarly, there are reports where the PE arises at the boundary of the thermal fluctuation regime, as in Nb_3Sn and $NbSe_2$ [113, 121]. Thus, the data discussed here on the Re_3M materials seems to point in the same direction; i.e., with thermal fluctuations dominating the PE region. In this picture, the early ideas from Pippard are suitable, in which a FLL softening guides the development of the peak effect. The disorder strength could tune this softening, effectively altering the PE extension in the phase space, in agreement with our results from parent compounds and its solid solutions. Nevertheless, a more in-depth study of the effect is required to answer whether the order-disorder transition is relevant in these Re-based systems.

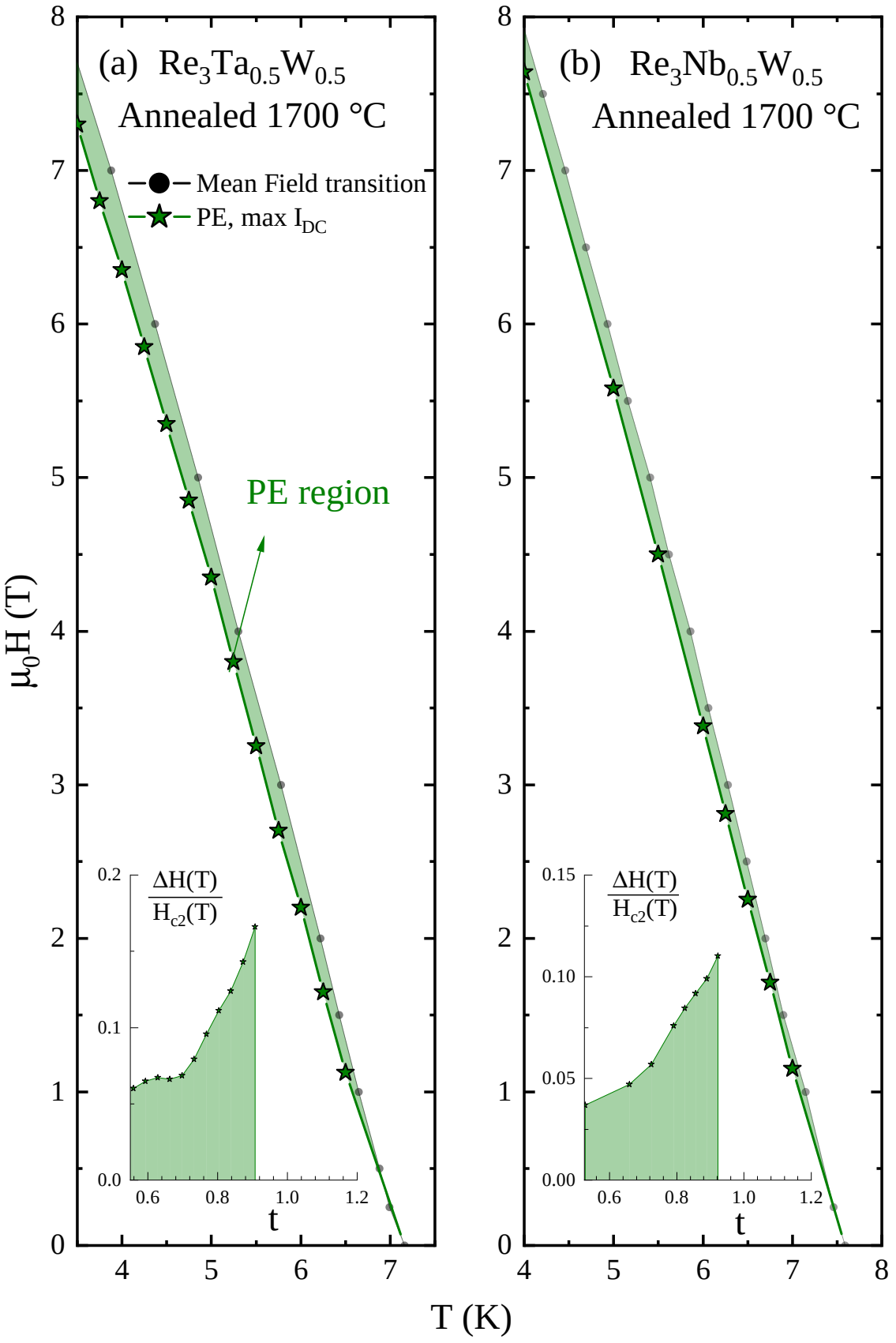

Figure 4.35: Superconducting phase diagrams of the (a) $Re_3Ta_{0.5}W_{0.5}$ and (b) $Re_3Nb_{0.5}W_{0.5}$ materials, with the PE region shaded in light green. The insets show the difference ΔH between the mean field $H_{c2}(T)$ and PE $H_p(T)$ lines, normalized by $H_{c2}(T)$, as a function of the reduced temperature t.

4.4 Re_3M superconducting parameters

The various SC properties in Re-M materials are displayed in the tables below. Tables 4.4 and 4.5 show the results obtained in the Re-W system. The SC properties of the annealed solid solution materials are presented in tables 4.6 and 4.7.

Table 4.4: SC properties of the Re-W samples having Re:W ratio close to 3:1. The table has entries for both the annealed (HT) and as cast (AC) results of each material.

Quantity	Unity	$Re_{0.75}W_{0.25}$		$Re_{0.735}W_{0.265}$		$Re_{0.727}W_{0.273}$		$Re_{0.72}W_{0.28}$	
		AC	HT	AC	HT	AC	HT	AC	HT
T_c	K	9.30	7.68	9.23	7.75	8.98	7.63	9.29	7.46
H_{c2}^{GL} (0)	10^4 Oe	9.7	12.0	10.6	12.2	12.2	11.9	11.0	11.8
RRR	-	1.48	1.15	1.46	1.14	1.64	1.13	1.37	1.12
ρ_0	$\mu\Omega$ cm	308	150	120	205	80	149	170	245
a	Å	–	9.601	–	9.602	–	9.607	–	9.609
$\xi_{GL}(0)$	Å	61	52	56	52	52	53	55	53
ℓ_{tr}	Å	5	8	13	7	24	9	7	6
γ_n	mJ mol^{-1} K^{-2}	11.1	17.1	11.4	17.0	10.3	17.6	14.5	16.7
θ_D	K	291	314	297	307	319	293	353	298

Table 4.5: Values of some basic properties of the AC Re-W materials. Their corresponding crystal structure are also designated.

Quantity Structure	Unity -	$Re_{0.90}W_{0.10}$ Re $h.c.p$	$Re_{0.82}W_{0.18}$ Re $h.c.p$	Re_3W mixture	$Re_{0.67}W_{0.33}$ σ	$Re_{0.5}W_{0.5}$ σ
T_c	K	6.49	8.19	9.02	8.19	5.21
H_{c2}^{GL} (0)	10^4 Oe	4.4	5.5	9.7	6.3	6.3
γ_n	mJ mol^{-1} K^{-2}	13.5	–	11.1	11.3	12.7

Table 4.6: Summary of the SC and normal-state properties of the annealed $Re_3Ta_xW_{1-x}$ materials in the Re-Ta-W system.

Quantity	Unity	Re_3W	$Re_3Ta_{0.1}W_{0.9}$	$Re_3Ta_{0.25}W_{0.75}$	$Re_3Ta_{0.5}W_{0.5}$	Re_3Ta
T_c	K	7.75	7.63	7.35	6.99	4.75
H_c (0)	kOe	1.55	1.56	1.51	1.36	0.87
H_{c1}(0)	Oe	69	69	63	55	34
H_{c2}^{GL} (0)	10^4 Oe	12.0	12.4	12.4	12.4	8.2
H_p	10^4 Oe	14.3	14.0	14.7	14.0	8.7
α_M	-	1.10	1.25	1.19	1.24	1.33
RRR	-	1.15	1.17	1.10	1.14	1.04
ρ_0	$\mu\Omega$ cm	150	149	244	260	267
a	Å	9.601	9.608	9.624	9.594	9.691
l_{tr}	Å	8	9	10	8	8
λ_0	Å	3483	3489	3728	3882	5324
ξ_{GL}(0)	Å	52	51	51	51	63
κ	-	67	68	72	75	84
γ_n	mJ mol^{-1} K^{-2}	17.1	18.4	17.1	17.4	13.3
θ_D	K	314	300	317	318	333
Δ(0)	meV	1.29	–	1.22	1.14	0.75
λ_{ef}	-	0.73	0.74	0.72	0.70	0.61
$2\Delta/k_BT_c$	-	3.86	–	3.84	3.85	3.65
$\Delta C/\gamma_nT_c$	-	1.58	1.68	1.60	1.61	1.57
G_i	10^{-7}	0.8	0.8	0.9	1.2	1
J_0	$10^{11} Am^{-2}$	1.5	1.6	1.4	1.3	0.5

Table 4.7: Summary of the SC and normal-state properties of the annealed $Re_3Nb_xW_{1-x}$ materials in the Re-Nb-W system.

Quantity	Unity	Re_3W	$Re_3Nb_{0.1}W_{0.9}$	$Re_3Nb_{0.25}W_{0.75}$	$Re_3Nb_{0.5}W_{0.5}$	Re_3Nb
T_c	K	7.75	7.66	7.68	7.59	6.15
H_c (0)	kOe	1.55	–	1.65	1.42	–
$H_{c1}(0)$	Oe	57	–	70	99	34
H_{c2}^{GL} (0)	10^4 Oe	12.0	12.5	13.1	13.8	11.9
H_p	10^4 Oe	15.6	14.1	15.6	15.7	11.7
α_M	-	1.09	1.25	1.22	1.32	1.34
RRR	-	1.15	1.11	1.12	1.10	1.06
ρ_0	$\mu\Omega$ cm	150	141	135	177	208
a	Å	9.601	9.612	9.623	9.647	9.689
λ_0	Å	3483	–	3481	3607	4188
$\xi_{GL}(0)$	Å	52	51	49	47	54
l_{tr}	Å	8	–	9	6	9
κ	-	67	–	71	37	39
γ_n	mJ mol^{-1} K^{-2}	17.1	–	18.4	17.9	16.3
θ_D	K	314	–	321	293	316
$\Delta(0)$	meV	1.29	–	1.29	1.28	–
λ_{ef}	-	0.73	–	0.72	0.74	0.68
$2\Delta/k_BT_c$	-	3.86	–	3.89	3.91	–
$\Delta C/\gamma_n T_c$	-	1.58	–	1.65	1.71	1.48
G_i	10^{-7}	0.8	–	0.9	1.9	–
J_0	$10^{11} Am^{-2}$	1.6	–	1.7	1.6	1.1

In the above tables, the major part of the parameters has been defined during the previous discussion, but some of them did not appeared explicitly. Then, the relations used to calculate these parameters are presented below.

The GL coherence length was calculated by inverting Equation 2.55:

$$\xi_{GL}(0) = \sqrt{\frac{\phi_0}{2\pi H_{c2}^{GL}(0)}}.$$

The low temperature magnetic penetration depth λ_0 was estimated using both GL and BCS results by employing the following relation [37, 209]:

$$\lambda_0 = \frac{k_B}{\Delta(0)}\sqrt{\frac{\phi_0 H_{c2}^{GL}(0)}{24\gamma}}.$$

In the annealed Re_3W material, the estimated value of 3519 Å agrees remarkably well with those measured in previous studies: tunnel diode oscillator and μ-SR measurements yielded λ_0 $\sim$ 3000 and 4180 Å[41, 47]. In the case of $Re_3Ta_{0.1}W_{0.9}$ and $Re_3Nb_{0.1}W_{0.9}$ materials, whose $\Delta(0)$ were not estimated, the weak-coupling BCS result $\Delta(0)/k_B$ = 1.76T_C has been used to calculate λ_0.

The GL parameter κ is obtained as the ratio of λ_0 to $\xi_{GL}(0)$, confirming the materials as hard type-II superconductors having κ $\sim$ 70.

Additionally, the electronic mean free path ℓ_{tr} is estimated by using a semi-classic approach mixing the SC and normal-state parameters [82]:

$$\ell_{tr} \sim \frac{1.0095}{\gamma T_c \rho_0 \xi_{GL}(0)} \cdot 10^8.$$

From this relation, the resulting value of the electronic mean free path is in nanometers when the values of ρ_0, γ, and ξ_{GL} are in Ω cm, erg cm^{-3}K^{-2}, and cm, respectively. Then, the ℓ_{tr} values obtained indicate that the Re_3M materials are in the dirty limit, since the estimated ℓ_{tr}'s are of the same magnitude as the lattice parameter a and almost an order of magnitude smaller than the respective $\xi_{GL}(0)$.

Although the lower critical field H_{c1} can be estimated from the low-field region of the

isotherm M-H loops (see Figure 4.25in page 118), this method did not give reliable results in all of the Re_3M samples. Alternatively, $H_{c1}(0)$ can also be estimated by the GL relation [3]:

$$H_{c1}(0) = \frac{\phi_0}{4\pi\lambda_0^2} ln(\kappa). \tag{4.9}$$

The $H_{c1}(0)$ values presented in tables 4.6-4.7 were obtained by employing Equation 4.9. These values are slightly smaller than those obtained from the M-H loops estimates, even though effects of the remnant field must be considered in the latter.

Chapter 5

Conclusions and Outlook

The discussions of the above results compose a comprehensive study on the α-Mn phase stability and the SC properties in the Re-W system as well as in the Re-Ta-W and Re-Nb-W ternary systems. In the Re-W system, various materials have been studied systematically using both their AC and annealed forms in order to test some possible scenarios arising in NCS superconductors. The experimental data, however, do not support the NCS hypothesis of mixed parity Cooper pairs, and are reasonably well understood within the conventional s-wave picture. In this context, as cast $Re_{1-x}W_x$, $0.25 \leq x \leq 0.28$, materials are suggested to possess multi superconducting phases, presenting intricate SC properties related to this mixture of phases. Ideally, powder X-ray or neutron diffraction experiments are desirable to confirm the structural properties of these AC samples.

The experimental results of the AC solid solution materials have suggested that low levels of W substitution by Ta or Nb in $Re_3(Ta,Nb)_{0.1}W_{0.9}$ do not alter substantially the phase composition of the AC samples, whose SC properties are very similar to the AC Re_3W samples. The NCS phase is almost stabilized by increasing the substitution level to 25 at% in AC solid solutions: while the XRD data suggest that these samples are mainly composed of the α-Mn phase, flux jumps in the M-H loops resemble the AC Re_3W results and probably indicate two SC phases. By further increasing the Ta or Nb content to 50 at%, all results in AC samples indicate that single phase NCS SC materials are fully established in this composition.

Single NCS α-Mn phase materials were obtained by annealing (at 1700°C) the specimens with the Re:M (M = W, Ta, and Nb) ratio of 3:1. Nonetheless, no clear signature of odd parity

superconducting ground state was found in the Re-based NCS materials; instead, the zero field specific heat has been shown to exponentially decrease in low temperatures while upper critical fields are in close proximity to the Pauli limiting scenario. In the parent compounds Re_3W and Re_3Ta, the low temperature side of the phase diagrams, however, can not be described by the conventional picture: two transitions in the Re_3W ρ(H) data are separated by a resistance plateau, while a finite slope of the upper critical field in low temperatures is observed in Re_3Ta. Except for the $Re_3Nb_{0.5}W_{0.5}$ material, the electrical transport of solid solutions has not been explored in the low temperature and high magnetic field limit yet.

The PE is ubiquitously found among the Re_3M materials, being more pronounced in the annealed solid solutions. In these materials, the PE region is restricted to the vicinity of the mean-field boundary line, and the starting point of the PE region is certainly related to the degree of quenched disorder. A lower degree quenched disorder is believed to occur in the non-substituted NCS Re-W materials. Indeed, the PE region in these materials is very close to, and almost overlapping with, the mean-field boundary line. On the other hand, the effective PE region varied in different solid solution samples (or even pieces of the same sample) with the same composition; presumably, the samples have distinct levels of quenched disorder, which would be tuned by the atomic substitution.

The very low values of RRR in all NCS samples agree with a picture of sizable quenched disorder, which would be a feature of the highly packed α-Mn structure itself. When combining this structure with the atomic substitution in solid solutions, an enhancement of the quenched disorder is expected to occur. Additionally, the suitability of the parallel resistor model also points to the disorder scenario. This scenario is corroborated even further by the low electronic mean free path ℓ_{tr} values. As ℓ_{tr} have the same order of magnitude as the NCS lattice parameter a, a high density of defects is probably present, being the main contribution for the measured electrical resistance. These defects, or impurities, also serve as pinning centers, and its high density is one of the key ingredients for the PE phenomena to emerge.

The dynamic features of ρ in the PE region are complex: the vortex matter is believed to crossover from the elastic to plastic dynamic regimes as the pinning enhancement induces defects in the ordered vortex configuration, effectively tearing the FLL in the plastic regime.

These dynamically generated defects are healed and the FLL returns back to a elastic picture, resembling a fluid flow as the FLL softens with the approach of the mean-field superconducting-to-normal line boundary. In the context of ρ measurements, the healing of defects would work as a dynamic annealing of the metastable disorder by the transport current [210]. Irreversibility effects are observed in the PE region, where crossovers among different types of dynamic response are believed to occur.

Then, the present study lays the ground to advance in understanding the unusual magnetic response of the Re_3M SC properties. More experimental results are required to describe the emergence of the PE phenomena in Re_3M materials in further detail; these results would include: (i) explore further the responses from the vortex matter; (ii) study more Re-based NCS materials in the low T, high field limit, specially the Re-W compounds with Re:W ratio close to 3:1; (iii) microstructural studies of a representative Re_3M sample by means of electron backscattered diffraction or even by atom probe tomography. Those techniques could be used to test a possible correlation between structural defects and the PE strength in the Re-M NCS materials. Ideally, high quality Re_3M single crystals are required to conduct a detailed study on the vortex states, and growing single crystals is the next experimental challenge to be overcome on the production side of this project. Regarding the topic (i), few ideas are currently being considered:

- Order-disorder transition study
  - from thermodynamic data: magneto-caloric transport experiments could be conducted to test the PE and its correlation with fluctuation effects. This study would extend the findings observed in the specific heat measurements.
- Irreversibility on the PE region:
  - I-V curves: the straightforward way to conduct this study would be to analyze the I-V curves. An experimental apparatus coupled to the PPMS is being set to measure the D.C. I-V curves in the Re_3M materials.
  - Imaging the sample's surface: another approach to study irreversibility effects would be to use some kind of decoration experiment, such as Bitter decoration, in a similar

way to what has been done in $NbSe_2$ material [203, 211]. Eventually, fast scans through a scanning tunneling microscope would also achieve the goal of tracking down the slow vortices movement on the sample's surface, as previously done in $NbSe_2$ [204].

Another natural extension of the present study would be conducting electrical measurements in other solid solutions, specially the annealed materials, at the lowest temperature with the dilution refrigerator probe. Such a study would provide valuable information and could hint whether there is a link between the PE and the SC phase diagram anomalies at low temperatures.

Other experimental study planned to be conducted on the Re_3M materials is to directly probe their SC gaps through electron tunneling measurements. Various attempts were made to grow tunnel junctions on the samples surfaces, but none resulted in good quality SC junctions. This task still is in active development and our close collaboration with the micro-fabrication facility of the LNNano will certainly result in proper devices to conduct the tunneling measurements.

List of Publications

During the development of the present project, which spanned the 2016-2021 time interval, I have also participated in other studies in condensed matter physics. A list of publications including all the studies conducted throughout this interval is indicated below.

- **F. Abud**, M.S. Torikachvili, and R.F. Jardim, Stabilization of the noncentrosymmetric α-Mn structure in the $Re_3(Ta,Nb)_xW_{1-x}$ solid solutions by partial atomic substitution (in preparation).

- **F. Abud**, and R.F. Jardim, Emergence of the peak effect in $Re_3(Ta,Nb)_{0.5}W_{0.5}$ superconductors (in preparation).

- M. Assis, A. Tello, **F. Abud**, P. Negre, L. Ribeiro, R. Ribeiro, S.H. Masunaga, A. Lima, G. Luz Jr., R.F. Jardim, A. da Silva, J. Andrés, and E. Longo, Bridging experiment and theory: morphology, optical, electronic, and magnetic properties of $\mathrm{MnWO_4}$ (submitted).

- Valentina Martelli, **Fabio Abud**, Julio Larrea Jiménez, Elisa Baggio-Saitovich, Li-Dong Zhao, and Kamran Behnia, Thermal diffusivity and its lower bound in orthorhombic SnSe, Physical Review B **104**, 035208 (2021).

- V. Stoeberl, E. B. Guedes, **F. Abud**, R. F. Jardim, M. Abbate and R. J. O. Mossanek, Partial contributions to the valence band of $\mathrm{MoO_2}$, $\mathrm{RuO_2}$, and $\mathrm{Rh_2O_3}$: Cooper minimum and extended cluster model calculations, Europhysics Letters **132**, 47004 (2020).

- V. Stoeberl, E. B. Guedes, M. Abbate, **F. Abud**, R. F. Jardim, and R. J. O. Mossanek, Charge screening effects in the resonant photoemission of $\mathrm{Rh_2O_3}, \mathrm{RuO_2}$, and $\mathrm{MoO_2}$, Physical Review B **102**, 155112 (2020).

- M. Hernández-Wolpez, L. C. Gutiérrez-Rivero, I. García-Fornaris, E. Govea-Alcaide, **F. Abud**, R. F. Jardim, and P. Muné, Magnetic relaxation in (Bi, Pb)-2223 superconducting ceramics doped with α-Al_2O_3 nanoparticles, Revista Mexicana de Física **66**, 42 (2019)

- E. B. Guedes, **F. Abud**, H. P. Martins, M. Abbate, R. F. Jardim, and R. J. O. Mossanek, Role of Ti-Ru interaction in $SrTi_{0.5}Ru_{0.5}O_3$: Physical properties, x-ray spectroscopy, and cluster model calculations, Physical Review B **100**, 075132 (2019).

- B.S.de Lima, N. Chaia, T.W. Grant, L.R.de Faria, J.C. Canova, F.S.de Oliveira, **F. Abud**, and A.J.S. Machado, Large enhancement of the CDW resistivity anomaly and traces of superconductivity in imperfect samples of $NbTe_4$, Materials Chemistry and Physics **226**, 95-99 (2019)

- **F. Abud**, L. E. Correa, I. R. Souza Filho, A. J. S. Machado, M. S. Torikachvili, and R. F. Jardim, Absence of superconductivity in NbB, Physical Review Materials **1**, 044803 (2017).

- E. B. Guedes, M. Abbate, **F. Abud**, R. F. Jardim, F. C. Vicentin, and R. J. O. Mossanek, Spectroscopy and electronic structure of Sr_2YRuO_6 and $Sr2YRu_{0.75}Ir_{0.25}O_6$, Physical Review B **94**, 045109 (2016).

References

[1] C. Kittel, *Introduction to Solid State Physics*, 8th ed. (Wiley, Hoboken, NJ, 2005).

[2] T. P. Orlando and K. A. Delin, *Foundations of Applied Superconductivity* (Addison-Wesley, Reading, Mass, 1991).

[3] M. Tinkham, *Introduction to Superconductivity*, 2nd ed., International Series in Pure and Applied Physics (McGraw Hill, New York, 1996).

[4] J. Bardeen, L. N. Cooper, and J. R. Schrieffer, Phys. Rev. **108**, 1175 (1957).

[5] B. D. Cullity, *Elements of X-Ray Diffraction*, 2nd ed., Addison-Wesley Series in Metallurgy and Materials (Addison-Wesley Pub. Co, Reading, Mass, 1978).

[6] S. S. Saxena and P. Monthoux, Nature **427**, 799 (2004).

[7] E. Bauer, G. Hilscher, H. Michor, C. Paul, E. W. Scheidt, A. Gribanov, Y. Seropegin, H. Noel, M. Sigrist, and P. Rogl, Phys. Rev. Lett. **92**, 027003 (2004).

[8] M. Yogi, Y. Kitaoka, S. Hashimoto, T. Yasuda, R. Settai, T. D. Matsuda, Y. Haga, Y. Onuki, P. Rogl, and E. Bauer, Phys. Rev. Lett. **93**, 4 (2004).

[9] K. Izawa, Y. Kasahara, Y. Matsuda, K. Behnia, T. Yasuda, R. Settai, and Y. Onuki, Phys. Rev. Lett. **94**, 197002 (2005).

[10] H. Q. Yuan, D. F. Agterberg, N. Hayashi, P. Badica, D. Vandervelde, K. Togano, M. Sigrist, and M. B. Salamon, Phys. Rev. Lett. **97**, 017006 (2006).

[11] M. Nishiyama, Y. Inada, and G. Q. Zheng, Phys. Rev. Lett. **98**, 047002 (2007).

[12] L. Jiao, J. L. Zhang, Y. Chen, Z. F. Weng, Y. M. Shao, J. Y. Feng, X. Lu, B. Joshi, A. Thamizhavel, S. Ramakrishnan, and H. Q. Yuan, Phys. Rev. B **89**, 060507 (2014).

[13] M. Mondal, B. Joshi, S. Kumar, A. Kamlapure, S. C. Ganguli, A. Thamizhavel, S. S. Mandal, S. Ramakrishnan, and P. Raychaudhuri, Phys. Rev. B **86**, 094520 (2012).

[14] D. C. Peets, A. Maldonado, M. Enayat, Z. Sun, P. Wahl, and A. P. Schnyder, Phys. Rev. B **93**, 174504 (2016).

[15] X. B. Yan, Y. Xu, L. P. He, J. K. Dong, H. Cho, D. C. Peets, J. G. Park, and S. Y. Li, Supercond. Sci. Technol. **29**, 065001 (2016).

[16] T. Klimczuk, F. Ronning, V. Sidorov, R. J. Cava, and J. D. Thompson, Phys. Rev. Lett. **99**, 257004 (2007).

[17] I. Bonalde, R. L. Ribeiro, W. Bramer-Escamilla, G. Mu, and H. H. Wen, Phys. Rev. B **79**, 052506 (2009).

[18] G. Mu, Y. Wang, L. Shan, and H.-H. Wen, Phys. Rev. B **76**, 064527 (2007).

[19] G. M. Pang, M. Smidman, L. X. Zhao, Y. F. Wang, Z. F. Weng, L. Q. Che, Y. Chen, X. Lu, G. F. Chen, and H. Q. Yuan, Phys. Rev. B **93**, 060506 (2016).

[20] M. X. Wang, Y. Xu, L. P. He, J. Zhang, X. C. Hong, P. L. Cai, Z. B. Wang, J. K. Dong, and S. Y. Li, Phys. Rev. B **93**, 020503 (2016).

[21] M. N. Wilson, A. M. Hallas, Y. Cai, S. Guo, Z. Gong, R. Sankar, F. C. Chou, Y. J. Uemura, and G. M. Luke, Phys. Rev. B **95**, 224506 (2017).

[22] S. Maeda, K. Matano, and G.-q. Zheng, Phys. Rev. B **97**, 184510 (2018).

[23] J. Wang, X. Xu, N. Zhou, L. Li, X. Cao, J. Yang, Y. Li, C. Cao, J. Dai, J. Zhang, Z. Shi, B. Chen, and Z. Yang, J Supercond Nov Magn **28**, 3173 (2015).

[24] U. S. Kaluarachchi, Y. Deng, M. F. Besser, K. Sun, L. Zhou, M. C. Nguyen, Z. Yuan, C. Zhang, J. S. Schilling, M. J. Kramer, S. Jia, C.-Z. Wang, K.-M. Ho, P. C. Canfield, and S. L. Bud'ko, Phys. Rev. B **95**, 224508 (2017).

[25] J. Chen, M. B. Salamon, S. Akutagawa, J. Akimitsu, J. Singleton, J. L. Zhang, L. Jiao, and H. Q. Yuan, Phys. Rev. B **83**, 144529 (2011).

[26] A. Harada, S. Akutagawa, Y. Miyamichi, H. Mukuda, Y. Kitaoka, and J. Akimitsu, J. Phys. Soc. Jpn. **76**, 023704 (2007).

[27] S. Kuroiwa, Y. Saura, J. Akimitsu, M. Hiraishi, M. Miyazaki, K. H. Satoh, S. Takeshita, and R. Kadono, Phys. Rev. Lett. **100**, 097002 (2008).

[28] S. Akutagawa and J. Akimitsu, J. Phys. Soc. Jpn. **76**, 024713 (2007).

[29] T. Ekino, A. Sugimoto, A. M. Gabovich, H. Kinoshita, and J. Akimitsu, Physica C **484**, 52 (2013).

[30] N. P. Butch, P. Syers, K. Kirshenbaum, A. P. Hope, and J. Paglione, Phys. Rev. B **84**, 220504 (2011).

[31] P. M. R. Brydon, L. M. Wang, M. Weinert, and D. F. Agterberg, Phys. Rev. Lett. **116**, 177001 (2016).

[32] H. Kim, K. Wang, Y. Nakajima, R. Hu, S. Ziemak, P. Syers, L. Wang, H. Hodovanets, J. D. Denlinger, P. M. R. Brydon, D. F. Agterberg, M. A. Tanatar, R. Prozorov, and J. Paglione, Sci. Adv. **4**, eaao4513 (2018).

[33] T. V. Bay, M. Jackson, C. Paulsen, C. Baines, A. Amato, T. Orvis, M. C. Aronson, Y. K. Huang, and A. de Visser, Solid State Commun. **183**, 13 (2014).

[34] J. M. Joubert and M. Phejar, Prog. Mater. Sci. **54**, 945 (2009).

[35] J.-M. Joubert, J.-C. Crivello, M. Andasmas, and P. Joubert, Acta Materialia **70**, 56 (2014).

[36] F. Boakye, Solid State Commun. **117**, 103 (2000).

[37] J. Chen, L. Jiao, J. L. Zhang, Y. Chen, L. Yang, M. Nicklas, F. Steglich, and H. Q. Yuan, Phys. Rev. B **88**, 144510 (2013).

[38] J.-C. Crivello, A. Breidi, and J.-M. Joubert, Inorg. Chem. **52**, 3674 (2013).

[39] R. Steadman and P. M. Nuttall, Acta Cryst **17**, 62 (1964).

[40] P. K. Biswas, M. R. Lees, A. D. Hillier, R. I. Smith, W. G. Marshall, and D. M. Paul, Phys. Rev. B **84**, 184529 (2011).

[41] Y. L. Zuev, V. A. Kuznetsova, R. Prozorov, M. D. Vannette, M. V. Lobanov, D. K. Christen, and J. R. Thompson, Phys. Rev. B **76**, 132508 (2007).

[42] T. Shang, D. J. Gawryluk, J. A. T. Verezhak, E. Pomjakushina, M. Shi, M. Medarde, J. Mesot, and T. Shiroka, Phys. Rev. Mater. **3**, 024801 (2019).

[43] R. D. Blaugher and J. K. Hulm, J. Phys. Chem. Solids **19**, 134 (1961).

[44] B. T. Matthias, V. B. Compton, and E. Corenzwit, J. Phys. Chem. Solids **19**, 130 (1961).

[45] B. W. Roberts, J. Phys. Chem. Ref. Data **5**, 581 (1976).

[46] Y. Huang, J. Yan, Y. L. Wang, L. Shan, Q. Luo, W. Wang, and H. H. Wen, Supercond. Sci. Technol. **21**, 075011 (2008).

[47] P. K. Biswas, A. D. Hillier, M. R. Lees, and D. M. Paul, Phys. Rev. B **85**, 134505 (2012).

[48] E. M. Savitskiĭ, V. V. Baron, Y. V. Efimov, M. I. Bychkova, and L. F. Myzenkova, *Superconducting Materials* (Springer US, Boston, MA, 1973).

[49] A. B. Karki, Y. M. Xiong, N. Haldolaarachchige, S. Stadler, I. Vekhter, P. W. Adams, D. P. Young, W. A. Phelan, and J. Y. Chan, Phys. Rev. B **83**, 144525 (2011).

[50] R. P. Singh, M. Smidman, M. R. Lees, D. M. Paul, and G. Balakrishnan, J. Cryst. Growth **361**, 129 (2012).

[51] C. Cirillo, R. Fittipaldi, M. Smidman, G. Carapella, C. Attanasio, A. Vecchione, R. P. Singh, M. R. Lees, G. Balakrishnan, and M. Cuoco, Phys. Rev. B **91**, 134508 (2015).

[52] C. Cirillo, G. Carapella, M. Salvato, R. Arpaia, M. Caputo, and C. Attanasio, Phys. Rev. B **94**, 104512 (2016).

[53] T. Shang, M. Smidman, S. K. Ghosh, C. Baines, L. J. Chang, D. J. Gawryluk, J. A. T. Barker, R. P. Singh, D. M. Paul, G. Balakrishnan, E. Pomjakushina, M. Shi, M. Medarde, A. D. Hillier, H. Q. Yuan, J. Quintanilla, J. Mesot, and T. Shiroka, Phys. Rev. Lett. **121**, 257002 (2018).

[54] T. Shang, C. Baines, L.-J. Chang, D. J. Gawryluk, E. Pomjakushina, M. Shi, M. Medarde, and T. Shiroka, npj Quantum Mater. **5**, 76 (2020).

[55] T. Mamiya, K. Nomura, and Y. Masuda, J. Phys. Soc. Jpn. **28**, 380 (1970).

[56] J. A. T. Barker, B. D. Breen, R. Hanson, A. D. Hillier, M. R. Lees, G. Balakrishnan, D. M. Paul, and R. P. Singh, Phys. Rev. B **98**, 104506 (2018).

[57] Arushi, D. Singh, P. K. Biswas, A. D. Hillier, and R. P. Singh, Phys. Rev. B **101**, 144508 (2020).

[58] T. Shang, G. M. Pang, C. Baines, W. B. Jiang, W. Xie, A. Wang, M. Medarde, E. Pomjakushina, M. Shi, J. Mesot, H. Q. Yuan, and T. Shiroka, Phys. Rev. B **97**, 020502 (2018).

[59] R. P. Singh, A. D. Hillier, B. Mazidian, J. Quintanilla, J. F. Annett, D. M. Paul, G. Balakrishnan, and M. R. Lees, Phys. Rev. Lett. **112**, 107002 (2014).

[60] D. Singh, J. A. T. Barker, A. Thamizhavel, D. M. Paul, A. D. Hillier, and R. P. Singh, Phys. Rev. B **96**, 180501 (2017).

[61] C. S. Lue, H. F. Liu, C. N. Kuo, P. S. Shih, J. Y. Lin, Y. K. Kuo, M. W. Chu, T. L. Hung, and Y. Y. Chen, Supercond. Sci. Technol. **26**, 055011 (2013).

[62] K. Matano, R. Yatagai, S. Maeda, and G. Q. Zheng, Phys. Rev. B **94**, 214513 (2016).

[63] M. A. Khan, A. B. Karki, T. Samanta, D. Browne, S. Stadler, I. Vekhter, A. Pandey, P. W. Adams, D. P. Young, S. Teknowijoyo, K. Cho, R. Prozorov, and D. E. Graf, Phys. Rev. B **94**, 144515 (2016).

[64] G. M. Pang, Z. Y. Nie, A. Wang, D. Singh, W. Xie, W. B. Jiang, Y. Chen, R. P. Singh, M. Smidman, and H. Q. Yuan, Phys. Rev. B **97**, 224506 (2018).

[65] K. Stolze, F. A. Cevallos, T. Kong, and R. J. Cava, J. Mater. Chem. C **6**, 10441 (2018).

[66] I. A. Tregubov, L. N. Evseyeva, O. S. Ivanov, and I. D. Marchuko, Russ. Metall. **1**, 144 (1973).

[67] E. Savitskii, M. A. Tylkina, and L. L. Zhdanova, in *ASM Alloy Phase Diagrams Database*, ASM Handbook, Vol. 3, edited by P. Villars, H. Okamoto, and K. Cenzual (ASM International, 2006).

[68] P. Coleman, *Introduction to Many-Body Physics* (Cambridge University Press, Cambridge, 2015).

[69] L. N. Cooper, Phys. Rev. **104**, 1189 (1956).

[70] M. Sigrist, AIP Conference Proceedings **789**, 165 (2005).

[71] V. P. Mineev and K. V. Samokhin, *Introduction to Unconventional Superconductivity* (Gordon and Breach Science Publishers, Amsterdam, The Netherlands, 1999).

[72] P. W. Anderson, J. Phys. Chem. Solids **11**, 26 (1959).

[73] P. W. Anderson, Phys. Rev. B **30**, 4000 (1984).

[74] M. Sigrist, AIP Conference Proceedings **1162**, 55 (2009).

[75] E. Bauer, M. Sigrist, and SpringerLink (Online service), *Non-Centrosymmetric Superconductors Introduction and Overview*, Lecture Notes in Physics, (Springer Berlin Heidelberg,, Berlin, Heidelberg, 2012).

[76] F. Kneidinger, E. Bauer, I. Zeiringer, P. Rogl, C. Blaas-Schenner, D. Reith, and R. Podloucky, Physica C **514**, 388 (2015).

[77] S. Yip, Annu. Rev. Condens. Matter Phys. **5**, 15 (2014).

[78] M. Smidman, M. B. Salamon, H. Q. Yuan, and D. F. Agterberg, Rep. Prog. Phys. **80**, 46 (2017).

[79] H. Suhl, B. T. Matthias, and L. R. Walker, Phys. Rev. Lett. **3**, 552 (1959).

[80] K. Maki and T. Tsuneto, Prog. Theor. Phys. **31**, 945 (1964).

[81] A. M. Clogston, Phys. Rev. Lett. **9**, 266 (1962).

[82] T. P. Orlando, E. J. McNiff, S. Foner, and M. R. Beasley, Phys. Rev. B **19**, 4545 (1979).

[83] H. Padamsee, J. E. Neighbor, and C. A. Shiffman, J. Low Temp. Phys. **12**, 387 (1973).

[84] T. Yasuda, H. Shishido, T. Ueda, S. Hashimoto, R. Settai, T. Takeuchi, T. D Matsuda, Y. Haga, and Y. Ōnuki, J. Phys. Soc. Jpn. **73**, 1657 (2004).

[85] V. P. Mineev and K. V. Samokhin, Phys. Rev. B **75**, 184529 (2007).

[86] V. G. Kogan and R. Prozorov, Rep. Prog. Phys. **75**, 114502 (2012).

[87] N. R. Werthamer, E. Helfand, and P. C. Hohenberg, Phys. Rev. **147**, 295 (1966).

[88] A. Gurevich, Phys. Rev. B **67**, 184515 (2003).

[89] A. Abrikosov, J. Exp. Theor. Phys. **5**, 1174 (1957).

[90] A. M. Campbell and J. E. Evetts, Advances in Physics **50**, 1249 (2001).

[91] H. F. Hess, R. B. Robinson, R. C. Dynes, J. M. Valles, and J. V. Waszczak, Phys. Rev. Lett. **62**, 214 (1989).

[92] D. Dew-Hughes, Philos. Mag. **30**, 293 (1974).

[93] D. Dew-Hughes, Low Temp. Phys. **27**, 713 (2001).

[94] J. Bardeen and M. J. Stephen, Phys. Rev. **140**, A1197 (1965).

[95] C. P. Bean, Rev. Mod. Phys. **36**, 31 (1964).

[96] Y. B. Kim, C. F. Hempstead, and A. R. Strnad, Phys. Rev. **129**, 528 (1963).

[97] V. V. Chabanenko, A. I. D'yachenko, M. V. Zalutskii, V. F. Rusakov, H. Szymczak, S. Piechota, and A. Nabialek, J. Appl. Phys. **88**, 5875 (2000).

[98] V. Chabanenko, A. Nabiałek, R. Puźniak, O. Kuchuk, O. Chumak, F. Pérez-Rodríguez, U. Pal, V. Garcia-Vazquez, R. Cortés-Maldonado, J. Qian, X. Yao, and H. Szymczak, Sci Rep **9**, 6233 (2019).

[99] P. W. Anderson, Phys. Rev. Lett. **9**, 309 (1962).

[100] M. R. Beasley, R. Labusch, and W. W. Webb, Phys. Rev. **181**, 682 (1969).

[101] G. Blatter, M. V. Feigel'man, V. B. Geshkenbein, A. I. Larkin, and V. M. Vinokur, Rev. Mod. Phys. **66**, 1125 (1994).

[102] E. H. Brandt, Rep. Prog. Phys. **58**, 1465 (1995).

[103] T. Giamarchi and S. Bhattacharya, in *High Magnetic Fields: Applications in Condensed Matter Physics and Spectroscopy*, Lecture Notes in Physics, edited by C. Berthier, L. P. Lévy, and G. Martinez (Springer, Berlin, Heidelberg, 2001) pp. 314–360.

[104] A. I. Larkin and Y. N. Ovchinnikov, J. Low Temp. Phys. **34**, 409 (1979).

[105] M. P. A. Fisher, D. A. Huse, and D. S. Fisher, Phys. Rev. B **43**, 130 (1991).

[106] T. Nattermann, Phys. Rev. Lett. **64**, 2454 (1990).

[107] T. Giamarchi and P. Le Doussal, Phys. Rev. Lett. **72**, 1530 (1994).

[108] T. G. Berlincourt, R. R. Hake, and D. H. Leslie, Phys. Rev. Lett. **6**, 671 (1961).

[109] A. B. Pippard, Philos. Mag. **19**, 217 (1969).

[110] N. D. Daniilidis, I. K. Dimitrov, V. F. Mitrović, C. Elbaum, and X. S. Ling, Phys. Rev. B **75**, 174519 (2007).

[111] G. P. Mikitik and E. H. Brandt, Phys. Rev. B **64**, 184514 (2001).

[112] R. Toft-Petersen, A. B. Abrahamsen, S. Balog, L. Porcar, and M. Laver, Nat Commun **9**, 901 (2018).

[113] S. Mohan, J. Sinha, S. S. Banerjee, and Y. Myasoedov, Phys. Rev. Lett. **98**, 027003 (2007).

[114] G. Blatter and V. B. Geshkenbein, in *Superconductivity: Conventional and Unconventional Superconductors*, edited by K. H. Bennemann and J. B. Ketterson (Springer, Berlin, Heidelberg, 2008) pp. 495–637.

[115] S. S. Banerjee, N. G. Patil, S. Ramakrishnan, A. K. Grover, S. Bhattacharya, P. K. Mishra, G. Ravikumar, T. V. C. Rao, V. C. Sahni, M. J. Higgins, C. V. Tomy, G. Balakrishnan, and D. M. Paul, EPL **44**, 91 (1998).

[116] M. Marchevsky, M. J. Higgins, and S. Bhattacharya, Nature **409**, 591 (2001).

[117] W. DeSorbo, Rev. Mod. Phys. **36**, 90 (1964).

[118] A. M. Troyanovski, J. Aarts, and P. H. Kes, Nature **399**, 665 (1999).

[119] C. Reichhardt and C. J. O. Reichhardt, Rep. Prog. Phys. **80**, 026501 (2016).

[120] M. J. Higgins and S. Bhattacharya, Physica C **257**, 232 (1996).

[121] R. Lortz, N. Musolino, Y. Wang, A. Junod, and N. Toyota, Phys. Rev. B **75**, 094503 (2007).

[122] S. Dutta, I. Roy, S. Basistha, S. Mandal, J. Jesudasan, V. Bagwe, and P. Raychaudhuri, J. Phys.: Condens. Matter **32**, 075601 (2019).

[123] D. Jaiswal-Nagar, A. D. Thakur, S. Ramakrishnan, A. K. Grover, D. Pal, and H. Takeya, Phys. Rev. B **74**, 184514 (2006).

[124] Z. F. Weng, M. Smidman, G. M. Pang, O. Prakash, Y. Chen, Y. J. Zhang, S. Ramakrishnan, and H. Q. Yuan, Phys. Rev. B **95**, 184501 (2017).

[125] I. K. Dimitrov, N. D. Daniilidis, C. Elbaum, J. W. Lynn, and X. S. Ling, Phys. Rev. Lett. **99**, 047001 (2007).

[126] R. Lortz, F. Lin, N. Musolino, Y. Wang, A. Junod, B. Rosenstein, and N. Toyota, Phys. Rev. B **74**, 104502 (2006).

[127] H. M. Rietveld, J. Appl. Crystallogr. **2**, 65 (1969).

[128] H. M. Rietveld, Acta Cryst. **22**, 151 (1967).

[129] J. Rodriguezcarvajal, Physica B **192**, 55 (1993).

[130] G. Ventura and L. Risegari, *The Art of Cryogenics: Low-Temperature Experimental Techniques*, 1st ed. (Elsevier, Amsterdam ; Boston, 2008).

[131] J. W. Ekin, *Experimental Techniques for Low-Temperature Measurements: Cryostat Design, Material Properties, and Superconductor Critical-Current Testing* (Oxford University Press, Oxford ; New York, 2006).

[132] A. I. Braginski and J. Clarke, in *The SQUID Handbook*, edited by J. Clarke and A. I. Braginski (Wiley-VCH Verlag GmbH & Co. KGaA, Weinheim, FRG, 2005) pp. 1–28.

[133] J. R. Clem, in *Magnetic Susceptibility of Superconductors and Other Spin Systems* (Springer, Boston, MA, 1991) pp. 177–211.

[134] F. Pobell, *Matter and Methods at Low Temperatures*, 3rd ed. (Springer, Berlin ; New York, 2007).

[135] G. K. White, *Experimental Techniques in Low-Temperature Physics*, 3rd ed., Monographs on the Physics and Chemistry of Materials No. 43 (Clarendon Press ; Oxford University Press, Oxford : New York, 1987).

[136] T. H. K. Barron and G. K. White, *Heat Capacity and Thermal Expansion at Low Temperatures* (Springer US, Boston, MA, 1999).

[137] N. Dilley, R. Black, L. Montes, A. Wilson, and M. Simmonds, MRS Proceedings **691**, G3.5 (2001).

[138] Z.-K. Liu and Y. A. Chang, J. Alloys Compd. **299**, 153 (2000).

[139] E. M. Forgan, S. J. Levett, P. G. Kealey, R. Cubitt, C. D. Dewhurst, and D. Fort, Phys. Rev. Lett. **88**, 167003 (2002).

[140] D. Singh, K. P. Sajilesh, S. Marik, A. D. Hillier, and R. P. Singh, Supercond. Sci. Technol. **30**, 125003 (2017).

[141] D. Singh, J. A. T. Barker, A. Thamizhavel, A. D. Hillier, D. M. Paul, and R. P. Singh, J. Phys.: Condens. Matter **30**, 075601 (2018).

[142] D. Singh, S. K. P., S. Marik, A. D. Hillier, and R. P. Singh, Phys. Rev. B **99**, 014516 (2019).

[143] N. Môri, J. Phys. Soc. Jpn. **37**, 1285 (1974).

[144] O. Gunnarsson, M. Calandra, and J. E. Han, Rev. Mod. Phys. **75**, 1085 (2003).

[145] Z. Fisk and G. W. Webb, Phys. Rev. Lett. **36**, 1084 (1976).

[146] H. Wiesmann, M. Gurvitch, H. Lutz, A. Ghosh, B. Schwarz, M. Strongin, P. B. Allen, and J. W. Halley, Phys. Rev. Lett. **38**, 782 (1977).

[147] M. Cyrot, in *The Gap Symmetry and Fluctuations in High-Tc Superconductors*, NATO Science Series: B:, edited by J. Bok, G. Deutscher, D. Pavuna, and S. A. Wolf (Springer US, Boston, MA, 1998) pp. 73–89.

[148] M. Gurvitch, Phys. Rev. B **24**, 7404 (1981).

[149] D. Singh, A. D. Hillier, A. Thamizhavel, and R. P. Singh, Phys. Rev. B **94**, 054515 (2016).

[150] D. A. Mayoh, J. A. T. Barker, R. P. Singh, G. Balakrishnan, D. M. Paul, and M. R. Lees, Phys. Rev. B **96**, 064521 (2017).

[151] Y. Jing, S. Lei, L. Qiang, W. Wei-Hua, and W. Hai-Hu, Chinese Phys. B **18**, 704 (2009).

[152] R. Lortz, Y. Wang, U. Tutsch, S. Abe, C. Meingast, P. Popovich, W. Knafo, N. Shitsevalova, Y. B. Paderno, and A. Junod, Phys. Rev. B **73**, 024512 (2006).

[153] W. L. McMillan, Phys. Rev. **167**, 331 (1968).

[154] A. Carrington and F. Manzano, Physica C **385**, 205 (2003).

[155] B. Ramachandran, J. Y. Jhiang, Y. K. Kuo, C. N. Kuo, and C. S. Lue, Supercond. Sci. Technol. **29**, 035003 (2016).

[156] J. Bardeen, G. Rickayzen, and L. Tewordt, Phys. Rev. **113**, 982 (1959).

[157] J. B. Sousa, J. Phys. C: Solid State Phys. **3**, 2516 (1970).

[158] P. Carruthers, Rev. Mod. Phys. **33**, 92 (1961).

[159] S. Paul, L. S. S. Chandra, and M. K. Chattopadhyay, J. Phys.: Condens. Matter **31**, 475801 (2019).

[160] L. G. Radosevich and W. S. Williams, Phys. Rev. **188**, 770 (1969).

[161] N. Morton, B. W. James, G. H. Wostenholm, and N. S. McCartney, J. Less Common Met. **81**, 321 (1981).

[162] H. Pfau, M. Nicklas, U. Stockert, R. Gumeniuk, W. Schnelle, A. Leithe-Jasper, Y. Grin, and F. Steglich, Phys. Rev. B **94**, 054523 (2016).

[163] A. Kapitulnik, S. A. Kivelson, and B. Spivak, Rev. Mod. Phys. **91**, 011002 (2019).

[164] N. Mason and A. Kapitulnik, Phys. Rev. B **64**, 060504 (2001).

[165] D. Ephron, A. Yazdani, A. Kapitulnik, and M. R. Beasley, Phys. Rev. Lett. **76**, 1529 (1996).

[166] Y. Wang, R. Lortz, Y. Paderno, V. Filippov, S. Abe, U. Tutsch, and A. Junod, Phys. Rev. B **72**, 024548 (2005).

[167] G. Volovik, J. Exp. Theor. Phys. **58**, 469 (1993).

[168] C. Caroli, P. G. De Gennes, and J. Matricon, Phys. Lett. **9**, 307 (1964).

[169] P. E. Gregers-Hansen, M. Krusius, and G. R. Pickett, Phys. Rev. Lett. **27**, 38 (1971).

[170] D. R. Smith and P. H. Keesom, Phys. Rev. B **1**, 188 (1970).

[171] B. Chen, Y. Guo, H. D. Wang, Q. P. Su, Q. H. Mao, J. H. Du, Y. X. Zhou, J. H. Yang, and M. H. Fang, Phys. Rev. B **94**, 024518 (2016).

[172] C. Tien, C. S. Wur, K. J. Lin, E. V. Charnaya, and Y. A. Kumzerov, Phys. Rev. B **61**, 14833 (2000).

[173] M. J. Graf, T. E. Huber, and C. A. Huber, Phys. Rev. B **45**, 3133 (1992).

[174] Y. Liu, M. A. Tanatar, V. G. Kogan, H. Kim, T. A. Lograsso, and R. Prozorov, Phys. Rev. B **87**, 134513 (2013).

[175] M. B. Maple, J. W. Chen, S. E. Lambert, Z. Fisk, J. L. Smith, H. R. Ott, J. S. Brooks, and M. J. Naughton, Phys. Rev. Lett. **54**, 477 (1985).

[176] G. M. Schmiedeshoff, J. A. Detwiler, W. P. Beyermann, A. H. Lacerda, P. C. Canfield, and J. L. Smith, Phys. Rev. B **63**, 134519 (2001).

[177] L. Kuerten, E. Fillis-Tsirakis, C. Richter, J. Mannhart, and H. Boschker, Phys. Rev. B **98**, 054509 (2018).

[178] Z. Ren, M. Kriener, A. A. Taskin, S. Sasaki, K. Segawa, and Y. Ando, Phys. Rev. B **87**, 064512 (2013).

[179] B. Sacépé, J. Seidemann, F. Gay, K. Davenport, A. Rogachev, M. Ovadia, K. Michaeli, and M. V. Feigel'man, Nat. Phys. **15**, 48 (2019).

[180] Y. Nakajima, H. Hidaka, T. Nakagawa, T. Tamegai, T. Nishizaki, T. Sasaki, and N. Kobayashi, Phys. Rev. B **85**, 174524 (2012).

[181] B. Y. Wang, D. Li, B. H. Goodge, K. Lee, M. Osada, S. P. Harvey, L. F. Kourkoutis, M. R. Beasley, and H. Y. Hwang, Nat. Phys. **17**, 473 (2021).

[182] T. V. Bay, T. Naka, Y. K. Huang, and A. de Visser, Phys. Rev. B **86**, 064515 (2012).

[183] E. M. Carnicom, W. Xie, T. Klimczuk, J. Lin, K. Górnicka, Z. Sobczak, N. P. Ong, and R. J. Cava, Sci. Adv. **4**, eaar7969 (2018).

[184] D. A. Mayoh, M. J. Pearce, K. Götze, A. D. Hillier, G. Balakrishnan, and M. R. Lees, J. Phys.: Condens. Matter **31**, 465601 (2019).

[185] S. Arumugam, N. Subbulakshmi, K. Manikandan, M. Kannan, D. A. Mayoh, M. R. Lees, and G. Balakrishnan, Physica C , 1353586 (2019).

[186] H. Yang, G. Chen, X. Zhu, J. Xing, and H.-H. Wen, Phys. Rev. B **96**, 064501 (2017).

[187] R. P. Kaur, D. F. Agterberg, and M. Sigrist, Phys. Rev. Lett. **94**, 137002 (2005).

[188] J. Garaud, M. N. Chernodub, and D. E. Kharzeev, Phys. Rev. B **102**, 184516 (2020).

[189] A. Samoilenka and E. Babaev, Phys. Rev. B **102**, 184517 (2020).

[190] M. Sigrist and D. F. Agterberg, Prog. Theor. Phys. **102**, 965 (1999).

[191] C. Iniotakis, S. Fujimoto, and M. Sigrist, J. Phys. Soc. Jpn. **77**, 083701 (2008).

[192] C. F. Miclea, A. C. Mota, M. Nicklas, R. Cardoso, F. Steglich, M. Sigrist, A. Prokofiev, and E. Bauer, Phys. Rev. B **81**, 014527 (2010).

[193] C. F. Miclea, A. C. Mota, M. Sigrist, F. Steglich, T. A. Sayles, B. J. Taylor, C. A. McElroy, and M. B. Maple, Phys. Rev. B **80**, 132502 (2009).

[194] T. Ideue, S. Koshikawa, H. Namiki, T. Sasagawa, and Y. Iwasa, Phys. Rev. Research **2**, 042046 (2020).

[195] Y. M. Itahashi, Y. Saito, T. Ideue, T. Nojima, and Y. Iwasa, Phys. Rev. Research **2**, 023127 (2020).

[196] R. Wakatsuki, Y. Saito, S. Hoshino, Y. M. Itahashi, T. Ideue, M. Ezawa, Y. Iwasa, and N. Nagaosa, Sci. Adv. **3**, e1602390 (2017).

[197] W. A. Fietz and W. W. Webb, Phys. Rev. **178**, 657 (1969).

[198] W. Henderson, E. Y. Andrei, M. J. Higgins, and S. Bhattacharya, Phys. Rev. Lett. **77**, 2077 (1996).

[199] N. R. Dilley, J. Herrmann, S. H. Han, and M. B. Maple, Phys. Rev. B **56**, 2379 (1997).

[200] A. E. Koshelev and V. M. Vinokur, Phys. Rev. Lett. **73**, 3580 (1994).

[201] M. Hilke, S. Reid, R. Gagnon, and Z. Altounian, Phys. Rev. Lett. **91**, 127004 (2003).

[202] P. Le Doussal and T. Giamarchi, Phys. Rev. Lett. **76**, 3408 (1996).

[203] F. Pardo, F. de la Cruz, P. L. Gammel, E. Bucher, and D. J. Bishop, Nature **396**, 348 (1998).

[204] M. Marchevsky, J. Aarts, P. H. Kes, and M. V. Indenbom, Phys. Rev. Lett. **78**, 531 (1997).

[205] S. Banerjee, S. Mohan, J. Sinha, Y. Myasoedov, S. Ramakrishnan, and A. K. Grover, in *Superconductivity - Theory and Applications - Chapter 4: Nonlinear Response of the Static and Dynamic Phases of the Vortex Matter*, edited by A. Luiz (InTech, 2011) pp. 55–84.

[206] S. Senoussi, J. Phys. III France **2**, 1041 (1992).

[207] P. Chaddah, S. B. Roy, and M. Chandran, Phys. Rev. B **59**, 8440 (1999).

[208] M. Matin, L. S. Sharath Chandra, M. K. Chattopadhyay, R. K. Meena, R. Kaul, M. N. Singh, A. K. Sinha, and S. B. Roy, J. Appl. Phys. **113**, 163903 (2013).

[209] F. Gross, B. S. Chandrasekhar, D. Einzel, K. Andres, P. J. Hirschfeld, H. R. Ott, J. Beuers, Z. Fisk, and J. L. Smith, Z. Physik B - Condensed Matter **64**, 175 (1986).

[210] Y. Paltiel, E. Zeldov, Y. N. Myasoedov, H. Shtrikman, S. Bhattacharya, M. J. Higgins, Z. L. Xiao, E. Y. Andrei, P. L. Gammel, and D. J. Bishop, Nature **403**, 398 (2000).

[211] M. Menghini, Y. Fasano, and F. de la Cruz, Phys. Rev. B **65**, 064510 (2002).